E-632

HIGH RESOLUTION IMAGING OF PARTICLE INTERACTIONS IN A LARGE BUBBLE CHAMBER USING HOLOGRAPHIC TECHNIQUES

A Thesis

Submitted by

Homaira Akbari

In partial fulfillment of the
requirements for the degree of

DOCTOR OF PHILOSOPHY

in

PHYSICS

TUFTS UNIVERSITY

June 1987

FERMILAB
LIBRARY

AA31752

ABSTRACT

Particle interactions were recorded holographically in a large volume of the 15-foot Bubble Chamber at Fermilab. This cryogenic bubble chamber was filled with a heavy Neon-Hydrogen mixture and was exposed to a wide-band neutrino beam with mean energy of 150 GeV. The use of holography in combination with conventional photography provides a powerful tool for direct detection of short-lived particles. Holography gives a high resolution over a large depth of field which can not be achieved with conventional photography.

A high-power pulsed ruby laser was used as the holographic light source. Since short pulses of some 50 ns duration at the required energy were found to give rise to boiling during the chamber´s expansion, a reduction of the instantaneous power at a given energy was required to suppress this unwanted after-effect. This was achieved by developing a unique technique for stretching the pulses using an electro-optic feedback loop.

One hundred thousand holograms were produced during a wide-band neutrino experiment (E-632, 1985) using a dark-field holographic system. Analysis of a sample of holograms shows a resolution of 150 μm was achieved in an ovoidal shape fiducial volume of 0.48 m^3, 3 % of the 14 m^3 total fiducial volume of the chamber.

ACKNOWLEDGMENTS

I would like to thank the E-632 collaboration, the 15-foot Bubble Chamber crew, Tufts University physics department staff, University of Hawaii high energy physics group, and the Fermi National Accelerator Laboratory technical staff.

Dr. R. H. Milburn, my thesis advisor, is thanked for his patience in proof reading this thesis and his continuous support during my graduate work at Tufts.

Among my colleagues, Dr. R. Burnstein, Dr. M. Jones, Dr. D. Jovanovic, Dr. G. Harigel, Dr. D. Morrison, Dr. M. Peters, Dr. J. Schneps, and Dr. W. Smart are acknowledged for providing me with many useful advice and help.

I am especially grateful to my two colleagues and dear friends, Dr. H. Bjelkhagen, and Dr. R. Sekulin.

Marco Incagli and Stephane Willocq are thanked for their help with some parts of this thesis. The Vaughan family are thanked for their kindness during my stay in Hawaii.

I would like to thank my family, in particular my parents –Karamali and Agdhas– and those who have enlightened my life: Azadeh, Laleh, and Sahand.

I would like to dedicate this work to my last year high school classmates, many of whom lost their lives and ideals during Iran´s revolution in 1979.

TABLE OF CONTENTS

Abstract ii

Acknowledgments iii

Introduction 2

Chapter 1 Particle Detection in Bubble Chambers 5

1.1 Heavy Flavor Decays and Tau-Neutrino Observation 5
1.2 Detection of Short-Lived Particles in Bubble Chambers 13
1.2.1 Track Measurements and Impact Parameter 13
1.2.2 Depth of Field Limits to Conventional Photography 16
1.3 The Holographic Solution 19
1.4 Holography 24
1.4.1 Bubble Chambers for Hadron Physics 25
1.4.2 Bubble Chambers for Neutrino Physics 29
1.5 The Fermilab 15-foot Hybrid Bubble Chamber 32
1.5.1 Experimental Setup 32
1.5.2 Operational Mode 38

Chapter 2 Theory of Holography 44

2.1 Basic Theory of Holography 44
2.1.1 Hologram Formation 44
2.1.2 Recording Medium 53
2.1.3 Hologram Reconstruction 60
2.2 Dark-Field Method of Bubble Chamber Holography 70
2.2.1 Historical Summary of Development of the Method 70
2.2.2 Definition of Holographic Parameters 73
2.2.3 Light Scattering from Bubbles 75
2.2.4 Beam Balance Ratio 77
2.2.5 Bubble Movement and Growth 78

Chapter 3 High Power Pulsed Ruby Laser 86

3.1 Characteristics of the Holographic Sources 86
3.1.1 Theory of the Laser 87
3.1.2 Spatial Coherence 92
3.1.3 Temporal Coherence 93
3.1.4 Q-Switching 101
3.2 The Laboratory Laser 105
3.3 The Commercial Laser 108

Chapter 4 Pulse Stretching 111

4.1 Negative Feedback Loop 111
4.2 Pulse Stretching Circuitries 116
4.2.1 2-μs pulse circuitry (Version 1) 116
4.2.2 Characteristics of Pulses Produced by Version-1 Circuit 118
4.2.3 2 - 100-μs pulse circuitry (Version 4) 120

4.2.4 Characteristics of Pulses Produced by Version-4 Circuit 126
4.3 Effect of Back Reflection and High Pumping 135

Chapter 5 Bubble Formation in a Bubble Chamber 138

5.1 Bubble Formation Concepts 139
5.2 Bubble Formation by Ionizing Particles 140
5.3 Laser-Induced Boiling 144
5.4 Experimental Results 146

Chapter 6 Bubble-Chamber Holography: Dark-Field Method 159

6.1 Apparatus 159
6.1.1 Beam Transport and Profile 159
6.1.2 Dispersing Lens 162
6.1.3 The Holographic Camera 166
6.1.4 Holographic Recording Material and Processing 168
6.1.5 Production Mode 174
6.2 Replay Systems 177
6.3 Experimental Data from Test Holograms 180
6.3.1 Resolution 180
6.3.2 Scotchlite Reflections 185
6.3.3 Microboiling 187
6.3.4 Turbulence 188
6.4 Experimental Data from Holograms 191
6.4.1 The Experimental Data 191
6.4.2 Signal Detectability 200
6.4.3 Resolution 211
6.4.4 Holographic Fiducial Volume 212
6.4.5 Holographic Efficiency 223
6.4.6 Pulse Length Dependence 235
6.4.7 Hologram Quality Variation with Ping 239
6.5 Summary 245

Conclusion 247

References 249

Appendix I 259

Ia 5-μs Pulse Circuitry (Version 2) 259
Ib Tens of Microseconds Pulse Circuitry (Version 3) 259

Appendix II 264

IIa Holographic Alignment 264
IIb Holographic Parameter Codings 267

Appendix III 268

HIGH RESOLUTION IMAGING OF PARTICLE INTERACTIONS IN A LARGE BUBBLE CHAMBER USING HOLOGRAPHIC TECHNIQUES

INTRODUCTION

Since the discovery of the J/ψ particle in November 1974, there has been an increasing interest to search for the particles containing heavy-flavor quarks, (charm, bottom,...). These charm and bottom particles, as well as the heavy lepton (τ), have lifetimes of the order of 10^{-12} - 10^{-13} s which are shorter than many previously observed lifetimes, (~ 10^{-10} s for K_s^0, $\Sigma^{\pm}$,...).

Short-lived particles and their decay products can be efficiently identified using a high precision vertex detector. A high resolution vertex detector allows a close investigation of the interaction point and an accurate association of the tracks to their corresponding vertices on individual events which is essential for a detailed study of production mechanisms. There exist a number of possible designs for vertex detectors. The ideal vertex detector depends on the specific experimental application and the physics aims which are expected to be achieved using the vertex detector.

Large-volume bubble chambers equipped with high-resolution imaging systems are the most prominent vertex detectors for studying neutrino produced charm particles, tau-leptons, and most importantly for obtaining direct evidence of the tau-neutrino existence.

Since neutrino beams have large dimensions, (cross sectional diameters of ~ 2 m), the optical imaging system must be capable of obtaining high resolutions, (~ 100 μm) necessary for efficient detection of short-lifetimes of $\lesssim 10^{-12}$ s, over large depths of field, (~ 2 m). In conventional photography, improving the resolution results in a rapid decrease of the depth of field, (resolution $\propto 1/a$; depth of field $\propto 1/a^2$; where a is the aperture diameter), thereby resulting in a small usable photographed volume. Using holography

to supplement conventional photography remedies this problem. Holography decouples resolution and depth of field, and achieves a high resolution over a long depth of field, (resolution α 1/a; where a is the size of holographic film used; depth of field α coherence of the two interfering wavefronts).

In a large bubble chamber, there are two methods to illuminate the bubble tracks holographically. One is to illuminate the tracks from the bottom of the chamber (dark-field illumination). The other method is to illuminate the tracks using light reflection from the retrodirective Scotchlite which lines the walls and bottom of the 15-foot Bubble Chamber (bright-field illumination). For the reference beam, various geometries can be considered depending on the medium it travels through and the angle it exposes the holographic film.

Two holographic techniques, dark- and bright-field schemes, have been proposed and studied for the 15-foot Bubble Chamber. In the dark-field scheme a single beam entering the chamber from the bottom provides both the reference and object beams. The reference beam exposes the film at zero angle (In-line holography). The object beam illuminates the tracks from behind, and the bubbles appear as bright spots against a black background. In the bright-field scheme the reference and object beams travel through optical fibers. The reference beam exposes the film at an angle (Off-axis holography). The object beam illuminates the chamber from the top, and the bubbles appear as black spots against the bright background light retrodirected from scotchlite. The dark-field scheme has been tested in the laboratory and used in the 1985 E-632[1] physics run (Bjelkhagen et al., 1984b; Harigel et al., 1984; Akbari and Bjelkhagen, 1986). The bright-field

1. See Appendix III for the list of E-632 collaboration.

scheme has been tested in the laboratory (Pouyat, 1981; Royer, 1981; Bjelkhagen et al., 1984d; Bjelkhagen, Sekulin, and Walton, 1984e). This document aims to present the theoretical and technical aspects of the dark-field technique.

The organization of this dissertation is as follows: Chapter 1 gives the experimental motivation and a summary of early experiments in which holographic techniques have been used. Chapter 2 gives the developmental history and discusses the theoretical aspects of the dark-field holographic method after a summary of the general theory of holography. Chapters 3 and 4 describe the characteristics of the illuminating source, the electro-optic feedback loop, and the light pulses produced by the laser equipped with the feedback loop. In Chapter 5 is given the experimental information as well as the theoretical concepts to explain the bubble formation induced by light in the bubble chambers. In Chapter 6 the experimental arrangements for the dark-field scheme are described and the experimental results from the 1984 - 1985 holographic tests and physics run are presented. The thesis is concluded with a discussion of future prospects for the 15-foot Bubble Chamber holographic techniques.

CHAPTER 1 PARTICLE DETECTION IN BUBBLE CHAMBERS

1.1 Heavy Flavor Decays and Tau-Neutrino Observation

Quarks and leptons are grouped in three doublets in the standard model. At present strong evidence for the existence of ten of these twelve entities have been accumulated, and their lifetimes are measured rather accurately (Table 1.1).[2] The existence of the top quark, t, and the tau-neutrino, ν_τ, has yet to be established. A more extensive study of tau-lepton, charm, and bottom particles is necessary to obtain a complete knowledge of their production mechanisms and properties.

Particles and their Approximate Lifetimes			
Quarks		Leptons	
u	d	e	ν_e
(1969)	(1969)	(1896)	(1934)
stable	stable	stable	stable
c[2]	s	μ	ν_μ
(1974)	(1969)	(1937)	(1962)
~ 10^{-13} s	10^{-10}–10^{-8} s	10^{-6} s	stable
t	b	τ	ν_τ
?	(1977)	(1975)	?
	~ 10^{-12} s	~ 10^{-13} s	

- Table 1.1 -

2. Typical lifetime of particles containing charm quark.

Charm, Bottom, and Tau-Neutrino Production in Fixed Target Experiments

In fixed target experiments, charm searches are limited by large backgrounds from processes involving only the u, d, and s quarks. The relative ratio of charm to non-charm hadron production is strongly dependent on the nature of the beam. Table 1.2 gives the order of magnitude of charm production cross section, (Derrick, 1981), and the relative production rate of charm, bottom, and tau-neutrino by hadron, photon, and neutrino beams, (Morrison, 1981). The precise values for the cross sections are a function of the beam energy and vary from one experiment to another.

Beam	Charm Prod. Cross Section (approx.)	Charm Events / All Events	Beauty Events / All Events	Tau Events / Charm Events
Hadron	20 - 100 μb	0.1 %	0.01 %	---
Photon	0.5 - 1 μb	1.0 %	---	---
Neutrino	10^{-38} cm^2	10 %	---	0.1 %

- Table 1.2 -

The charm to non-charm hadron production ratio is much higher in neutrino interactions (~ 10 %) as compared to photon and hadron interactions (~ 1 % and 0.1 %, respectively). However, the absolute cross section of the neutrino-produced charm is small. This can be compensated for by using a long running period and a large-volume detector.

In all three cases, beauty production has very low rates due to its dependence on the mixing angles of the Kobayashi-Maskawa matrix. For neutrino interactions, the ratio of bottom to overall production cross section is less than 0.01 %, as compared to ~ 10 % for charm production, (Derrick, 1981).[3] This and the very small total cross section makes bottom-production studies using a neutrino beam very difficult.

Two main sources of tau-neutrinos are: a) from neutrino oscillations, and b) from the decay of D_s-mesons. Since the branching ratio of the D_s-meson decaying into the tau-neutrino is small, ~ 2 %, the search for the tau-neutrino via tau-lepton detection in hadron and photon interactions is difficult. For neutrino beams, the first possibility has been investigated by experiment-531 group, (Reay et al., 1981; Ushida et al., 1986). No taus were found, and the limit obtained for the direct coupling of $\nu_\mu \nu_\tau$ was less than 0.2 % at the 90 % confidence level, (loc. cit.). The second possibility can be investigated with reasonable statistics using high energy accelerators such as the Tevatron at Fermilab.

Charm Production in Neutrino Experiments

The production mechanisms of charm particles in neutrino interactions are well-understood. The predominant quark transitions for charm particle production by neutrino and antineutrino beams, and the subsequent weak decays of the charmed hadrons are shown in Figure 1.1. For νN interactions, the charm production rate is ~ $d(x)\sin^2\theta_c + s(x)\cos^2\theta_c$; for $\bar{\nu}$N interactions, the charm production rate is ~ $\bar{d}(x)\sin^2\theta_c + \bar{s}(x)\cos^2\theta_c$. The former is inhibited due to the $\sin^2\theta_c$ term for the d-valence quark, and the

3. This is a theoretical value calculated for most favorable quark-quark transition (u → d) for bottom production.

necessity of using an s-quark from the $s\bar{s}$ sea; the latter is inhibited due to using sea quarks, $\bar{d}$ and $\bar{s}$, as well as the suppression imposed on the $\bar{d}$ term due to $\sin^2\theta_c$. From experimental data it is shown that the overall production rates of charmed particles are ~ 10 % in νN and 5 % in $\bar{\nu}$N interactions, (Derrick, 1981). Charmed particles subsequently decay weakly to strange particles (Cabibbo-allowed) or to non-strange particles (Cabibbo-suppressed) with lifetimes of ~ 10^{-13} seconds.

In neutrino experiments, the charm events are identified by observing a second opposite-sign lepton in the final state of an interaction ($\mu^-\mu^+$, μ^-e^+ for ν_μ beam, and μ^+e^-, $\mu^+\mu^-$ for $\bar{\nu}_\mu$ beam). The second muon in the 2μ final state is identified by a minimum momentum cut of 4 to 6 GeV/c both in the counter and bubble chamber experiments, (Fisk, 1981). This cut eliminates a large portion of the charm signal. However, for μe final states which are readily identified in the bubble chamber experiments, a lower cut on the electron's momentum, typically $p_e > 0.3$ GeV/c, eliminates only a small fraction of the charm signal, (loc. cit.). The K^* production also gives another definite signature in identifying the charmed states in the bubble chamber experiments.

It should be mentioned here that observation of 2μ like-sign final states is another interesting topic which can be studied by neutrino experiments. The second muon seems to originate at the secondary hadron vertex and several possible mechanisms are suggested for its production. One of these processes is bottom production at the primary hadronic vertex decaying to charm, which, in turn can give a muon of the same sign as the muon produced at the primary leptonic vertex. The experimental data for like-sign

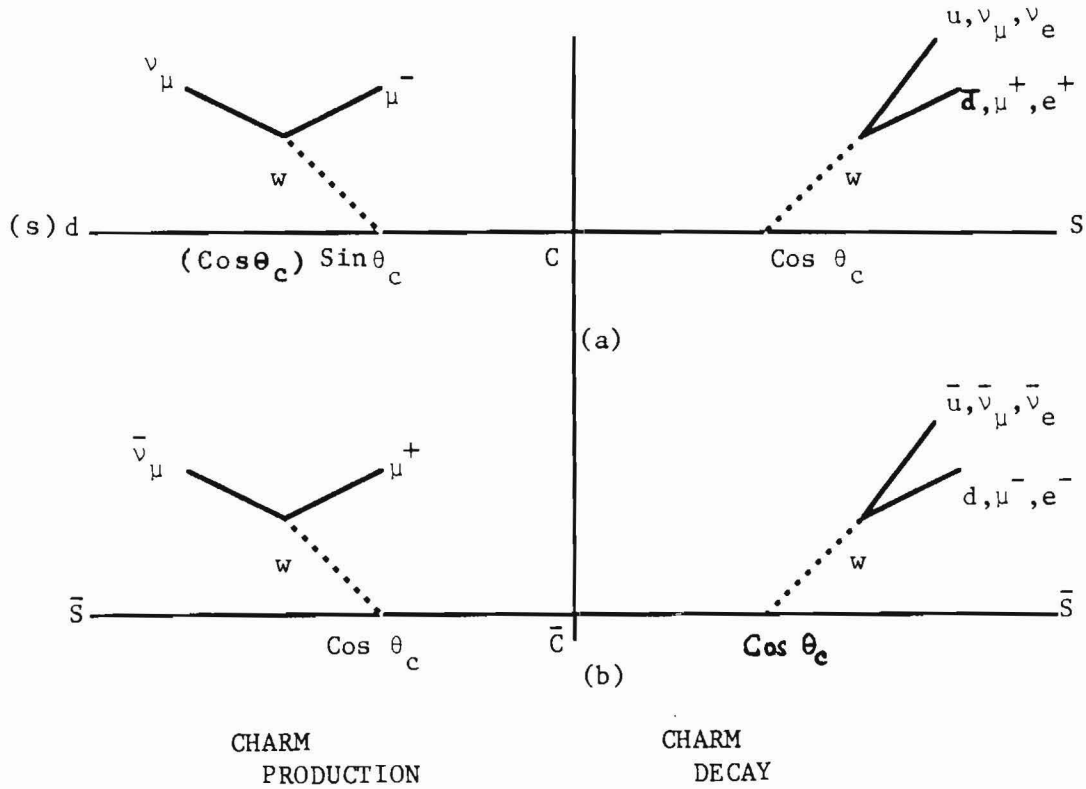

Fig. 1.1 Diagrams for charm production by (a) neutrinos and (b) antineutrinos, and subsequent charm decay, (Trilling, 1981).

$$P + \text{dump} \longrightarrow D_s^{\pm} + D_s' + \ldots$$

$$D_s^+ \longrightarrow \tau^+ + \nu_\tau$$

$$\hookrightarrow \bar{\nu}_\tau + \text{hadrons}$$

(a)

$$\nu_\tau + N \longrightarrow \tau^- + \text{hadrons}$$

$$\hookrightarrow \nu_\tau \text{ hadrons}$$

$$\mu^- \bar{\nu}_\mu \nu_\tau$$

$$e^- \bar{\nu}_e \nu_\tau$$

(b)

Fig. 1.2 (a) Production of ν_τ beam in a neutrino beam-dump experiment, and (b) detection of ν_τ through a τ lepton decay.

dilepton production rate are larger by one or two orders of magnitude than the theoretical rate.[4]

Tau-Neutrino Production

Since the discovery of the tau-lepton by Perl et al. (1975) a question has arisen whether the tau-lepton is coupled to a new neutrino, the tau-neutrino (ν_τ), composing the third doublet in lepton groups. The most prominent experiment for verifying the existence of ν_τ is a neutrino beam-dump experiment. In such an experiment, an enriched beam of "prompt" ν_τ is produced from the decay of charmed D_s-mesons into $\tau\nu_\tau$, (Figure 1.2). Reasonable fluxes of D_s-mesons can only be expected from a high energy proton beam incident on a dense target since the threshold for producing strange charmed mesons is high. Both D_s and τ have short lifetimes and are expected to decay before they are absorbed in the dump. On the other hand the secondary π's and K's will be typically absorbed in the dump before they decay. The main background is from other types of neutrinos produced by decay of charmed particles.

A tau-neutrino will interact with nucleons in the target and produces a τ and other hadrons; the τ-lepton will subsequently decay either semileptonically into a visible electron or muon, or hadronically into one or more visible charged hadrons. Thus the most direct signature for the existence of the tau-neutrino is interactions with a secondary vertex of tau decay, and with no muon or electron coming from the primary vertex.

---

4. However, recent results from CCFR collaboration at Fermilab have shown no significant signal (Merritt, et al., 1987).

Detection of Short-Lived Particles; Vertex Detectors

The detection and lifetime measurements of heavy leptons and hadrons with heavy-flavor quarks require detectors with high efficiencies for providing accurate event location and detailed information on the decay products, and with high spatial resolutions for identifying the decays with different mean-lives and measuring proper flight-times. The latter requires a powerful vertex detector.

Decay vertex and parent identification are essential for lifetime determination and also constitute an effective method to study the other properties, including the spectroscopy of higher mass states.

The experimental difficulties of decay vertex detection of short-lived particles with mean lifetimes $\sim 10^{-13}$ s (e.g. the $D^{\bullet}$) is that their flight-paths before decay is $\sim (p/m)c\tau \lesssim (p/m) \times 30\ \mu m$,[5] thus ranging between several hundred micrometers to a few centimeters. This requires a vertex detector with a spatial resolution better than several tens of micrometers. The most ideal vertex detector is one that tags short-lifetime particles by precisely measuring the impact parameter of their decay products, and efficiently assigning the tracks to their correct parents.

Some of the common vertex detectors are nuclear emulsion, bubble chamber, drift chamber, and silicon detectors. The first two are visual, non-electronic detectors, and can only be used in fixed target experiments. The last two are electronic detectors, and can be used both in fixed target and collider experiments. The silicon detectors are most promising and variety of them are commonly used in many different experiments. They have high spatial and energy resolutions.

---

5. See Section 1.2 for a more quantitative discussion of short-lived particles' flight-paths and impact parameters.

In case of the nuclear emulsion, the vertex detector is followed by a multiparticle spectrometer. Despite their high spatial resolutions (~ 1 μm), nuclear emulsions can not be used for systematic studies of heavy flavors for a number of disadvantages: the absence of time resolution to be used for triggering, and the slow processes of linking the tracks into emulsion and volume scanning for neutrals. High precision bubble chambers equipped either with a downstream spectrometer (in case of small bubble chambers) or with a set of proportional chambers (in case of large bubble chambers) can also be used as a "visual" vertex detector. The spatial resolutions of these chambers varies in range of 10 - 100 μm; their imaging systems can be selectively triggered using the electronic counters which reduces the scanning effort. Thus, although bubble chambers have a lower spatial resolution for detecting the short-lived particles than do the emulsion detectors, the events are easier to locate and to measure using a bubble chamber detector.

1.2 Detection of Short-Lived Particles in Bubble Chambers

1.2.1 Track Measurements and Impact Parameter

Locating and measuring decay lengths of short-lived particles near the primary production vertex has a limited efficiency. This efficiency is a function of the bubble density along the track, the track multiplicity, and the momentum of the event products. Low bubble densities can create long gaps faking a short-lived neutral decay. High track multiplicity and momentum of the event can result in many high momentum leaving tracks in the forward cone, obscuring secondary vertices which are close to the primary vertex. In this case, the decay can be detected by the impact parameter.

Impact parameter measures the distance by which the trajectory of a charged particle coming from a secondary vertex misses the production vertex. Figure 1.3 shows an example of such an interaction, and gives a sketch of the definitions of the decay length, the impact parameter, and other related quantities.

For a particle, P, decaying into several products, the following can be defined:

c	:	speed of light.
B_x	:	impact parameter of one of the decay products in the laboratory frame,
L_p	:	decay length of the parent in the laboratory frame,
τ_p	:	proper decay time of the parent production,
$\beta_p = v_p/c$	:	velocity of the parent in the laboratory frame,
γ_p	:	$(1 - \beta_p^2)^{-1/2}$,
θ_x	:	production angle of the decay product in the laboratory frame,

θ'_x : production angle of the decay product in the rest frame of the parent,

E'_x : energy,

P'_x : momentum, and

$\beta'_x = v'_x/c$: velocity of the decay product in the rest frame of the parent.

The impact parameter and decay length can then be written:

$$B_x = L_p \tan\theta_x \qquad [1.2.1]$$

$$L_p = \beta_p c \gamma_p \tau_p, \qquad [1.2.2]$$

with $\tan\theta_x$ expressed as, (Costa et al., 1979):

$$\tan\theta_x = \frac{P'_x \sin\theta'_x}{\gamma_p(\beta_p E'_x + P'_x \cos\theta'_x)} = \frac{\sin\theta'_x}{\gamma_p((\beta_p/\beta'_x) + \cos\theta'_x)} \qquad [1.2.3]$$

For β_p and $\beta'_x \simeq 1$, and assuming that the average decay angle in the rest frame of the parent, $\langle\theta'_x\rangle$, is 90°, we have

$$\tan\theta_x = 1/\gamma_p. \qquad [1.2.4]$$

Substituting Equations [1.2.2] and [1.2.4] in [1.2.1], an expression for the impact parameter is obtained which depends on the proper decay time of the parent and is independent of the momentum.

$$B_x \simeq c\tau_p. \qquad [1.2.5]$$

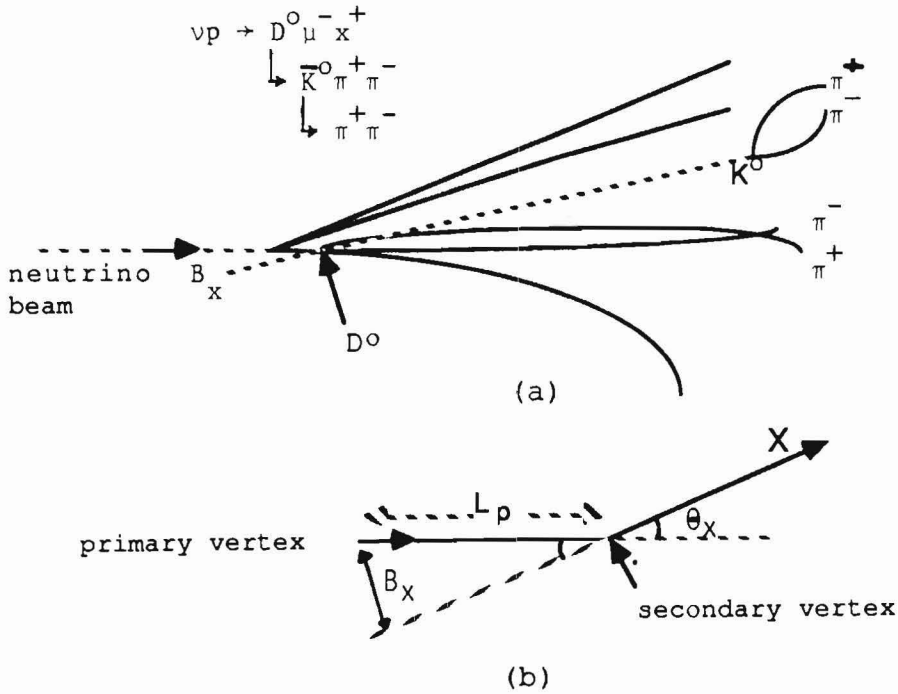

Fig. 1.3 Impact parameter. a) An example of a bubble chamber event with a secondary vertex and its impact parameter, b) definition of the impact parameter and decay length.

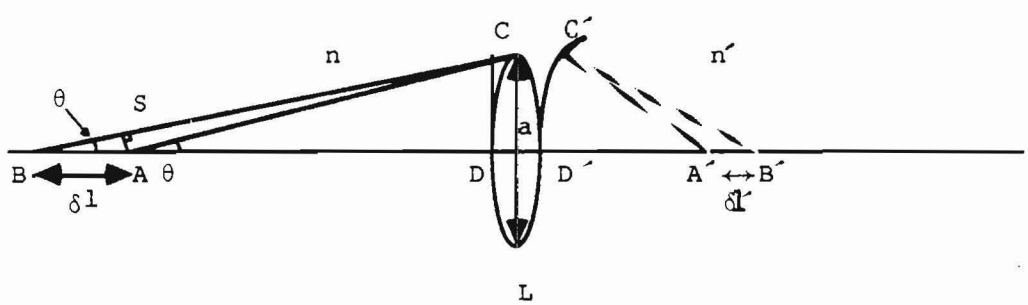

Fig. 1.4 Depth of focus.

For a typical decay of a D_s-meson with momentum of 10 GeV/c, mass of 2 GeV, and lifetime of 1.9×10^{-13} s, L_p is about 300 μm and B_x is about 60 μm.

For an efficient detection of a secondary vertex the smallest impact parameter is required to be $B_x \sim c\tau_p \geq 3\sigma$, where σ is the error on the position measurement of the track. The precision for which the tracks are measured in the 15-foot Bubble Chamber can be reduced to one-tenth bubble diameter, (or track width), i.e. $\sigma \sim b/10$, where b is the bubble diameter. For $c\tau_p \geq 3b/10$, the bubble diameter of the track images have to be $\leq$ 180 μm for the above example. Thus, a high resolution imaging system capable of resolving bubble images of diameter of $\leq$ 180 μm must be used in the 15-foot Bubble Chamber in order to efficiently search for short-lived particles.

1.2.2 Depth of Field Limits to Conventional Photography

In conventional optics both resolution and depth of field depend on the aperture of the viewing lens. An increase in the lens aperture results in better resolution but a smaller depth of field.

Resolution for an imaging system with a circular aperture is defined using the Rayleigh criterion. This criterion is based on the fact that a lens system forms an image of a point source in an Airy pattern. The radius of the Airy disk (central circular spot) is given by $r_1 = 1.22(\lambda U/a)$ where U is the object distance and ´a´ is the aperture of the lens (Born and Wolf, p. 419, 1964). Two point sources adjacent to each other are regarded as resolved when the center of the Airy disk of one falls on the edge of the other (in other words, on the first minimum of the Airy pattern of the

other). Thus the centers of the two images have to be separated by at least

$$R = (\Delta l)_{min} = 1.22(\lambda U/a), \qquad [1.2.6]$$

which defines the resolution limit ("diffraction limit") of the system.

The depth of field of a lens[6] is defined as the distance that an object in focus can be moved along the optical axis before its image is out of focus. An expression for the depth of field can be derived using geometric or physical optics. Here the physical optics approach is taken since it is closely tied to the expression for the resolution.

An object in focus by the lens L at position A, (Figure 1.4), can be moved to a position B and still be in focus as long as the phase shifts induced in the object wavefronts at the lens do not exceed $\pi/2$. This maximum allowable phase shift corresponds to a maximum allowable optical path difference of $\lambda/4$. Now assuming a large object distance, AD >> a, and an index of refraction of 1 for the propagation medium an expression for depth of field, d_f, can be derived. Note that for an infinitesimal δl, $\delta l << AD$, both angles at A and B can be set as θ.

---

6. Depth of field and depth of focus of a lens are closely related. Depth of focus is the distance that the imaging screen can be moved along the optical axis before the image is out of focus. The derivation of depth of focus is parallel to that of depth of field and the two are related by the square of the lens' transverse magnifying power, $\delta l_{focus} = m^2 \delta l_{field}$, for a simple and symmetric lens.

$$P_1 = AD - AC \qquad \text{for in focus case}$$

$$P_2 = BD - BC \qquad \text{for out of focus case}$$

$$P_2 - P_1 \leq \lambda/4 \qquad \text{Rayleigh Criterion}$$

$$(BD - BC) - (AD - AC) = \lambda/4$$

$$(BD - AD) - (BC - AC) = \lambda/4$$

$$\delta l - \delta l \cos\theta = \lambda/4$$

$$2\delta l \sin^2(\theta/2) = \lambda/4 \quad ; \quad \sin\theta = (a/2)/AD$$

$$\delta l = 2\lambda(U/a)^2 \quad \text{for small } \theta \quad ; \quad AD = U$$

$$d_f = 2\delta l = 4\lambda(U/a)^2 \qquad [1.2.7]$$

And an expression for the resolution in terms of depth of field can be written

$$R = 0.52 \sqrt{\lambda d_f} \qquad [1.2.8]$$

A conventional 15-foot Bubble Chamber camera with resolving power of 500 μm at an object distance of 2 m has a depth of field of 200 cm while a high resolution camera with resolving power of 100 μm has a depth of field of about 10 cm. Such a high resolution imaging system is not desirable for the 15-foot Bubble Chamber with a total volume of 35 m^3.

1.3 The Holographic Solution

The key advantage in using holography is that it is capable of obtaining a high resolution with large depth of field. Its three-dimensional reconstructed image is also useful in that it is not necessary to have separate stereoscopic cameras to locate a vertex position in space. Furthermore, it allows the recording of a large number of interactions per hologram. This is due to the fact that tracks at different depths in the chamber are not all in focus at the same time at a given image location at reconstruction stage.

In holography, as we are still working with the same diffraction phenomena, the earlier resolution limit argument remains valid. However, here the factor of 1.22 is replaced by 1.54 since the object is illuminated by coherent light (Born and Wolf, p. 424, 1964). For orthogonal directions to the hologram field of view axis, the lateral resolution, R_l, is thus

$$R_l = 1.54(\lambda U/a), \qquad [1.3.1]$$

where ´a´ is the usable hologram diameter at the reconstruction stage assuming no lenses or other limiting apertures are present. The resolution in depth, (the direction of the hologram´s field of view), is however, smaller than in the lateral directions for a reconstructed image. Here the holographic system is analogous to an ordinary imaging system, and the resolution in depth, R_d, is the same as δl, Equation [1.2.7], (Hariharan, p. 168, 1984),

$$R_d = 2\lambda(U/a)^2 = 1.3R_l(U/a). \qquad [1.3.2]$$

Thus, at any one time one can only resolve a region of image of dimension about $R_l \times R_l \times R_d$; the focus has to be adjusted in order to bring new parts of the image into a clear focus. Throughout this dissertation the symbol R is used to indicate the lateral resolution of a holographic system.

The depth of field of a holographic system is no longer limited by the allowable variation in phase shift of the object beam rays. It is limited by the amount of coherence of the two interfering beams generating the hologram. This coherence is a function of both the laser quality in transverse and frequency mode selection, and the path length difference between the object and reference beams. For large objects, the object beam arrives at the hologram at times spread by the range of paths. For a laser with narrow bandwidth, the allowable time delays can be very large. Section 3.1.3 treats this subject in more detail.

An expression for the depth of field of a holographic system can be derived using an approximate approach in geometrical optics. Let us use the criterion that in order to obtain a good hologram of an object with a diameter ´d´, it is required that the central maximum and at least three side orders of its diffraction pattern be recorded and resolved (Hariharan, p. 175, 1984), (Figure 1.5). This is in principle the equation for the resolution, (Equation [1.3.1]), where its right-hand side is multiplied by a factor 4.

$$a/2 = (4 \times 1.54U\lambda)/d. \qquad [1.3.3]$$

It is convenient to express the object distance, U, in terms of the object size and the light wavelength. 'U' can be written as a multiple, n, of far-field distances, where one far field distance is defined as d^2/λ. Substituting this expression for U in Equation [1.3.3] it follows,

$$a/2 = 6.2 \times nd. \qquad [1.3.4]$$

Geometrically, the path difference between the two beams, δ, is $((a/2)^2/U)$, and combining this with Equation [1.3.3], an expression δ for can be obtained.

$$\delta = 38 \times n\lambda \qquad [1.3.5]$$

The maximum allowable path difference between the two beams is called the coherence length, l_c. In order to obtain an interference pattern of the two beams, l_c has to be equal or greater than δ.

$$l_c \geq 38 \times n\lambda \qquad [1.3.6]$$

As long as the Equation [1.3.6] is satisfied for a given holographic system, the maximum recordable range of an object with diameter d, using Equation [1.3.3], is given by,

$$U_{max} = ad \ / \ (12.3 \times \lambda). \qquad [1.3.7]$$

Equation [1.3.7] shows that the depth of field of a holographic system is directly proportional to the hologram size; an increase in the hologram size results in both a better resolution and longer depth of field. In this manner holography decouples the problems of achieving high resolutions and large depths of field which are intrinsically incompatible in a conventional lens-based photographic system.

The disadvantage of holography is that it does not give a simultaneous, overall image of the bubble chamber volume at the reconstruction stage. The scanning and measuring of the entire chamber volume is a tedious and slow process. To use holography most efficiently, it must be combined with the conventional photography from which the coordinates of the events can be obtained by a quick scan and measurement. The holograms can then be used for a detailed study of the vertex region. In this context holography is not an independent technique.

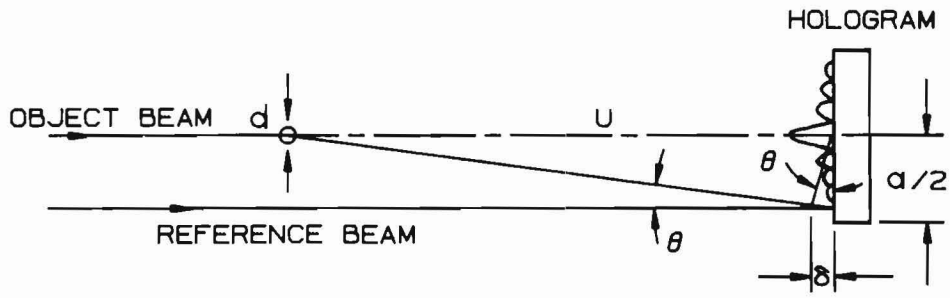

Fig. 1.5 Holographic coherence parameters.

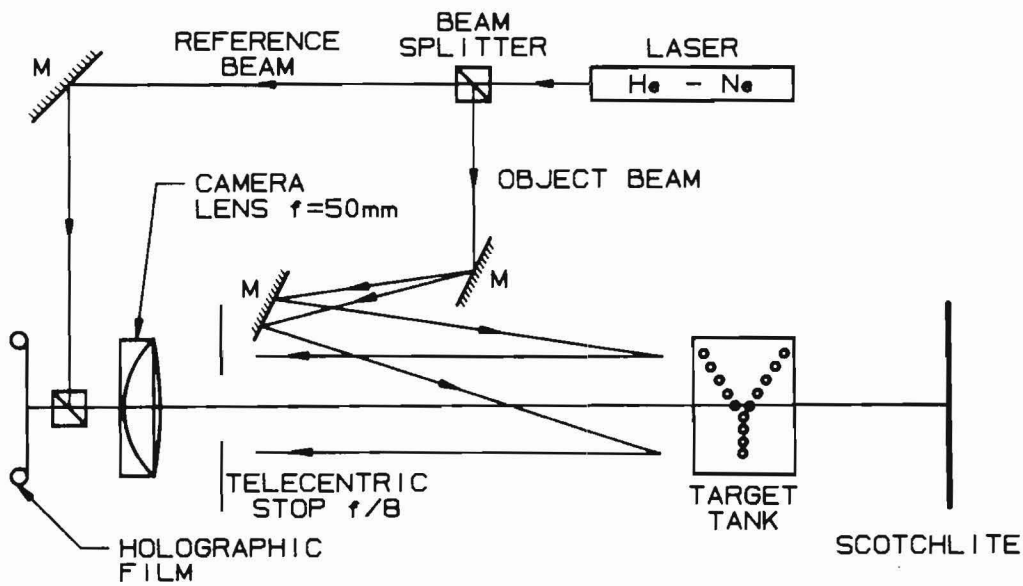

Fig. 1.6 Experimental arrangment for taking holograms of a mock bubble chamber.

1.4 Holography

The concept of using holography in high energy physics where a visual detector is the means of recording particle interactions is not new. Holographic techniques have already been developed and used for the collection of physics data from various types of bubble chambers. The development of this technique for streamer chambers, (Eckardt, Lecoq, Wenig, Wiatrowski, 1984; Majka, 1984), and large volume bubble chambers is in progress. This section will summarize the main work in this field.

The idea of using holography in bubble chambers to overcome the focal depth problem of conventional photography was first mentioned by Welford (1966). He proposed the use of a telecentric lens to form images of bubble tracks near the photographic emulsion, (Figure 1.6). The interference of the diverging wavefronts of these images with almost plane wavefronts of the reference beam forms an image-plane hologram. This system was designed to avoid some of the difficulties (not then solved) in forming holograms and yet to exploit their focal depth property. These difficulties arose from the unavailability of high resolution photographic emulsions, the impracticality of using film whose flatness is crucial for accurate reconstruction of the images, and the Faraday rotation of the object beam polarization by the magnetic field. However, the similarity of image plane holograms to ordinary photographs facilitates quick scanning of holograms on conventional projection tables prior to holographic scanning. By 1970 the first designs of such a system had already been tested in the laboratory under simulated bubble chamber conditions (Welford, 1970; Withrington, 1970; Dainty, 1972). Bright field illumination of targets simulating 500 μm bubble tracks in liquid

hydrogen was achieved by using Scotchlite[7] as the retrodirective source, (Figure 1.6). Successful holograms with moderately good diffraction efficiency (contrast and brightness) were made, demonstrating the capability of holograms to achieve the required depth of field.

These ideas, despite their attractiveness for decoupling the depth of field and resolution parameters, did not seem practical due to the lack of sufficiently powerful pulsed lasers with long coherence length, and the lack of photographic films with high enough resolution.

Interest in holography for bubble chambers was revived in the late 1970's in the search for the new massive short-lived particles with lifetimes as small as 10^{-14} s (Eisler, 1979).

1.4.1 Bubble Chambers for Hadron Physics

Small, rapid-cycling bubble chambers equipped with the high resolution imaging systems can be used as vertex detectors with a downstream spectrometer in dense hadron beams. The use of a high resolution vertex detector is necessary to study the heavy-flavor state production mechanisms and to observe their decays. Purely electronic detectors are difficult to use as a result of the large combinatorial backgrounds, the large number of decay modes, and the small cross sections of hadroproduced short-lived states (cf. Section 1.1.2). Furthermore, the purely electronic detectors provide only an indirect method for observing these states. Using a visual high resolution vertex detector in combination with electronic counters provides a method to

---

7. Tradename for a retrodirective material, manufactured by Minnesota Mining & Manufacturing Company (3M), that sends incoming light back almost parallel independent of its angle of incidence up to ~ 60°. The interior of the bubble chamber is wall-papered with Scotchlite.

directly "see" the decays of the states, along with a restrictive trigger to reduce the amount of scanning, and powerful particle-identification mechanisms. In such cases, holography can be used as the high resolution optical system for the small bubble chambers.

The first feasibility test of holography in a small bubble chamber BIBC (Berne Infinitesimal Bubble Chamber) was successful (Dykes et al., 1981). The success of this test led to proposals for construction of several small holographic bubble chambers. HOLEBC (HOlographic LExan Bubble Chamber) and HOBC (HOlographic Bubble Chamber), were built to include holographic recording of the particle tracks explicitly (Allison et al., 1980; Baland et al., 1980). The total visible fiducial volume was about 1200 cm^3 for HOLEBC and HOBC and 116 cm^3 for BIBC.[8]

Holographic schemes were tested and used in BIBC and HOLEBC exposed to a particle beam in feasibility tests (Dykes et al., 1981; Ramseyer, Hahn, Hugentobler, 1982; Sekulin, 1981), and in HOBC in CERN experiment NA25 (Hervé et al., 1982). An in-line (Gabor) method was used in all three chambers where a single collimated beam illuminated the chamber volume through one of the windows, (Figure 1.7). This beam formed both the reference beam and the object beam which consisted of the wavefronts diffracted by the track bubbles. The holographic film was placed on the other side of the chamber. As holographic light sources pulsed lasers (pulse duration between 10 - 1000 ns) with repetition rates ~ 30 Hz[9] and

---

8. The dimensions for the three bubble chambers are as following, BIBC: 65 mm diameter x 35 mm depth; HOLEBC: 12 cm length x 7 cm depth x 5 cm height; HOBC: 5 x 6 x 11 cm^3.

9. For BIBC tests a ruby laser with repetition rate of about 1 pulse/s was used, but the authors noted that this laser was unsuited for the physics run.

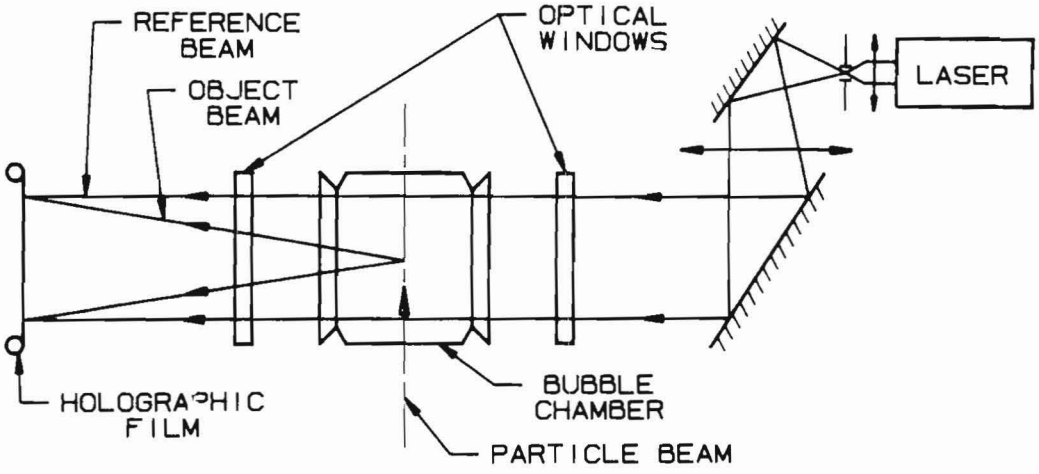

Fig. 1.7 A typical optical layout used for in-line method in small bubble chambers.

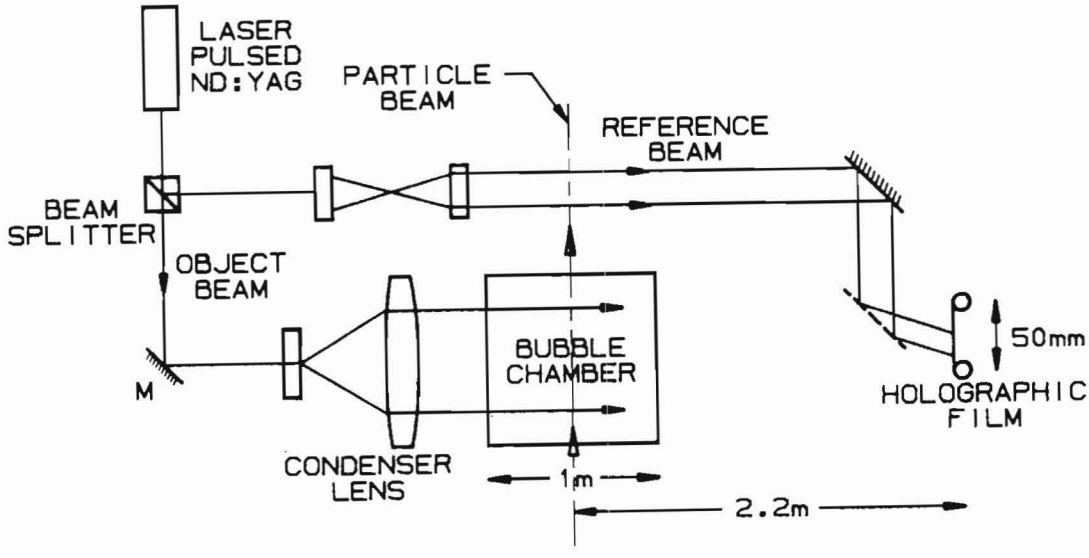

Fig. 1.8 Optical set-up for taking holograms in Tohoku bubble chamber.

maximum output energy of ~ 200 mJ were used (but only about 3 mJ was used for making the holograms in HOBC).

The results from these tests and experiments can be summarized as follows.

1. Good holograms were made of particle beam tracks and interactions over the whole volume of the small bubble chambers with resolution of 10 μm when the bubble chambers were operated under suitable conditions.
2. A large number of tracks (maximum of a few hundreds) can be recorded per hologram, a fact particularly useful when interaction cross-sections (or rates) are small (low).
3. The authors demonstrated the feasibility of operating holographic bubble chambers in a magnetic field. For the in-line setup both the reference and object beams polarization rotate (due to the Faraday effect) in the same way and the interference pattern remains unchanged.
4. Adverse effects of turbulence were observed in holograms when the bubble chamber was operated at a high repetition rate and/or to produce fast bubble growth. The turbulence distorted both the reference and object beam wavefronts giving variations in phase and amplitude of the beams.

Furthermore, Benichou et al. (1983) compared holograms made in HOBC with an in-line arrangement, where both the object and reference beams passed through the bubble chamber, and with a two-beam arrangement, where the reference beam traveled separately through air. It was found that the effects of turbulence was similar for both types of

holograms. The contrast of the bubble images was, however, better for the in-line holograms. They concluded that to minimize the effects of turbulence the bubble chamber should be operated under conditions for which the rates of growth of the bubbles would be small.

1.4.2 Bubble Chambers for Neutrino Physics

The success of holographic techniques for the small chambers encouraged the utilization of these techniques in the bigger bubble chambers required to study neutrino interactions and in which a large depth of field is essential. Since neutrinos are neutral and are made from pion and kaon decays, the neutrino beam cannot be focused and thus its dimensions are large. For the 15-foot Bubble Chamber at a distance of 1.5 km from the production target, about 86 % of the neutrino events are in a cross sectional area of diameter 1 m centered at the y-z bubble chamber plane, and about 100 % of the events are in an area of diameter of 2 m.

Using a neutrino beam to study charm production has two advantages over using hadron or photon beams. 1) The charm production ratio is much higher for neutrino beams, ~ 10 %, as compared to that in hadron and photon beams, ~ 0.1 % and 1 %, respectively; 2) the strange particle production rate, which is the main source of background for the charm particles, is smaller, (Morrison, 1981). Furthermore, using a neutrino beam-dump, the production of τ leptons by the ν_τ could be extensively studied.

Holographic systems have been proposed, developed, and tested for two large bubble chambers: the Tohoku Bubble Chamber (Haridas et al., 1985), and the 15-foot Bubble Chamber at Fermilab (Bjelkhagen et al., 1984). These bubble chambers have large fiducial volumes, ~ 0.5 and 14 m^3,

respectively. The first operation of both bubble chambers equipped with holographic systems was during the 1985 physics run at Fermilab. They were exposed to a high energy wide-band neutrino beam ($E_p \simeq 800$ GeV, $\langle E_\nu \rangle \simeq 150$ GeV). The two experiments, E-745 using the Tohoku Bubble Chamber and E-632 using the 15-foot Bubble Chamber, analyzed data for high energy neutrino interactions.

Here, a brief description of the Tohoku Bubble Chamber is given. Sections 2.2.1 - 2.6 give an overview of the developments of the dark-field system for the 15-foot Bubble Chamber.

The Tohoku Bubble Chamber, 80 cm diameter x 100 cm depth, was designed and constructed for holography, (Haridas et al., 1985). The chamber, filled with Freon, was used as a vertex detector for a hybrid spectrometer system. This "moderately big" bubble chamber was designed to facilitate holography. Its operation with Freon above the ambient temperature (38 °C) avoided the complications in the optical systems which are encountered when using cryogenic bubble chambers.

During the E-745 physics run the Tohoku Bubble Chamber was equipped with three high resolution cameras (R = 55 μm) and one holographic camera (R = 30 μm). A two-beam holographic scheme was used in which a single beam was split into a reference beam, traveling via mirrors outside of the chamber, and an object beam which illuminated the chamber after passing through condensing lenses, (Figure 1.8). Direct light from the illuminating beam was baffled by a circular obstacle (80 mm diameter) placed on the optic axis of the condenser lenses and the hologram. The reference beam exposed the film at an angle of 0° during the first period of the run and at an angle of 14° during the second period. This

change in the reference beam angle was to improve the hologram quality which was degraded due to the conjugate image problem of in-line holography.[10] Since the object beam passing through the chamber was subject to a Faraday rotation due to the 2.8 T magnetic field, the polarization of the laser output beam was made circular using a quarter-wave plate. This rotation was measured in Freon to be 126° per T x m (Tavernier, 1984). The laser source was a frequency-doubled Nd:YAG pulsed laser with a maximum pulse energy of 300 mJ.

During the 1985 E-745 physics run, 63,000 holograms were produced. The holograms made in the first period of the physics run had low contrast (see previous paragraph); however, most of the holograms produced in the second period of the physics run were of good quality with resolutions of about 35 μm. Yet there was a small percentage of holograms which were spoiled due to instability and the poor coherence length of the laser.[11]

---

10. In in-line holography both real and conjugate images occupy the same space in the x-y plane which degrades the image contrast (Section 2.1.3).

11. The pulses used were of duration of 15 ns fwhm and coherence length of about 10 cm. This coherence length is not sufficient to cover the whole fiducial volume of the chamber which can have path differences as large as 40 cm.

1.5 The Fermilab 15-foot Hybrid Bubble Chamber

1.5.1 Experimental setup

The visual detector is a cryogenic bubble chamber located in lab. B at the end of neutrino beam line, N1. The central part is a sphere of 3.8 m diameter, having on the upper part a hemispherical cap which contains the windows for the optic ports, and on the lower part an expansion piston which is made of stainless steel, (Figure 1.9). A floating disk with a diameter of 2 m is installed on top of the piston to provide a more homogenous optical background, hiding the bubbles created around the piston top-seal. The interior wall of the chamber, except the hemispherical top, is covered with Scotchlite. The total volume of the bubble chamber is about 35 m^3. The chamber vessel is supported by three legs and is enclosed inside a vacuum tank. The chamber is equipped with a superconducting magnet which is composed of two large coils and generates a vertical field of 3 Tesla. Refrigerators cool down the bubble chamber vessel, the magnet, and maintain the liquid in the bubble chamber at an operating temperature of ~ 30 K. A pump subcools the piston seal region. It also recirculates the liquid when the chamber is not expanding for a period of a few hours or longer to maintain the liquid´s cleanness and homogeneity for a Ne/H_2 mixture. A more detailed description of the 15-foot Bubble Chamber can be found in the safety report of the 15-foot Bubble Chamber (1972).

The bubble chamber operation mechanism is based on the thermodynamic principle that a phase can be brought into a metastable state which is well into another phase. For a substance in such a metastable state a localized phase transition can occur for minute amounts of energy brought to it. In bubble chambers the liquid is superheated by

expanding the volume and decreasing the chamber pressure. At this stage the chamber is called sensitized. A minute amount of heat released through ionization when a charged particle passes through this superheated liquid creates bubbles along its path. After this period, the liquid is recompressed and the bubbles are recondensed. A typical expansion/recompression cycle for the 15-foot Bubble Chamber (with a resonant expansion system) is about 100 ms, with the chamber sensitized for a time $\lesssim$ 20 ms, (Figure 1.14).

The bubble chamber is equipped with six optic ports arranged on the top of it and can be photographed simultaneously by 6 cameras, (Figure 1.10). Each camera has a wide-angle lens and is installed behind three concentric hemispherical lenses, called fisheye windows. These fisheye windows have a focal length of about -300 mm. The largest one is made of BK7 glass, and the two smaller ones are made of quartz. The annular flashtubes around the conventional-picture camera lenses photograph the tracks in bright-field illumination using the retrodirective property of Scotchlite.

The fiducial volume of the chamber is defined as the volume in which the tracks can be photographed simultaneously with a good quality with all cameras and leaving enough track length (70 cm) downstream for momentum measurement. The fiducial volume varies with the optical system used to image the tracks. For conventional photography, this value depends on the depth of field of the optical system, and for holography it depends on the illumination light as well as the scattering angle from the bubble. In the 1985 E-632 physics run three optical systems were used: a) three conventional cameras (fiducial volume ~ 14 m^3, resolution ~ 500 μm), b) one

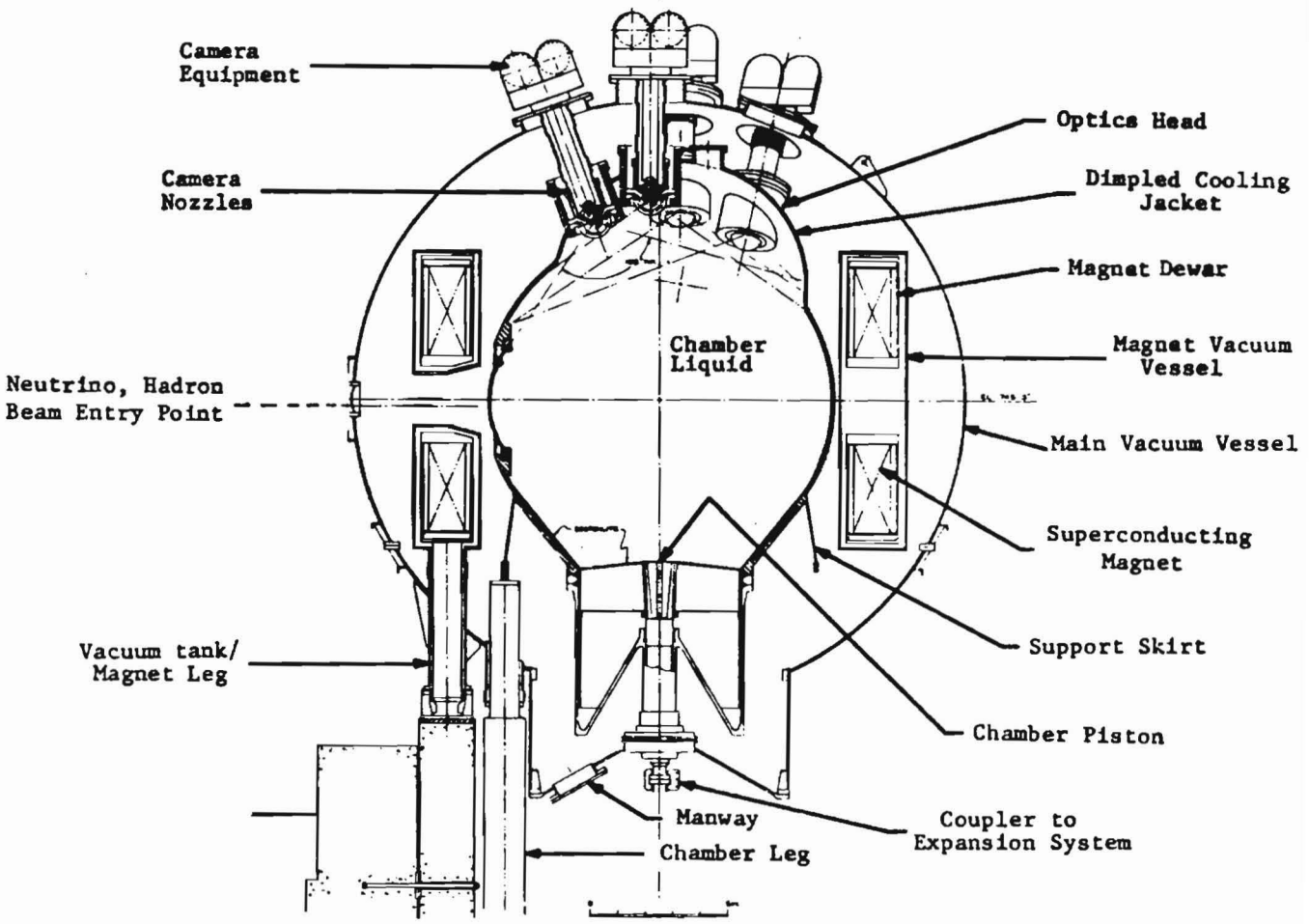

Fig. 1.9 The 15-foot bubble chamber, (side view).

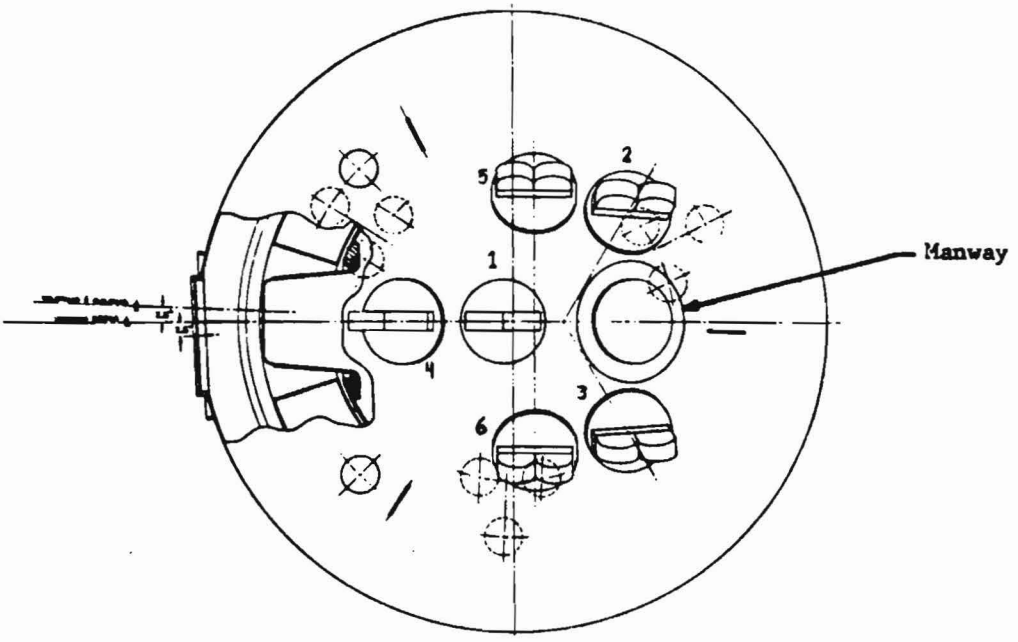

Fig. 1.10 The 15-foot bubble chamber, (top view).

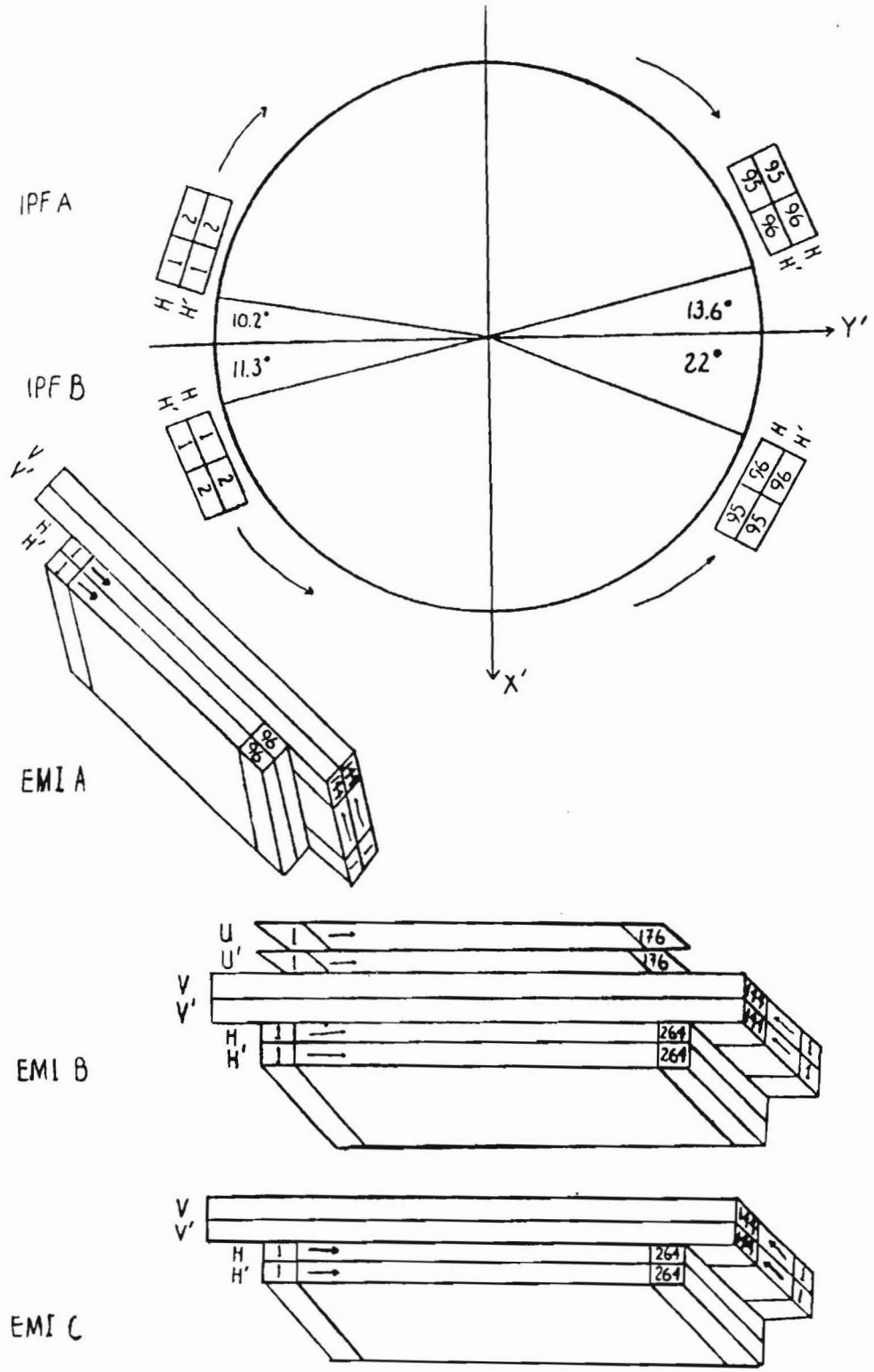

Fig. 1.11 Location of IPF and EMI planes with respect to the bubble chamber.

high-resolution camera (fiducial volume ~ 1 m^3, resolution ~ 200 μm), and c) one holographic camera (fiducial volume ~ 0.3 m^3, resolution ~ 150 μm).

A heavy Neon/Hydrogen liquid mixture (75/25 mole % Ne/H_2) of mass about 9070 kg was used in the E-632 physics run. The heavy Ne/H_2 mix has a density ρ = 0.71 g/cm^3 at 30 K, a radiation length $\lambda_{rad} \simeq 42$ cm, and a hadronic interaction length $\lambda_{int} \simeq 125$ cm. The purpose of the Neon was to obtain a higher conversion efficiency for photons, to facilitate electron identification, to produce a spin-0 target of large A (A is the number of the nucleons in the nucleus), and to increase the number of interactions per unit volume and the stopping power of the liquid.

The counter detector is composed of two sets of electronic chambers: the Internal Picket Fence (IPF) and the External Muon Identifier (EMI). Using the IPF and EMI a space-time dimension, with a temporal resolution of about 1 μs, can be associated with the muon tracks of momentum larger than 4 GeV. The EMI counters identify the muons produced in Charged Current neutrino (CC) events. The IPF gives timing information for muons in CC events and for the hadrons produced in either CC or the Neutral Current (NC) events. Furthermore the upstream IPF provides information about the N^* and V° produced in the upstream coils and faking neutrino interactions.

The IPF is an array of vertical proportional tubes, with a horizontal spatial resolution of 5.2 cm, mounted inside the vacuum tank of the bubble chamber. It is located about 2 m from the center of the bubble chamber and extends $\pm$1 m vertically. It surrounds the bubble chamber except for two gaps as shown in Figure 1.11. The EMI is composed of three sets of planes which are made of proportional tubes also shown in the same figure.

EMI A and B are located at ~ 3.5 m from the center of the chamber in two orientations, and EMI C is at ~ 7 m with a concrete and lead shielding wall in front of it. They extend to -170 cm and +196 cm, ±182 cm, and -145 cm and +219 cm, respectively. All the EMI planes extend about 190 cm above and below the beam axis. Each of the three planes has two vertical and two horizontal layers of proportional tubes. EMI B in addition has two layers in a diagonal direction. The transverse spatial resolution of the EMI layers is ~ 13 mm (Jones, 1986).

The data from the IPF and EMI proportional tubes are read out in a time-multiplexed scheme to reduce the number of cables between the detectors and the control room. The data are monitored using both on-line and off-line software.

The IPF together with the EMI are used for selectively triggering the high resolution and holographic cameras (the "event trigger").

The IPF and EMI counters were gated on about 0.5 - 1 ms before the injection of the neutrino beam in the bubble chamber, and remained sensitive for 3.0 - 3.5 ms. The 4 ms period in which the counters were sensitive was divided into 4000 time windows, "EMI time slots," each with 1 μs width.

1.5.2 Operational Mode

During the 1985 E-632 physics run the proton beam was extracted from the main accelerator ring three times a minute. The extraction of the beam was in "fast spill mode" with 2 ms width. The three beam spills were separated by 10 sec followed by a pause of about 42 sec. A typical configuration for the proton-beam-extraction timing is given in Figure 1.12.

Each extraction is labelled by a "ping number" (1 - 3) for which the number of extracted protons are registered.

The protons extracted from the accelerator with an energy of 800 GeV produced pions and kaons upon their interaction with the Beryllium target. The secondary pions and kaons then passed through the decay tunnel where they decayed mainly to muon neutrinos. The neutrinos produced from a monochromatic beam of pions and kaons have two distinct bands of energy distribution which decrease with increasing radial distance from the beam axis (Perkins, p. 246, 1982). The high-energy band is from the kaon decays, and the low-energy band is from the pion decays. For the wideband neutrino beam the high-energy flux is enhanced and the low-energy flux is suppressed by momentum selection using quadrupole focusing and dipole bending magnets. The mean energy of neutrinos produced during the 1985 E-632 physics run was about 150 GeV. The muons produced from the decay of pions and kaons were first monitored using four ion-chambers and were then absorbed by concrete and iron shielding. High energy muons that escaped this process as well as the muons which were regenerated in the berm would act as a source of background. In the case of the 15-foot Bubble Chamber this background was not serious.[12]

As a consequence of the accelerator timing, the bubble chamber was expanded three times a minute. A higher rate of expansion of the bubble chamber is not of interest due to the low interaction rate per picture (0.2 event per picture) and due to the possible shorter lifetimes of the various bubble chamber systems. The maximum expansion rate of the 15-foot Bubble Chamber is once in six seconds.

---

12. Depending on the polarity of the toroids of the lab. E detector the
(Footnote 12 Continued on Next Page

Figure 1.13 shows a typical EMI time slot configuration. The maximum of the proton beam spill occurs at 1500 - 2000 μs time slot. The event trigger is active during the first 1.3 ms of the beam spill; otherwise a default trigger at ~ 2100 μs time slot triggers the flashes for the high resolution photography and the laser for the holography. However, for holography the event trigger was only operational towards the end of the run; eighty percent of the holograms were taken with a fixed trigger for which the laser was triggered about 2 ms after the beginning of the proton beam spill as measured using the accelerator time.

A typical timing for neutrino beam injection and the photographic and holographic exposures with respect to the pressure change in the bubble chamber is shown in Figure 1.14. Since the bubbles should have sizes of about 100 and 200 μm for holography and high resolution photography, respectively, both films are exposed at short delay times after the injection of particle beam near the minimum of the expansion pressure. The high resolution photographs and the holograms were taken about 1 - 2.3 ms and the conventional photographs were taken about 10 - 12 ms after the beginning of the proton beam spill.

Bubbles created along the path of an ionizing particle begin small, (diameter << 0.1 μm) and grow with time, (in proportion to $t^{1/2}$, where t is the growth time) until recompression of the liquid.[13] Bubbles have diameters of 100 - 200 μm at 1 ms after their nucleation for typical bubble chamber operation. The quality of these 100 - 200 μm bubble tracks is

---

(Footnote 12 Continued from Previous Page)
beam track rates, for muons of momenta > 2 GeV/c, varied from 1.06 - 0.37 for μ^+, and 1.28 - 3.50 μ^- per 1×10^{12} protons.

13. The subject of bubble growth is dealt with in detail in Section 5.2.

faint in conventional pictures where the resolving power is 500 μm. However, a timing error which occurred for rolls 2247 - 2323 resulted in the exposure of the conventional photographs only 1 ms after the pressure minimum instead of 12 ms. As a consequence of this faulty timing (not known then), the bubble chamber operating conditions were changed in order to improve the track quality in these conventional pictures.

The operating conditions of the bubble chamber are primarily determined by the liquid temperature (T), the pressure of the liquid before the start of the expansion, P_{st}, the vapor pressure, P_v, the pressure at which the liquid is sensitized, P_{sen}, and the piston stroke (S) which determines the expansion ratio.[14] To produce tracks of good quality at flash delays of 1 ms the chamber must be operated such as to give fast bubble growth rate and high bubble density. This can in principle be achieved by decreasing the expanded pressure in the chamber and/or by increasing the operating temperature. Table 1.3 gives the approximate values for the bubble chamber operating conditions for different periods of the run. The last two columns are the laser beam injection delay, and the conventional-cameras-flash delay with respect to the expansion pressure minimum.

---

14. For S = 6.0 cm, the expansion ratio, (S x piston surface area / the chamber volume), is about 0.5 %.

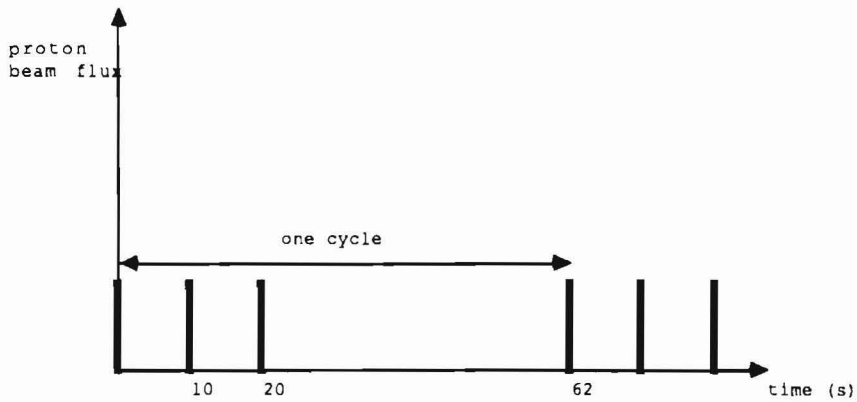

Fig. 1.12 A typical proton-beam-extraction-time graph for the E-632 physics run (1985).

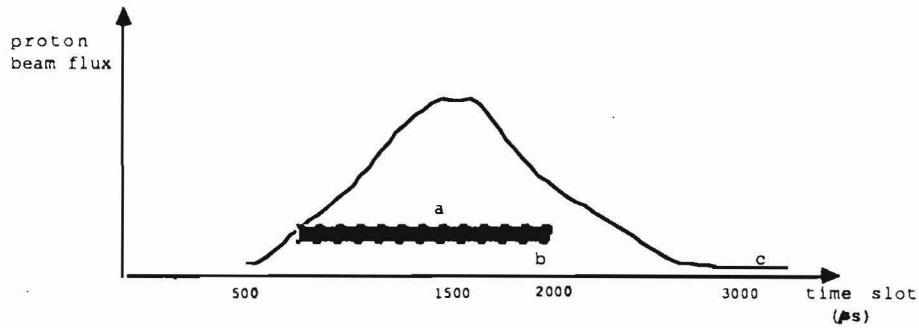

Fig. 1.13 A typical EMI-time slot configuration for the E-632 physics run (1985). Cross hatch: possible EMI event trigger, a: minimum pressure of bubble chamber, b: default EMI event trigger, c: high resolution and holography exposure.

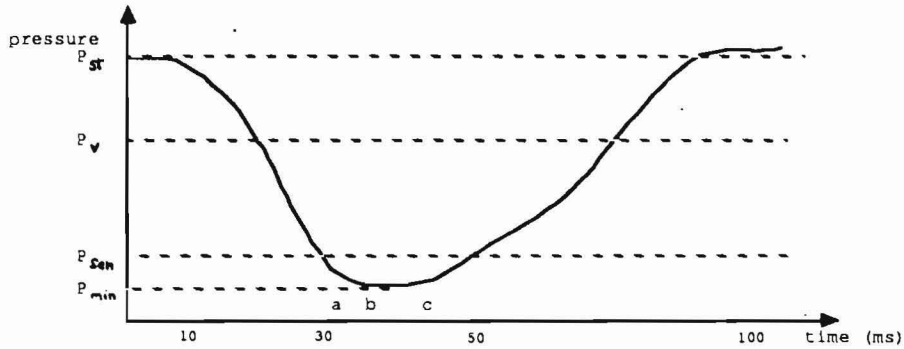

Fig. 1.14 A typical pressure-time graph for the E-632 physics run (1985). a: Neutrino beam, b: high resolution and holography exposure, c: conventional photography exposure.

Period	Roll	T (K)	P_{st}(bar)	P_v (bar)	S(cm)	Δt_{conv}(ms)	Δt_{laser}(ms)
I	2224-2240	29.8	8.0	7.6	5.6	12	2
II	2241-2246	30.6	9.0	8.5	6.0	12	2
III	2247-2294	30.6	9.0	8.5	6.0	1	2
IV	2295-2301	30.0	8.3	7.8	6.4	1	2
V	2302-2322	29.7	8.1	7.4	6.6	1	evt trigger
VI	2323-2323	29.3	7.4	7.0	6.6	1	2
VII	2324-2326	30.3	8.6	8.1	6.0	10	evt trigger

- Table 1.3 -

CHAPTER 2 THEORY OF HOLOGRAPHY

2.1 Basic Theory of Holography

In this section, the basic principles of holography are given. Holographic concepts which are used in bubble chamber holography are emphasized and elaborated upon. Used here as references are: Collier, Burckhardt, and Lin (1971), and Smith (1975).

2.1.1 Hologram Formation

Holography, in its most general form, is defined as the recording of the interference of the complex amplitudes of a diffracted beam, (the "object" beam), and an undisturbed beam, (the "reference" beam). A hologram carries information about the amplitude and phase of the wavefronts diffracted by the object. The information recorded on a photographic emulsion may then be retrieved by reconstructing the hologram, i.e. by illuminating the hologram with a beam identical to the original reference beam or "time reversed" with respect to the original reference beam.

Assume $U_r(x,y)$ and $U_o(x,y)$ are the complex amplitudes of the reference and object beams, respectively, at the hologram plane, (x-y plane). The intensity distribution at this plane is

$$I(x,y) = |U_r(x,y) + U_o(x,y)|^2 \qquad [2.1.1]$$

$$= |U_r(x,y)|^2 + |U_o(x,y)|^2 + U_r^*(x,y)U_o(x,y) + U_r(x,y)U_o^*(x,y). \qquad [2.1.2]$$

Let $U_r(x,y) = u_r(x,y)\ e^{i\phi_r(x,y,t)}$, and $U_o(x,y) = u_o(x,y)\ e^{i\phi_o(x,y,t)}$

[2.1.3]

where $u_r(x,y)$ and $u_o(x,y)$, and $\phi_r(x,y,t)$ and $\phi_o(x,y,t)$ are the magnitudes of the amplitude and the phases of the reference and object waves, respectively.

Assume both waves are temporally coherent and that the reference wave has a constant amplitude, and is propagating along an axis which makes an angle of α with the z-axis in the x-z plane, (Figure 2.1b). Substituting for $U_r(x,y)$ and $U_o(x,y)$ into [2.1.2], we have

$$U_r(x,y) = u_r\ e^{i\phi_r \sin\alpha}, \text{ and } U_o = u_o(x,y)\ e^{i\phi_o(x,y)} \qquad [2.1.4]$$

$$I = u_r^2 + [u_o(x,y)]^2 + u_r u_o(x,y)\,[e^{i(-\phi_r \sin\alpha + \phi_o(x,y))} + e^{i(\phi_r \sin\alpha - \phi_o(x,y))}],$$

[2.1.5]

where $\phi_r = (2\pi/\lambda)x$. The first term is the intensity of the reference beam and in reconstruction represents the reference wavefronts. The second term is the intermodulation intensity of the object beam with itself which does not carry any useful information and is in fact a source of noise. It is important to keep this term small. For $u_r >> u_o$, this term can be neglected. The third term is the modulation between the two waves which carries all the information about the object. It is the third term which is of interest to holography.

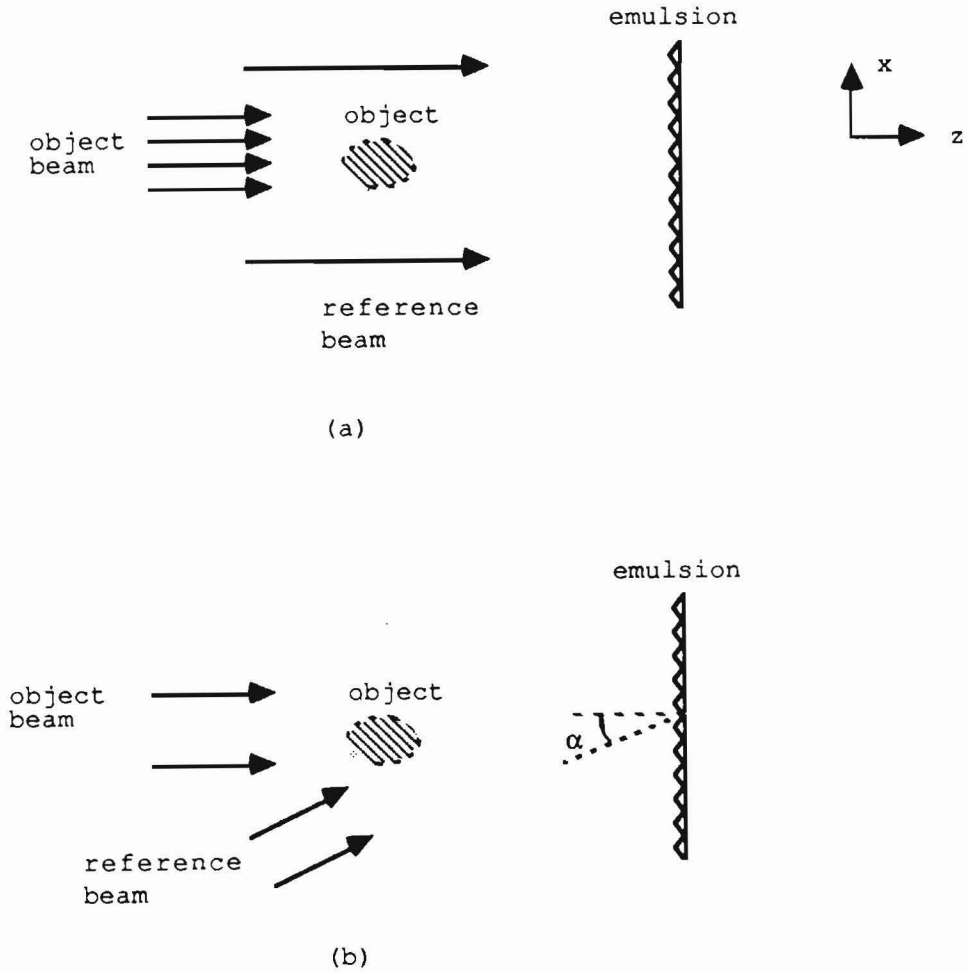

Fig. 2.1 **Recording arrangements: a) In-line hologram, b) Off-axis hologram.**

Signal to Noise Ratio during Recording

Noise in holography can have different origins, the noise created during the recording, the noise created due to processing, and the noise created due to the scattering of light in the emulsion during both recording and reconstruction stages. Here is given a discussion of the noise created merely in the recording stage.

a) K-Value

The ratio of the average of reference beam intensity to that of the object beam is defined as

$$\text{K-value} = I_r/I_o = |U_r|^2/|U_o|^2 = u_r^2/u_o^2. \qquad [2.1.6]$$

Since the intermodulation term $|U_o|^2$ is a source of noise during reconstruction, it is desirable to reduce u_o to small values by using a large K-value. However, reducing u_o will also reduce the modulation between U_r and U_o, suppressing the information carrier term. The optimum K-value is between 3 and 10, but much higher values of K can be utilized. In case of the 15-foot Bubble Chamber application this value was about 10^6 - 10^8 for the scattered light from a single bubble.

b) Fringe Visibility

The fringe visibility, V, is defined as

$$V = (I_{max} - I_{min})/(I_{max} + I_{min}), \qquad [2.1.7]$$

where I is the time-average of the modulation term between the reference and object waves $(U_r U_o)$. V varies between $V_{max} = 1$ and $V_{min} = 0$. It

should be noted that in calculating V the variation in the phase of the wavefronts is not taken into consideration.

c) Fringe Modulation

The fringe modulation, m, is closely related to the fringe visibility and is defined as

$$m = 2(I_r I_o)^{1/2} \ / \ (I_r + I_o). \qquad [2.1.8]$$

The intensity pattern in Equation [2.1.5] is related to the complex transmittance function of the film. Yet before describing the process of encoding this interference pattern in the emulsion we discuss various arrangements for the recording setup which result in different types of holograms.

<u>In-Line and Off-Axis Holograms</u>

Holography was first suggested with an in-line arrangement (Gabor, 1948). In this arrangement both beams expose the emulsion at the same angle, (Figure 2.1a). For this method the third term in Equation [2.1.5] would take the following form

$$I = u_r^2 + [u_o(x,y)]^2 + u_r u_o(x,y)[e^{i\sin\theta(-\phi_r + \phi_o(x,y))} + e^{i\sin\theta(\phi_r - \phi_o(x,y))}] \qquad [2.1.9]$$

where θ is the incidence angle of both reference and object beams at the emulsion. It is merely a constant multiplying the modulation term. This angle is zero for the case that the reference beam is perpendicular to the hologram plane which is the most common arrangement for in-line holography.

In-line holography has the disadvantage that the two images created at the reconstruction stage occupy the same region of x-y coordinates. The superposition of the two images makes it difficult to distinguish them from each other and reduces the contrast. Furthermore, this method is suitable only for small objects which do not obstruct the reference beam.

In an off-axis hologram, as first suggested by Leith and Upatnieks (1962), the reference and object beams expose the hologram at two different angles, (Figure 2.1b). In Equation [2.1.5], the third term will take its most general form

$$I = u_r^2 + [u_o(x,y)]^2 + u_r u_o(x,y)\,[e^{i(-\phi_r \sin\alpha + \phi_o(x,y)\sin\beta)} + e^{i(\phi_r \sin\alpha - \phi_o(x,y)\sin\beta)}] \qquad [2.1.10]$$

where β is the angle that the object beam makes with the normal to the hologram. To make an off-axis hologram either or both of the angles, α and β, have to be nonzero. Due to this nonzero angle the two holographic images formed when the hologram is replayed will be separated from each other by twice the angle between the reference and object beams.

Thin and Thick Holograms

"Thin" and "Thick" holograms (plane or volume) are distinguished from each other by the average spacing of fringes formed by the interference of the reference and object beams. A hologram is called thick if the fringe spacing, d, is smaller or of the order of the emulsion thickness, d_h,

$$d \sim \lambda/\sin(\phi/2) \leq d_h \qquad [2.1.11]$$

where λ is the wavelength of the recording light and ϕ is the angle of separation between the two beams.[15] This characteristic of the hologram imposes a condition on the angle and wavelength of the illuminating beam in order to give a constructive interference between the successively diffracted waves. This is called Bragg's condition which determines the angle (wavelength) of the illuminating beam for a given fringe spacing and wavelength (angle). The relation is simply Bragg's Law, given by

$$2d\sin(\phi/2) = \lambda_a/n_m, \qquad [2.1.12]$$

where λ_a is the wavelength in air and n_m is the recording medium index of refraction.

For off-axis holography and emulsions which are usually thicker than 5 μm, nearly all the holograms are "thick." Nevertheless the principle of image formation in thick holograms is the same as in thin holograms, with the equations expressed in three-dimensions. For the discussion of bubble chamber holography it is sufficient to use the thin hologram equations and all the future discussions assume a thin hologram unless otherwise stated.

Transmission and Reflection Holograms

A hologram for which both reference and object beams expose the emulsion from same side of the hologram is called a transmission hologram. If the emulsion receives the reference beam from one side and the object beam from another side it is called a reflection hologram, (Figure 2.2). In the latter the interference of the two beams results in a standing wave

15. This definition is somewhat crude, but is sufficient for our qualitative discussion here. A more precise definition uses a parameter called $Q = 2\pi\lambda_a d_h/n_m d^2$. For $Q > 1$ the hologram is called "thick."

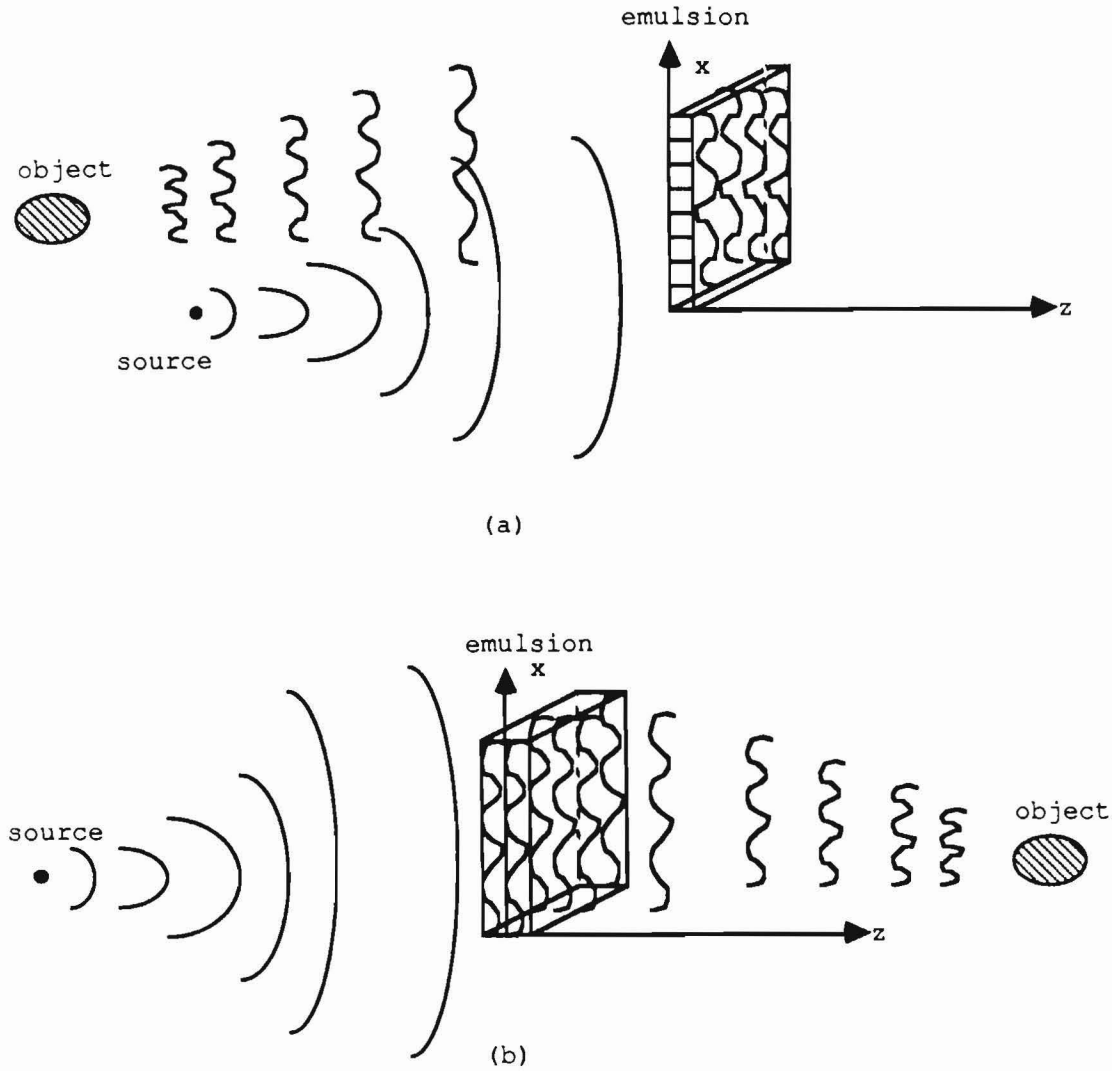

Fig. 2.2 Recording arrangements: a) Transmission hologram, b) Reflection hologram.

pattern with fringes that are approximately planes perpendicular to the z-axis with separations of about half a wavelength ($d = \lambda_a/[2n_m \sin(\pi/2)]$), as determined by Bragg's law. The image formed in reconstruction of this hologram is viewed in reflection rather than in transmission as with the usual hologram. Since the fringe planes are separated in depth it is possible to reconstruct reflection holograms with white light. The successive planes select and reflect back only those monochromatic components which were registered on the hologram. This type of hologram is mainly used for display holography.

All the studies in this thesis were based on transmission holograms. These cannot normally be reconstructed with white light[16] and the images formed are viewed in transmission.

Fresnel and Fraunhofer Holograms

The difference between the Fresnel and Fraunhofer holograms is that the diffraction patterns formed at the image plane are in the Fresnel or Fraunhofer regions defined relative to the object. For Fresnel (Fraunhofer) holograms the object size is comparable (small) as compared to its distance from hologram. For objects at large distances from the holographic plate it can be assumed that the waves originating from each point of the object are plane waves traveling in the direction defined by the angle β, the obliquity angle of the object beam from the z-axis. Thus each point of the hologram stores both the reference beam and the scattered light from each point of the object.

16. Image plane and Benton (Rainbow) holograms are transmission holograms which can be viewed in white light.

For Fraunhofer holograms, $((x_o^2 + y_o^2)/\lambda << z_o$ with (x_o,y_o,z_o) as object coordinates), the quadratic and higher order terms in x_o and y_o can be ignored when expanding r in product of $\vec{k}.\vec{r}$ at the hologram plane (x,y,0).

$$r = [(x_o - x)^2 + (y_o - y)^2 + (z_o)^2]^{1/2} \qquad [2.1.13]$$

$$r \simeq z_o + \frac{x_o^2 + y_o^2}{2z_o} + \frac{x^2 + y^2}{2z_o} - \frac{xx_o}{z_o} - \frac{yy_o}{z_o} + \ldots\ldots. \qquad [2.1.14]$$

For Fresnel holograms, (x_o and $y_o \lesssim z_o$), the quadratic terms cannot be ignored.

For bubble chamber applications where an object of 100 μm in diameter is holographed at 200 cm from the hologram by a light with wavelength of 694 nm, the diffraction pattern produced by the bubble at the hologram is in the Fraunhofer region.

2.1.2 Recording Medium

<u>Response of the Holographic Emulsion</u>

The response of the emulsion is characterized by an "H&D" curve (Collier, Burckhardt, and Lin, Section 2.5.1, 1971) which is a plot of the optical density of the processed film versus the logarithm of the exposure, (Figure 2.3). The density of film, D, is related to its exposure, E, along the straight line portion of the curve by

$$D = c + \gamma \log_{10}(I\tau_e) \qquad [2.1.15]$$

for exposure defined as $E = I\tau_e$. c is the constant, uniform background density, I is the intensity distribution of the interference pattern (Equation [2.1.2]), τ_e is the exposure time, and γ is the linear slope of the curve which is a function of both the recording material and processing procedure.

This density is defined as the logarithm of the reciprocal of the intensity transmittance, T

$$D = \log_{10}(1/T). \qquad [2.1.16]$$

The two expressions of the density are related to each other by the amplitude transmittance of film which itself is a function of exposure. The amplitude transmittance-exposure curve (t_a-E curve) is of interest to holography and is commonly used. The form of this curve determines whether the recording is linear. A linear recording is desirable in holography to avoid the effects of the noise produced from higher order terms of the amplitude transmittance function.

Amplitude Transmittance of the Emulsion

The amplitude transmittance, t_a, may be expressed as

$$t_a = k_0 + k_1(I\tau_e) + k_2(I\tau_e)^2 + k_3(I\tau_e)^3 + \ldots. \qquad [2.1.17]$$

where k_0, k_1, ... are constants. A typical t_a-E curve is shown in Figure 2.4. The linear portion of this curve can be parameterized by the first two terms, $t_1 = k_0 + k_1(I\tau_e)$. A linear recording is when the amplitude transmittance is characterized by this linear portion. This assures that the density of film is in the linear section of the H&D curve for a proper processing.

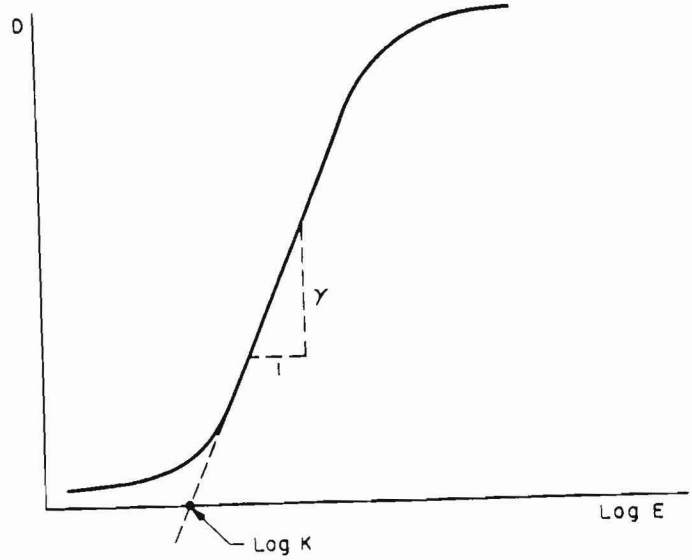

Fig. 2.3 The H&D curve.

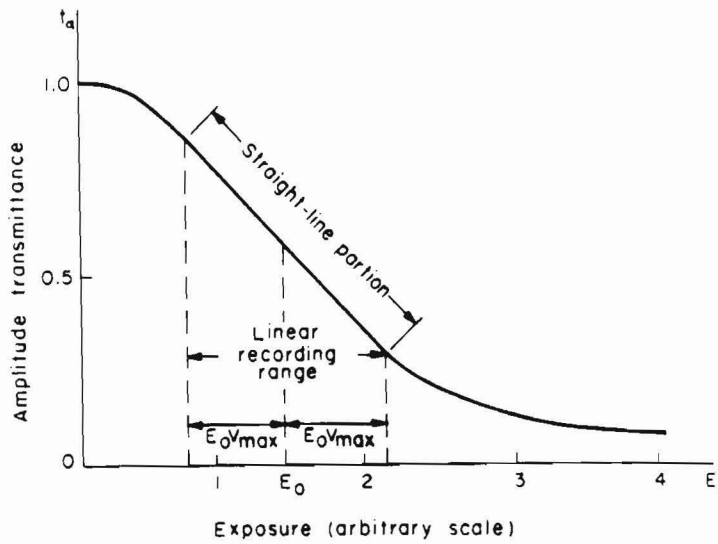

Fig. 2.4 Amplitude transmittance versus exposure.

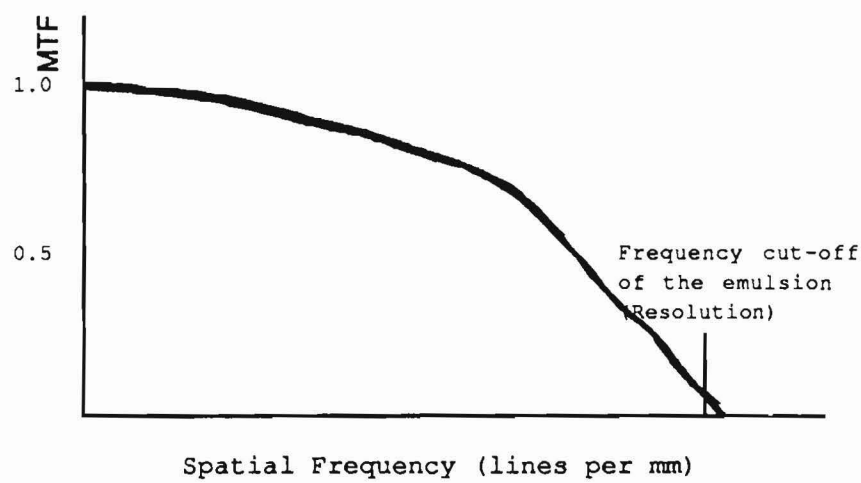

Fig. 2.5 Modulation Transfer Function (MTF) for a typical photographic emulsion.

Expansion of an amplitude transmittance with quadratic term included and substituting the expression [2.1.2] for I gives

$$t_a = \text{linear terms} + k_2\tau_e^2[(|U_o|^2)^2 + U_r^{*2}U_o^2 + U_r^2U_o^{*2} + 2|U_o|^2U_o^*U_r + 2|U_o|^2U_oU_r^*] \qquad [2.1.18]$$

where all terms proportional to $|U_r|^2$ are not shown. The last two terms are linear in U_r (U_r^*) which will result in diffraction of light in the direction of the image when reconstructed with U_r^* (U_r) illuminating beam. These terms give rise to flare light (noise) surrounding the image. The other terms are also scattered light and give ghost images but do not in principle affect the image.

From this discussion it can be seen that assuring a linear recording is essential to obtain a high quality holographic image. For a linear recording, dt_a/dE must be constant and the exposure range between $E_0(1 - V_{max})$ and $E_0(1 + V_{max})$ must remain within the linear portion of the t_a-E curve. Here E_o is the uniform background exposure on the emulsion (bias level), and V_{max} is the maximum fringe visibility of the modulation term.

Amplitude and Phase Holograms

The information stored in the hologram can be extracted either by using the amplitude variation or phase variation of the interference pattern. The cases considered in previous pages have been amplitude holograms. The function t_a is amplitude dependent and real. For a phase hologram the transmittance function, t_p is formed on recording media to be (see processing of the emulsion) a complex function and phase dependent. The principle of phase holograms can be shown by considering t_p as pure imaginary. For a pure phase hologram, the transmittance function is:

$$t_p = k_0 e^{icI\tau_e} \qquad [2.1.19]$$

$$t_p = k_0 e^{ic|U_r|^2\tau_e} \times e^{ic|U_o|^2\tau_e} \times e^{icU_r^*U_o\tau_e} \times e^{icU_rU_o^*\tau_e} \qquad [2.1.20]$$

$$t_p = k_0 e^{ic|U_r|^2\tau_e} \times e^{ic|U_o|^2\tau_e} \times e^{2icu_ru_o\tau_e \cos(\phi_r \sin\alpha - \phi(x,y))}$$

[2.1.21]

where c is a constant of proportionality. Expanding [2.1.20], multiplying out and neglecting the cubic and higher order terms in c, we obtain

$$t_p = k_0\{1 + ic[\text{linear terms}] - c^2|U_o|^2[U_r^*U_o + U_rU_o^* + |U_r|^2] + [\text{higher order terms in } U_rU_o]\}$$

[2.1.22]

We can see that in addition to the linear image forming terms, we obtain another set of object image terms, $|U_o|^2U_r^*U_o$ and $|U_o|^2U_rU_o^*$, which are multiplied by $c^2|U_o|^2$. $|U_o|^2$ is the noise term which normally appears around the illuminating beam, but in this case appears around the images (both primary and conjugate images) as well.

Rewriting the Equation [2.1.22] in form of cosine and sine terms, ($e^{ix} = \cos x + i\sin x$), one can write an expression for t_p in terms of the Bessel function (of the first kind) expansions for cosine and sine.

In general all higher orders of the Bessel function, $J_n(a)$, are present which diffract the illuminating beam in higher order images. This is not the case for the amplitude holograms for which the sinusoidal variation of the amplitude gives only the first order images if the recording is linear.

For vacuum, n = 1, the same terms can be derived for the reconstructed wave (primary and conjugate images) except with some phase and amplitude factors which are not important.

$$t_p = kJ_1(a)(e^{i\theta} + e^{-i\theta}) \qquad [2.1.23]$$

where $k = k_0 e^{ic|U_r|^2\tau_e} \times e^{ic|U_o|^2\tau_e}$

$$a = 2cU_rU_o\tau_e$$

$$\theta = \phi_r \sin\alpha - \phi(x,y)$$

The advantage of phase holograms is their very high diffraction efficiency, the ratio of usable diffracted to incident flux at reconstruction stage, but their inherently higher noise level makes them unattractive. A discussion of diffraction efficiency of the amplitude and phase holograms is presented in Section 2.1.3.

Modulation Transfer Function (MTF) of the Emulsion

When the emulsion is exposed to the interference pattern of Equation [2.1.5], the light scattered within the emulsion during exposure lowers the modulation (contrast) of the signal. This change in modulation is characterized by the modulation transfer function (MTF). The modulation transfer function can be more formally defined for an optical system,[17] using the concept of Fourier transform, as the modulus of the optical transfer function.

The optical transfer function is a complex function and is a characterization of the optical system. It's multiplication with the object

17. Here, an optical system is defined as a system which is capable of imaging an object, e.g. a lens or a hologram.

complex amplitude produces the image spectrum in the spatial frequency domain. Its counterpart in the spatial domain is the spread function. The modulus of the optical transfer function which produces a change in the amplitude of the various frequency components of the object spectrum is then called MTF, and is equal to the ratio of the modulation in the image to that in the object. It is merely a measure of the reduction in contrast from object to image.

The MTF of an optical system decreases with increasing spatial frequency which in case of the hologram corresponds to increasing angle between the reference and object beams. This is due to the diffraction effects which becomes more pronounced for larger angles. At large enough angle the spatial frequency exceeds the resolution limit of the emulsion for which MTF becomes zero. Figure 2.5 shows the MTF for a typical photographic emulsion.

Processing of the Emulsion

As the nature of the holographic process is similar to that of the photographic process, photographic emulsions are widely used as the recording media in holography. The most commonly used are silver-halide emulsions due to their high sensitivity.[18]

Processing silver-halide emulsions in holography is similar to that in photography.

In case of phase holograms the phase modulation of the illuminating beam can be achieved either by changing the thickness, d_h, or the index of refraction, n_m, of the emulsion as a function of the exposure. In either case

---

18. Other common emulsions in holography are: dichromated gelatin films, photoconductor-thermoplastic films, photochromic materials, and photopolymers.

the phase of the transmittance function, ϕ_t, varies with the optical path $n_m d_h$,

$$\phi_t = (2\pi/\lambda) n_m d_h. \qquad [2.1.25]$$

The most common and simplest method to produce a phase hologram is to convert an absorption hologram by bleaching the silver image in the photographic emulsion. The bleaching process can be done by soaking the hologram in a bleach bath in which the developed silver is converted to a transparent silver salt with a refractive index higher than that of the gelatin, (Rehalogenating bleach method).

The sensitivity or speed of an emulsion is determined primarily by the size of the grain. Larger grains are developable upon absorption of the same number of photons as the smaller grains, and thus resulting in a hologram with a higher optical density. However, large grains scatter more light resulting in a larger scattering noise level. The demands for high sensitivity and low noise level are in conflict with each other, and a compromise has to be made between the two. The material has also to have the correct spectral sensitivity to the wavelength of the laser light at the recording stage.

2.1.3 Hologram Reconstruction

To develop the concept of hologram reconstruction in a simple approach we use Equation [2.1.5] for discussion of image formation. But in fact the amplitude transmittance, $t_a = F(E)$, should be used instead of the intensity pattern, I.

Virtual Image Reconstruction

If the emulsion which has encoded the intensity pattern in Equation [2.1.5] is illuminated with the original reference beam (Figure 2.6a), then the illuminating beam has the same complex amplitude as the reference beam, $U_i(x,y) = U_r(x,y)$. The complex amplitude of the light after passing through the hologram is

$$W \propto u_r^3 e^{i\phi_r \sin\alpha} + [u_o(x,y)]^2 u_r e^{i\phi_r \sin\alpha} + u_r^2 u_o(x,y) e^{i\phi_o(x,y)} + u_r^2 u_o e^{i(2\phi_r \sin\alpha - \phi_o(x,y))}. \qquad [1.2.26]$$

The first term represents the reference beam wavefronts and is slightly diverging. The second term is the object beam modulation term. These two terms form "flare light" and are a source of noise. The third term is proportional to the object wave and generates a virtual image at exactly the same location as was the object. This virtual image can be viewed by looking through the hologram. The fourth term is proportional to the conjugate of the object wave and generates a real conjugate image. This image is at an angle of $-\alpha$ from the illuminating beam for small α, and is on the other side of the hologram.

Real Image Reconstruction

If the hologram is illuminated with a time reversed reference beam (the original reference beam but traveling in reverse direction) from the opposite side, $U_i(x,y) = U_r^*(x,y)$, (Figure 2.6b), we have

$$W \propto u_r^3 e^{-i\phi_r \sin\alpha} + [u_o(x,y)]^2 u_r e^{-i\phi_r \sin\alpha} + u_r^2 u_o e^{i(-2\phi_r \sin\alpha + \phi_o(x,y))} + u_r^2 u_o e^{-i\phi_o(x,y)}. \qquad [1.2.27]$$

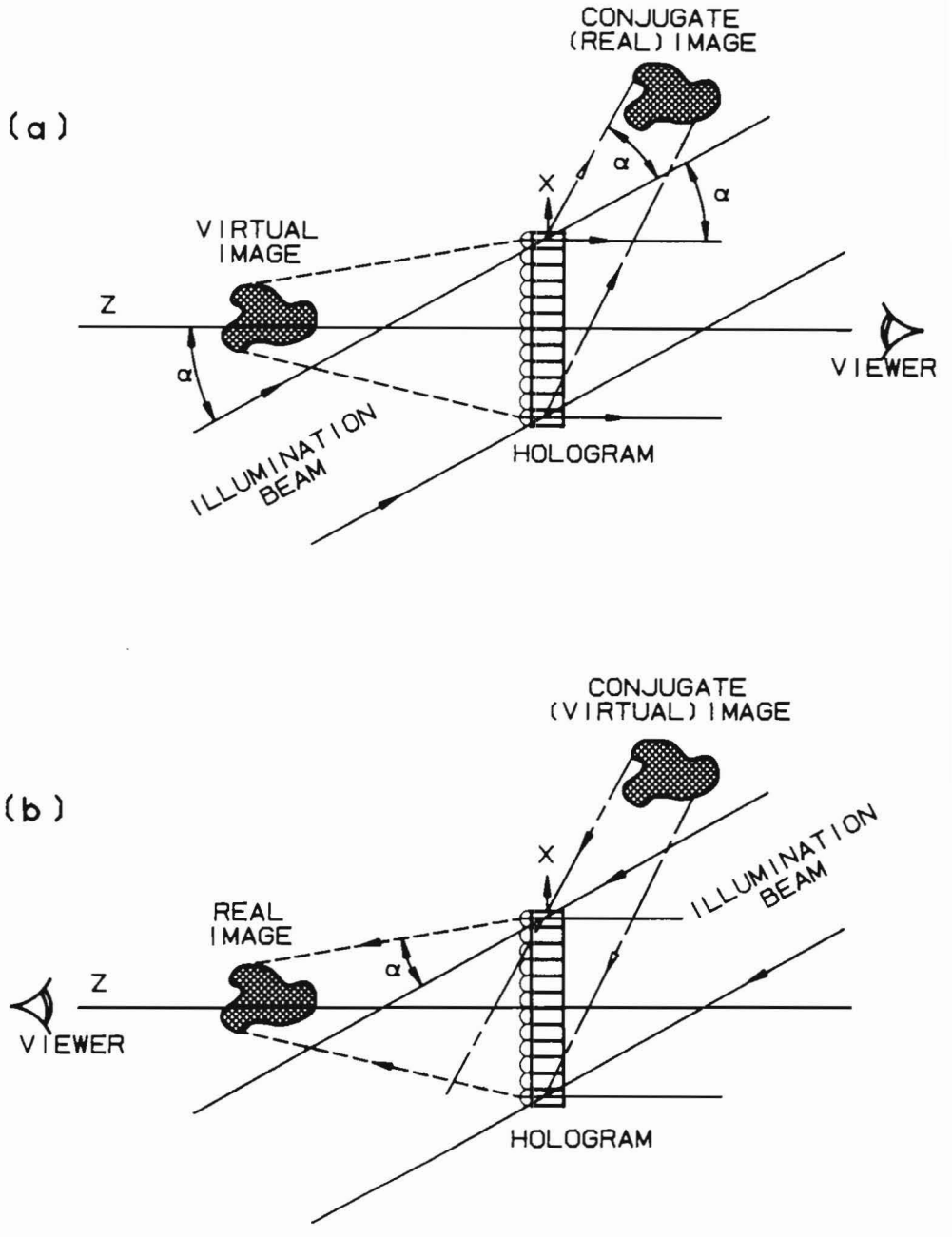

Fig. 2.6 Reconstruction of a hologram. (a) Virtual image replay, (b) Real image replay.

The first term represents the reference beam wavefronts converging to a point source. The second term, as before, is the object beam intermodulation term which is of no interest. The third term is the virtual conjugate image of the object which again is formed at an angle of $-\alpha$ from the illuminating beam on the other side of the hologram and the last term is the real image of the object and is proportional to the original object wavefronts but propagating in the opposite direction. This real image can be viewed using a white screen at the object location relative to the hologram.

It should be noted that in an in-line method the angle α is zero and the virtual or real image is accompanied by the corresponding conjugate image. The diffracted beam from these conjugate images would then interfere with the main image and reduce the image contrast.

Diffraction Efficiency

Diffraction efficiency is defined as the ratio of the total useful light flux diffracted into the first order primary image by the hologram to the total light flux used to illuminate the hologram.

For a plane absorption hologram the amplitude transmittance using Equation [2.1.5] and [2.1.17] can be written as

$$t_a = k'_0 + k'_1 \cos(\phi_r \sin\alpha - \phi_o(x,y)) \qquad [2.1.28]$$

where $k'_0 = k_1 \tau_e (u_r^2 + u_o^2)$

$k'_1 = k_1 \tau_e (2u_r u_o)$

For maximum diffraction efficiency, t_a should vary between 0 and 1. This maximum range is achieved when $k'_0 = 1/2$ and $k'_1 = 1/2$. Then,

$$t_a = 1/2 + 1/2 \cos(\phi_r \sin\alpha - \phi_o(x,y)) \qquad [2.1.29]$$

$$= 1/2 + 1/4\ e^{i(\phi_r \sin\alpha - \phi_o(x,y))} + 1/4\ e^{-i(\phi_r \sin\alpha - \phi_o(x,y))} \qquad [2.1.30]$$

From this equation it can be seen that the maximum diffracted amplitude of either the primary or conjugate image is one-fourth of the amplitude of the illuminating beam, giving a maximum diffraction efficiency of 6.25 % for an ideal absorption hologram (Collier, Burckhardt, and Lin, p. 261, 1971).

For a thin phase hologram, it can be seen from Equation [2.1.22] that the amplitude of a first-order diffracted wave is simply $J_1(a)$. This first order Bessel function describes a maximum diffraction efficiency of 33.9 %, (loc. cit.).

An expression for the diffraction efficiency, η, can be derived in terms of MTF of the emulsion, (Smith, Chapter 7, 1975),

$$\eta = 0.188\ \frac{\alpha^2(E_{ave})}{K}\ M^2(\nu_{ave}) \qquad [2.1.31]$$

where $\alpha(E_{ave})$ is the slope of linear portion of t_a-E curve at the average exposure E_{ave}, K is the K-value, and $M(\nu_{ave})$ is the MTF of the emulsion at the average spatial frequency ν_{ave}.

The important characteristic of the diffraction efficiency is $\alpha^2(E_{ave})$, where α can be written as a function of the amplitude transmittance, t_a, and the slope of the H&D curve, γ:

$$\alpha(E_{ave}) = \left[\frac{dt_a}{d\log E}\right]_{E_{ave}} \qquad [2.1.32]$$

$$= \left(\frac{dt_a}{dD}\right)_{E_{ave}} \times \left(\frac{dD}{d\log E}\right)_{E_{ave}}$$

$$= -\frac{\ln 10}{2}\, t_a(E_{ave})\ \gamma(E_{ave}) \qquad [2.1.33]$$

The two variables, t_a and γ, change in opposite directions with increasing exposure. The maximum diffraction efficiency is obtained at an average exposure for which t_a-E curve of the recording material has its maximum slope (near the toe of the linear portion of the H&D curve), and that the background density should be as low as possible.

2.1.4 Resolution in Holography

For a lensless holographic system, the resolution of the holographic image is limited by the size of the recording medium, size and bandwidth of the point source of the reference and replay beam sources, geometrical aberrations, resolution of the recording medium, and processing methods used.

By an appropriate choice of the recording and reconstruction optical systems, the reference and the replay beams, the recording medium, and the processing methods all effects except the diffraction-limited one due to finite size of the recording medium, can be made negligible. In practice this is difficult to achieve. Here, a brief discussion of some of these resolution-limiting factors is given.

Size of the Recording Medium

For a lensless system the linear size of the hologram at reconstruction stage determines the diffraction-limited resolution. The simple diffraction-limited formula for the resolution is $R = 1.54(\lambda U/a)$ (Equation [1.2.6]),

where the factor 1.54 is used for a circular aperture illuminated with coherent light, λ is the wavelength of the light, U is the distance of the object from the hologram, and a is the diameter of the hologram.

For the 15-foot Bubble Chamber holography this resolution for an object at 2 m from the hologram, using ruby wavelength (λ = 694 nm), and hologram diameter of 60 mm, is

$$R = \frac{1.54 \times 694 \times 2 \times 10^{-9} \times n}{0.06} = n \times 35.5\ \mu m,$$

where n is the index of refraction of the medium. For a heavy mixture of Ne/H_2 (75/25 %) the index of refraction is 1.088 and the resolution 39 μm.

Size of the Reference and Replay Beam Sources

In any real case, both the reference and replay beam sources have finite diameters. This finiteness of the sources introduces a spreading of light in the image and thus a limitation on the resolution of the holographic system.[19] However, no loss in resolution is obtained from that of the diffraction-limited one if the size of sources is smaller than the size dictated by diffraction effects due to finite size of the recording medium. The rule is rather simple for Fraunhofer holograms, and can be stated as 'the image resolution can not be better than the "spot size" of the reference beam at an optical distance of the emerging point source.' For the 15-foot Bubble Chamber holography, the point source size is about 35 μm at an effective optical distance 4.6 m which gives the maximum possible resolution of the

19. The subject of the holographic image resolution due to the finite sizes of the reference and replay beam sources is treated extensively by Smith (Chapter 9, 1975).

system at this distance. The resolution at 4.6 m is limited by diffraction effects to 82 μm.

Geometrical Aberrations

The aberrations in the reconstructed image can be of different origins. One is the aberration originated during the recording of the hologram as a result of disturbances introduced in the reference beam either by the optical surfaces or by variations in the medium that the reference beam traverses. Another is the aberration created in the reconstruction stage due to misalignment and/or impreciseness of the optical system. There are additional chromatic aberrations if different wavelengths are used for recording and reconstruction of the holographic image. These aberrations can deform the image and thus degrade the resolution. The severity of this degradation varies with the image distance and with the angle of the reference beam.

Resolution of the Recording Medium

The recording medium must be capable of recording the basic fringe pattern created by the interference of the reference and object beams. Thus its resolution has to be comparable to the highest spatial frequencies in the fringe pattern. Spatial frequency, as defined earlier, is $\nu_s = 2\sin(\psi/2)/\lambda$ where ψ is the angle between the reference and object beams, and λ is the wavelength of light.

For the 15-foot Bubble Chamber holography, the highest spatial frequency is about

$$\nu_s = \frac{2 \sin (15)}{694 \times 10^{-9}} = 750 \text{ lines/mm},$$

for $\psi = \pm 30^\circ$ and $\lambda = 694$ nm. Thus the recording material must have a resolution of at least 750 lines/mm. For a recording material with a resolution smaller than this the hologram will suffer from loss of image field size and image resolution.

Definition of the Resolution

In the 15-foot Bubble Chamber context the resolution is defined as the size of the smallest bubble (full width at half maximum of the bubble image profile) which can be observed with acceptable contrast. (This is half of the optical resolution which is defined in "line pairs per mm" on a standard resolution test target. Figure 2.7 illustrates these definitions.) Through the remaining of this dissertation the bubble chamber resolution will be used.

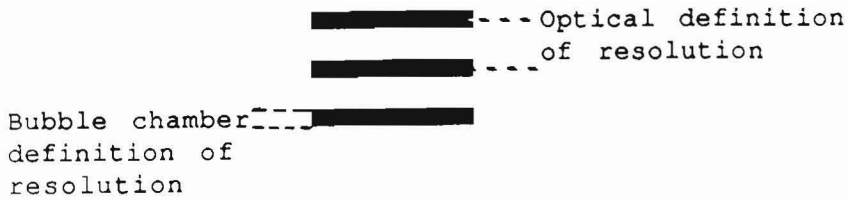

(a)

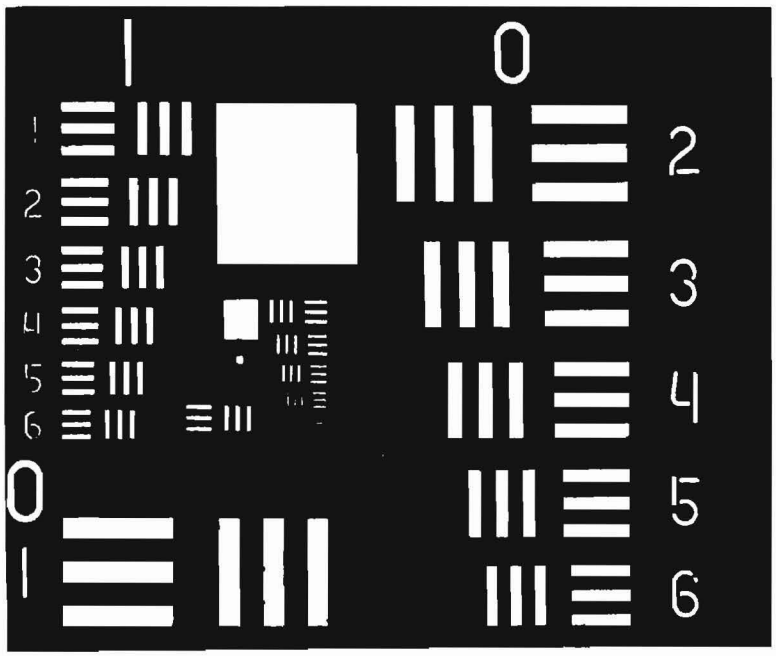

(b)

Fig. 2.7 a) Definition of resolution, b) USAir Force 1951 resolution target.

2.2 Dark-Field Method of Bubble Chamber Holography

In this section, first a summary of development of the dark-field method is given. This serves as an introduction to this section as well as Chapters 4, 5, and 6. It provides the reader with a global understanding of important aspects of the method which are discussed more extensively afterwards.

2.2.1 Historical Summary of Development of the Method

A modified in-line scheme was proposed by Baltay et al. (1982). In this scheme a single laser beam enters the bubble chamber at the bottom where it is split into two beams by an aspheric diverging lens. The central part of the beam comprises the reference beam and is on the optical axis of the recording film. The rest of the light emerges in a conical volume about the reference beam and when scattered by bubbles, forms the object beam. The intensity of the light from the lens increases with the cone angle to compensate for the decrease at larger angles of the light scattered by bubbles, (Section 2.2.2).

A preliminary test of this scheme at Nevis Laboratories, Columbia University showed the feasibility of the method (Cence, 1982).

A more realistic test of the system was performed in the Big European Bubble Chamber (BEBC) at CERN (Bjelkhagen et al., 1984b; Harigel et al., 1984). The chamber was filled with a heavy Neon-Hydrogen mixture. A pulsed ruby laser was used as the light source. The beam was transported through the air into the chamber and was diverged nonuniformly by the dispersing lens. The dispersing lens had an aspheric surface and diverged the beam into a cone with half angles $\leq 20°$.

The two main results from the BEBC test were:

1. High contrast holograms of 1 m long bubble tracks using Q-switched pulses could be made. The smallest bubble recorded in these holograms had an effective diameter $\geq$ 120 μm.
2. Q-switched pulses, 20 ns fwhm, with energy of 2 - 3 J caused catastrophic boiling of the liquid. This boiling did not affect the quality of the holograms but spoiled conventional photographs taken ~ 8 ms after the injection of the laser beam. This boiling was largely suppressed when the laser was operated in the free lasing mode (low peak power, discrete lasing over 1 ms range).

In order to use holography in combination with conventional photography a solution was sought to reduce the laser-induced boiling to a level that would not obstruct any usable volume in the conventional pictures.

The phenomena of light-induced boiling has been reported by a number of authors (Askaryen et al., 1963; Stamberg and Gillespie, 1965; Peoposoetjipto and Hugentobler, 1970; Hilke, 1980; Harigel, Hilke, and Linser, 1981). It is generally agreed that the impurities in the bubble chamber liquid could absorb and accumulate the laser light energy and provide a center for bubble nucleation (cf. Chapter 5 of this dissertation). This interpretation and the results from the BEBC test led to the conclusion that decreasing the peak power of the laser light would reduce the instantaneous energy below the threshold required for bubble formation. This could be achieved by increasing the laser pulse width while still depositing the large total energies into the bubble chamber needed to illuminate all of the volume.

As a result, an electro-optic negative-feedback loop was developed, incorporated, and tested in a ruby laser oscillator at Nevis Laboratories, Columbia University. This circuit stretched 20 ns laser pulses to 2 - 3 μs. A test of these pulses in the 15-foot Bubble Chamber at Fermilab during an engineering run in 1984 showed that even longer pulses would be needed to suppress boiling at energies of several joules. Thus a new circuit capable of stretching the laser pulses up to 100 μs had to be developed (Harigel et al., 1986; Chapter 4 of this dissertation).

The results of an empty-chamber test in the 15-foot Bubble Chamber during January 1985 showed that the resolution of a test target (standard resolution test target) degraded with increasing diameter of the input laser beam. Lateral resolutions of 110 μm and 200 μm were obtained for laser input beam diameters of 2.5 and 4.4 cm, respectively, incident on the diverging lens. This decrease in resolution was found to be due to an increase in the background coherent light scattered by the Scotchlite either directly towards the holographic film or retro-illuminated from the Scotchlite around the holographic camera onto the dispersing lens region and back towards the film (Section 6.3.2 of this dissertation).

The installation of the dark-field scheme was completed at the end of March 1985 and the scheme was used in the E-632 experimental run during April-August 1985. In this setup, similar to the BEBC test setup, a laser beam entered the bubble chamber through a small window at the bottom of the chamber after traversing 30 m from the laser in an underground vacuum pipe. The laser beam was diverged $\pm$ 20° using the same dispersing lens as used at BEBC (Akbari and Bjelkhagen, 1986). A description of the laser and the other apparatus is given in Chapters 3 and 6 of this dissertation.

Early trials of the boiling and holographic tests showed that pulses of duration $\geq$ 10 μs caused little boiling in the conventional pictures, but that they adversely affected the hologram quality. This was due to the small amount of boiling occurring near the laser window during the laser pulse which scattered light towards the holographic film. This light acted as a secondary source of reference beam, one of large "spot size". These spurious reference beams increased the coherent noise level on the hologram, giving multiple and fuzzy images. As a consequence, pulses of duration longer than 40 μs were used to suppress the boiling effects (Section 6.3.3 of this dissertation). Increasing the pulse length to 40 μs resulted in holograms with lower diffraction efficiency (brightness and contrast) arising from the bubble growth and movement during the hologram exposure, as well as from a deterioration of the optical quality of the primary reference beam. For pulses of duration of $\geq$ 10 μs the bubble growth and movement can easily exceed several wavelengths of light; changing the phase between the interfering reference and object beams by many times 2π (Section 2.2.5 of this dissertation).

The detailed results of these tests are given in Chapter 6 of this dissertation.

2.2.2 Definition of Holographic Parameters

Every point in bubble chamber space (x,y,z) is characterized by a number of holographic parameters:

θ_i : The angle between a ray from the dispersing lens to the point and the optical axis of the lens, "illumination angle."

α : The angle between a ray from the lens to the point, and a ray from the point to the hologram, "scattering angle."

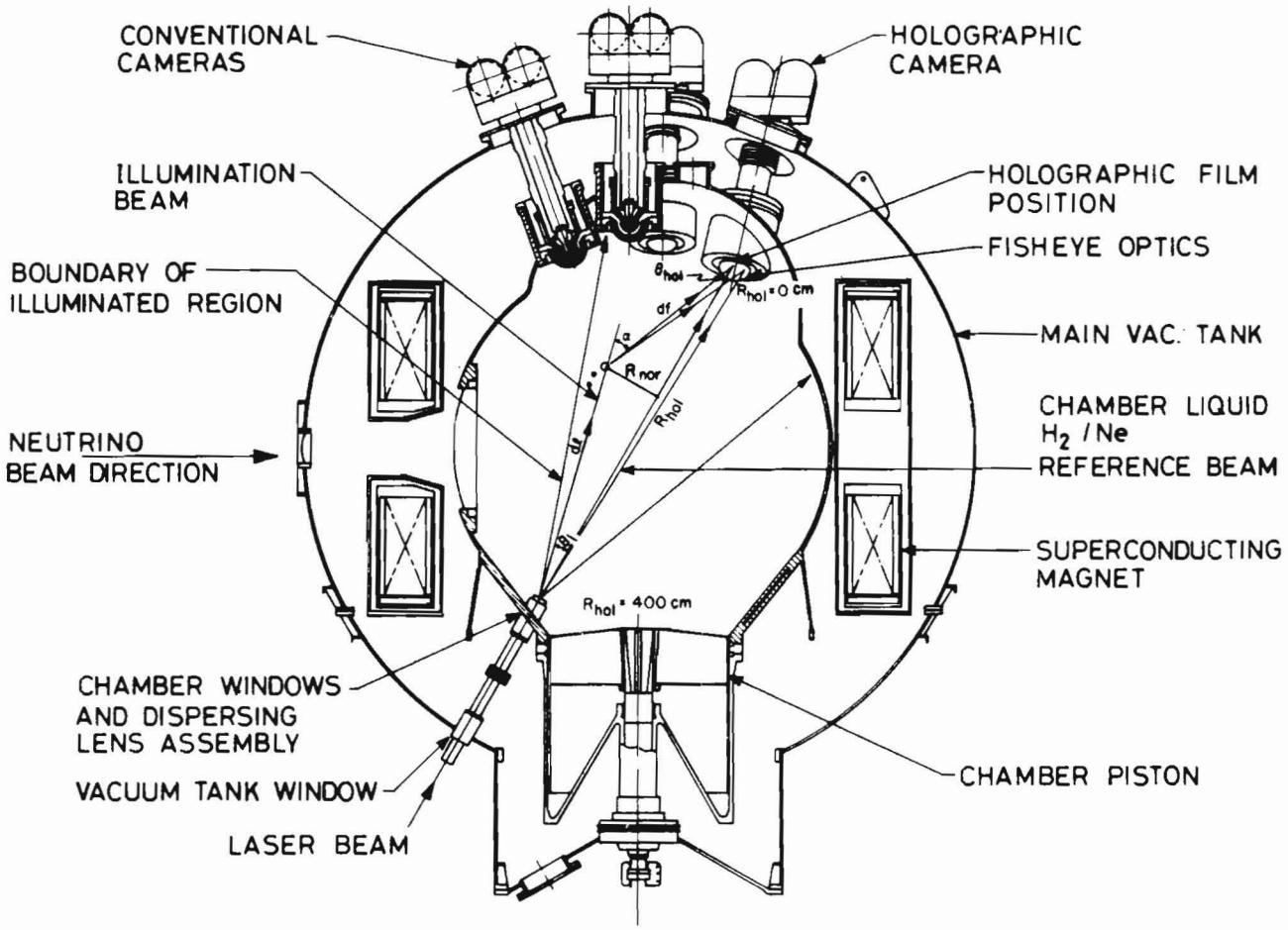

Fig. 2.8 15 foot bubble chamber with the holographic components, (side view).

θ_{hol} : The angle between a ray from the point to the hologram and the line of the reference beam, the "holographic axis."

R_{hol} : The projection along the holographic axis of a line from the hologram to the point. R_{hol} is zero at the camera and 400 cm at the lens.

R_{nor} : The perpendicular distance from the point to the holographic optical axis.

d_l : The distance from the dispersing lens to the point.

d_f : The distance from the point to the hologram.

I_{ref} : The intensity of the reference beam at the hologram.

An illustration of the holographic parameters for a given point is shown in Figure 2.8.

The hologram produced in the dark-field method has the following characteristics: it is of "single-beam," "off-axis," "transmission," "thick," and "amplitude" type. The first four are consequences of the recording arrangement and the emulsion type used. The last characteristic is a function of the processing procedure.

2.2.3 Light Scattering from Bubbles

The scattering of a plane electromagnetic wave by spherical obstacles was described exactly by Mie in 1908. The Mie solutions are complicated and are easily interpretable only when various approximations are assumed. For spheres with radii much larger than the scattered light wavelength, the diffraction and interference effects can be neglected, and the problem may be solved using geometric optics. For the 15-foot Bubble Chamber application, this approximation is valid since the bubbles have diameters about 100 μm which is about 150 wavelengths of the ruby laser light used, (λ = 694 nm).

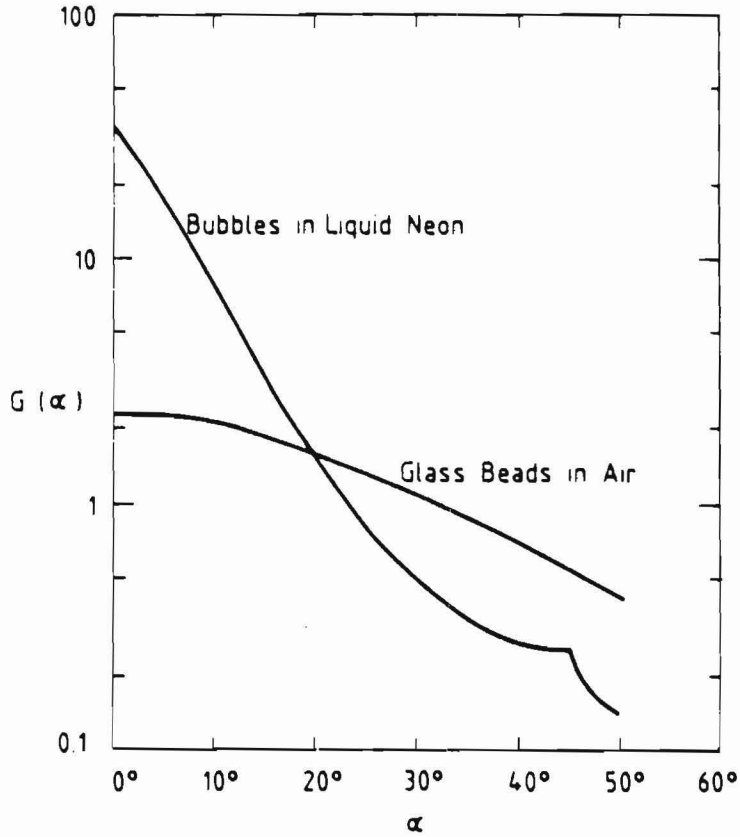

Fig. 2.9 Geometrical scattering function $G(\alpha)$ for bubbles (n_b=1.0) in neon-hydrogen (n_{ne}=1.085), and for glass beads (n_g=1.5) in air (n_a=1.0).

A simple geometrical analysis of light scattered by spherical bubbles for scattering angles in the range of $2^\circ < \alpha < 60^\circ$ at a large distance D_f is given by Welford (1967).[20]

$$I_{obj} = \frac{I_{inc} \times r^2 \times G(\alpha)}{D_f^2} \qquad [2.2.1]$$

where I_{inc} is the intensity of light incident on the bubble, r is the bubble radius, and $G(\alpha)$ is the geometrical scattering coefficient. This coefficient decreases rapidly with the angle of scattering α as shown in Figure 2.9. Most of the scattered flux falls within a forward cone with half angle of 15°. The function $G(\alpha)$ is not valid for scattering angles less than 2° since the Fraunhofer scattering function becomes appreciable. The discontinuity of $G(\alpha)$ at about 45° is a purely geometric effect, (Withrington, 1968).

2.2.4 Beam Balance Ratio

The Beam Balance Ratio (BBR) is defined:

$$\text{Beam Balance Ratio} = \frac{\text{Scattered light intensity from a bubble at the hologram}}{\text{Reference light intensity at the hologram}}$$

This is the inverse of the K-value of the bubble. Using Welford's expression for I_{obj}, Equation [2.2.1], BBR can be written:

20. A more detailed description of geometrical scattering by bubbles is given by Davies (1955).

$$BBR = \frac{I_{obj}}{I_{ref}} = \frac{F(\theta_i) \times r^2 \times \cos(\theta_{hol}) \times G(\alpha)}{d_l^2 \times d_f^2 \times I_{ref}} \qquad [2.2.2]$$

where I_{inc} is replaced by $F(\theta_i)$, the light intensity distribution after the lens which is a function of the illuminating angle, θ_{hol} is the angle of the tilt of the film with respect to the scattered light from a bubble, d_l is the distance from the lens, d_f is the distance from the holographic film, and I_{ref} (= F(0)) is the intensity of the reference beam at the hologram.

2.2.5 Bubble Movement and Growth

A certain degree of incoherence can be introduced into the intensity distribution of the interference pattern of the two beams when the optical path of one beam (usually the object beam) changes during the exposure. This occurs as a result of either the object movement or the vibration of the media in which the beam traverses.

A general expression for the intensity distribution of two coherent interfering beams can be written as, (Equation [2.1.5]),

$$I = u_r^2 + u_o^2 + 2u_r u_o \cos(\phi_r - \phi_o), \qquad [2.2.3]$$

where $\phi_r = kr_r$ and $\phi_o = kr_o$, with r_r and r_o as the reference and object path lengths from the laser to the hologram, respectively. Assuming that the two beams are both spatially and temporally coherent, an expression for the degree of coherence when the object moves can be obtained. For a system in which the object moves as $r_o(t)$ with no appreciable change in u_o, the interference pattern remains approximately constant except for the fringe motion. The exposure on the hologram, $E = I\tau_e$ with τ_e as the exposure time, can then be written as a time integral of intensity,

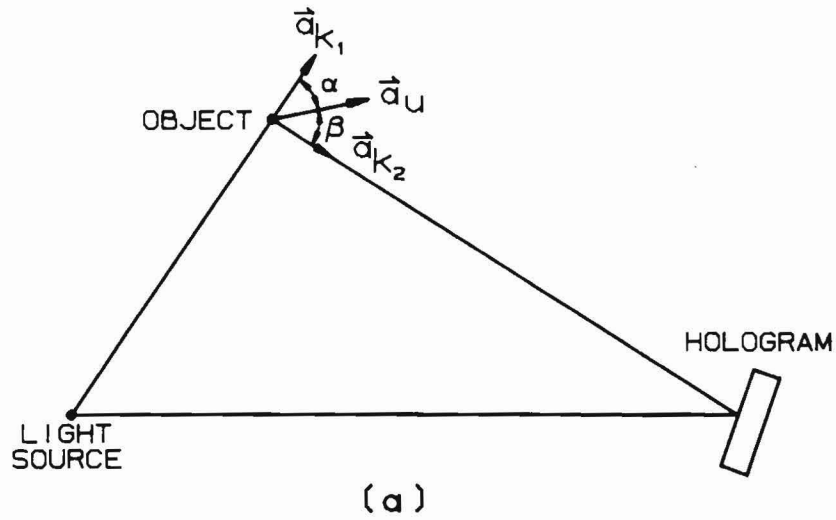

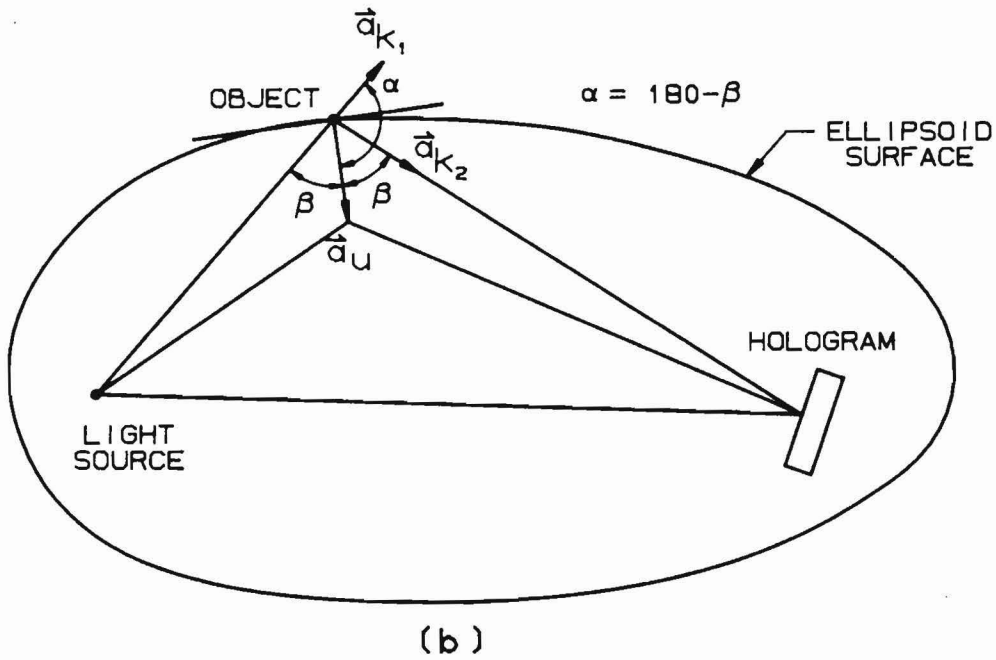

Fig. 2.10 (a) Definition of vectors and angles used in subject movement analysis.
(b) Geometry used for computing maximum allowable speed of a point subject.

$$E = \int_{-\tau_e/2}^{+\tau_e/2} \{u_r^2 + u_o^2 + 2u_r u_o \cos(kr_o(t) - kr_r)\}dt \qquad [2.2.4]$$

$$E = \tau_e \{u_r^2 + u_o^2 + 2u_r u_o \frac{1}{\tau_e} \int_{-\tau_e/2}^{+\tau_e/2} \cos(kr_o(t) - kr_r)dt\} \qquad [2.2.5]$$

Equation [2.2.5] gives the exposure on the hologram as a function of motion of the object during the exposure. It now remains to obtain the function $r_o(t)$. Neumann (1968) has given a general form of this problem. Using a similar argument to his and assuming $r_o(t)$ is a linear function of time, dr_o/dt can be written as two parts, the distance between the source and the object and the distance between the object and the hologram.

$$dr_o/dt = \vec{v}.\vec{a}_{k1} - \vec{v}.\vec{a}_{k2}, \qquad [2.2.6]$$

where $\vec{v}$ is the vector velocity of the object, $\vec{a}_{k1}$ and $\vec{a}_{k2}$ are the directional unit vectors from the source to object and from the object to the hologram, respectively, (Figure 2.10a). For $\vec{v} = v\vec{a}_v$ with $\vec{a}_v$ as the direction of the movement, the Equation [2.2.6] becomes,

$$dr_o/dt = v\vec{a}_v.(\vec{a}_{k1} - \vec{a}_{k2}). \qquad [2.2.7]$$

Equation [2.2.7] shows that dr_o/dt is zero when $\vec{a}_v.(\vec{a}_{k1} - \vec{a}_{k2})$ is zero which would occur when the angles between the directional vectors are equal, i.e. $\alpha = \pm \beta$, where the two angles are defined in Figure 2.10a. This condition defines a circular cone about the velocity vector for which the fringe contrast is not affected by the motion of the object. A specific case is

when $\alpha = \beta = 0$, for which the object moves along the axis joining the source to the hologram, (in-line method).

The worst-case is when the vector $(\vec{a}_{k1} - \vec{a}_{k2})$ is parallel to $\vec{a}_v$. This occurs when the particle moves in a direction perpendicular to an ellipsoidal surface as shown in Figure 2.10b,

$$\vec{a}_v.\vec{a}_{k1} - \vec{a}_v.\vec{a}_{k2} = \cos(180 - \beta) - \cos\beta = -2\cos\beta \qquad [2.2.8]$$

For this case the path change of the object beam is maximum. Since our concern here is to obtain an upper limit on the length of the exposure time for which the fringe contrast is still preserved, we limit the discussion to this case.

At this stage, the maximum allowable velocity of the object, i.e. the bubble, can be calculated. Assuming that the object-reference beam optical path length difference must not change by more than one-tenth of wavelength of light during the exposure duration, the v_{max} can be obtained from Equation [2.2.6],

$$\delta r_o = 2 \times v\tau_e\cos\beta, \qquad [2.2.9]$$

$$v_{max} = \lambda \ / \ (20 \times \tau_e\cos\beta). \qquad [2.2.10]$$

In the bubble chamber the maximum allowable velocity of each bubble depends on laser pulse duration, and its location $(2\beta = 180 - (\theta_i + \theta_{hol}))$. For bubbles closer to the holographic axis both θ_i and θ_{hol} are small and β gets closer to 90° which results in large v_{max}. Table 2.1 gives v_{max} values for different laser pulse durations and bubble locations.

				v_{max} (cm/s)			
R_{hol}(cm)	θ_i °	θ_{hol} °	β °	τ_e : 100 ns	2 μs	10 μs	40 μs
200	10	10.5	79.8	200	10	2.0	0.50
200	20	20.9	69.6	100	5	1.0	0.25
200	30	31.2	59.4	68	3	0.7	0.17
100	15	39.9	62.5	37	1.9	0.4	0.09
200	15	15.8	74.6	131	6.5	1.3	0.33
300	15	5.7	79.7	200	10	2.0	0.50

- Table 2.1 -

It can be seen that for a given R_{hol} the maximum velocity of motion of the bubble decreases with increasing angle, and for a given θ_i this velocity decreases for bubbles closer to the hologram. Furthermore, v_{max} decreases drastically with increasing pulse length; for 40-μs pulses it is only 0.33 cm/s at R_{hol} = 200 cm, and θ_i = 15°.

In the 15-foot Bubble Chamber three phenomena may disturb the bubble-reference beam optical path difference during the exposure: the growth of the bubble, bubble drift due to buoyancy forces, and the mechanical movements of the beams due to the piston motion. The first two phenomena change the object beam path and are discussed in this section. The piston motion most likely change the optical path of both beams; however, since we have no exact knowledge of these changes, no discussion of this effect is given here.

A bubble grows in proportion to the square root of its growth time after it is nucleated. The detail of bubble growth phenomenon is described in Section 5.2. Here it suffices to use the bubble-growth equation,

$$r = A\ t^{1/2}, \qquad [2.2.11]$$

where r is the bubble radius, A is a proportionality constant determined by the operating condition of the bubble chamber, and t is the growth time. From Equation [2.2.11] it can be seen that a smaller bubble grows linearly faster than a larger bubble. Thus the object path change is a function of the bubble size at the time of exposure. Assuming the bubble is an opaque particle where only the reflective terms may be considered for the light scattering, the object path change can then be written as a function of bubble radius change during the exposure, Δr, using Equation [2.2.9].

$$\delta r_o = 2 \times \Delta r \cos\beta. \qquad [2.2.12]$$

It is interesting to know for the 15-foot Bubble Chamber operating conditions during the 1985 physics run what were the object beam path changes for a given bubble size during exposures of duration of 40 μs. Table 1.3 gives the path length change in units of $(\lambda/10)$ for different bubble sizes and exposure durations 1 ms after the bubble is nucleated. In this table the calculated values with $A = 0.57\ cm/(s^{1/2})$ and bubble radius of 180 μm represent typical values of these parameters for the run; all the calculations are for a bubble at $R_{hol} = 200$ cm and $\theta_i = 15°$.

		Δr (μm) ; δr_o ($\lambda/10$)			
r (μm)	A(cm/s$^{1/2}$)	τ_e : 100 ns	2 μs	10 μs	40 μs
50	0.16	0.002;0.013	0.05;0.26	0.25;1.29	1.00;5.11
100	0.32	0.005;0.026	0.10;0.52	0.51;2.57	2.00;10.2
180	0.57	0.009;0.046	0.18;0.92	0.90;4.59	3.57;18.2

- Table 2.2 -

Table 2.2 shows that only for pulses of duration 100 ns and 2 μs will the bubble-reference beam optical path changes be well below the $\lambda/10$ criterion for all bubble sizes. For pulses of duration $\geq$ 10 μs, the bubble growth changes the optical path by at least $\lambda/10$. From Table 1.3, it can be seen the choice of bubble position used for these calculations is an intermediate one, and for larger illumination angles a smaller v_{max}, and as a consequence a smaller bubble radius change is allowed.

The upward velocity of the bubble due to buoyancy forces is also a function of the bubble size, (Harigel, Riche, Horlitz, and Wolff, 1968). For bubbles with radii smaller than 10 μm, this velocity is negligible and for bubbles with radii greater than 200 μm, the upward velocity is constant and is a function of the liquid properties. For bubbles with radii in range of $10 < r < 200$ μm, this velocity is proportional to r^2. The upward velocities for bubbles of radius 50, 100, and 180 μm for a 75/25 % Ne/H_2 mix are estimated to be 0.9, 3, and 10 cm/s, respectively. These values are much larger than the v_{max} allowed for 40-μs pulses.

The above discussion shows that for exposures of duration of 40 μs the object beam optical path length changes by several $\lambda/10$. It is then

appropriate to understand how this path change will affect the modulation of the interference pattern intensity. Substituting the expression for $r_o(t)$ in Equation [2.2.5] and using Equations [2.2.6] and [2.2.9], it follows that

$$E = \tau_e \{u_r^2 + u_o^2 + 2u_r u_o \frac{1}{\tau_e} \int_{-\tau_e/2}^{+\tau_e/2} \cos(kr_{o1} + 2kv\cos\beta t - kr_r)dt\} \qquad [2.2.13]$$

$$E = \tau_e \{u_r^2 + u_o^2 + (2u_r u_o \cos(kr_{o1} - kr_r)) \frac{\sin(kv\cos\beta\tau_e)}{kv\cos\beta\tau_e}\} \qquad [2.2.14]$$

$$E = \tau_e \{u_r^2 + u_o^2 + 2u_r u_o \cos(kr_{o1} - kr_r)\mathrm{sinc}(kv\cos\beta\tau_e)\} \qquad [2.2.15]$$

where sinc(x) is sinx/x. Thus the reconstructed image field is spatially modulated in proportion to $\mathrm{sinc}(kv\cos\beta\tau_e)$. For the no-motion case, ($v = 0$), the sinc function is equal to unity. For large values of v the sinc argument is large and the contrast is poor. For specific values, $kv\cos\beta\tau_e = n\pi$ (where n is an integer), the contrast is zero. Neumann (1968) has studied the effect of such motions on the hologram fringe pattern and on the reconstructed image quality both theoretically and experimentally. Here, only the results will be stated. For motions transverse to the hologram, as in the case we are considering here, the fringe pattern obtained is composed of strips with maximum intensities at the center and with minima occurring when the sinc argument is $n\pi$. This motion-induced fringe pattern results in reduced diffraction efficiency of the image.

CHAPTER 3 HIGH POWER PULSED RUBY LASER

3.1 Characteristics of the Holographic Sources

Pulsed ruby lasers (λ = 694 nm) were used for the holography described in this thesis. The preliminary experimental tests were carried out using a laboratory laser system. For the physics run a commercial laser system was adapted to our requirements. Both systems will be described in this Chapter following a discussion of the general characteristics of pulsed ruby lasers.

A ruby laser was chosen because it satisfied all the following requirements.

1. A pulsed source is necessary to avoid the adverse influence of growth and movement of the bubbles during the exposure upon the hologram quality.
2. The source must produce high enough energies to illuminate a large volume.
3. Operation of the source in single longitudinal and transverse modes is essential to obtain the long coherence length needed to accommodate the range of object beam path lengths.

Pulsed ruby lasers can satisfy all the above requirements. A frequency-doubled Nd:YAG (Neodymium-Doped Yttrium Aluminum Garnet, λ = 532 nm) is another possibility. However, Nd:YAG material has a higher inversion gain[21] (lower threshold) compared to ruby and stores less

---

21. Ruby lasers are three-level systems as compared to Nd:YAG lasers which are four-level systems. The three-level systems require a large number of atoms to be excited to the metastable level before emission can occur.

energy which makes it more difficult to obtain energies of the order of 10 J required for illuminating a conical volume with half angle of 20°.

The choice of the ruby laser is also convenient since the effect of the conventional photography flashlamps ($\lambda \sim 500$ nm) upon the holograms can be cut off by using color filters both in front of the hologram and the flashlamps, (cf. Section 6.1.3).

The disadvantages of ruby lasers are their higher noise levels,[22] their higher sensitivity to temperature variations, and their lower maximum repetition rate. The latter is not a major disadvantage at the 15-foot Bubble Chamber which was only expanded at the rate of 3 pulses/minute during the 1985 E-632 physics run (cf. Section 1.6.2).

3.1.1 Theory of the Laser

Pink ruby is made of sapphire, Al_2O_3, doped with small amounts of Cr^{3+} ions (0.035 - 0.05 % by weight of Cr_2O_3) which are the active ions. The crystal is uniaxial, has a hexagonal unit cell and an axis of symmetry, the c-axis, (Figure 3.1). For lasers the ruby crystal boules are usually grown along an axis making a 60° angle with the crystallographic c-axis, and they are usually cut in the shape of a cylindrical rod. The ends can be cut and polished plane-parallel, wedged, or at Brewster angles, and are usually antireflection coated.

The light radiated from the ruby crystal is highly polarized. The polarization direction depends on the alignment of the c-axis with respect to the crystal axis. If the ruby crystal is aligned so that the c-axis is vertical,

---

22. There are many more atoms which can contribute to spontaneous emission which is a source of noise in three-level systems due to its higher threshold for emission (see previous footnote).

(in which direction the crystal appears darkest), the light emerging from the crystal has a horizontal polarization, (Figure 3.2). The direction of polarization is normal to the c-plane, a plane formed by the rod axis and the crystal c-axis.

The Cr^{3+} ions which are the active material in ruby have three d-electrons in their unfilled shell with a ground state of ^4A for the free ion. The principal radiative transition for Cr^{3+} ions in ruby is shown in Figure 3.3. Ruby is a three-level system. For a three-level laser the atoms of the active material in the lowest level, ^4A, are first excited into the broad pump bands, $^4F_2$ and $^4F_1$; each is 1000 Å wide. The lifetimes of these bands are of the order of a few nanoseconds; with the ions returning to a metastable level, ^2E. This metastable level itself is composed of two sublevels, 2A and E, each being 5 Å wide at room temperature. The emission lines are R_1 and R_2, 6943 and 6929 Å. The linewidth of these metastable levels, with fluorescence lifetime, ~ 4.3 ms, is relatively long. Since there are more atoms excited into the E state due to its lower energy level as compared to 2A, the E level reaches the laser threshold sooner and becomes depleted faster. Although both R_1 and R_2 lines contribute to fluorescence of the ruby, the laser action only occurs through line R_1 unless the emission of line R_2 is enhanced externally.

Light can be extracted from a ruby crystal in a two-step process. First, the electrons of the active material are excited into the absorption bands with the radiation emitted by the pump flashlamp. For the case of ruby with well-located blue and green broad bands, Xenon flashlamps are used. Xenon has relatively high radiation at 400 - 500 nm wavelengths when operated at high current densities (~ 1700 A/cm^2), (Koechner, p. 254,

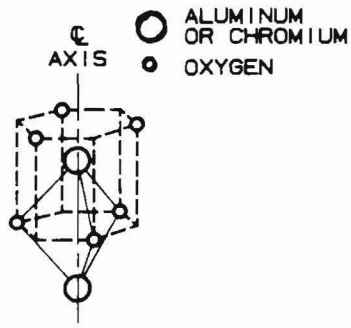

Fig. 3.1 Crystal structure of sapphire.

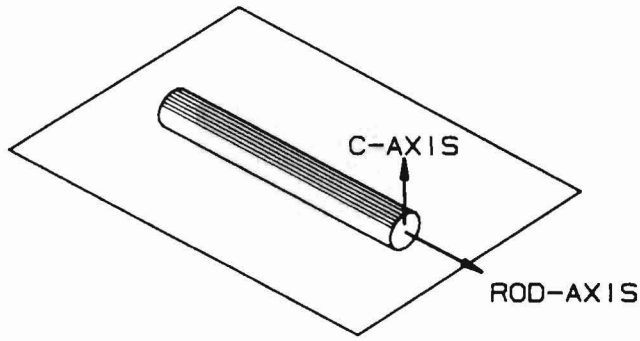

Fig. 3.2 Location of c-axis of a ruby rod. The emerging light has horizontal polarization.

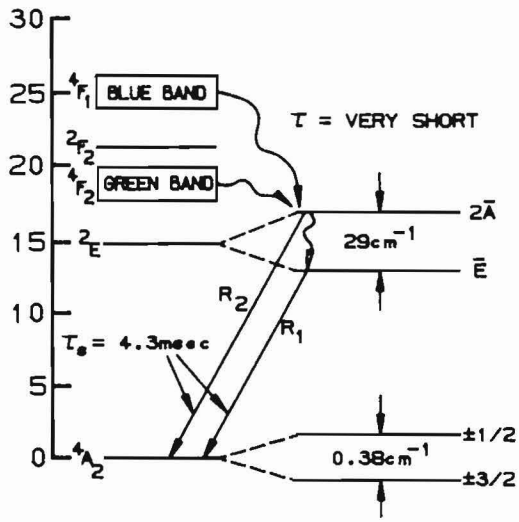

Fig. 3.3 Energy level diagram of pink ruby.

1976). Xenon also has high efficiency in converting the electrical energy to radiation.

Once the electron population in the crystal is inverted to the metastable level, the energy can be released either by stimulated emission or by oscillation initiated by some spontaneous noise radiation. In stimulated emission an optical beam of same wavelength as of the emission lines, R_1 and R_2, is amplified when passing through the crystal, which forms an optical amplifier. In resonating emission the photon oscillation can be initiated by some spontaneous radiation along the crystal axis between two reflecting surfaces. With a gain sufficiently larger than the external and internal losses the radiation is subsequently amplified by stimulated emission upon passage through the rod.

The light emitted from a laser oscillator composed of a pump cavity (laser rod and pump source) and two reflectors (front and rear mirrors) normally has poor temporal and spatial coherence due to the inherent fluorescent linewidth of ruby, 5.5 Å at room temperature, which permits a large number of transverse modes with unrelated frequencies to oscillate simultaneously. For holography it is desirable to operate the laser at a single frequency in one transverse mode. Sections 3.1.2 - 3.1.3 elaborate the concepts of spatial and temporal coherence, their necessity in holography, and the methods used to obtain temporally and spatially coherent light output for the study reported in this thesis.

For holographic applications where a pulsed laser is used, the length of the pulse and the temporal energy distribution of the light are also important. It is desirable to have a single pulse with a uniform power distribution. The most suitable pulse length depends upon the application.

Pulsed solid-state lasers are generally operated in one of three modes: free-lasing, mode-locked, and Q-switched. A ruby laser with no sudden change in its cavity losses emits a stream of light pulses of duration $\Delta\tau_{fwhm} \simeq 100$ ns over $\lesssim 1$ ms range in the free-lasing mode. The emission of the light pulses begins after the cavity gain has reached the threshold level (~ 0.8 ms after the flashlamp trigger) and continues for $\lesssim 1$ ms until the population inversion is depleted.[23] For each pulse several longitudinal and transverse modes oscillate simultaneously without any amplitude or phase relationship. Although methods for selecting single transverse and longitudinal modes can be used, the frequency selectivity varies from pulse to pulse. This inefficient frequency selection of the cavity in the free-lasing mode, its low peak power and its multi-pulsing features make it undesirable for most holographic applications.

A single, energetic pulse of duration $\Delta\tau \simeq 20$ ns can be obtained from laser cavities operating in the Q-switched mode. A dye cell (a passive Q-switch) or a controllable birefringent crystal (an active Q-switch) can introduce losses in the cavity until the gain reaches its maximum, when a sudden decrease in the loss enables the cavity to emit a giant pulse. Q-switched pulses contain 70 - 80 % of the total energy available in the free-lasing mode, and thus have large peak powers. Operating the laser in Q-switched mode is appealing due to its efficient frequency selection mechanism[24] and the possibility of extraction of large amounts of energy in a single pulse. The concept of Q-switching and the methods to obtain a Q-switched pulse are described in Section 3.1.4.

---

23. These values vary depending on the flashlamps voltage.

24. A Q-switched pulse enhances the oscillation of a mode with a high gain, (cf. Section 3.1.3).

3.1.2 Spatial Coherence

Spatial coherence is defined in terms of the difference in phase at a fixed time and at points on a plane perpendicular to the light propagation. The visibility of the interference fringes made by interfering two parts of a beam which are in time with each other gives a measure of how good this coherence is. If the illuminating light is composed of a number of uncorrelated transverse modes, each produces an interference pattern independent from the others. The resultant intensity is thus a random combination of these interference patterns and the contrast of the fringes in the hologram becomes very poor.

A laser operating in any one transverse mode produces a spatially coherent output beam. It is preferable to operate the laser in the lowest mode, TEM_{00}. This mode is of particular interest for holography because of its uniform, uniphase, Gaussian radial intensity distribution, its low divergence, and its high power density and brightness (power/unit area/solid angle) relative to the higher modes. Furthermore, the higher order modes are less stable, and there is a tendency for two or more such modes to oscillate simultaneously. Figure 3.4 shows the intensity distribution and the mode pattern for the three lowest modes. The $TEM_{01}{}^{*}$ mode is a linear superposition of two TEM_{01} modes, one rotated 90° about the axis relative to the other.

A laser can be biased against the higher modes by choice of resonator configuration, aperture size, internal beam focusing components, and use of thermally controlled rods. The most suitable resonator configuration to generate the TEM_{00} mode is a plano-concave resonator where the back mirror is curved with a large radius (to give small divergency) and the front

mirror is plane (Koechner, Section 5.1, 1976). In this resonator the beam narrows down at the plane mirror where an aperture can be located to select the mode. The size of this aperture determines the oscillating mode. A small aperture introduces large losses for the higher modes, thus selecting the lowest ones. Such a mechanism can produce a diffraction-limited spot. The diameter of the aperture should be chosen to be twice that of the beam waist, w_0, to give only 0.3 % power loss for the TEM_{00} mode where intensity distribution is $I(r) = I_0 \exp(-2r^2/w_0^2)$. The beam waist at the plane mirror for a plano-concave resonator with a resonator length of ΔL and a mirror of curvature of R_2 is given by Koechner, (p. 181, 1976), as

$$w_0^2 = \left(\frac{\lambda}{\pi}\right) \times (\Delta L \ (R_2 - \Delta L))^{1/2}. \qquad [3.1.1]$$

It should be noted that a slight misalingment, or imperfection of the laser reflectors can cause a change in the mode character, favoring higher order modes. In order to minimize optical and thermal distortions in the wavefront of the TEM_{00} mode, the rod must also be pumped and cooled uniformly.

3.1.3 Temporal Coherence

Temporal coherence is defined as the variation in phase at a single point in space as a function of time. The fringe contrast of the pattern produced by a beam interfering with itself gives a measure of the temporal coherence of the beam. If a beam is composed of a number of longitudinal modes differing from one another by integer multiples of the central wavelength, the output spectral distribution will be highly modulated.

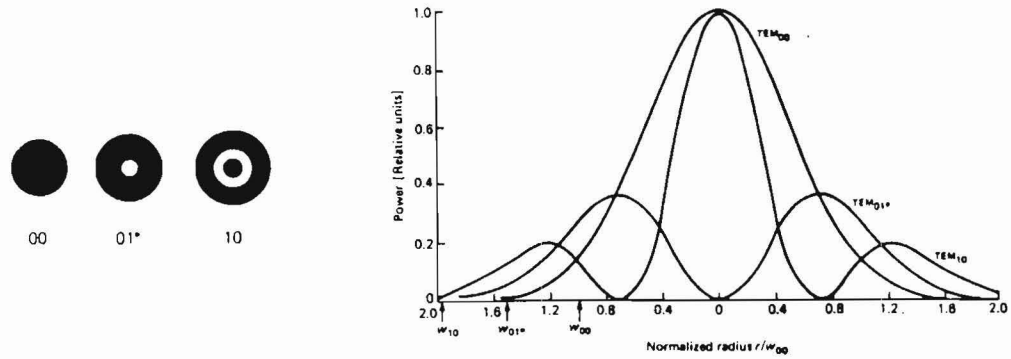

Fig. 3.4 (a) Radial intensity distribution, (b) transverse mode pattern for TEM_{00}, TEM_{01}*, and TEM_{10}.

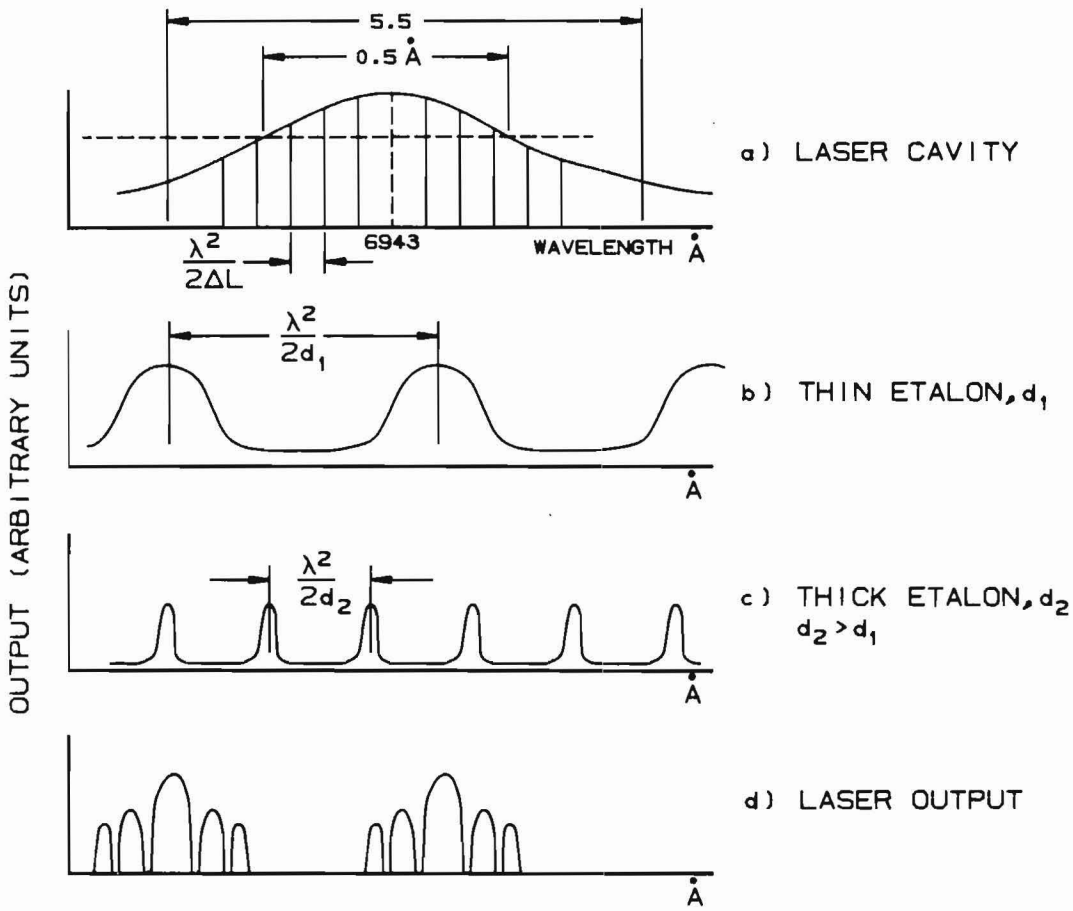

Fig. 3.5 Spectral output of a ruby laser with two single plate intracavity etalons.

To obtain an output beam of high temporal coherence, one has to reduce the number of longitudinal modes to a small number, ideally one.

Longitudinal Mode Selection

Every laser amplifies light at a specific frequency with a natural linewidth which is inherent to the active material used. This linewidth will be broadened by additional effects among which crystal inhomogeneity and thermal lattice vibrations are the most important for solid-state lasers. A ruby laser has an inherent fluorescence linewidth of 5.5 Å at room temperature. For oscillators with gains just above threshold, this linewidth narrows to 0.5 Å. The number of oscillating longitudinal modes in a cavity of typical length $\Delta L = 114$ cm with spacing $\Delta\lambda$ between the modes can be calculated as following:

$$\# \text{ Modes} = 0.5 \ / \ \Delta\lambda \qquad [3.1.2]$$

where

$$\Delta\lambda = \lambda^2 \ / \ 2\Delta L \qquad [3.1.3]$$

$$= (6943 \text{ Å})^2 \ / \ 2 \times 114 \times 10^{18} \text{ Å} = 0.002 \text{ Å}$$

$$\# \text{ Modes} = 0.5 \ / \ 0.002 = 250.$$

Thus the envelope of the 0.5-Å-wide laser line contains about 250 longitudinal modes spaced 0.002 Å apart.

To reduce the number of longitudinal modes, Fabry-Perot etalons can be introduced into the cavity. An etalon is a short (e.g. 10 mm) cavity with correspondingly large mode separation such that only a few of the longitudinal modes oscillate in the two cavities, (Equation [3.1.3]). The bandwidth of the allowed modes is determined by the reflectivity of the etalon. Superposition of the laser and etalon will limit oscillation to those few common modes, preferably one, which have a large enough gain.

Etalons can in fact be used in place of the front laser mirror in the form of a resonant reflector; alternatively it can be inserted in the cavity (an intracavity etalon). They are made of two or more parallel and precisely spaced optical surfaces of quartz or sapphire which have high power thresholds for damage. An incident wave on the etalon is multiply-reflected between the optical surfaces. The individual frequency components of the wave interfere with their reflected or transmitted members at the optical surfaces. At normal incidence the phase of each component differs from that of the preceding one by twice the path through the etalon gap, divided by the wavelength. At other angles this phase difference is

$$\delta = \frac{2\pi}{\lambda} (2nd) \cos\phi, \qquad [3.1.4]$$

where n is the index of refraction of the optical surface, d is the spacing between the surfaces, and ϕ is the refraction angle in the gap.

Using etalons either as resonant reflectors or as intracavity elements gives the net result that only some longitudinal modes can oscillate. For an etalon composed of more than two plates equally spaced, resonances can occur between all the pairs of parallel optical surfaces. Superposition of all these resonances determines the allowed modes. The superposition of these allowed modes with the longitudinal modes of the active material allows one to select a single mode with a gain above threshold for oscillation. It is most efficient to superimpose the resonant transmission peak of an intracavity etalon (in case of resonant reflector the reflection peak) on the peak of the fluorescence curve of the active material. This can be achieved by adjusting the temperature or/and tilt of the etalon. Figure 3.5 shows

the mode selectivity of a cavity with two intracavity tilted etalons with thicknesses $d_2 > d_1$.

A slight change in the temperature of an etalon would change the index of refraction and thickness of the plates, and their spacings; these changes shift the wavelength of the resonant peaks. It is thus necessary to control the temperature of the etalons to within 0.1 °C.

An intracavity etalon also has to be tilted to prevent the formation of resonances between the etalon and other optical surfaces in the cavity.

Mode selection can be further enhanced by:

1. cooling the rod to decrease the linewidth of the material,
2. operating the laser close to threshold so that only a small number of modes have sufficient gain to oscillate,
3. increasing the output mirror reflectivity to lengthen the pulse build-up time and allow more round trips before the light is emitted which narrows the line-widths of the allowed modes,
4. increasing the Q-switching rise time to prevent the build-up of modes with smaller gain,
5. reducing the length of the cavity which increases the spacing between the longitudinal modes (Equation [3.1.3]) and thus makes it easier to discriminate against unwanted ones.

Coherence Length

The degree of coherence for two interfering beams traveling via different paths is limited by the path length difference of the two beams, the linewidth of the longitudinal modes of the laser pulse, and the length of the pulse. The maximum path length difference of the two beams which still results in a constructive interference –the coherence length of the pulse–

can be expressed in terms of the linewidth of the mode and the pulse length.

An expression for the coherence length is derived by Collier, Burckhardt, and Lin (Section 11.3, 1971) for a single-frequency and spatially coherent pulsed laser.

$$l_c = \sqrt{\ln 2}\ \frac{c \times 0.5\Delta\tau}{(1 + (\pi \times 0.5\delta\nu \times 0.5\Delta\tau)^2)^{1/2}} \qquad [3.1.5]$$

where c is the speed of light, $\Delta\tau$ is the length of pulse, and $\delta\nu$ is the linewidth of the longitudinal mode of the pulse. This linewidth is determined by the length of the cavity, the mechanical and thermal stability, and the optical losses of the cavity structure. The factor of $[(0.5 \times (\ln 2)^{1/2}) \simeq 0.42]$ is an arbitrary criterion which assumes a minimum fringe visibility. This minimum occurs when ~ 58 % of the reference beam interferes with the object beam.

Equation [3.1.5] shows that the coherence length for a single frequency pulsed laser with infinitely small linewidth is limited by the pulse duration. A finite bandwidth $\delta\nu$ reduces this maximum value by a factor $[1 + (\pi \times 0.5\delta\nu \times 0.5\Delta\tau)^2]^{1/2}$. A typical value of $\delta\nu$ for a ruby laser operating in moderately controlled conditions is 3 MHz. For this linewidth the Equation [3.1.5] yields a coherence length of 2.5 m for a 20 ns pulse, 57 m for 2 μs, and 58 m for pulses with durations equal or greater than 2 ms. Thus the coherence length is limited by the pulse length for short pulses of nanosecond duration and by the linewidth for the longer pulses. For an infinitely long pulse, (i.e. continuous wave laser), the Equation [3.1.5] only depends on the linewidth ($l_c \propto c/\delta\nu$).

If the laser light is composed of two or more longitudinal modes, the interference among them creates a modulated pattern. The modes are then said to "beat" with one another. These beats have a sinusoidal pattern and repeat every $2\Delta L$, where ΔL is the oscillator length. The length over which the modes interfere constructively, L_s, is given by

$$L_s = 2\Delta L \ / \ s, \qquad [3.1.6]$$

where s is the number of the oscillating modes. In this case the coherence length is twice this length

$$l_c = 2L_s = 4\Delta L \ / \ s. \qquad [3.1.7]$$

Thus with increasing number of the oscillating modes the coherence length falls very rapidly.

Coherence Length Measurements

Coherence lengths can be measured by various techniques among which observing the rings produced by a Fabry-Perot interferometer, and measuring the fringe-free depth of field in a hologram are most common. For holographic applications, as in case of the bubble chambers, the second, holographic, method is more directly interpretable. In this method, a long object is used to reflect back the illuminating beam over its length thus providing a range of path differences from zero to several meters long between it and the fixed reference beam.

Figure 3.6 shows such a holographic setup. A single laser beam illuminates both the object (a long bar of length L_1 covered with

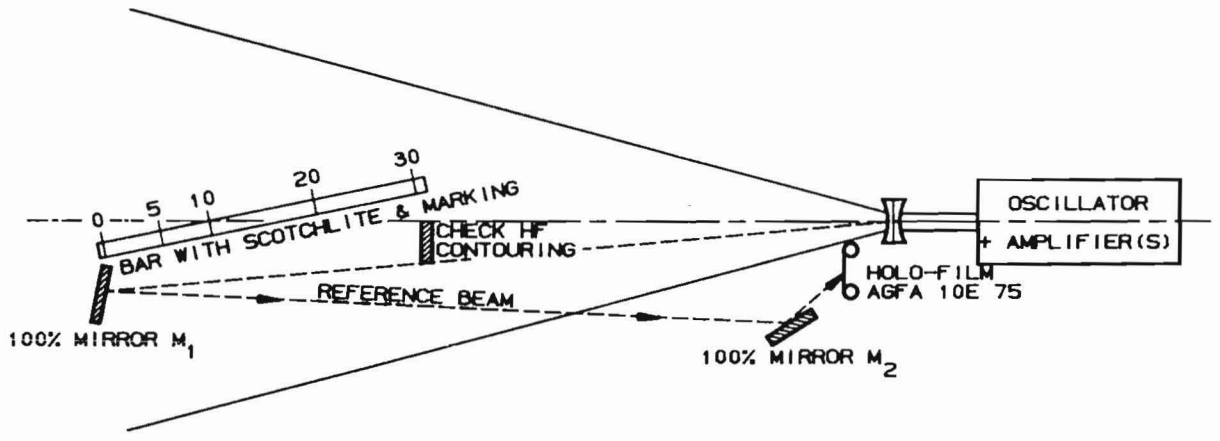

Fig. 3.6 Layout for the holographic measurement of the coherence length.

retrodirective Scotchlite) and a mirror M_1 at the end of the bar. Mirror M_1 reflects the light via mirror M_2 into the holographic film plane and comprises the reference beam. The hologram can be reconstructed by means of a Helium-Neon laser and by looking through it to observe the virtual image of the bar. In the replayed hologram the bar appears dark when the light reflected from it is no longer coherent with the reference light. When more than one longitudinal mode is present bands appear on the bar which are spaced by the length L_s defined by Equation [3.1.6].

Generally, if F (F>0) bands are visible on a test bar of length L_1, the coherence length, l_c, is given by

$$2L_1/(F+1) < l_c < 2L_1/F. \qquad [3.1.8]$$

For a hologram with F=0, $l_c > 2L_1$. Examples of such holograms are shown in Figure 4.9.

3.1.4 Q-Switching

Operation of the laser in a single-pulse mode, "Q-switched," can be achieved by inserting devices which control the cavity losses. Most popular devices are electro-optic shutters (Pockels cells, Kerr cells), saturable absorbers (Dye cells), rotating mirrors, and devices which utilize acousto-optic effects. Since Pockels cells were used in the lasers for the 15-foot Bubble Chamber experiment, we limit our discussion to a description of this device. Nevertheless, the principle of Q-switching is essentially the same for the other methods.

A Pockels cell is composed of a crystal enclosed in an index matching fluid with electrodes attached to apply an electric field. The crystal is

oriented so as to become birefringent under the influence of an external field, and is characterized by perpendicular "slow" and "fast" axes with different indices of refraction for plane polarizations parallel to these axes. In absence of an applied voltage, the index ellipsoid is a circle with the same index of refraction in both directions. When a voltage is applied to the crystal the ellipsoid changes its shape, not its orientation, and the crystal become an optical retardation plate of electrically variable retardation. Incident polarized light will in general emerge with its polarization altered; the polarization change depends on the voltage applied to the crystal and on the orientation of the incident polarization relative to the crystal axes. Two important parameters are the quarter- and half-wave voltages, $V_{1/4}$ and $V_{1/2}$. Incident light linearly polarized at 45° to the fast and slow axes after passing the crystal changes to circular when $V_{1/4}$ is applied and linear with 90° rotation when $V_{1/2}$ is applied. It is more common to use the crystal with $V_{1/4}$ applied since this voltage is lower than $V_{1/2}$, and there is no or fewer polarizers needed. If the laser radiation is plane polarized, as it is for rubies, there is essentially no need for an additional polarizer. Alternatively, the unwanted polarization can be extracted from the cavity by a polarizing prism.

In ruby lasers the Pockels cell is usually placed between the rear mirror and the rod. The vertically (horizontally) polarized light becomes horizontally (vertically) polarized after two passes through the Pockels cell, and is not amplified as much in the ruby. Insertion of a polarizing prism between the Pockels cell and the laser rod assures a complete suppression of the radiation, and thus prevents the laser pulse build-up. When $V_{1/4}$ is removed the linearly polarized beam passes the polarizer-Pockels cell combination with no loss, the gain will increase, and lasing will commence.

The most popular crystal is KD^*P (Potassium di-Deuterium Phosphate, KD_2PO_4) because it has the lowest $V_{1/2}$ and $V_{1/4}$ which simplifies fast switching of the Pockels cell.

Figure 3.7 shows schematically the variation of resonator parameters as a function of time in the development of a Q-switched pulse. The mathematical problem of evolution of a Q-switched pulse in a laser has been formulated and solved by Wagner and Lengyel (1962). They showed that the rate of change of photon density in the cavity depends on two competing terms: amplification and fractional loss terms per traverse.

For Q-switched pulses the loss coefficeint, γ, is composed of two parts: γ_0 and γ_1. γ_0 is the loss in the optical elements in the cavity (most important of all are the output mirror with typical 20 % reflectivity and the etalons), and γ_1 is the induced effective loss due to the Pockels cell used for Q-switching. In the case of a polarizer-Pockels cell combination this loss is $\gamma_1 = \ln(\cos^2((\pi/2) \times V/V_{1/4}))$, where V is the voltage on the Pockels cell. To form a Q-switched pulse the quarter-wave voltage is applied to the Pockels cell ($V = V_{1/4}$, $\gamma = \gamma_1 = \infty$) and the laser rod is pumped until the peak population inversion is reached. The voltage is then set to zero ($V = 0$, $\gamma_1 = 0$, $\gamma = \gamma_0$). At this stage a large amplification in photon density in a short time results in a single, giant, high power pulse. If the laser is operated at suitable settings for the flashlamp voltages, and Pockels cell voltage and delay, most of the energy stored in the rod can be depleted during the Q-switched pulse and no post-lasing pulses are observed. In practice this is difficult to achieve, and sometimes a second Pockels cell is used outside the cavity to filter out the post-lasing.

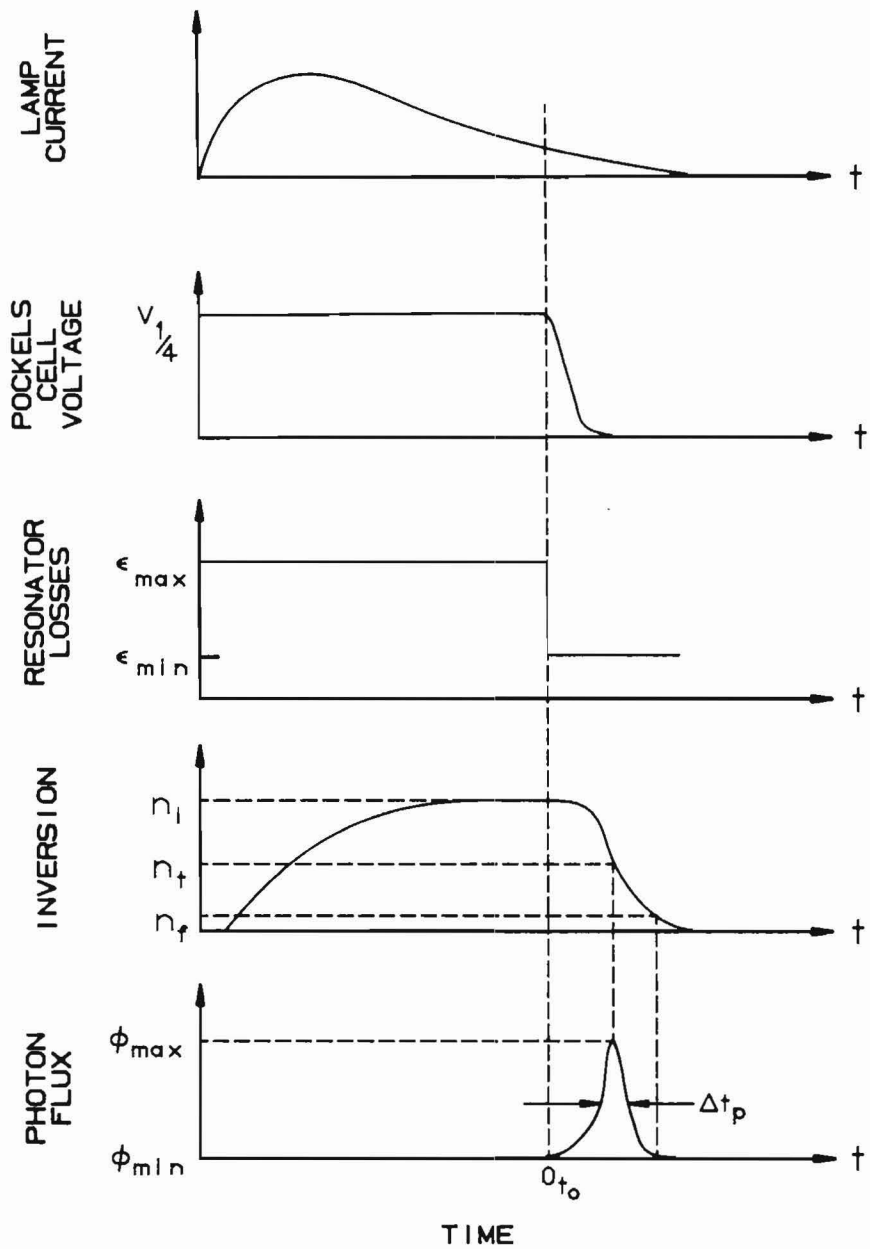

Fig. 3.7 Development of a Q-switched pulse. Shown is the flashlamp output, pockels cell voltage, resonator loss, population inversion, and photon flux as a function of time.

3.2 The Laboratory Laser

The laser used during the developmental tests of holography was composed of an oscillator and four amplifiers mounted on the axis of a rigid optical bench. A sketch of the oscillator and amplifier chain is shown in Figure 3.8. The lengths and diameters of the ruby rods were as follows; oscillator and first amplifier: 10.2 x 1.0 cm, second amplifier: 10.2 x 1.4 cm, third amplifier: 20.3 x 1.9 cm, fourth amplifier: 20.3 x 2.5 cm. All the laser heads were water-cooled and were loaded axially inside helical Xenon-filled flashlamps. The rods were aligned with their c-axes in the vertical direction, so the polarization of the output light was horizontal. The rods ends were cut and polished plane-parallel with antireflection coatings except for the last amplifier which had ends that were wedged antiparallel at 0.5°. A beam expander between the first and second amplifiers expanded the beam so that it filled the rods in the subsequent amplifiers.

The plano-concave oscillator cavity, 114 cm long, was composed of a 95% back reflector with a 20 m radius of curvature, a Quantum Technology Pockels cell (model QK-10, KD^*P crystal, $V_{1/4}$ = 2100 V), an 80 % reflectivity intracavity single-plate etalon, the laser rod, a brass aperture (2 mm ϕ), and a 48 % multi-plate resonant reflector. The 5 % of the light which was extracted from the rear mirror was amplified by a 10.2 x 1.0 cm laser rod. This light flux activated the feedback electronics described in Section 4.3.1.

As described earlier, for an ideal cavity with plano-concave configuration, the beam waist would be at the plane mirror. The cavity length, 114 cm, was much smaller than the radius of curvature of the rear mirror, 20 m, and thus the position of the aperture was not critical within

a few centimeters. The aperture was placed close to the front mirror. The diameter of the aperture was calculated from Equation [3.1.1] to be 2 mm, twice the beam waist. This aperture selected the TEM_{00} mode and retained more than 95 % of the energy in that mode.

The oscillator's resonant reflector and intracavity etalon were thermally stabilized to within 0.1°C. After the intracavity etalon axis was aligned parallel to the front and rear mirror axes, the etalon plate was tilted just enough to stop lasing between the etalon and the front mirror. The temperature of the etalon was varied in steps of 0.1°C to obtain the best coherence length.

A description of the characteristics of the output beam of the laser is given in Section 4.3.2.

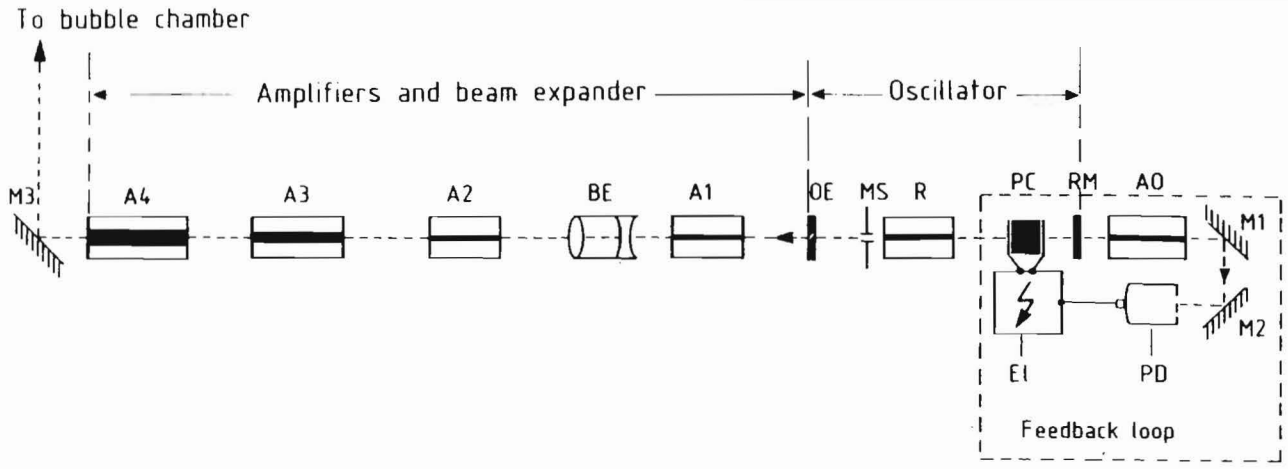

Fig. 3.8 Layout of the Korad oscillator with feedback optics and four amplifiers (schematic): OE - output etalon, MS - mode selection, R - ruby rod, PC - Pockels cell, RM - rear mirror, AO - amplifier, M1, M2, M3 - mirrors, PD - photodiode, E1 - feedback electronics, A1, A2, A3, A4 - amplifiers, BE - beam-expander.

3.3 The Commercial Laser

A JK Laser System (model 2000, manufactured at JK Lasers, Rugby, England) was used for the E-632 physics run. A sketch of the system is shown in Figure 3.9.

The oscillator had a plano-concave configuration and was 60 cm long. The rear mirror was an 80 % reflector with a radius of curvature of 5 m, and the front mirror was a 20 % reflector with a wedged surface at 0.5°. A Lasermetrics Pockels cell, (model 1042, two KD^*P crystals in series) was used for its low quarter-wave voltage, 1200 V. The low $V_{1/4}$ of the Pockels cell was useful in designing the feedback electronics. The ruby rod, 10.2 long x 0.6 cm diameter, had parallel wedged surfaces at 10′, and was antireflection coated. The rod was pumped by two linear Xenon-filled flashlamps and was water-cooled. A two-plate polarizer was mounted on the back end of the rod at the Brewster angle. A brass aperture (1.7 mm ϕ) between the rod and the exit mirror selected the TEM_{00} mode. Two tilted intracavity etalons which were thermally locked to the ruby rod selected the longitudinal mode. The two single-plate etalons were tilted 0.5° from each other. The thicker etalon, 10 mm ϕ, had 65 % reflectivity and discriminated against the adjacent longitudinal modes of the cavity. The thinner etalon, 2 mm ϕ, had 40 % reflectivity. The latter etalon prevented laser oscillations at the other etalons′ transmission resonances. The output mirror and the ruby rod ends were wedged to prevent oscillations from the etalons. About 20 % of the oscillator light flux was taken from the rear mirror to activate the feedback loop.

The output beam of the oscillator was focused by a positive 150 mm lens on a 250 μm aperture (made of diamond) to form a spatial filter which

removed the nonuniformities of the beam profile and gave sufficient divergence to the beam to fill the amplifier apertures. The beam was amplified through three amplifiers with increasing rod diameter; successively 20.6 long x 1.0 cm diameter, 20.6 long x 1.6 cm diameter, and 20.6 long x 2.5 cm diameter. The first two rods were wedged parallel at 3° and the last rod was wedged antiparallel at 0.5°. The first two amplifiers were pumped by four linear flashlamps each and the last by six. All were water-cooled. The oscillator and amplifiers rods were aligned with their c-axes horizontal and thus the polarization of the output beam was vertical. A beam expanding telescope composed of two lenses (-100 mm and +70 mm) was used to collimate the output beam with diameter of about 5 cm at 30 m.

The characteristics of the output beam of the laser is given in Section 4.3.4.

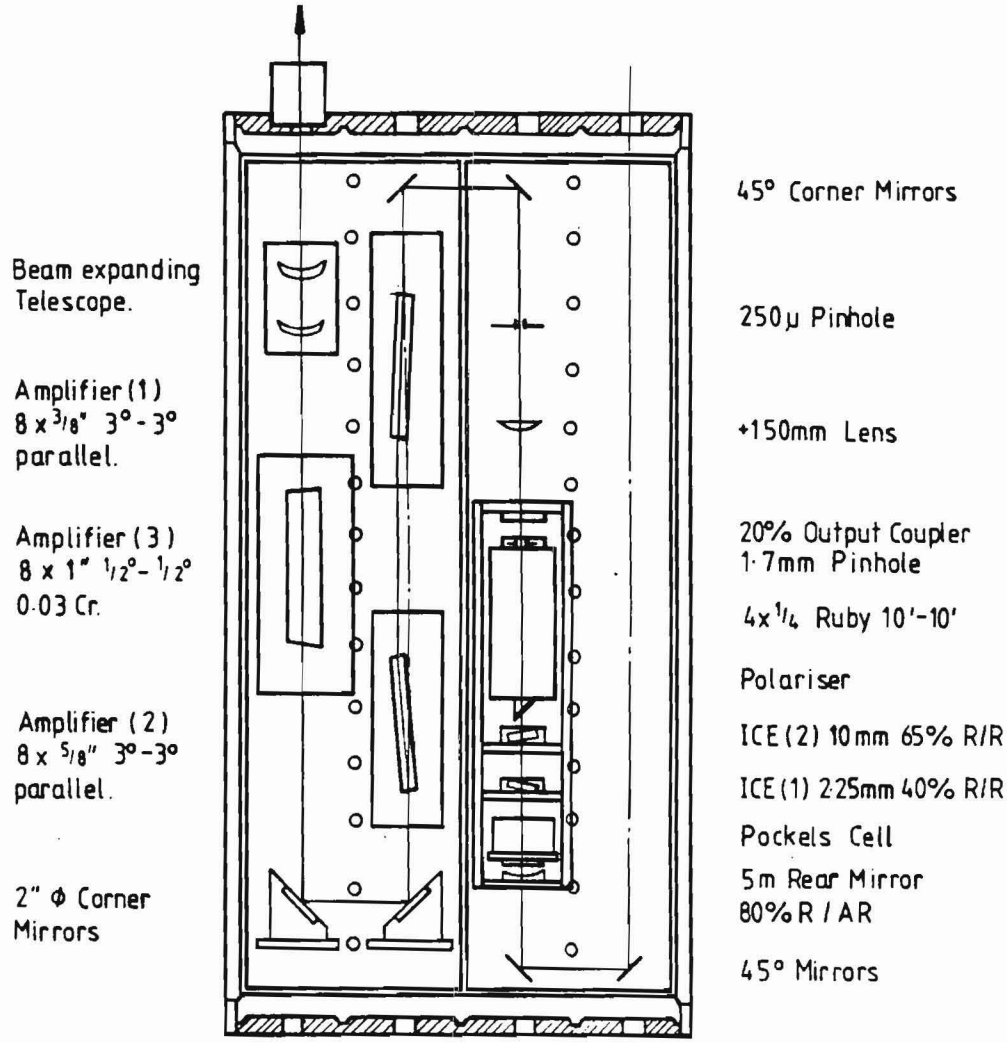

Fig. 3.9 Layout of the JK Laser System 2000 (schematic).

CHAPTER 4 PULSE STRETCHING

4.1 Negative Feedback Loop

The operation of solid state lasers in a Q-switched mode has already been discussed in Section 3.1.4. To operate the lasers in a single-pulse mode with moderately low peak power, non-linear losses which increase with intensity of the emitted light must be introduced into the cavity. This can be done by inserting either a non-linear element whose absorption increases with intensity, or an electro-optic shutter which controls the gain. Increasing the optical length of the cavity also results in longer pulses but is not a feasible method for obtaining pulses with durations longer than a few hundred nanoseconds.

In ruby lasers stretched pulses of durations in the range of 150 ns to 400 μs have been obtained by placing a non-linear absorber in the cavity (Hordvik, 1970; Pantell and Warszqwski, 1967; Callen, Pantell, and Warszawski, 1969; Young et al., 1971). Processes such as two-photon absorption in semiconductors, stimulated scattering in liquids, and frequency doubling in crystals can be used for this non-linear absorption. Above threshold, the absorption of the non-linear element increases with intensity. Thus as lasing begins its amplitude is kept nearly constant and it continues long enough to deplete the remaining population inversion above the threshold level.[25] The pulses produced by this method are either Gaussian or asymmetric with low energies.

---

25. This behavior is opposite to that of a dye cell whose absorption coefficient decreases with intensity, giving rise to a giant pulse.

By controlling the voltage applied to an electro-optic shutter long pulses in the range of 700 ns to 5 μs can be obtained. The retardation of the Pockels cell and therefore the laser gain is electrically modulated as a function of the light intensity. Thus a fraction of the photon flux can be directed to a phototube producing a voltage which is returned to the crystal in a negative feedback loop. The shape of the pulse is strongly dependent on the parameters of the circuit used to control the voltage on the crystal, by the gain and frequency response of the feedback loop, and by instabilities in the laser pumping source. Various attempts have been made to use this method to prolong Q-switched pulses (Marshall and Roberts, 1962; Thomas and Price, 1966; Mishin, 1971). The resulting stretched pulses were characterized by an initial spike and an exponentially decaying tail. More stabilized, rectangular pulses were obtained either by lengthening the cavity (Wooding and Yeoman, 1971) or by using compound feedback (Lovberg, Wooding, Yeoman, 1975). In the latter technique fairly flat pulses with no initial spike were produced. Stretched pulses with durations of 600 ns were amplified up to output powers of 15 MW with no apparent distortion in the pulse shape.

Since pulses for the 15-foot Bubble Chamber application must be flat over several microseconds and amplifiable to large energies with no distortions, the compound feedback system of Lovberg et al. (1975) appeared to be most promising. Thus the original developments for this application employed a compound negative feedback circuit similar to the one described in the reference.

Q-switching techniques using Pockels cells have already been discussed in Section 3.1.4. Here for completeness of the discussion we summarize the process of formation of a Q-switched pulse.

As the rod is pumped and the electron inversion is increasing, the Pockels cell under $V_{1/4}$ introduces a high cavity loss which prevents the lasing. If at a time t=0 when the electron inversion reaches a level far above the threshold, the voltage is removed from the cell, a sudden decrease in the cavity loss will result in emission of a Q-switched pulse.

Now if a percentage of the photon flux is transmitted via an optical element (e.g. the back mirror) to a phototube producing a voltage which is proportional to the photon flux, the voltage applied to the Pockels cell, and thus the loss coefficient can be modulated to obtain a stretched pulse with a constant amplitude. A simplified feedback circuit is shown in Figure 4.1.

Since a vacuum phototube is a pure current source, this current, i, is directly proportional to the photon density on the tube: $i = M\phi$, where M is the gain of the feedback loop. Then the voltage V produced by the resistor R is also directly proportional to the photon density, $V = k\phi$, where k is the proportionality constant. Using Kirchoff's laws, an expression for the voltage on the Pockels cell as a function of time can be obtained.

$$i = M\phi = i_1 + i_2 = C_1(dV/dt) + V/R$$
$$V = k\phi = \text{const. } e^{-(1/RC_1)\times(1-(RM/k))t} \qquad [4.1.1]$$

Thus if the photon density were proportional to the positive voltage on the phototube side of the Pockels cell, the photon density would decrease with time almost exponentially. To obtain flat, rectangular pulses a positive feedback must be added to the circuit reducing the negative feedback with time. This can be achieved with an inductor in series with the capacitor. The new circuit equations are:

$$i = M\phi = i_1 + i_2 + i_3 = C_1(dV_1/dt) + V_1/R + C_2(dV_2/dt)$$

$$LC_2(d^2V_2/dt^2) = V_1 - V_2 \qquad [4.1.2]$$

These circuit equations were used to estimate initial values of parameters for the original electro-optic feedback circuit. These parameters were then optimized experimentally using the laboratory laser.

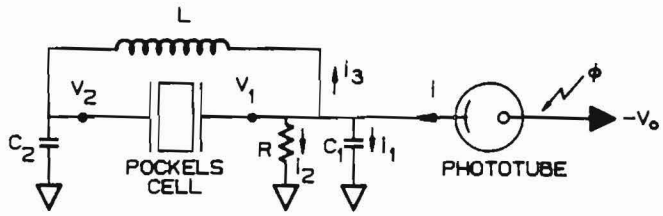

Fig. 4.1 A simplified compound feedback circuit.

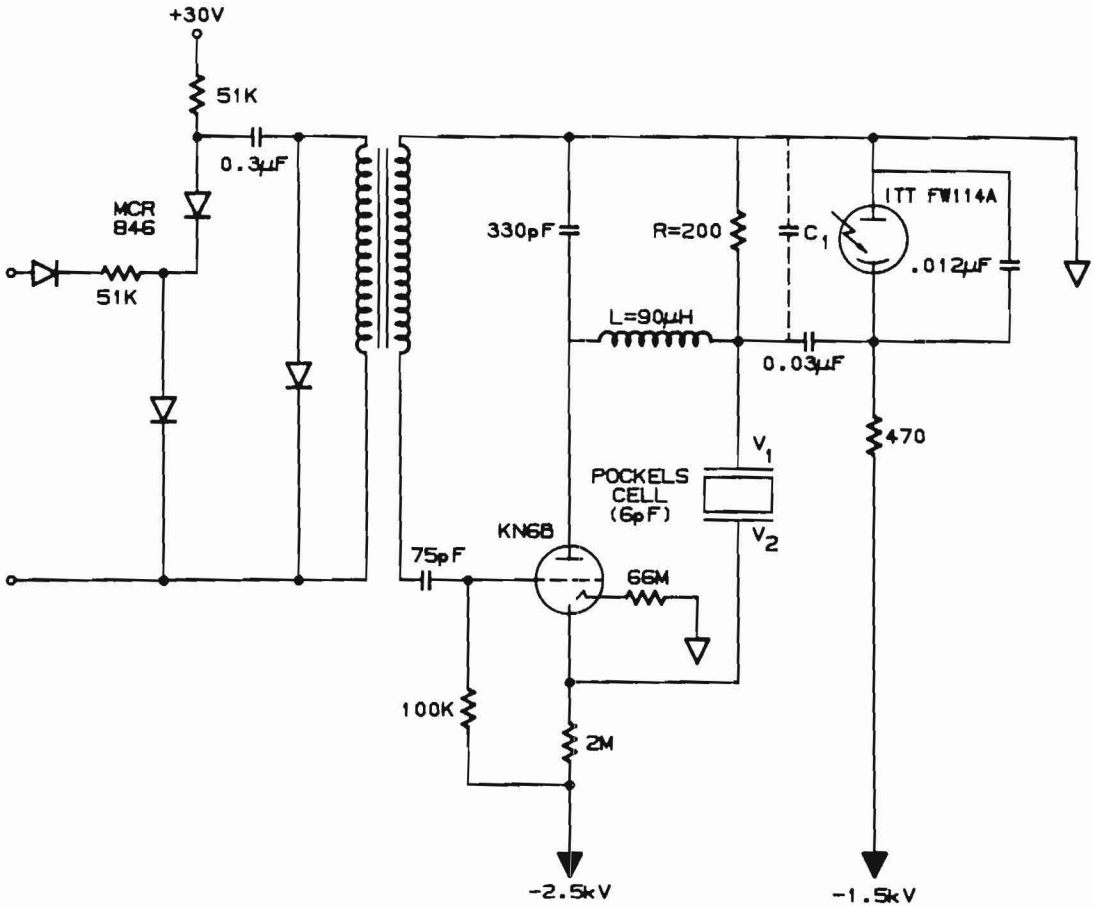

Fig. 4.2 Compound feedback circuit, Version 1.
FW114A-phototube, KN6B-krytron.

4.2 Pulse Stretching Circuitries

Four versions of the stretched-pulse circuitry were developed as dictated by the progressively severe demands of the experiment. The performance of each version was stable and satisfactory at its design level. Versions 1 and 2 were developed and used with the Korad Laser System, and Versions 3 and 4 with the JK Laser System. Version 1 was used during most of the developmental tests and during the 1984 engineering run. Version 4 was used during the 1985 E-632 physics run. Thus the detailed discussion of Versions 1 and 4, given in this section, is important for analyzing the holographic and boiling results. Versions 2 and 3 are described in Appendix I.

4.2.1 2-μs pulse circuitry (Version 1)

The Korad Laser System has already been described, (Section 3.2, Figure 3.8). The oscillator was equipped with the feedback loop. Five percent of the laser light was extracted through the 95% reflective back mirror and was amplified through a ruby amplifier, 95 mm diameter rod. This amplifier was needed to provide sufficient and flexible gain for the operation of the feedback electronics. The feedback light, expanded by a diverging lens, fell on the vacuum photodiode (I.T.T. FW114A)[26] and produced a voltage which was returned to the Pockels cell through the electronic circuit as shown in Figure 4.2. The Quantum Technology KD*P Pockels cell was chosen in the final system for its low quarter-wave voltage (2100 V) and low capacitance (6 pF).

---

26. The phototube was surrounded by twelve 1000-pF capacitors and was biased at 6000 volts to provide large charge storage with a response time of 0.5 ns.

The circuit worked as follows: initially, the Pockels cell is biased to its quarter-wave voltage, thus rotating the light polarization to prevent photon amplification in the cavity. No polarizer is used in the cavity since the ruby only amplifies one polarization. At a time t_1 after the flashlamp trigger (for Korad laser t_1 = 1.1 ms), when the population inversion is peaked, the Pockels cell voltage is reduced to zero by firing the krytron (EG&G, type KN6B).[27] A transformer-transistor coupling on the left side of the circuit in Figure 4.2 provides the triggering for the krytron. The response time is determined primarily by the resistor on the anode side of the krytron and the capacitance of the Pockels cell and its associated circuitry. For R = 200 Ω and C = 6 pF, this response time is 1 ns which is small compared to the pulse build-up time of about 200 ns. The krytron tube is then kept in the conducting mode for 14 μs (determined by the isolating resistor, 2 MΩ, and the Pockels cell capacitance). If the feedback loop were not activated a Q-switched pulse would emerge.

If the feedback loop is activated a positive voltage, V_1, appears on the other side of the Pockels cell after a time delay determined by the pathlength between the back mirror and the phototube (Δl = 30 cm; $\Delta\tau$ = 1 ns), the phototube response time (~ 0.5 ns), and the stray capacitance. Thus it is important to minimize the stray capacitance, since time delays larger than a few nanoseconds can result in a spike on the leading edge of the pulse (Arsen´ev, 1977). This is a persistent problem for most electro-optic loops.

---

27. A krytron is a cold-cathode, gas filled switch tube. It was chosen since it can conduct moderately high peak currents (maximum peak current: 3000 A) for short durations (pulse duration: 10 μs) with a repetition rate of 1 pulses/minute.

The voltage V_1 follows the photon density until a time t_2 determined by the LC constant, ~ 2 μs. At the approximate time t_2 the rising current through a 90-μH inductance has charged the 330-pF capacitor and reduced the net voltage (V_1 - V_2) on the Pockels cell. The voltage V_2 produced by the positive feedback on the krytron side of the Pockels cell continues increasing until it causes complete closing of the Pockels cell.

4.2.2 Characteristics of Pulses Produced by Version-1 Circuit

2-μs Pulses

Figure 4.3 shows some examples of the 1.5 - 2.0-μs pulses produced by this circuit. Longitudinal mode-beating was observed in almost all the pulses. The stretched pulses retained 80 - 90 % of the energy in the normal Q-switched pulses (about 40% of the energy in the free-lasing mode). Twenty percent of the pulses had a spike (maximum about twice the average amplitude) at the beginning. The pulses occasionally had pre- and/or post-lasing.

A Gaussian-like beam profile was observed in the near field. This profile was measured by burning a black photographic print paper ("burn paper").

Bright holograms were made with the stretched pulses exhibiting coherence lengths of ~ 4 m about 60 % of the time. The variability of the coherence length was due to the intrinsic fluctuations of the laser gain, and/or to the inefficiency of temperature control of the intracavity etalons.

3-μs Pulses

A deviation from the regular shape of 2-μs pulses was observed when the oscillator was pumped substantially above the threshold. In this case 3-μs pulses were produced, frequently accompanied with pre- or post-lasing.

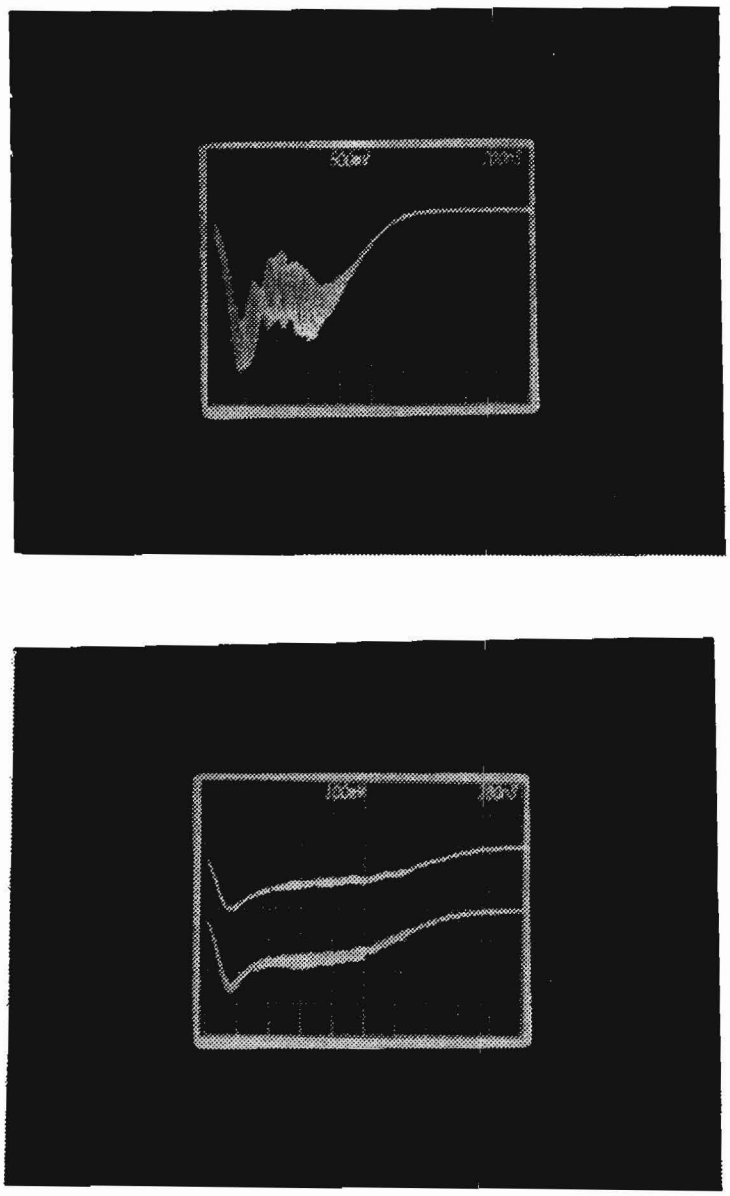

Fig. 4.3 Typical stretched pulses produced by compound feedback circuit, Version 1.

They had irregular shape and were highly unstable. No coherence length measurements were made for these pulses.

The effect of the pump power on the pulse length had been mentioned by Arsen´ev et al. (1977). Increasing the pump power results in a larger inhomogeneity of the population inversion in different regions of the rod. Lasing is then initiated at different times in different regions which increases the pulse length.

Q-Switched Pulses

When the feedback loop was inactivated by blocking the light to the phototube, the circuit produced a normal Q-switched pulse. These Q-switched pulses contained 45 - 55 % of the total energy of the laser light emitted in free-lasing mode. Energies of about 12 mJ were obtained from the oscillator in these pulses when operating the oscillator at threshold. This energy was subsequently amplified to 7 J through the amplifier chain.

The rather large width, 100 ns fwhm, of these pulses was due to the use of a 95 % back reflector. The Q-switched pulses had coherence lengths of about 2 m.

4.2.3 2 - 100-μs pulse circuitry (Version 4)

A description of the JK Laser System is given in Section 3.3, (Figure 3.9). For the feedback loop 20 % of the photon flux, extracted from an 80% reflective back mirror, reaches the phototube. The JK Pockels cell (model 560) was replaced with a Lasermetrics model 1042 dual-KD*P-crystal. The advantage of using this Pockels cell is its low quarter-wave voltage of 1200 V.

The circuit adapted to the JK laser system had to meet our requirements of producing a single, flat, moderately energetic pulse at short delays and high gain of the cavity. The Pockels cell delay in the conventional Q-switched pulses is determined by the time of peak population inversion (~ 1.2 - 1.3 ms for the JK oscillator). The extraction of the pulse at this point depletes most of the population inversion, and thus prevents post-lasing. Pre-lasing is prevented by the polarizer element of the oscillator when the quarter-wave voltage is applied to the Pockels cell. Now if the pulse is extracted at shorter delays (0.95 ms in the typical stretched-pulse case) post-lasing would occur frequently ~ 0.85 ms after the pulse. To prevent this post-lasing the quarter-wave voltage can be reapplied to the Pockels cell to set the transmission through the polarizing element to zero. This was achieved by adding an auxiliary switching circuit to the main stretched-pulse circuit which upon switching would clamp the voltage applied to the non-feedback side of the Pockels cell to the quarter-wave value.

Figure 4.4 shows the general layout of the JK Laser System, the feedback optics, and the diagram of the pulse stretching and clamping circuit's electronics. Since a fast switch was no longer needed for stretched-pulse application, and had to deal with voltages of the order of 1.2 kV, the krytron was replaced by SCR (2N5207) switches[28] capable of switching 1.2 kV in ~ 0.1 - 0.2 μs. In this slow turn-on circuit lasing did not occur until 1 - 2 μs after the start pulse.

---

28. Originally a krytron switch was used in the clamping circuit, but they failed due to frequently firing and conducting for long periods (~ 3 ms three times per minute). For long pulses the anode melted and the cathode sputtered which resulted in darkening of the glass envelope.

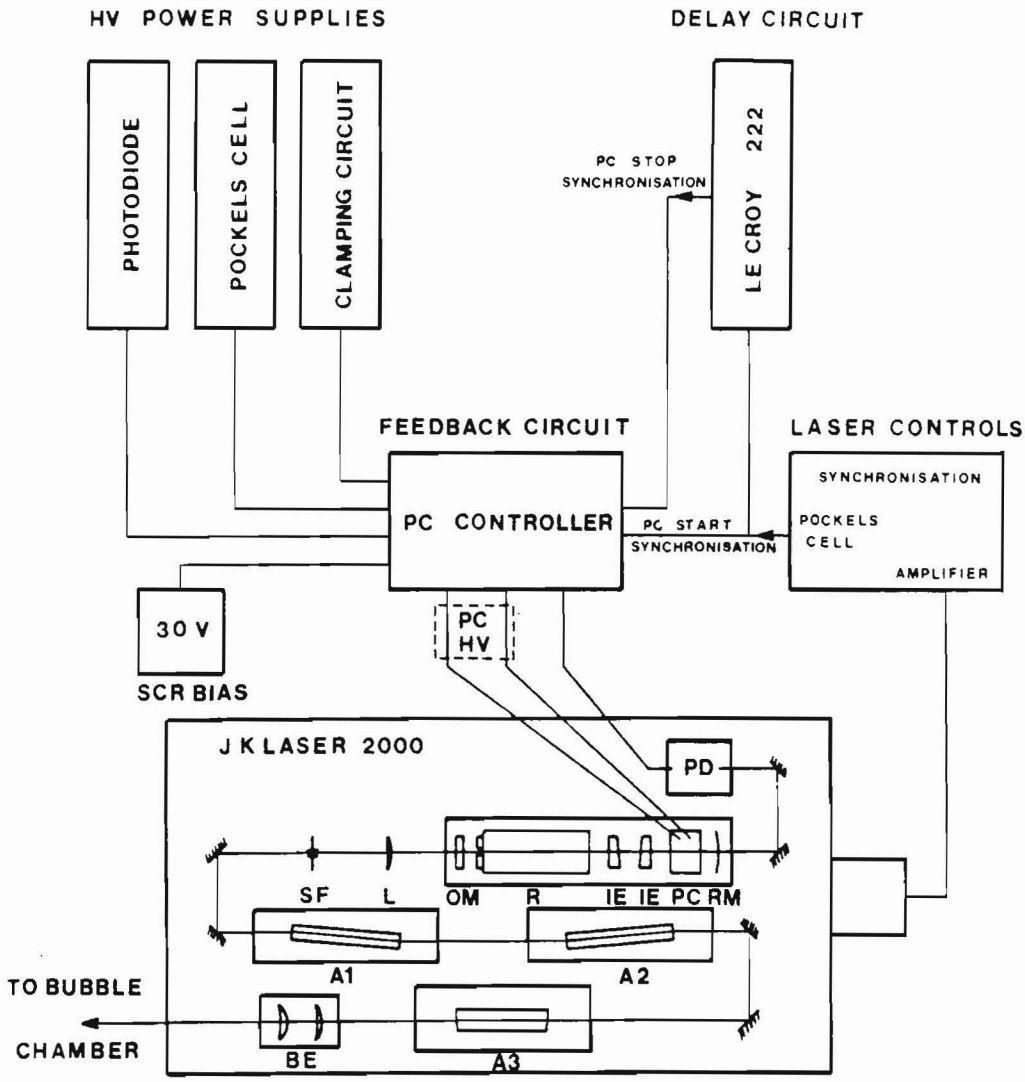

Fig. 4.4 Layout of the JK Laser System 2000, the feedback optics and the block diagram of the pulse stretching electronics (schematic): PD - photodiode, RM - 80% reflective rear mirror, PC - Pockels cell, IE - tilted etalons, R - ruby of oscillator, OM - output mirror, L - focusing lens, SF - spatial filter, A1, A2, A3 - amplifiers, BE - beam-expander.

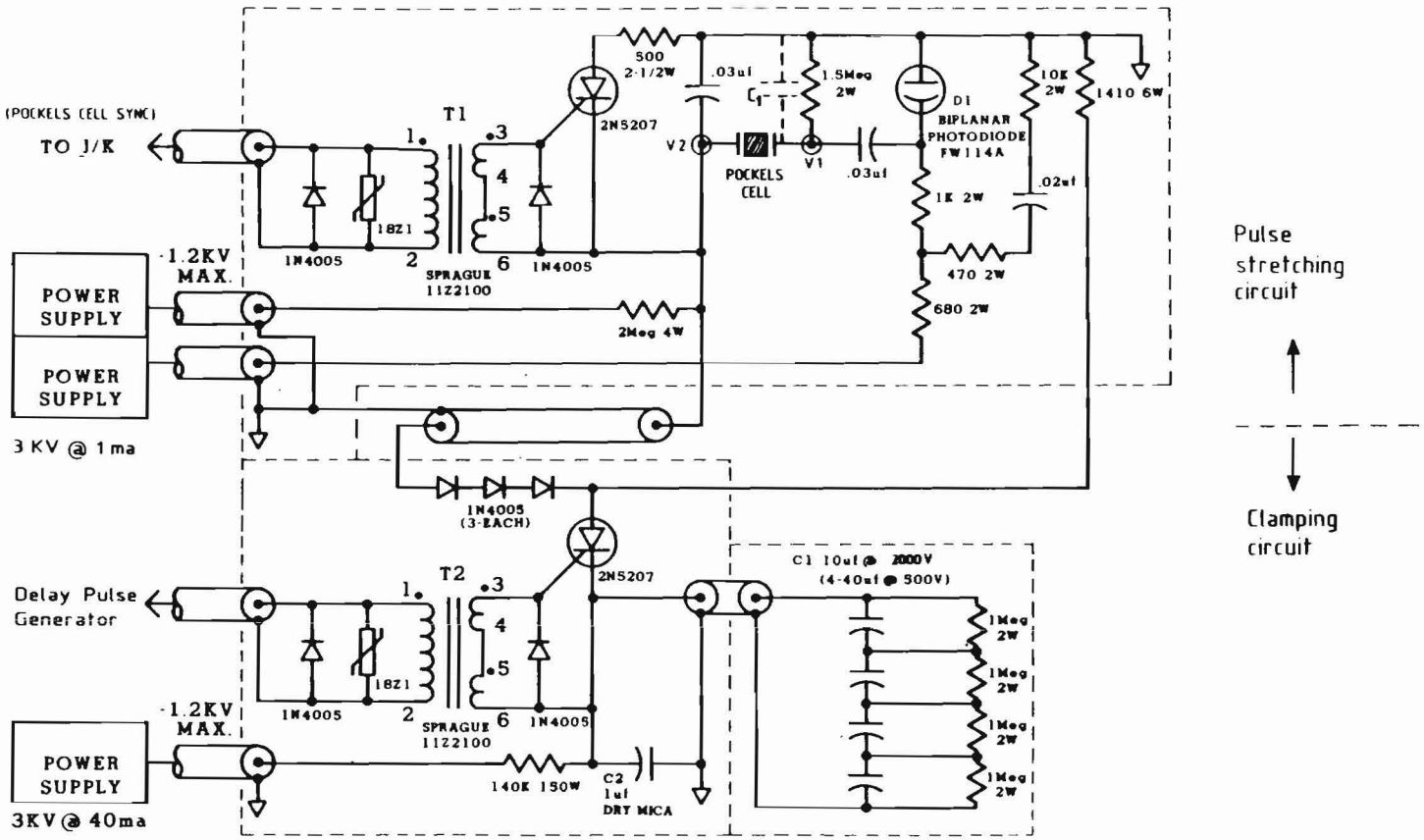

Fig. 4.5 The pulse stretching and clamping circuit electronics for the JK laser, Version 4. Upper part: stretching, lower part: clamping system.

The final version of the SCR circuit is shown in Figure 4.5. The transformer-transistor triggering circuit of SCR's is to the left of each switch. The pulse-stretching circuit is basically the same as Version-3 circuit (cf. Appendix I.b) with two exceptions: a) the 330-pF capacitor and 1-MΩ resistor which were in parallel with each other were removed to allow the SCR to retrigger; b) the 1-kΩ resistor in series with the 0.03-μF capacitor was removed to improve the bandpass of the feedback loop. The clamp circuit is connected to the stretched-pulse circuit via a series of 1N4005 diodes. The 10-μF capacitor bank to the right of clamp circuit was added to store enough charge to provide high peak currents upon switching the SCR and an average current of 40 mA for ~ 3 ms needed to hold the SCR on.

The SCR circuit functions as follows: initially the quarter-wave voltage is applied to the Pockels cell at V_2 while the feedback side of the cell, V_1, is at zero. At the time $\Delta_{pc.}$ (Pockels cell delay) a CMOS pulse from the JK control triggers the "feedback" SCR raising the potential at V_2 to zero with a rise time of 20 μs (R=500 Ω and C=0.03 μF). As lasing begins the current from the phototube builds up a positive voltage at V_1, partially closing the Pockels cell. This voltage follows the light pulse shape very closely and its magnitude is controlled by the high voltage applied to the phototube. In this case the voltage was between 250 and 400 V. A second TTL pulse from a LeCroy 222 delay generator triggers the "clamp" SCR with a time delay depending on the desired laser pulse length (in the range of 2.5 - 100 μs) after the "feedback" SCR is triggered. Upon closing this "clamp" SCR the quarter-wave voltage is applied to the Pockels cell at V_2 in ~ 2 μs. This ends the lasing and V_1 returns to zero voltage. After

about 3 ms the current through both SCR's drops below the holding level, turning them off, (Figure 4.6).

The minimum reliable pulse length is determined by the minimum switching time of the "feedback" SCR. A switching time of 20 μs is optimal for 40-μs pulses. For 2.5-μs pulses this time has to be decreased to 1 μs by reducing the resistor and capacitor. Thus the RC constant of the top SCR has to be adjusted to optimize the circuit parameters for various pulse lengths.

The spike at the beginning of the pulse was reduced by reducing the stray capacitance and thus the response time of the phototube circuit. This was done by shortening the RG58 cable connecting the phototube to the electronic circuit.

In order to obtain the most reliable pulses at different durations, some small adjustments of Pockels cell parameters (voltage $V_{pc.}$ and delay $\Delta_{pc.}$) in combination with the oscillator voltage, V_{osc}, are needed. As previously mentioned, it is desirable to operate the laser at small $\Delta_{pc.}$. The value of this delay is set by the population inversion build-up as a function of time and V_{osc}, and by the population inversion depletion as a function of pulse length. It should be chosen to deplete enough of the inversion to give the energy required for the pulse with no post-lasing. Thus, a longer delay must be used for shorter pulses. At shorter delays a lower voltage (60 - 80% of quarter-wave voltage) on the Pockels cell prevented pre-lasing. Adjusting this voltage for a particular oscillator voltage allowed a smooth start of the pulse. Table 4.1 gives the values of the operating parameters ($V_{cl.}$: clamping circuit voltage, $V_{pt.}$: phototube voltage, V_{A1}: pumping voltage of first amplifier, $V_{A2\&3}$: pumping voltage of the second and third amplifiers) for several pulse durations.

Pulse Length (μs)		4	10	20	40
Pockels cell Elec-tronics	$V_{cl.}$ (kV)	1.17	1.17	1.17	1.17
	$V_{pt.}$ (kV)	0.47	0.47	0.47	0.47
	$V_{pc.}$ (kV)	0.85	0.8	0.8	0.8
	$\Delta_{pc.}$ (ms)	1.02	0.99	0.98	0.98
Laser Head Voltage	V_{osc} (kV)	1.78	1.78	1.78	1.78
	V_{A1} (kV)	2.33	2.15	2.14	2.05
	$V_{A2\&3}$ (kV)	2.34	2.15	2.13	2.05
Energy	$E_{ave} \pm \sigma$ (J)	2.51±0.24	1.51±0.12	2.71±0.24	2.65±0.13
	σ/E_{ave} (%)	± 10	± 8	± 9	± 5

- Table 4.1 -

4.2.4 Characteristics of Pulses Produced by Version-4 Circuit

Temporal Profile

Seventy five percent of the pulses were flat with an amplitude modulation smaller than 5 %, (Figure 4.7a). Despite the slow switching of the SCR and short light delay times, 25 % of the pulses developed an overshoot, usually at the beginning of the pulse. This overshoot was 1.5 times greater than the rest of the pulse with 100 ns fwhm. The overshoot was a result of a sudden higher build-up of the oscillator gain and seemed to be unavoidable. None of the pulses exhibited any mode beating. A slight decrease in the amplitude with time for longer pulses (~ 100 μs) was due to gradual inversion depletion of the oscillator and amplifiers ruby rods, (Figure 4.7b), and it followed the general form of the flashlamp discharge voltage. This observation was also noted by Pantell and Warszawski (1967).

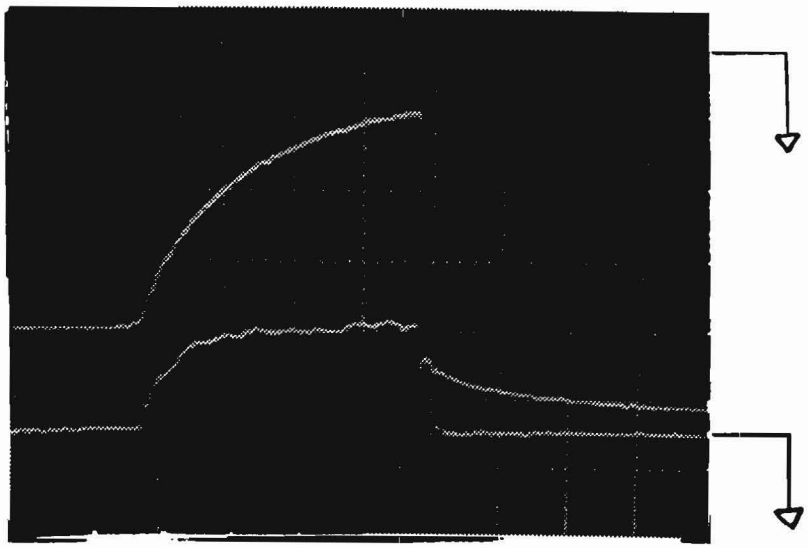

Fig. 4.6 Voltage waveform on the two sides of the Pockels cell (10 μs/div): The upper trace is the monotone increasing voltage V_2 (200 V/div). The initial value of V_2 is -1000 V. The lower trace is the feedback voltage V_1 (200 V/div).

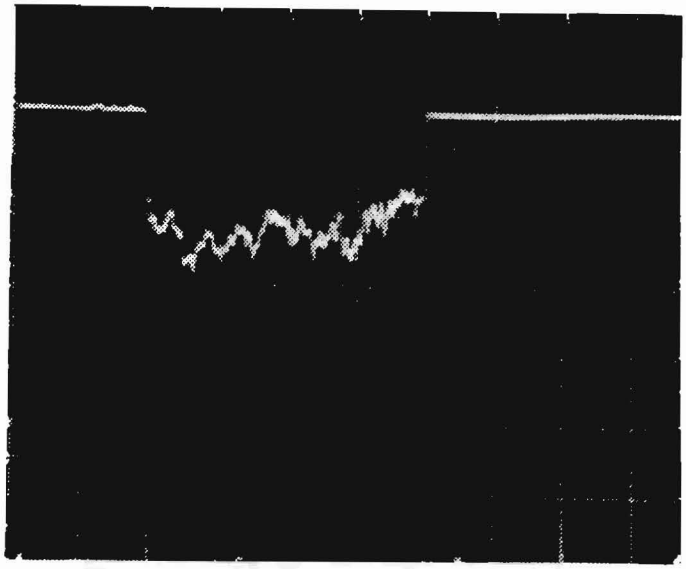

(a)

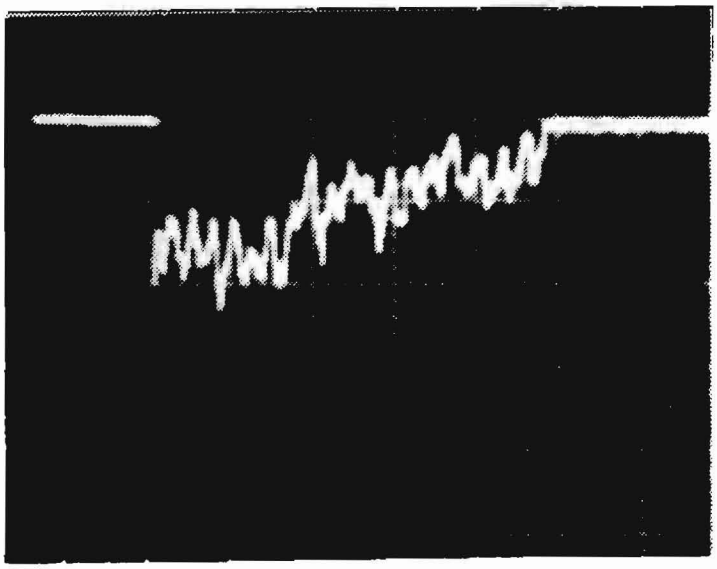

(b)

Fig. 4.7 Typical pulses obtained in the JK laser with Version-4 circuit: (a) 40-μs pulse (10 μs/div), (b) 100-μs pulse (20 μs/div).

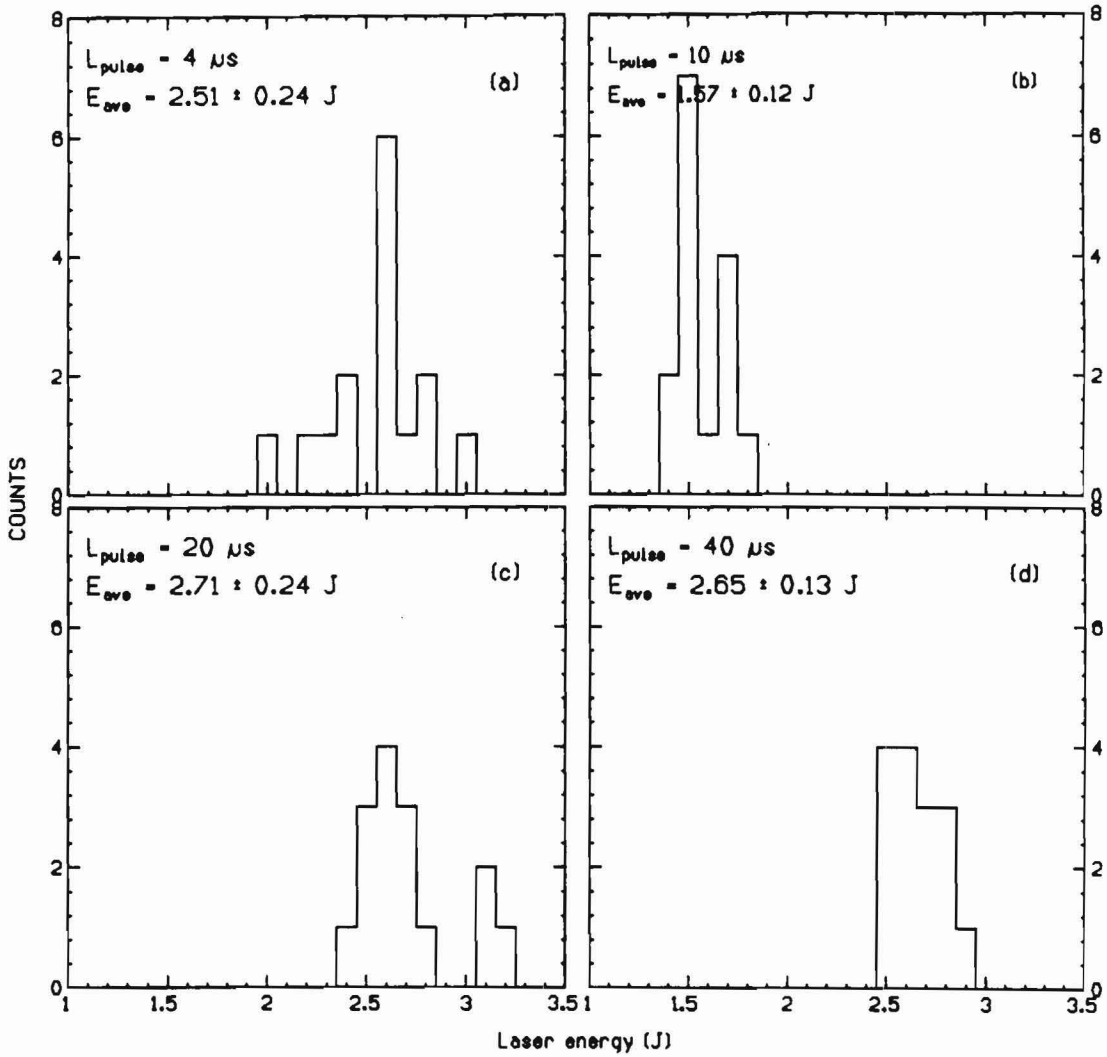

Fig. 4.8 Fluctuations in the output energy of the JK laser for typical pulse lengths.

Spatial Profile

An almost Gaussian profile was observed in the near field, four meters from the last amplifier. This profile was measured by a burn paper. No deviation in the beam profile from that of a conventional Q-switched pulse was observed.

Energy Stability

Typical output energy for 40-μs pulses was 20 - 25 mJ at the oscillator stage. It could then be amplified up to 5 J, retaining a smooth waveform in time. This energy was somewhat less for pulses shorter than 20 μs. The jitter in energy decreased for the longer pulses. The jitter was $\pm$ 10 % for 4-μs pulses and $\pm$ 5 % for 40-μs pulses, (Figure 4.8 and Table 4.1). This was due to variations in the length of shorter pulses.

Pre- and Post-Lasing

There was no post-lasing and occasional (5 %) pre-lasing after the feedback parameters, $V_{pc.}$, $\Delta_{pc.}$, V_{osc}, were adjusted for the given pulse length. The pre-lasing occurred within 8 μs before the main pulse and it was due to the marginal value of the Pockels cell voltage needed to prevent the pre-lasing. For a pulse with slightly higher gain than average some light would leak out in form of pre-lasing. The pre-lasing pulses had amplitudes less than 10 % of the main pulse with fwhm of 1 - 2 μs.

Repetition Rate

The repetition rate of the laser was mainly limited by the charging time of the capacitor banks in the laser power supply. This charging time is proportional to the pumping voltages. For final output energies of 8 J the maximum repetition rate was 7.5 pulses/minute. For this repetition rate the thermal cooling of the rods was not yet a limit. There was no

deterioration in the pulses' temporal and spatial profiles, energy, and coherence length as a function of repetition rate.

Coherence Length

The definition of the coherence length and the method used to measure it has been discussed in Section 3.1.3. The coherence length of the stretched pulses was measured as a function of both the repetition rate and the pulse duration. All the pulses had an energy of about 150 mJ (measured after the diverging lens, Figure 3.6), and a sample of 22 pulses was used for each pulse duration.

Pictures of replayed holograms for several pulse lengths are shown in Figure 4.9. Figure 4.10 summarizes the results. Three observations can be made.

1. There was an increase in coherence length of 2.5-μs pulses produced by Version-4 circuit, (in excess of 11 m),[29] as compared to that of Version-1 circuit, (4 m). This increase was due to both a slower opening of the Pockels cell at shorter delays used in Version-4 circuit, and better temperature stability of the double intracavity etalons used in JK laser.
2. There was a decrease in coherence length from 11 m for 2.5-μs pulses to 4 - 5 m for 60-μs pulses. This decrease in coherence length was almost certainly due to the failure of efficient frequency selectivity in the cavity. The temperature instability of the etalons and oscillator vibrations during these long pulses were probably responsible for the mode mixing.

---

29. The measurements of coherence length was limited to 11 m due to the layout and size of the room.

(a)

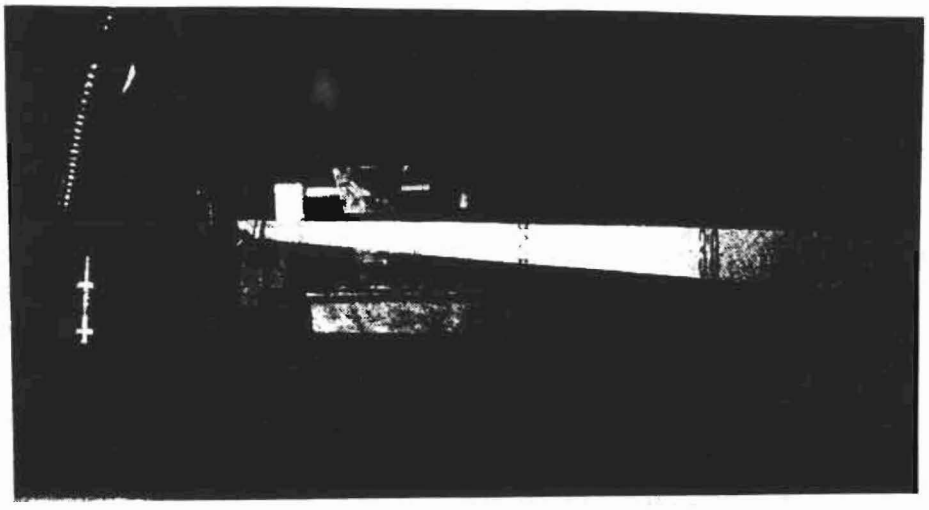

(b)

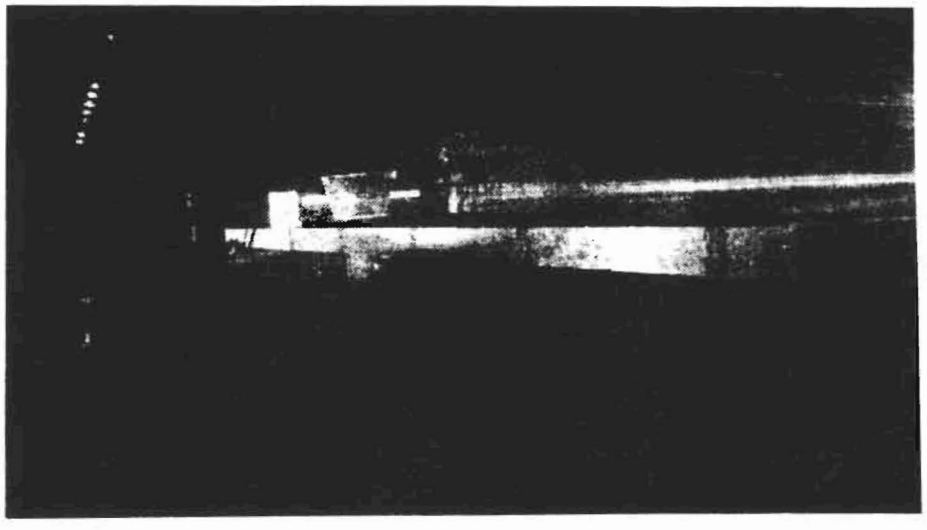

(c)

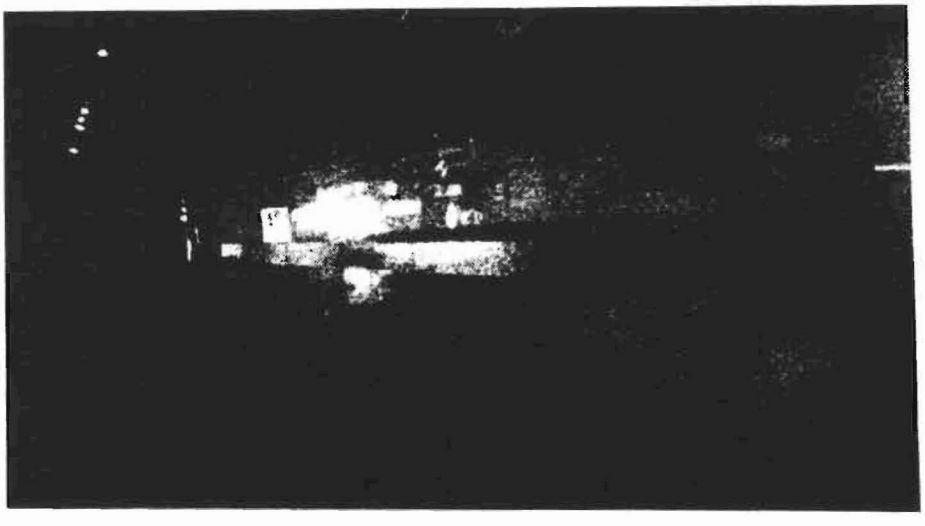

Fig. 4.9 Replayed holograms of stretched pulses from JK laser, obtained with Version-4 circuit: (a) 5-μs pulse, (b) 20-μs pulse, (c) 40-μs pulse. Mark 30 on the Scotchlite bar corresponds to 3 m length.

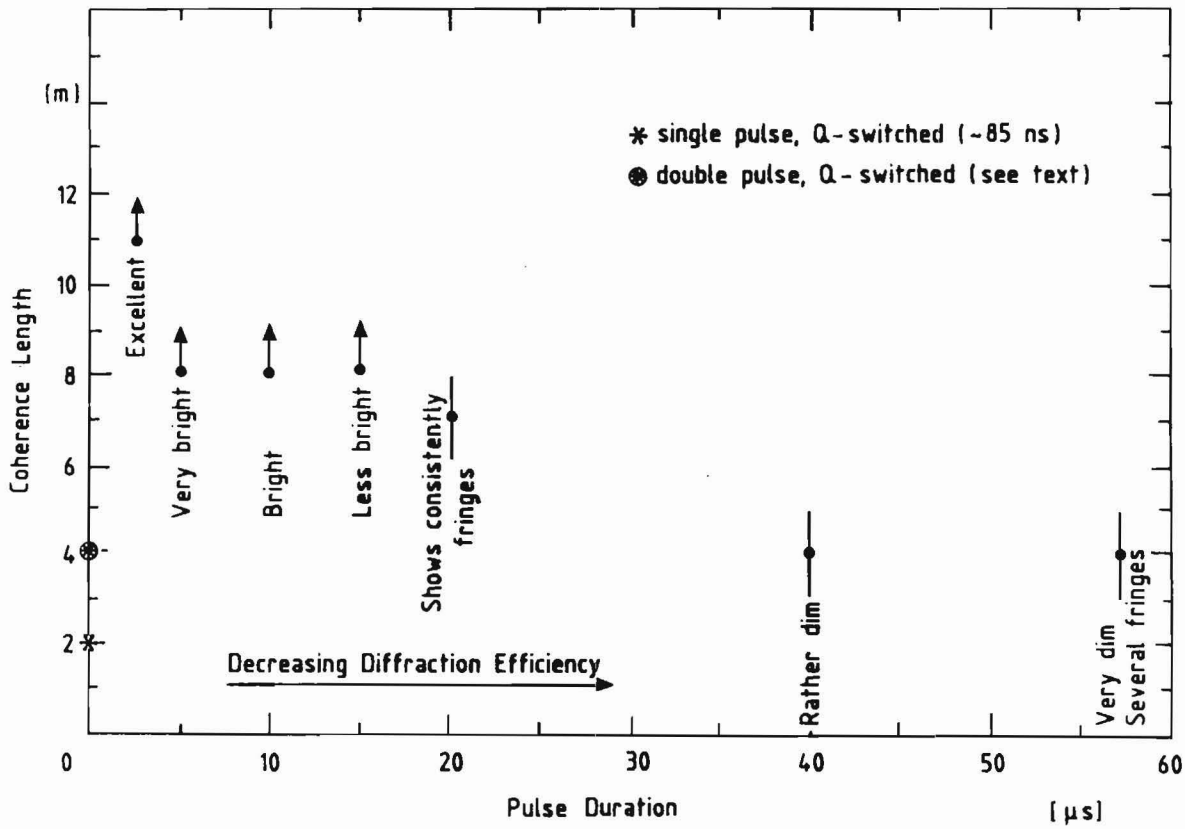

Fig. 4.10 Coherence length and diffraction efficiency as a function of pulse length.

3. A gradual decrease in the diffraction efficiency, (brightness), of the holograms was observed for the longer stretched pulses. This was coupled with the decrease in coherence length for the pulses. This was most likely due to variation of the optical path of the reference beam during the exposure.

Q-switched pulses

As a result of the slow switching rate of the SCR the Version-4 circuit could not produce ordinary (unstretched) Q-switched pulses. Yet another form of Q-switched pulse could be produced by "break-through" of the Pockels cell. A giant pulse with ~ 220 ns fwhm was obtained by setting V_{osc} ~ 2.3 kV, $\Delta_{pc.}$ ~ 1.55 ms, $V_{pc.}$ ~ 1.22 kV, and $V_{pt.}$ ~ 2.4 kV. Pumping the oscillator significantly above the threshold initiates this "break-through". The light produces a large response in the feedback voltage which forces the Pockels cell to open. The pulses occurred at ~ 0.9 ms after the flashlamp trigger with frequent post-lasing, and had coherence lengths of ~ 1 - 1.5 m.

4.3 Effect of Back Reflection and High Pumping

An effect on the pulses' temporal profile was observed when the light pulses were allowed to travel through the vacuum pipe to the bubble chamber. Large modulations with τ_{fwhm} of 2 μs appeared in the waveform of the pulses, (Figure 4.11). This was due to a minute amount of reflected light from the optical mounts and surfaces in the pipe[30] which was amplified as it traveled backward through the laser rods. This light could reach the feedback phototube, magnifying the oscillations of the Pockels cell voltage on the feedback side resulting in large modulations of the laser light output. A similar effect was observed upon pumping the amplifiers beyond 5 J in the stretched-pulse mode. This reasoning suggested that these unwanted effects might be suppressed largely by an optical isolator installed after the last amplifier.

An optical isolator is composed of a polarizer and a quarter-wave ($\lambda/4$) plate. The light output of the laser, which is linearly polarized, becomes circularly polarized after passing through the $\lambda/4$ plate. The back reflected light undergoes another $\lambda/4$ retardation, and it's polarization changes to linear but at 90° to its original direction. This light is subsequently stopped by the polarizer.

A preliminary test of this system proved to be useful. A vertical polarizer followed by a $\lambda/4$ plate was placed between the second and third amplifiers of the JK Laser System (the light output of JK laser was vertically polarized). The isolator could not be put after the last amplifier due to its limiting diameter of 1.3 cm (the laser beam has a diameter of

---

30. Most of the optical elements in the beam path had anti-reflection coating.

2.5 cm after the last amplifier). Almost all the effects presumed to come from the back reflected light were removed from both the light output and the feedback voltage response, (Figure 4.12).

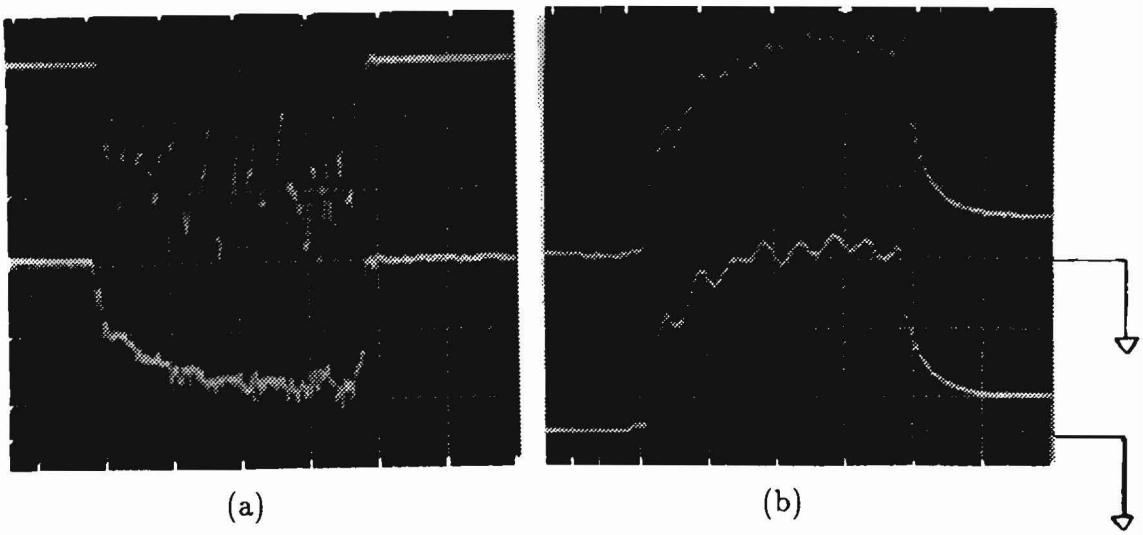

Fig. 4.11 Effect of back reflections (10 μs/div): lower trace: pulse stopped after last amplifier; upper trace: pulse going into bubble chamber. (a) Light output from laser, (b) voltage response of feedback phototube.

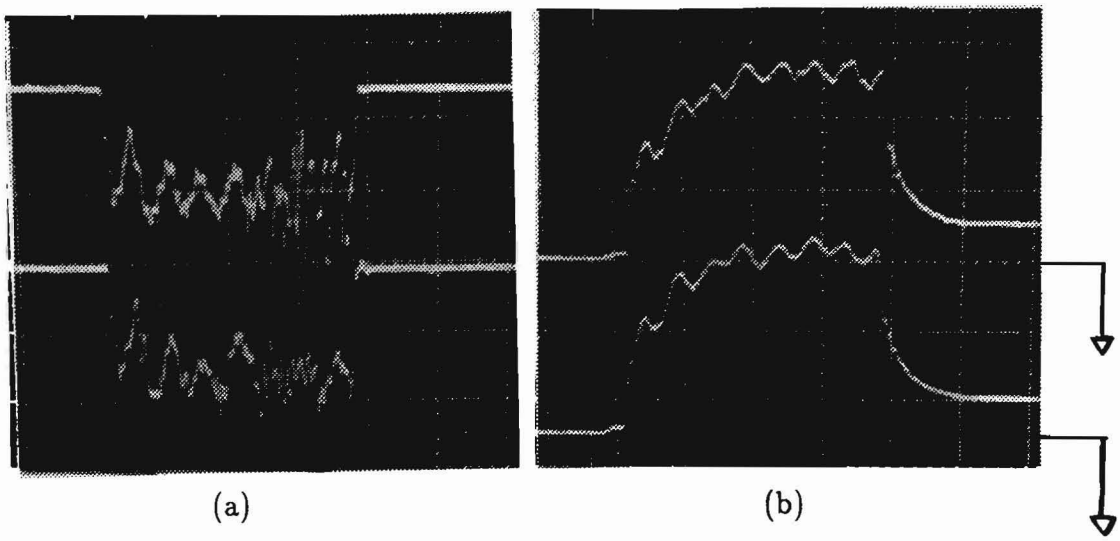

Fig. 4.12 Effect of back reflections (10 μs/div) with an optical isolator placed between the second and third amplifiers: lower trace: pulse stopped after last amplifier; upper trace: pulse going into bubble chamber. (a) Light output from laser, (b) voltage response of feedback phototube.

CHAPTER 5 BUBBLE FORMATION IN A BUBBLE CHAMBER

Bubble formation in liquids is not yet a well understood phenomenon. The difficulty lies in not having an exact knowledge of the thermodynamic processes and the required energy to form a bubble. However, a semi-quantitative formulation can be given to describe the phenomenon. In this Chapter, a brief discussion of the bubble formation concept is followed by a description of the theory of bubble formation due to ionizing particles in bubble chambers. A more complete discussion of this subject is given by Peyrou (1967). Possible explanations are given for light-induced bubble formation in various liquids by various light sources. These are applied to explain the observed boiling induced by ruby laser light in the 15-foot Bubble Chamber. Finally, the experimental dependence of laser-induced boiling on laser pulse duration and energy are described.

5.1 Bubble Formation Concepts

Consider a gas bubble of radius r and internal pressure p_{in} in the liquid with pressure p_{out}. The total external work done on the bubble is

$$W = 4\pi r^2\sigma + (p_{out} - p_{in}) \times (\frac{4\pi}{3} r^3), \qquad [5.1.1]$$

where σ is the surface tension of the liquid. If the bubble is in mechanical equilibrium, the net change in the total energy is zero for an incremental change of the bubble radius

$$dW/dr = 8\pi r\sigma + (p_{out} - p_{in}) \times (4\pi r^2), \qquad [5.1.2]$$

from which it follows that

$$p_{in} - p_{out} = 2\sigma/r. \qquad [5.1.3]$$

This equation gives the critical radius, r_c, for the bubble as

$$r_c = 2\sigma / (p_{in} - p_{out}). \qquad [5.1.4]$$

Bubbles with $r < r_c$ will collapse, and those with $r \geq r_c$ will grow to a visible size. Substituting r_c in Equation [5.1.1] an expression for the minimum work, W_m, necessary to form the critical bubble can be obtained:

$$W_m = (4/3)\pi r_c^2\sigma. \qquad [5.1.5]$$

5.2 Bubble Formation by Ionizing Particles

There are two plausible theories explaining bubble formation by ionizing particles. The first assumes the energy required for bubble formation is provided by the electric field and is due to the repulsion of the charges on the surface of the bubble, as suggested by Glaser in 1954. The second assumes that this energy comes from ionic recombinations producing heat spikes, as suggested by Seitz in 1958.

Glaser´s theory applied the same concept as that of the successful theory of droplet nucleation in cloud chambers and was initially successful in predicting the operating conditions of bubble chambers. Yet the theory was recognized to be incorrect as it made several wrong experimental predictions. The most important of all was the prediction that liquid Xenon should boil under suitable bubble chamber conditions (Brown, Glaser, and Perl, 1956). But experiments showed that this liquid would not boil unless a small amount of Ethylene was added. Ethylene, a radiation quenching agent, resulted in the release of the energy of ion recombination in the form of heat instead of radiation which supports the theory of Seitz.

Seitz´s theory is based on the heat released during the process of ionization of the liquid and the subsequent recombination of the ions. This heat must be sufficient to initiate bubble nucleation. It is thus most probable that the recombination of many ion pairs in a small volume, which occurs at the end of low energy δ-rays lying very close to the primary track, is responsible for bubble formation. The heat released in a single ion pair, a few tens of electronvolts, is not by itself a sufficient energy to form a bubble.

The energy loss of δ-rays in a volume of a bubble with the typical critical radius of 60 - 90 Å is about 200 eV for hydrogen and 3000 eV for heavier liquids, (Peyrou, 1967). The minimum energy necessary to form a bubble calculated either from purely energetic or dynamic considerations is about 10 to 40 eV for hydrogen and 200 to 400 eV for heavier liquids, (loc. cit.). Comparing this minimum energy to the δ-ray energies predicts bubble densities along ionizing particle tracks much higher than is found experimentally. This discrepancy can be described in terms of a low efficiency of δ-rays with sufficient energy in forming bubbles. Furthermore, this inefficiency apparently does not increase with energy.

The above assumption of nearly constant, low efficiency, ~ 10 %, of δ-rays in bubble formation was confirmed during the experimental observation of a relativistic rise in the bubble density, (Blinov et al., 1957; Argan et al., 1958; Hugentobler et al., 1963). A relativistic rise in the bubble density with increasing energy is expected[31] when the energy transfer from the fast charged particles to the electron is of the order of or smaller than the binding energy so that the electron may be considered to be in a bound state. If the energy transfer is several orders of magnitude larger than the binding energy of the electron, the electron can be considered free for which no relativistic rise of the bubble density should be observed. The experimental observation of the relativistic rise for different liquids (loc. cit.) reinforced the conclusion that the δ-rays responsible for bubble nucleation have small energies and a low efficiency which does not increase with

---

31. For fast charged particles the energy loss reaches a minimum and then increases with increasing kinetic energy of the particle in proportion to $\ln \gamma^2$, with $\gamma = (1 - (v/c)^2)^{-1/2}$ where v is the speed of the charged particle, and c is the speed of light (Jackson, Chapter 13, 1975).

energy. Thus these δ-rays must have energies of the order of the binding energy (13 eV for hydrogen and 100 eV or more for heavier liquids) and their low efficiency can be explained by fluctuations in ionization density, recombination time, and energy dispersion.

The other factor in the formation of bubbles is the time during which the necessary heat must be deposited. This time is determined by the dissipation of the heat contained in a sphere of radius $r \leq r_c$.

$$\tau = r^2 / D \qquad [5.2.1]$$

with D, the diffusion coefficient of heat, given by $\lambda_l/\rho_l c_l$ where λ_l is the thermal conductivity, ρ_l is the density, and c_l is the specific heat of the liquid. If the bubble is not formed in a time less or equal to τ, the heat required to nucleate it will diffuse out of the critical volume and no bubble can be formed thereafter. This time is of the order of 10^{-10} sec for heavy liquids with a critical radius taken as $r_c \sim 90$ Å, (Peyrou, 1967).

After the bubble has reached the critical size, its growth is determined mainly by the rate of heat flow from the surrounding liquid to the surface of the bubble. This heat is used to evaporate the molecules into the bubble volume. The mechanism of bubble growth is well understood in this domain and has been formulated mathematically by Plesset and Zwick (1954). They give an analytic expression for the bubble diameter, r, as a function of the growth time, t,

$$r = A\ t^{1/2}, \qquad [5.2.2]$$

where ´A´ is a proportionality constant. This constant ´A´ ($cm/s^{1/2}$) is given in turn by

$$A = 2\left(\frac{3}{\pi}\right)^{1/2} \times \frac{\lambda_l^{1/2}(\rho_l c_l)^{1/2}(T_l - T_v)}{L_v \ \rho_v} \qquad [5.2.3]$$

where the variables are defined as follows:

λ_l: thermal conductivity of the liquid,

ρ_l: density of the liquid,

c_l: specific heat of the liquid,

T_l: temperature of the liquid at large distance from the bubble,

T_v: temperature of the vapor inside the bubble,

L_v: latent heat of vaporization,

ρ_v: density of the vapor inside the bubble.

It can be seen from Equation [5.2.3] that ´A´ is strongly dependent on the conditions under which the bubble chamber is operated. For pure liquids such as H_2, D_2, C_3H_8, ´A´ can be calculated. Theoretical calculations to determine ´A´ for liquid mixtures (e.g. Ne/H_2) is difficult since the exact values of the thermodynamic parameters are not known. For these liquid mixtures, ´A´ can be measured rather accurately experimentally as a function of the bubble chamber operating conditions. Horlitz, Wolff, and Harigel (1974) have extensively studied the bubble growth in bubble chambers filled with Ne/H_2 mixtures and operated under various conditions. The experimental measurement of ´A´ is achieved by changing the picture-flash delays, (equivalent to the growth time of the bubbles), with respect to the pressure minimum of the bubble chamber and measuring the bubble size (or track width for the case that the bubble size is not resolved) in the photographs.

5.3 Laser-Induced Boiling

Laser-induced boiling has been observed in water (Askaryan et al., 1963) and in bubble chambers filled with various liquids (Stamberg and Gillespie, 1965; Peoposoetjipto and Hugentobler, 1970; Harigel, Hilke, and Linser, 1981). These authors conclude that the process responsible for bubble nucleation by light is the heating of microscopic impurities in the liquid which provide the hot centers for bubbles. These microparticles can have diameters of micrometers or smaller and float in the liquid randomly.[32] They can absorb and accumulate enough laser light energy to form microscopic bubbles which then grow in the superheated liquid. Quantitative analysis of this process is not possible since the exact mechanisms of light absorption, transmission and reflection, the thermal properties, the size, and the quantity of these particles are not known. The magnitude, ´I,´ of the required intensity to create boiling was estimated for inhomogeneities of diameter of ´a´ by Askaryan et al. (1963) to be

$$I = \epsilon\ (D/\delta), \qquad (a > \delta)$$
$$I = \epsilon\ (D/\delta)(\delta/a)^2, \quad (a << \delta) \qquad [5.3.1]$$

where δ is the thickness of liquid layer to be vaporized, ϵ is the energy required to vaporize a unit volume of liquid, and D is the thermal diffusivity coefficient of the liquid. Poesposoetjipto and Hugentobler (1970) calculated ´I´ for Freon liquid, $CBrF_3$, at 38.0 °C to be

32. For the bubble chambers the origin of the microparticles are the "dirt" which come off the interior of the chamber, the expansion system, the transfer lines and dewars, and the solidified residual air (nitrogen, oxygen) and water. The motion of the piston assures the uniform distribution of the microparticles.

3.3×10^{19} eV/cm^2/sec with $a \simeq \delta \simeq 1 \times 10^{-3}$ cm, $D = 0.4 \times 10^{-3}$ cm^2/s, and $\epsilon = 1.3 \times 10^{8}$ erg/cm^3.

Other possible mechanisms for release of sufficient energy to initiate the laser-induced boiling are:

1. multi-photon processes,

2. statistical temperature and/or density fluctuations in the liquid.

Light absorption by the Ne/H_2 liquid is an improbable explanation since this liquid mixture appears to the eye to be perfectly transparent to the visible spectrum over the depth of the bubble chamber (no quantitative measurements of the absorption coefficient of the Ne/H_2 mixture is known). Furthermore, Poesposoetjipto and Hugentobler (1970) have shown that there is no light-wavelength dependency for the light-induced boiling in Freon liquid whose absorption coefficient is $\sim 2 \times 10^{-2}$ cm^{-1} for the visible light.

5.4 Experimental Results

Accepting the above mechanisms for the laser-induced boiling in the bubble chamber, there are then two obvious methods to suppress the boiling effectively:

1. reduction of the impurities in the liquid to decrease the number of nucleation centers,
2. reduction of the instantaneous input power of the laser beam to allow the heat to dissipate before the tiny particles form a hot center, and to minimize any multiphoton processes which might occur.

Both methods were used in parallel during the 1985 E-632 physics run. The Ne/H_2 liquid mixture was pumped through 2 and 0.5-μm filters alternately during the times the chamber was not expanding for time periods of a few hours or longer. The removal of small particles was monitored by measuring the pressure drop across the filter.[33] A qualitative reduction of laser-induced boiling was observed as compared to an earlier technical run of the chamber, but no quantitative results can be given as it was difficult to reproduce the exact operating conditions of the bubble chamber.

Reducing the laser-induced boiling by increasing the laser-pulse length was the main effort. The length of laser pulses was increased from 20 ns to 1 μs and as much as 100 μs. A description of the production and characteristics of these laser pulses was given in Chapter 4.

---

33. Originally a 5-μm filter was used. This filter was replaced by a 0.5-μm one, (the smallest commercially available), since no drastic increase in the pressure drop was observed. (W. Smart is acknowledged for providing these information.)

The results presented here describe the boiling as a function of the laser-pulse length, energy, and spatial and temporal profiles. These results were strongly dependent on the operating conditions of the bubble chamber. Since the data were taken at different times and chamber conditions during the 1984 technical run and the 1985 physics run, only a qualitative comparison of these results is possible. Furthermore, in most cases we had no exact knowledge of the operating parameters of the bubble chamber. However, we can describe the effect of the laser parameters on the laser-induced boiling for data taken under given operating condition of the chamber.

Presentation of the results is divided into three sections:

1. laser-induced boiling as a function of laser pulse characteristics,
2. laser-induced bubble size, growth rate, and bubble density,
3. percentage of the conventional-picture-fiducial volume obstructed as a function of laser-pulse characteristics.

Laser-Induced Boiling as a Function of Laser-Pulse Characteristics

In the first test of the dark-field method in BEBC at CERN (Bjelkhagen et al., 1984b) it was shown that the laser-induced boiling was substantially suppressed for free-lasing pulses as compared to that for Q-switched pulses. More quantitative results were obtained during the 1984 technical run in the 15-foot Bubble Chamber. Figure 5.1 shows the conventional bubble chamber pictures taken ~ 10 ms after the injection of the laser pulse with three different pulse structures, each resulting in almost the same amount of boiling when no other condition of the bubble chamber was changed. It can be seen that changing the laser operation mode from Q-switching (120 ns fwhm) to a stretched-pulse (2.2 μs fwhm) and to free-

lasing (~ 1 ms) allows an increase in pulse energy by factors of about 5.5 and 7.5, respectively, resulting in the same amount of boiling. These results show the general tendency of decreased boiling with increased laser pulse length. However, as the structure of the free-lasing pulse was different from that of the stretched-pulses, (see Chapter 4), no useful quantitative comparison can be drawn between the amount of boiling induced by the two.

An alternative presentation of the dependence of the boiling on the laser-pulse length is given in Figure 5.2. This figure shows, as a function of pulse length and energy, the boiling observed in the conventional pictures taken 10 ms after the injection of the pulse. A laser pulse of duration of 40 μs with energy of about 600 mJ produces negligible boiling compared to that from sub-microsecond pulses of comparable energy.

The structure of the boiling depends strongly upon the spatial profile of the laser beam before it hits the diverging lens and enters the chamber, and less upon the temporal waveform of the pulse. Figure 5.3 shows two different boiling structures for two laser pulses of the same energy and overall pulse length but with different temporal and spatial profiles. The characteristics of the laser pulses corresponding to the different boiling structure is summarized as following:

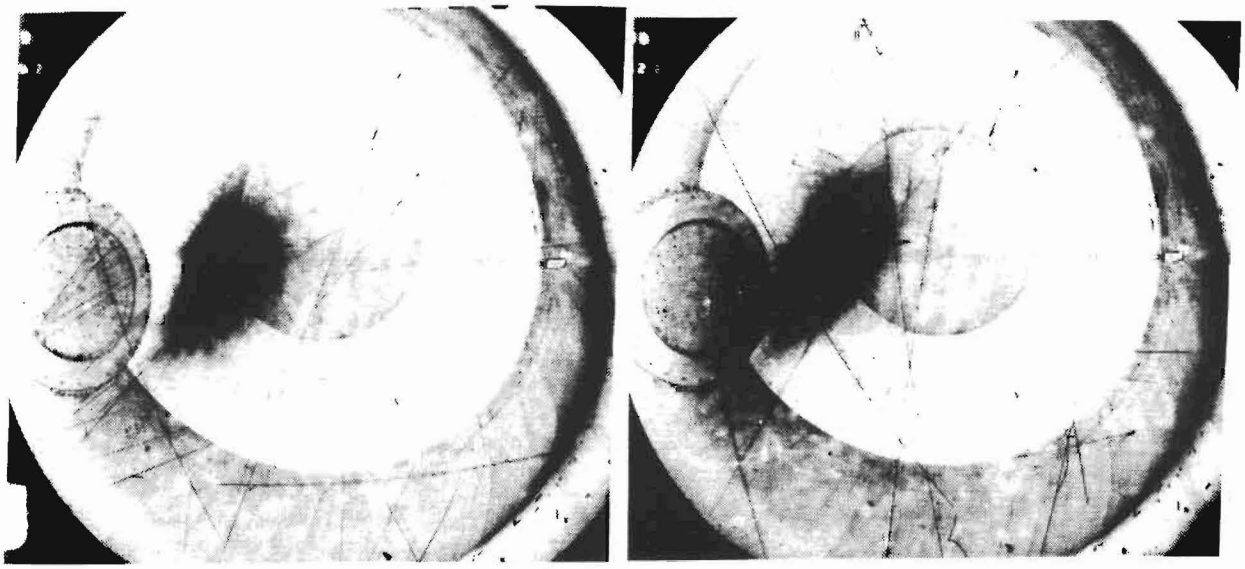

(a) (b)

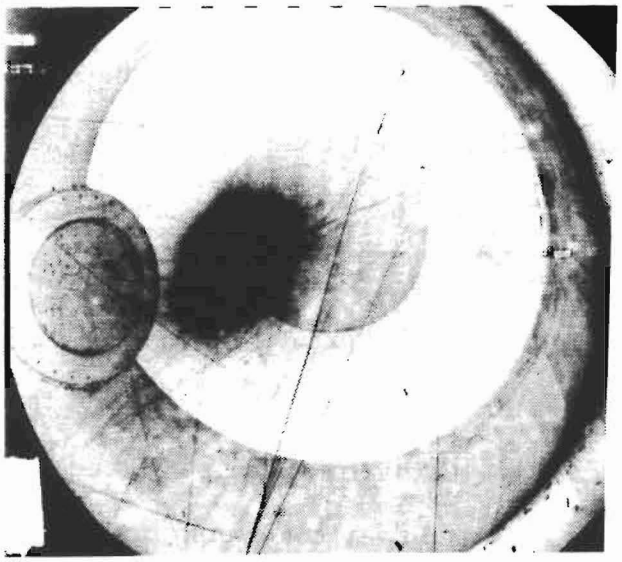

(c)

Fig. 5.1 Pictures of laser-induced boiling inside the chamber as seen from one conventional camera, view 2. The pictures were taken ~ 10 ms after the injection of the laser pulse.

		pulse duration	energy
(a)	Q-switched	120 ns	400 mJ
(b)	Stretched pulse	2.2 μs	2.0 J
(c)	Free-lasing	~ 1 ms	3.0 J

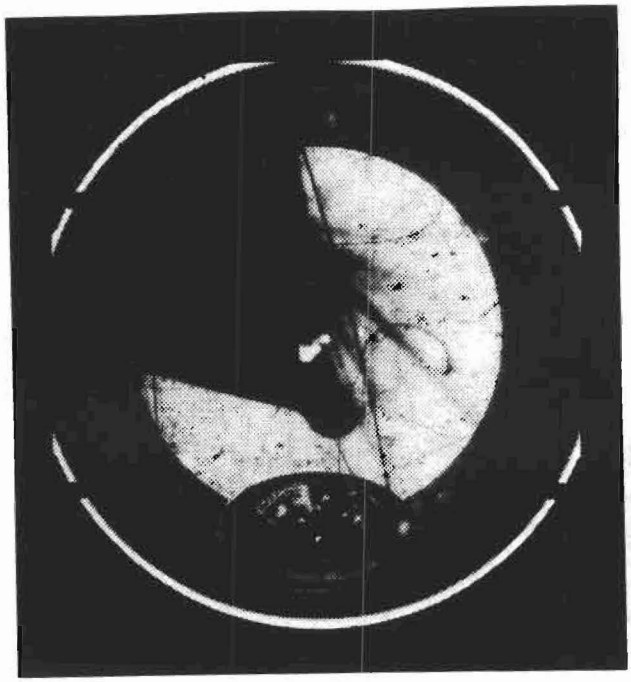

(a)

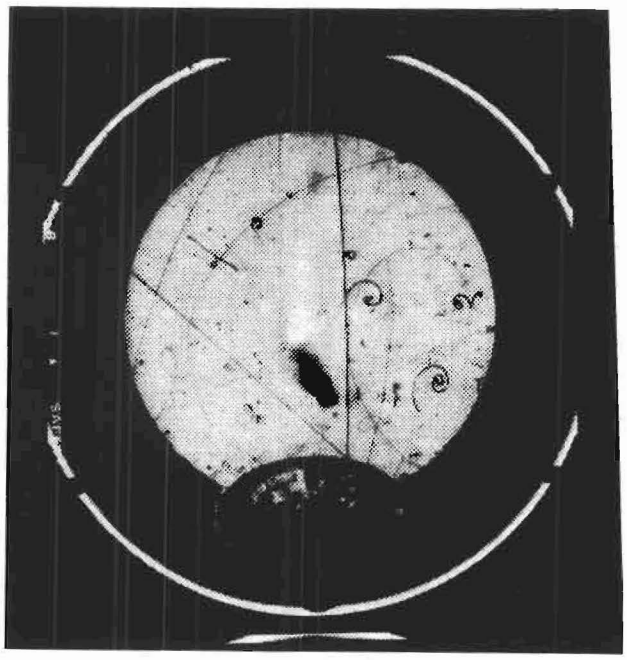

(b)

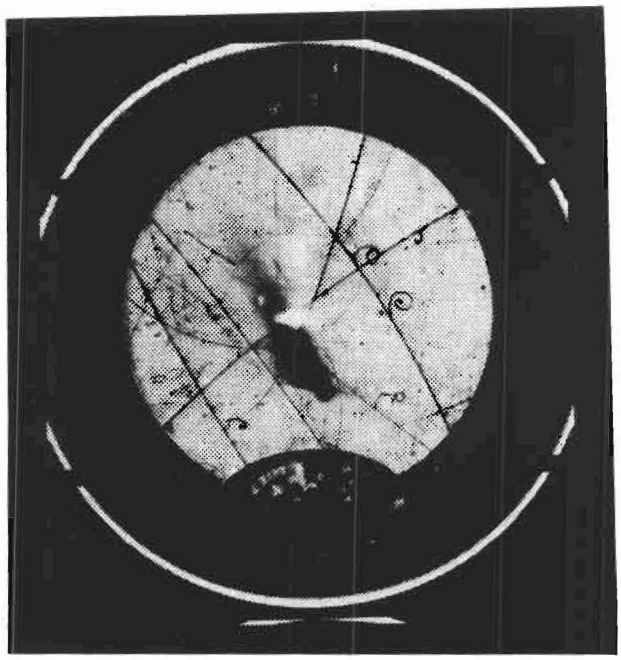

(b′)

Fig. 5.2 Pictures of laser-induced boiling inside the chamber as seen from one conventional camera, view 1. The pictures were taken ~ 10 ms after the injection of the laser pulse.

	pulse duration	energy (mJ)
(a)	200 ns	370
(b)	5 μs	370
(b′)	5 μs	600

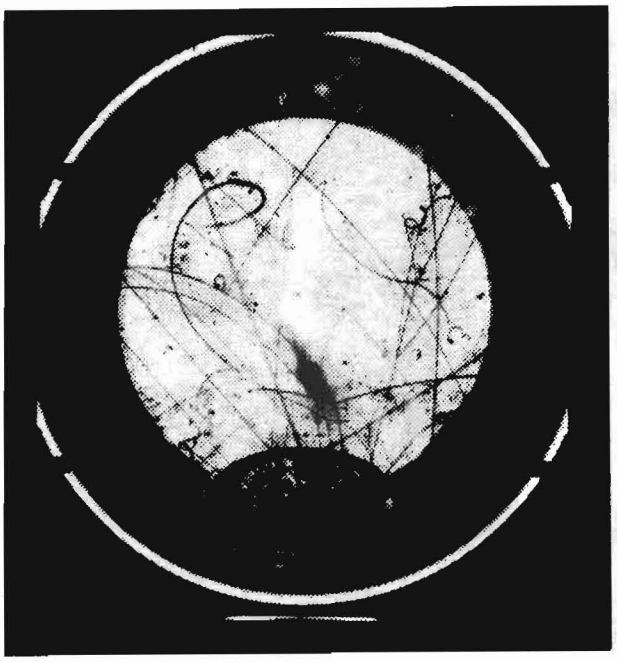

(c)

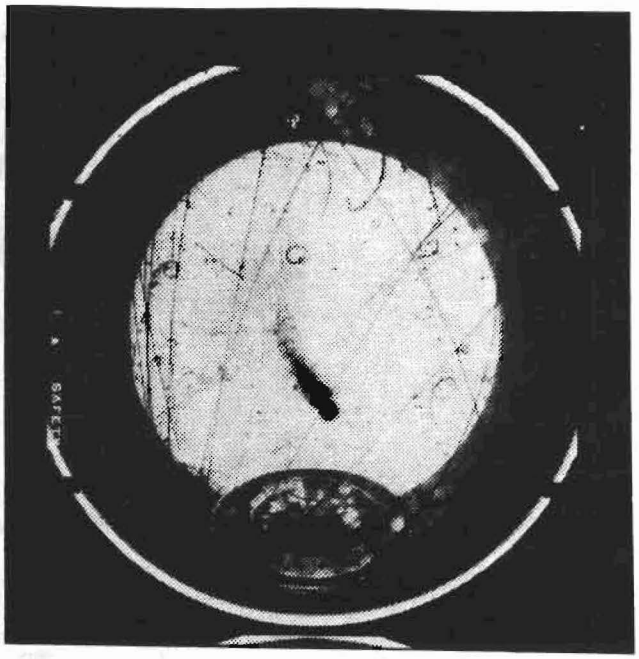

(c′)

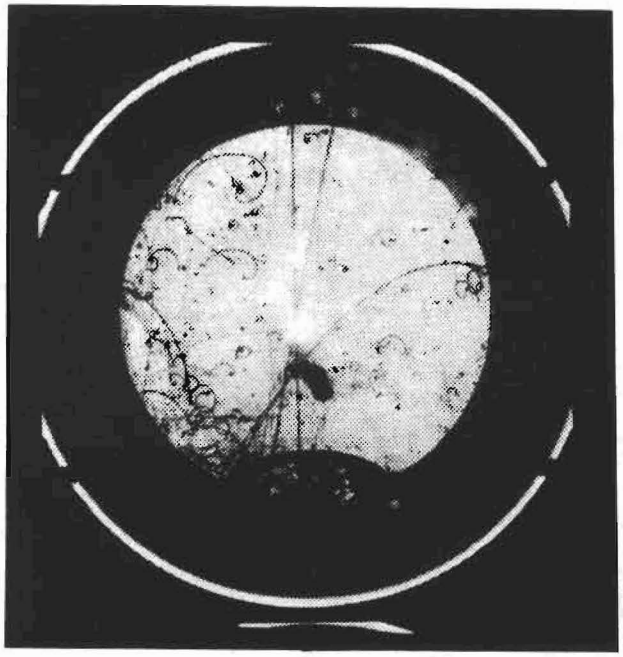

(d)

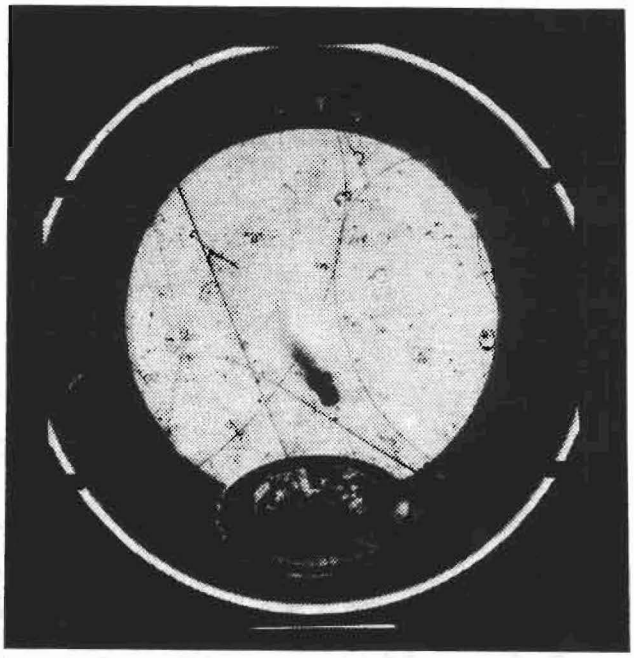

(d′)

Fig. 5.2 Pictures of laser-induced boiling inside the chamber as seen from one conventional camera, view 1. The pictures were taken ~ 10 ms after the injection of the laser pulse.

	pulse duration	energy (mJ)
(c)	15 μs	370
(c′)	15 μs	600
(d)	40 μs	370
(d′)	40 μs	600

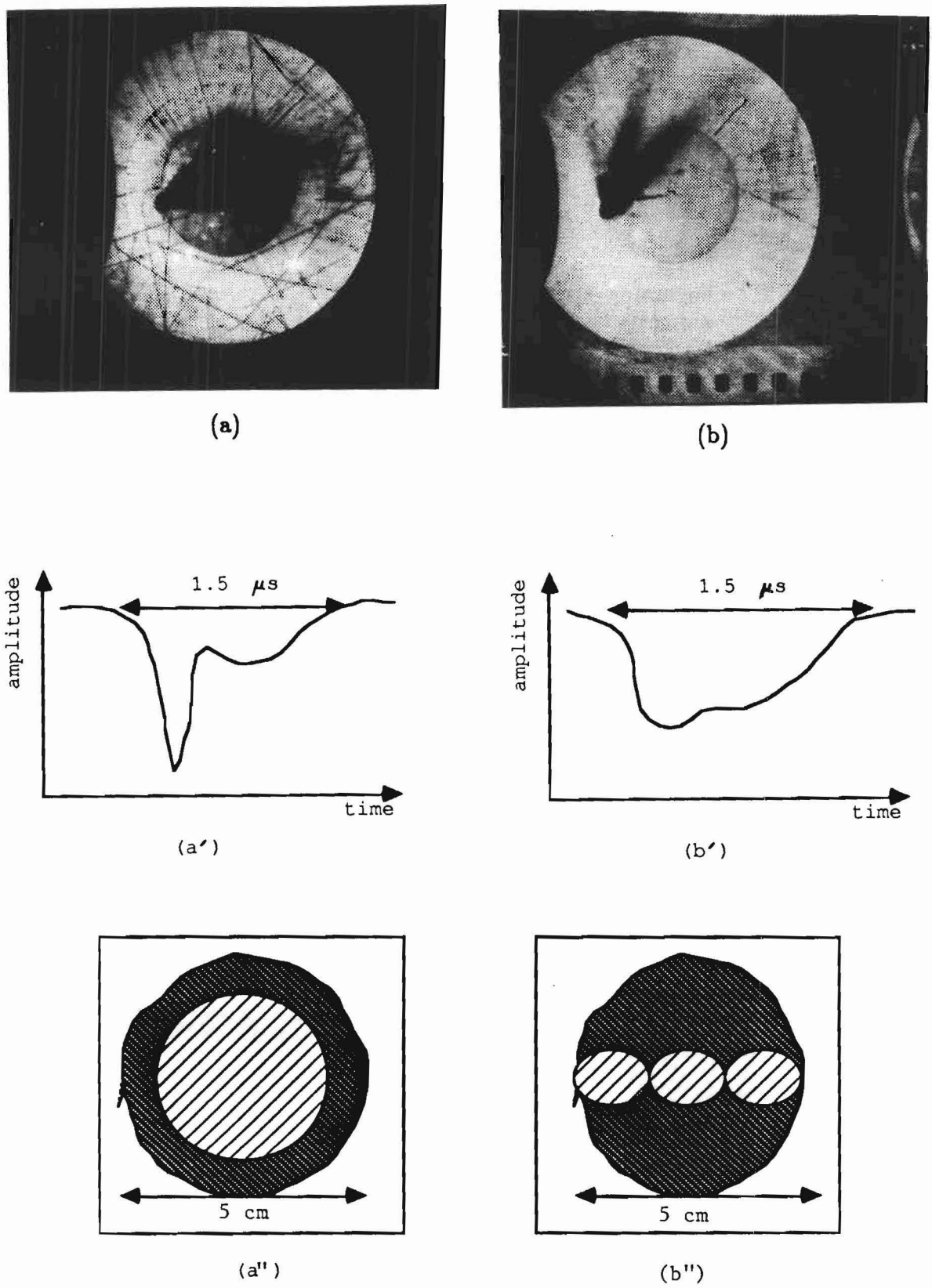

Fig. 5.3 (a) - (b): Pictures of laser-induced boiling inside the chamber as seen from one conventional camera, view 4. The characteristics of the light pulses giving rise to the boiling, (a′) - (b′): temporal waveform, (a″) - (b″): spatial profile.

	Figure 5.3a	Figure 5.3b
Laser-Pulse		
Length (μs)	1.5	1.5
Energy (J)	1.8	1.8
Laser-Pulse Profile		
Temporal	beginning spike,	smooth rise,
Spatial	almost uniform	three hot spot
Laser-Induced Boiling		
Structure	uniform,	three distinct boiling regions
Percentage of the floating disk obscured	~ 30 %	~ 23 %

Approximately the same amount of boiling is observed in both cases, while the boiling structure seems to follow the hot-spot format of the spatial profile of the laser beam.

Laser-Induced Bubble Size and Growth Rate

In order to understand the heat dissipation mechanism of the laser-induced boiling a test was performed where the laser injection timing was varied with respect to the pressure minimum of the bubble chamber expansion. The variations in the laser-induced boiling was studied in conventional photographs taken at a fixed time, 10 ms, after the pressure minimum. The data were also used to measure the proportionality constant, A (Equation [5.2.2]), of the laser-induced boiling and to determine the bubble size and density. The bubbles were projected on a conventional scanning table with high magnification of a factor of 65. The bubble-image sizes along the upward edge of the boiling cone were measured as full width at half maximum of their intensity profile using an array of photodiodes and an oscilloscope. The bubble chamber coordinates of the measured points were obtained using two-view reconstruction from which the demagnification of the fisheye windows and camera lenses were calculated.

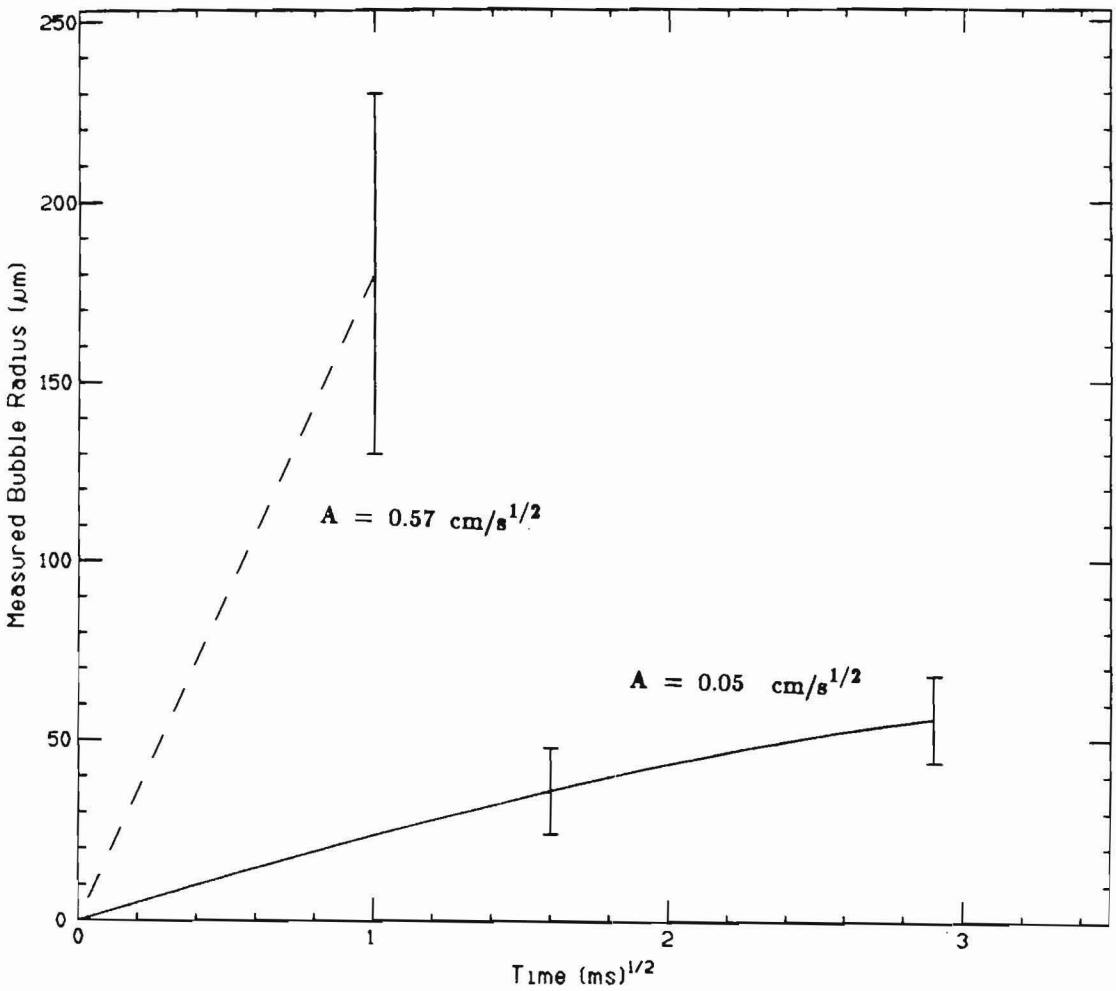

Fig. 5.4 Bubble growth rate, A ($cm/s^{1/2}$), for laser-induced boiling, (solid), and the boiling due to ionizing particles, (dashes).

The following observations were obtained from examination of the data: laser-induced bubbles have small size and do not appear to grow to the same size as the ionizing particle track bubbles for the same conventional-picture flash delays, (Figure 5.4). In this figure, laser-induced bubbles have diameters of about 45 ± 10 μm after 1 ms as compared to 360 ± 40 μm for ionizing particle track bubbles measured in high resolution photographs. Furthermore, the proportionality constant, ´A´ (Equation [5.2.2]), calculated from the slope of the bubble growth, (Figure 5.4), is 0.05 $cm/s^{1/2}$. This is smaller than ´A´ of the ionizing particles, (0.57 $cm/s^{1/2}$), by a factor of ~ 10. The slow growth rate of the laser-induced bubbles might be explained by their failure to extract sufficient heat for vaporization from their vicinity due to their high bubble densities. (It is difficult to give numbers for the laser-induced bubble density since it varies with the light-pulse energy, the distance from the diverging lens, and individual bubbles can not be identified in different views.)

Percentage of the Conventional-Picture-Fiducial Volume Obstructed

For the 15-foot Bubble Chamber application, we are concerned with the fiducial volume which is obstructed in the conventional bubble chamber pictures as a result of the laser-induced boiling. Since laser-induced boiling probably cannot be completely eliminated, a small percentage of the obscured volume in the conventional photographs must be accepted. The obstructed volume varies from one conventional camera view to another. Therefore, an event which lies in the obscured region of one view may be visible in one or two other views. Two independent efforts, (one during the 1984 technical run and another at the end of the 1985 physics run), were made to obtain a measure of the percentage of the obstructed conventional-picture-fiducial volume as a function of laser-pulse length and energy.

Figure 5.5 shows the height of boiling, above the diverging lens, as a function of laser beam energy for two pulse durations, 120 ns and 2.2 μs.[34] This level is reduced by a factor of ~ 2.5 as the pulse duration is increased from 120 ns to 2.2 μs.

Figure 5.6 shows the percentage of the floating disk obscured as a function of laser-pulse energy for three different pulse durations, 1.5, 3, and 8 μs.[35] This percentage is decreased by a factor of about 5 and 40 from 1.5 μs to 3 and 8 μs, respectively. For laser pulses with energies of 700 mJ entering the bubble chamber, 21, 4, 0.5 % of the floating disk was obscured by pulse durations of 1.5, 3, 8 μs, respectively.

---

34. P. Schmid is acknowledged for providing these measurements.

35. G. Harigel is acknowledged for providing these measurements.

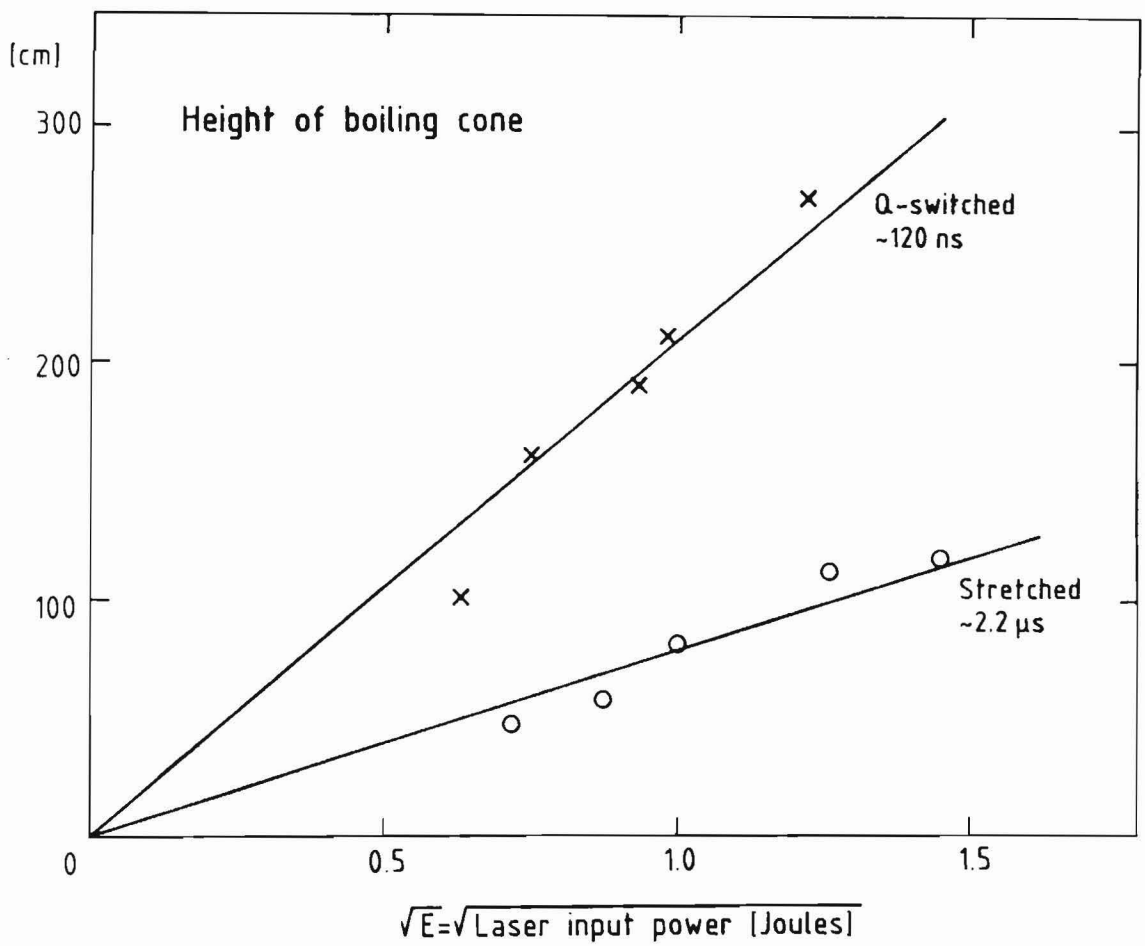

Fig. 5.5 Height of laser-induced boiling cone inside chamber liquid as a function of laser input power for two pulse durations.

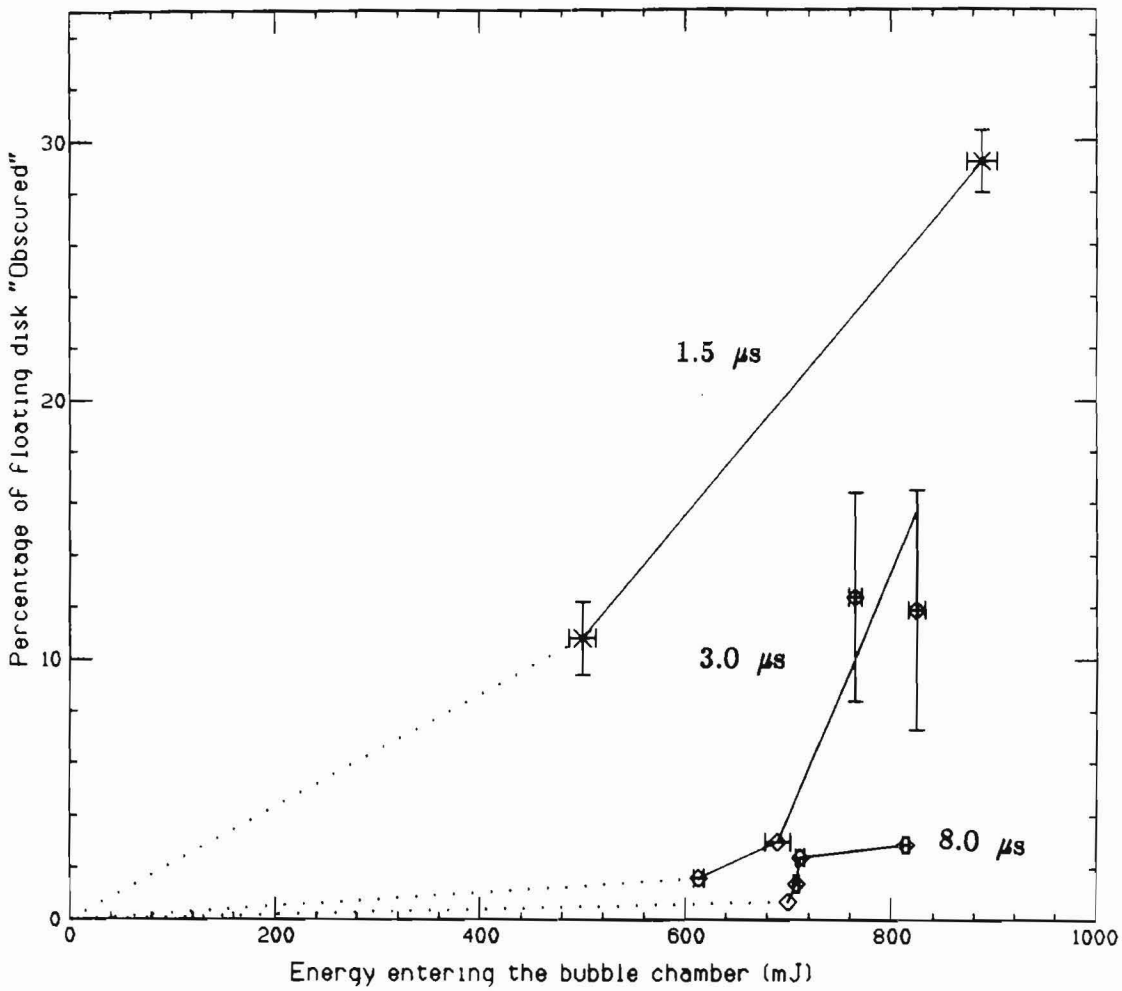

Fig. 5.6 Percentage of floating disk "obscured" by laser-induced boiling for three pulse durations. The dotted lines are an extrapolation of the results.

CHAPTER 6 BUBBLE-CHAMBER HOLOGRAPHY: DARK-FIELD METHOD

6.1 Apparatus

In Section 2.2 a general description of the system´s setup was given. Here a detailed description of each of the components of the apparatus is presented.

6.1.1 Beam Transport and Profile

The bubble chamber´s expansion-induced vibrations, its strong magnetic field, the potential danger of hydrogen leaks in the bubble chamber building, and the safety requirements for the operation of the laser made it difficult to install the laser near the bubble chamber. Instead, the laser was put in an air-conditioned, clean room at the end of lab. B and the laser beam was transported to the bubble chamber via an underground pipe.

Ideally, the beam should be transferred through a flexible light pipe, (e.g. optical fibers), both to relax the mechanical requirements on the beam transportation and to improve the alignment of the beam into the chamber. However, the transmission of high power holographic-quality laser beam using optical fibers is not yet feasible. Instead, the beam was sent through a rigid underground pipe of 30 cm diameter and 30 m length from the laser room to the bottom of the chamber, (Figure 6.1). The pipe was under vacuum in order to prevent the breakdown of air molecules and formation of plasma as a result of focusing the high power beam into a small spot. Furthermore, the transportation of the laser beam in the vacuum pipe was necessary to avoid the beam profile distortions introduced by air

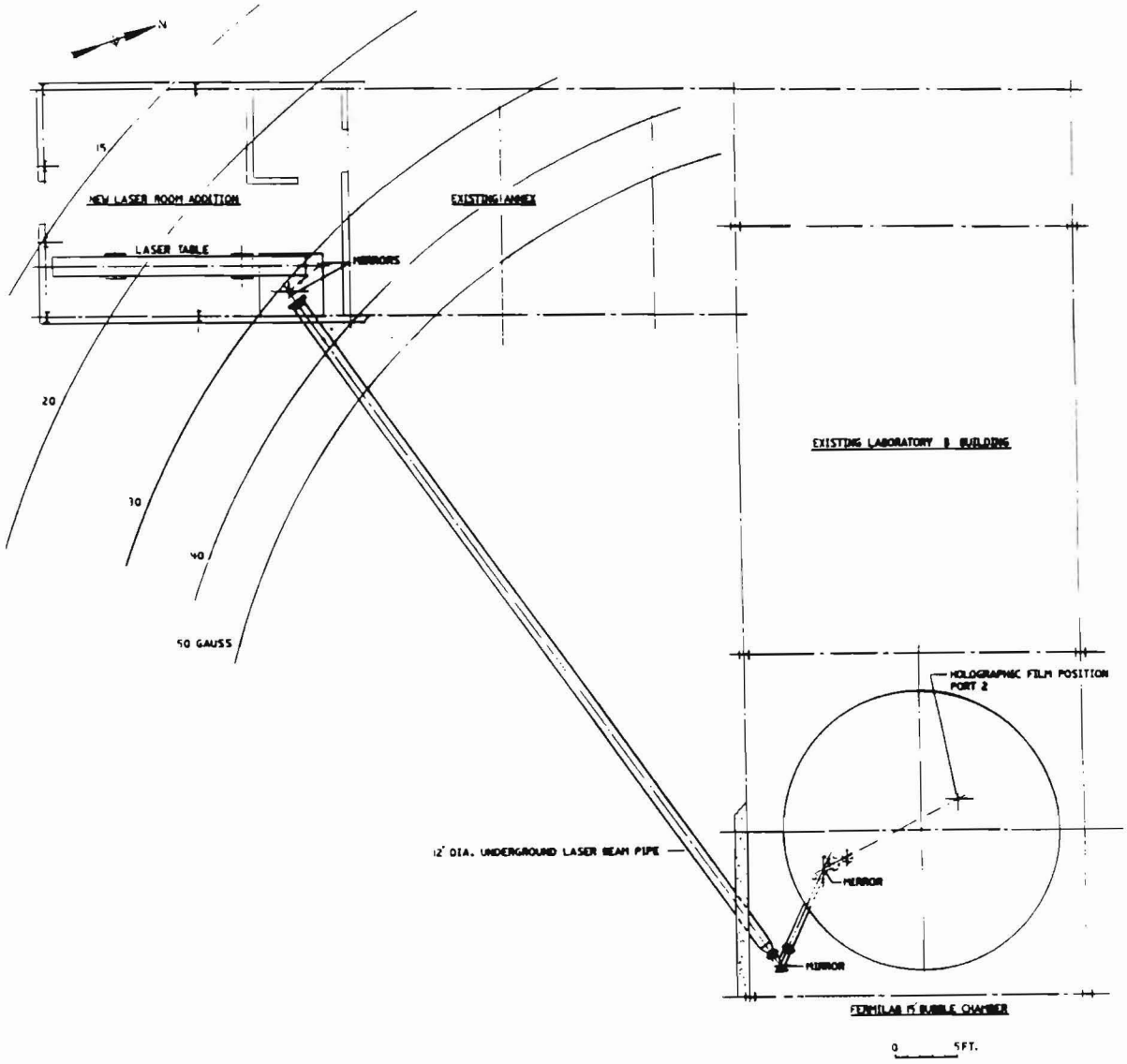

Fig. 6.1 Laser room, beam pipes, and bubble chamber, (top view). The lines of constant magnetic field near the laser room are shown.

inhomogeneities.

The laser beam was directed into the pipe by a mirror at the end of a stable, vibration-resistant table, on which the laser was mounted. The beam was then directed to the bubble chamber via three mirrors. A tee junction was placed on the pipe just before the entrance of the bubble chamber. A sliding mirror at the tee junction allowed the monitoring of the laser beam alignment using a burn paper. The diameter of the laser beam was approximately 5 cm at the tee. A sliding interchangeable aluminum sheets with various apertures installed in a joint between two flanges before the tee allowed the adjustment of the beam diameter entering the bubble chamber. The alignment procedure for these apertures utilized the tee junction and was somewhat crude. The procedure for alignment of the laser beam into the bubble chamber is described in Appendix II.

The laser beam enters the vacuum tank of the bubble chamber through a warm window and the pipe (with a diameter of 15 cm) continues through the vacuum tank to prevent oil contamination on the optical surfaces. This section of pipe carries the ~ 300 K temperature gradient, and contains a bellows to allow for movement of the bubble chamber vessel relative to the fixed vacuum tank during the expansion cycle. This section is evacuated by "ion getter" pumps. No movement of the beam spot has been observed at the tee due to chamber expansion.

All the mirrors and windows in the laser beam path to the bubble chamber are made from fused silica of optical grade "Homosil." This material has a small thermal expansion, excellent homogeneity, and a high damage threshold. The surfaces of all the windows have a single layer of dielectric antireflection coating (0.2 % reflectivity), and the mirrors are

99.9 % reflective for the 694 nm wavelength.

The output beam from both the experimental and commercial lasers had almost Gaussian profiles in the near field. However, for both lasers the beam profile was significantly distorted in the far field, some 30 m from the laser, where the tee junction was placed. Figure 6.2 shows a sketch of the beam profile at the tee. The spot, which resembles a $TEM_{01}{}^*$ mode, is composed of a uniform low intensity center surrounded by a bright, high intensity ring. Since the response of the photographic paper is not linear, the difference in the intensities can only be judged qualitatively from the burn paper. A quantitative measurement using a Lasermetrics powermeter showed that about 75 % of the energy is in the bright ring. The development of the bright ring appears in the beam profile at a distance of about 6 m after the last amplifier and is not dependent on the total beam energy.

6.1.2 Dispersing Lens

The dispersing lens used in the 1985 E-632 physics run was the same one-element $\pm$ 20° dispersing lens which was used in the BEBC test at CERN. Originally, a two-element lens which diverged the beam out to angles of $\pm$ 40° was planned to be used. A preliminary test of this two-element lens in the laboratory proved to be successful and rather good holograms were obtained. However, no holograms were successfully made in warm bubble chamber tests even when almost all of the chamber interior was covered with black cloth to absorb the scattered light from the bubble chamber walls. The two-element lens gives only $\sim 0.1\ \mu J/cm^2$ in the central reference beam. This intensity was barely sufficient to give a proper

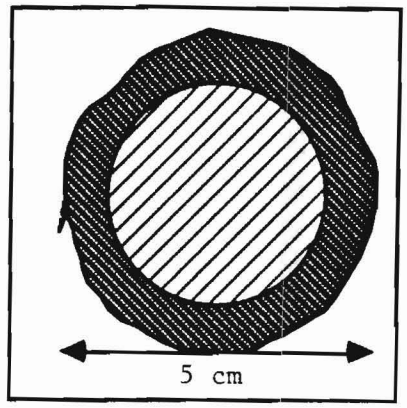

Fig. 6.2 A typical unrestricted beam profile at the tee junction.

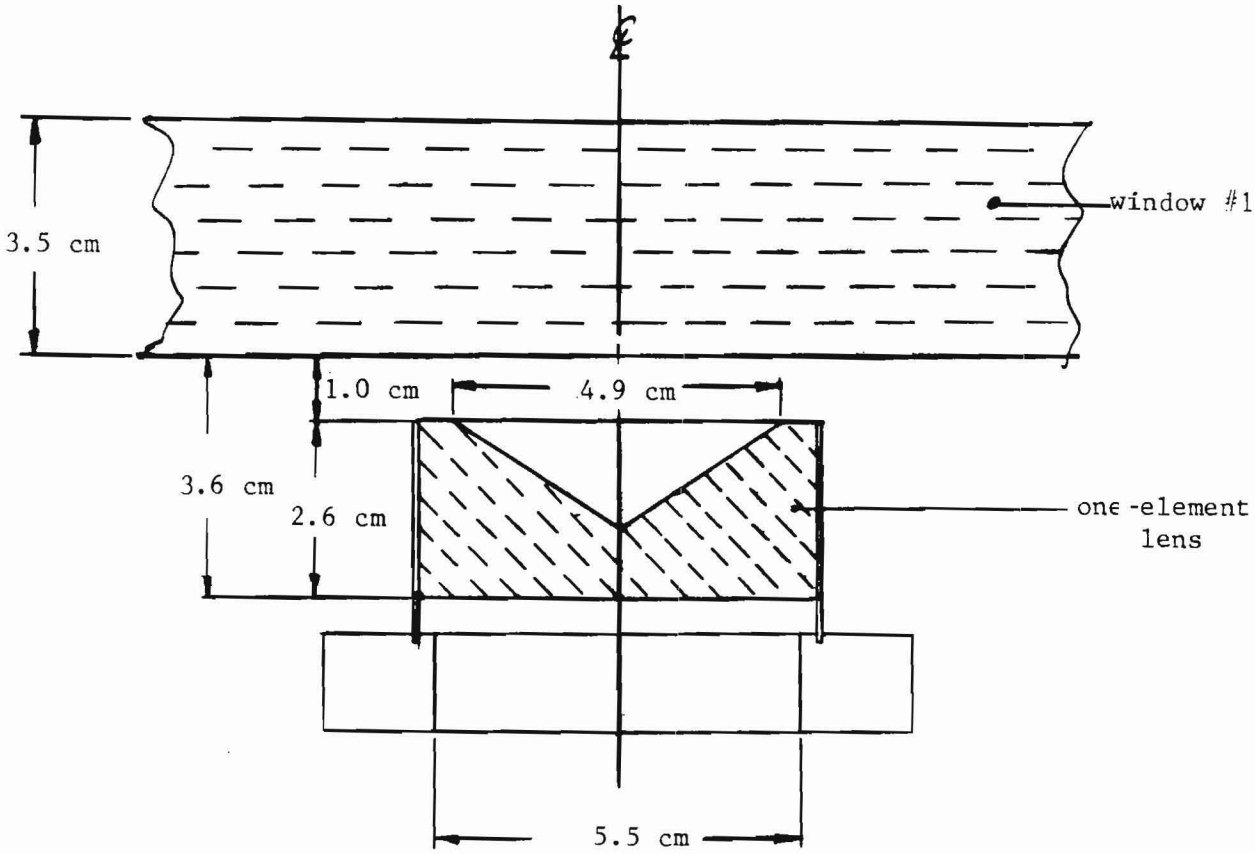

Fig. 6.3 One-element lens and the laser beam window entrance.

exposure on the hologram and to assure linear recording, and was easily overwhelmed by the background light. The source of this "noise" is the incoherent light scattered by the Scotchlite (or in the warm chamber test, the black cloth). For a laser beam with energy of 5 J entering the bubble chamber, the average intensity on the bubble chamber walls is about 10 $\mu J/cm^2$ which is 100 times larger than the intensity in the reference beam of the two-element lens. As a result of these tests, it was decided to use the one-element, $\pm$ 20°, lens for the physics run.

This one-element lens was manufactured out of fused quartz, had an outside diameter of 60 mm, an effective aperture of 50 mm and a thickness of 26 mm, (Figure 6.3). The aspheric surface was calculated by a computer program, taking into account the refractive indices of quartz ($n_Q = 1.45$) and of the 75/25 mole percent Ne/H_2 mixture at a temperature of about 30 K ($n_{Ne/H2} = 1.09$). The main parameter was the desired object beam light intensity, which was critically influenced by the curvature of the central part of the lens. Figure 6.4 shows the theoretical output light intensity for a Gaussian beam input as a function of the divergence angle, (the illumination angle, θ_i), together with experimental data measured in air using an Argon laser, ($\lambda \simeq 514$ nm), at a distance of 200 cm from the lens and an input beam of 3 cm diameter. A deviation from the theoretical curve is observed. The reference beam has an intensity four times more than the desired theoretical value (1 $\mu J/cm^2$). This was due to multiple internal reflections from the larger-angle rays towards the reference beam. Another feature of this lens is that the maximum output light intensity occurs for the angles of about 15° in air and 20° in the Ne/H_2 liquid. The intensity then falls off for the larger angles. This behavior results in a sudden

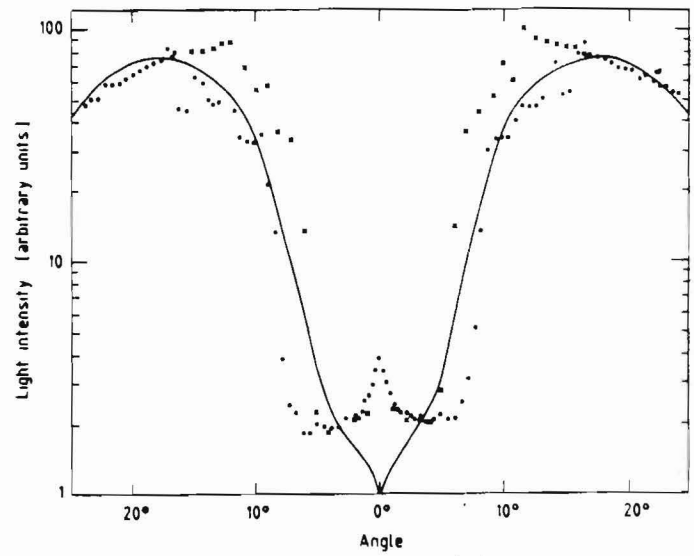

Fig. 6.4 Angular distribution of the light intensity after the one-element lens: design values for a gaussian beam and the lens in liquid neon-hydrogen; points: measured light distribution in air, at a distance of 200 cm, incoming beam of ϕ=30 mm, wavelength λ = 514 nm; measured data extrapolated to liquid neon-hydrogen.

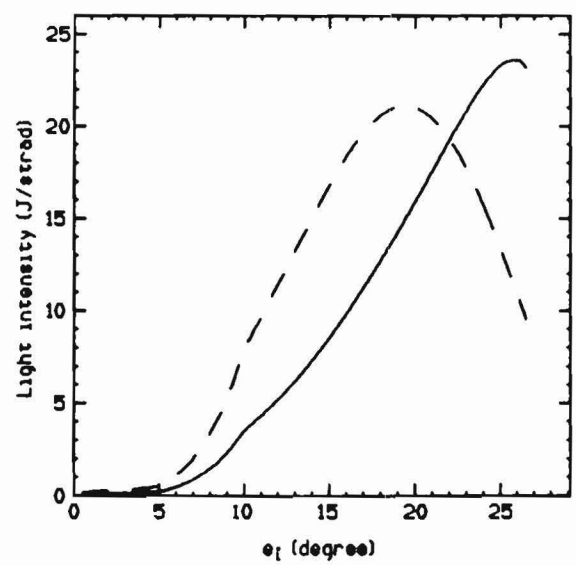

Fig. 6.5 Design values of angular distribution of the light intensity after the light has passed through one-element lens and laser entrance window in liquid neon-hydrogen for an incoming beam with flat profile, (solid line), and an incoming beam with gaussian profile, (dash line), both with energies of 10 J.

decrease in the beam balance ratio, and thus a sudden reduction in the bubble visibility at the larger angles. The one-element lens had been in fact designed in part to explore the range of beam balance ratios possible for bubble chamber holography, and was never intended to be ideal.

In the 15-foot Bubble Chamber the lens was installed immediately before the laser entrance window of the chamber. The refraction of light through the window and into the liquid extends the light distribution up to angles of 27°. Figure 6.5 shows the theoretical curves for the output light distributions for Gaussian and flat input beam profiles after the window as a function of the divergence angle.

The original test at BEBC (Bjelkhagen, 1984b) had the lens inside the bubble chamber where at the 15-foot Bubble Chamber the lens was outside. A lower peak power density of the beam at the window which is in contact with the liquid helps to reduce the problem of the laser-induced boiling. However, any accumulation of dirt and dust, or solidification of air and/or nitrogen gas on the window would act as a ground glass placed after the formation of the reference beam point source. This would result in diffusing the point source and increasing its effective "spot size," thus spoiling the quality of the reference beam.

6.1.3 The Holographic Camera

A standard 15-foot Bubble Chamber camera was modified for holography. The main modifications were to allow more spacing for the holographic film with its thick polyester base, the removal of the camera lenses, and the lowering of the film platen. Other components of the camera, the winding-on, and the feed and take-up mechanisms for the film were the same. The film platen was placed at the center of curvature of

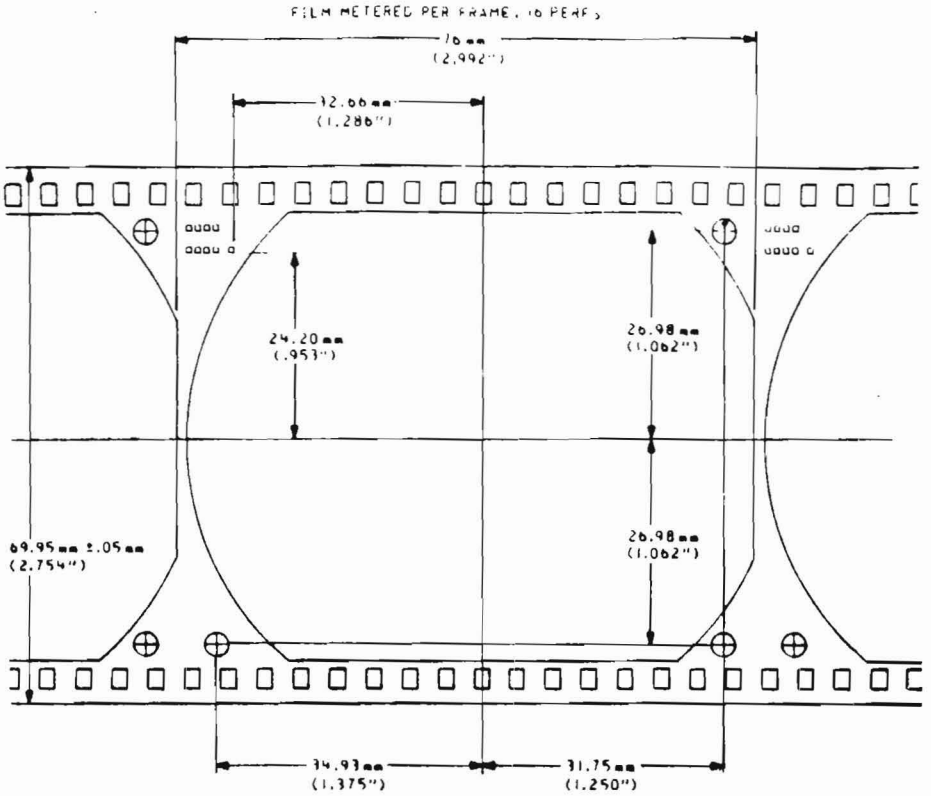

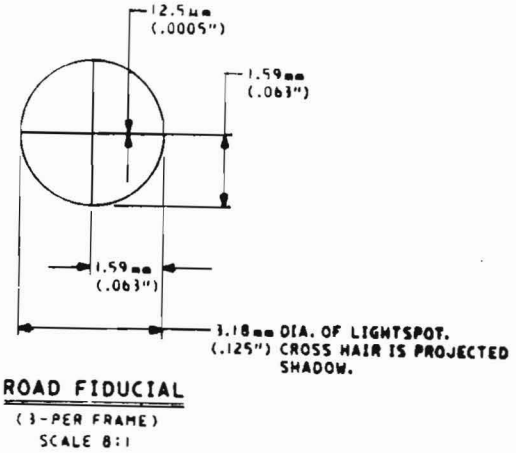

Fig. 6.6 The holographic film with the fiducial marks.

the fisheye windows at a distance of about 5 cm from the inner diameter surface. It was perpendicular to the reference beam with an accuracy of about 1°. The film was held flat against the platen by vacuum.

There were three camera-based fiducial marks which were exposed on the holographic film. Figure 6.6 shows the position of these marks for a frame. The camera-based fiducial marks served to define the position of the film with respect to the platen. Holding the film flat and positioning the film correctly with respect to the platen was extremely important at the recording stage so that both could be reproduced accurately at the reconstruction stage.

Different color filters were placed in front of the holographic film (RG 665) and in front of the flashtubes of the conventional cameras (BG 39). These filters prevented the light from the flashtubes from exposing the holographic film. Exposure of the conventional film by laser light was not a problem at the laser energy levels used, due to the high f-number of the conventional lenses (f/12), an existing Wratten 58 color filter in the conventional lenses, and the low sensitivity of the Kodak 2482 film to ruby laser light (λ = 694 nm). Using a mechanical shutter instead of filters could have been more difficult due to the strong magnetic field.

6.1.4 Holographic Recording Material and Processing

During the 1985 E-632 physics run all the holograms in the chamber were made on Agfa-Gevaert Holotest 10E75 material on polyester film. This material was chosen due to its high sensitivity, (~ 1 $\mu J/cm^2$) to relax the input energy requirements, and its rather high resolution (3000 lines/mm). During some of the laboratory tests Agfa-Gevaert Holotest 8E75HD material

on plates had also been used to obtain higher contrast holograms. The Holotest 8E75HD material had a finer grain size, higher resolution (5000 lines/mm), but a lower sensitivity (~ 10 $\mu J/cm^2$) which made it unattractive for the bubble chamber applications. All the Holotest film materials, (10E75 and 8E75HD), had a polyester base with a thickness of 170 μm. Their emulsion thickness was 5 μm on the films, and 7 μm on the plates. The data on the manufacturers response curves were obtained using a continuous-wave Helium-Neon laser (λ = 633 nm), long exposures of the order of seconds, and a specific processing procedure (development in Agfa-Gevaert G3P at 20 °C (5 min.), and fixing in G334 (4 min.)). These conditions are different from those we used for the bubble chamber holograms.

In order to determine the exact response of the materials under the conditions used in the bubble chamber holography, laboratory tests were performed. The density of a processed emulsion, using the same processing procedure as the physics run (Table 6.1), was measured as a function of the exposure for two different ruby laser pulse lengths and structures (stretched-pulse and free-lasing). Figure 6.7 shows the H&D curves and the sensitivity of the 10E75 material for the two cases. It is seen that for free-lasing an exposure of 1.0 $\mu J/cm^2$ was needed to obtain a density of 1 on the film as compared to the manufacturer value of ~ 0.7 $\mu J/cm^2$. This value for a 4-μs pulse was observed to be 1.4 $\mu J/cm^2$ which is larger than the free-lasing value by a factor of 1.4. The H&D curve for the stretched-pulse was shifted from that for the free-lasing by a constant value of about 0.4, and the γ for the two curves was about 11. The difference between the free-lasing value and that of the manufacturer value is due to the two different lasers used for exposure and the different processing. The larger value

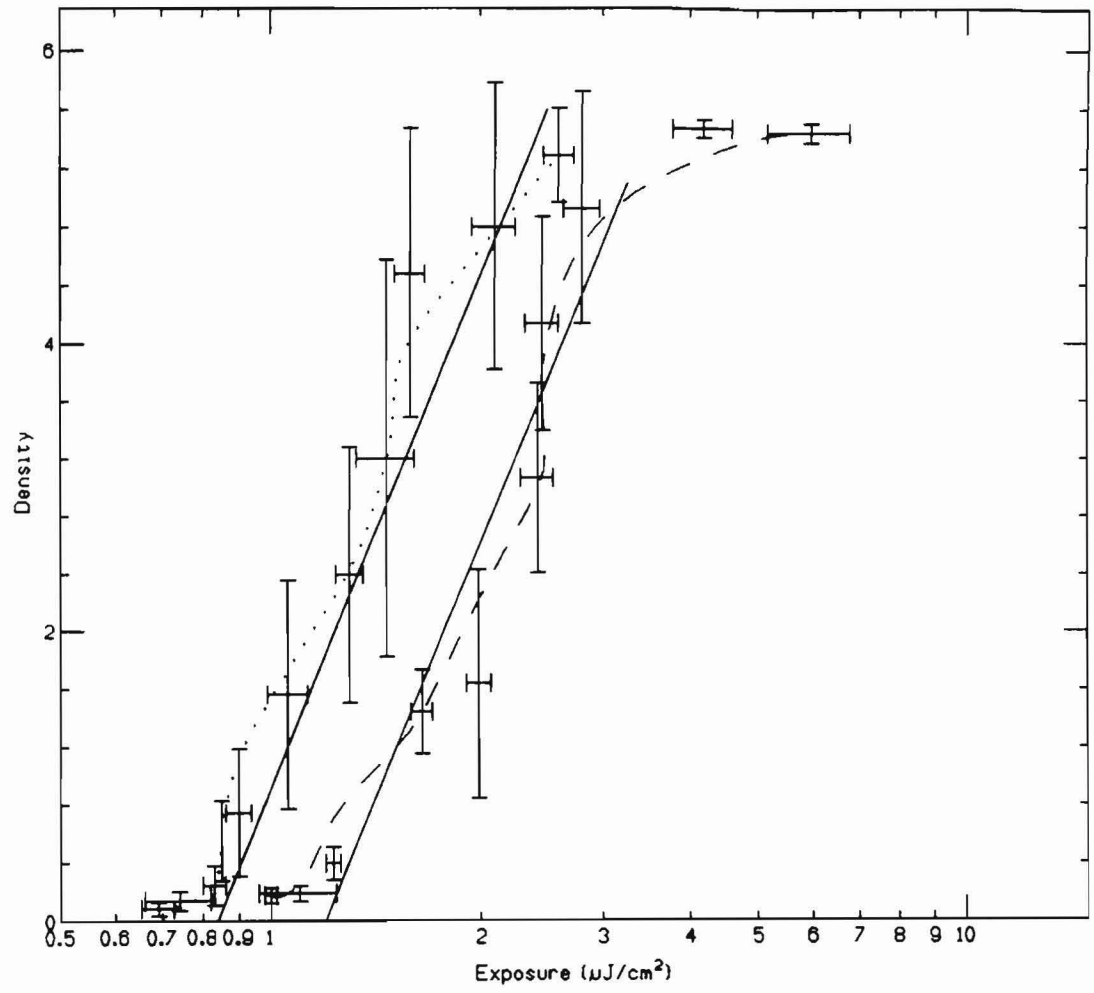

Fig. 6.7 H&D curve. Experimental data from a laboratory test for 4-μs pulse (dashed line), and free-lasing pulse (dotted line). The holographic film was developed in Phenidone-D19 for 4 min., (temperature: 23 °C), one hour after the exposure. Solid lines are the fitted data.

obtained for the stretched-pulse than for the free-lasing is most probably due to the reciprocity failure factor.

The high intensity reciprocity failure occurs for exposures of short length, $\tau_e < 10^{-5}$ s. For these exposures the production rate of the photoproduced electrons is so high that the mobile silver ions do not have a chance to neutralize the trapped electrons before additional incoming electrons reach the vicinity of the ions. As a consequence of the electrostatic repulsion between the electrons, the second electron is trapped at another site. This is an inefficient way of producing a latent image, defined as a collection of a few silver atoms at one site which are produced when the silver ions are reduced by photolysis. Unfortunately, to compensate for this effect requires a higher exposure which will further increase the laser-induced boiling.

During the run, rolls of 70 mm perforated film, 183 m long were used in the holographic camera. At the end of each roll a test strip was taken from the holographic film and developed in the bubble chamber dark room. These test strips were then examined both by eye with a Helium-Neon laser and using the Fermilab replay facilities (cf. Section 6.2) to investigate the holographic quality of the bubble tracks. The bulk of the rolls were processed commercially.[36] However, the commercial processing of the rolls usually involved a delay of 24 hours during which the latent image faded. Figure 6.8 shows the fading of two test plates as a function of time. After four hours both plates had a density which was only half of what they could have had were the plates developed immediately. After twenty-four hours both densities reached a constant value. This is a serious problem for

36. Smith & Cvetkovich Holography, Chicago, Illinois.

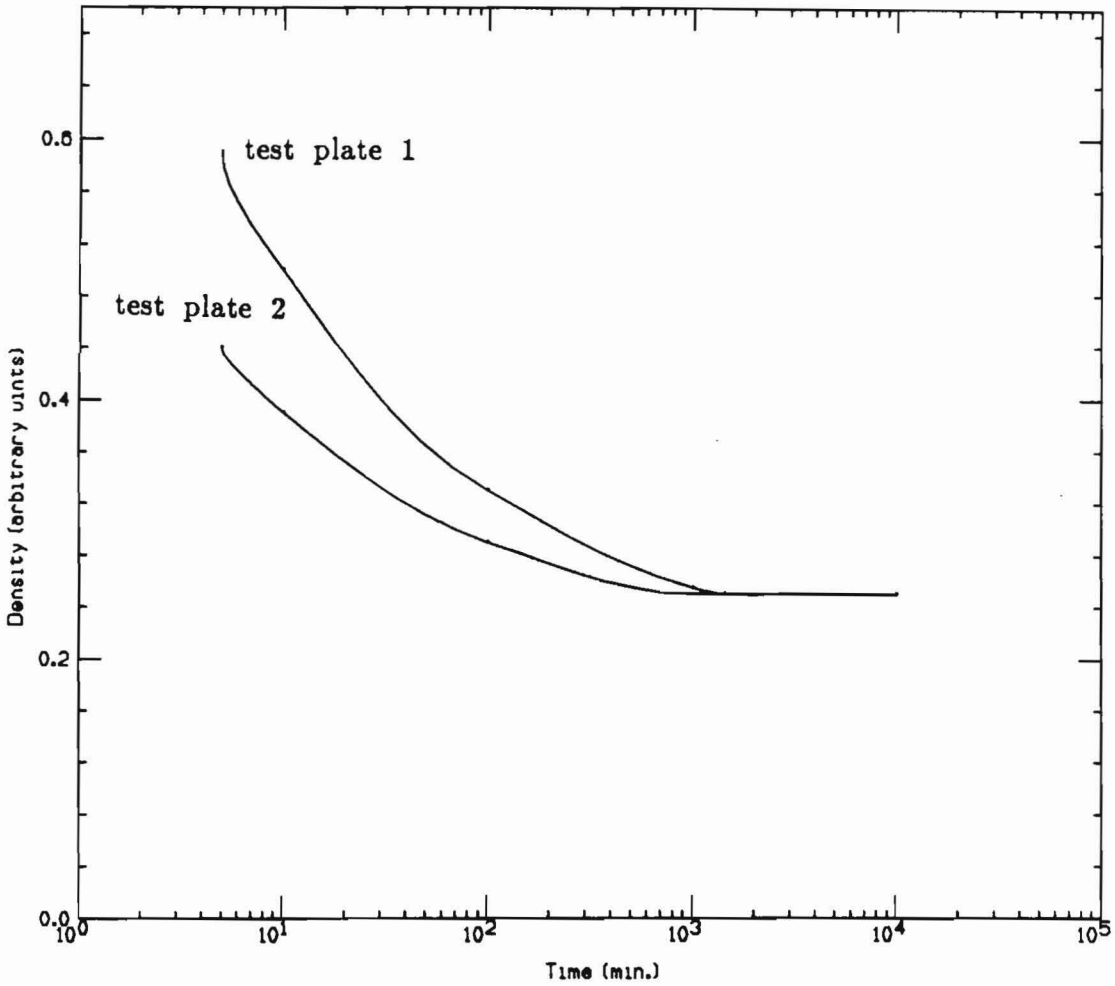

Fig. 6.8 The decrease in density, (fading), as a function of time delay between the exposure and developement for two test plates.

a bubble chamber application where a minimal energy input into the chamber is desired.

All of the production-mode holograms for the physics run were amplitude holograms. However, some of the test holograms were converted to phase holograms by bleaching. The stock bleaching solution used was composed of:

Ferric nitrate	150 g
Potassium bromide	33 g
Phenosafranine	300 mg
Glycerol	20 g
Isopropyl alcohol	500 ml
Water deionized	500 ml,

and was diluted with water. Tables 6.1 - 6.2 give the processing procedure for the development of two types of holograms. The 1.5 g/l of the phenidone (1-Phenyl-3 Pyrazolidone) added to Kodak D-19 increased the sensitivity of the emulsion by a factor of about 2.5 (Bjelkhagen, 1984a). Kodak D-19 is a high contrast developer, but it contains no silver halide solvent except the weak sodium sulfite. In order to develop the silver halide crystals completely a certain amount of silver halide solvent had to be added to the developer. Phenidone acts as such a solvent, and the crystal gets developed internally as well as on the surface.

The sensitivity of the emulsion can be further increased by pre-exposing and/or post-exposing the emulsion. A detailed discussion of the various methods can be found in an article by Bjelkhagen (1984a). However, most of these methods are not practical for the bubble chamber applications where a large number holograms is produced. Increasing the sensitivity of the emulsion would be desirable in order to relax the input energy requirements further.

Period I ; ~ 90,000 holograms produced.								
roll	L_p (μs)	E_p (mJ)	d_p (cm)	R_{hol} (cm)	θ_{imax}°	alignment	trigger	Δt (ms)
2228-2278	40	600	2.5	410	20.3	centered	fixed	2
comment: second amplifier rod was damaged roll 2243.								
2279-2280	40	600	2.5	410	20.3	misaligned	fixed	2
2281-2288	40	260	1.9	410	17.3	misaligned	fixed	2
2289-2293	40	600	2.5	410	20.3	misaligned	fixed	2
2294-2304	40	600	2.5	410	20.3	off-center	fixed	2
comment: the beam illuminated the lower half of the cone.								
2305-2307	40	600	2.5	410	20.3	centered	fixed	2
2308-2316	40	600	2.5	410	20.3	centered	event	
2317-2322	40	260	1.9	410	17.3	centered	event	
Period II, ~ 10,000 holograms were produced.								
2323-2328	18	150	1.3	420	15.9	off-center	fixed	2
2329-2329	18	150	1.3	420	15.9	off-center	event	
2330-2330	18	150	1.3	420	15.9	off-center	event	
comment: output telescope of the laser was damaged.								

Table 6.3 Holographic conditions during the E-632 physics run.

6.2 Replay Systems

Replay systems have been built at Fermilab, Rutherford Laboratory in England (HOLRED, "HOLographic REplay Device"), and the University of Hawaii. The first was a virtual image system and the last two were real image systems. Figures 6.9 - 6.10 show schematics for virtual and real image systems, respectively. A continuous-wave light beam generated at ruby wavelength by a dye laser, which was pumped by an argon-ion laser, was used for illuminating the hologram in all three systems. The aberrations are minimized if the same wavelength is used both for recording and replay. Here a summary of Fermilab and Hawaii replay systems is given. A more detailed description of the Hawaii replay system and of HOLRED are given by Nailor, (1984), and Peters and Cence, (1984).

At Fermilab a virtual-image replay system was used for inspection of hologram quality during the run. The light from the dye laser was transmitted through a single-mode optical fiber ($\phi_{core} = 4\ \mu m$). The output end of this fiber was positioned at a distance from the hologram corresponding to the reference point source position during recording (28.3 cm) as imaged by the fisheye windows. The light diverged from the fiber illuminated the hologram which was held flat on its mount by a vacuum. The hologram and fiber end could be rotated around vertical and horizontal axes through the plane of the hologram. By this arrangement, different areas of the bubble chamber volume were studied by means of a telephoto lens and a TV camera effectively looking through the reconstructed holographic image of the fisheye windows and bubble chamber liquid. By moving the TV camera along the Z-direction it was possible to focus at different depths in the chamber. An ordinary 35 mm camera was used for taking conventional pictures of the holographic image.

At Hawaii a holographic measuring machine using the real image and a "time-reversed" reference beam was built. A single-mode optical fiber transmitted the light from a dye laser to a stage where a converging beam was produced to illuminate the hologram. This stage was composed of two back-to-back microscope objectives to approximate a spatially uniform beam with desired diameter. The diverging beam, from the point focus of the last microscope objective, was then converged using a pair of achromatic lenses to a point at a distance corresponding to recorded point source (410 cm and 420 cm for Periods I and II, respectively). These lenses also compensated for the aberrations due to the fisheye windows in the reference beam. A second optical doublet was rigidly mounted in front of the hologram. This doublet was designed to duplicate the effects of the fisheye windows, including the change of the index of refraction from liquid to air, on the reconstructed image.

The assembly of light source, lenses, and the hologram could be rotated around two orthogonal axes intersecting at the center of the hologram. Motion in the third direction, along the line from the hologram to the point source at the bottom of the chamber, was accomplished by moving two 45-degree mirrors on a linear stage, thus changing the length of the optical path to the vidicon. An on-line computer moved the film and adjusted the path length based upon the premeasured coordinates of the vertex to find holographed event images. The operator then took control of the three axes to make detailed measurements.

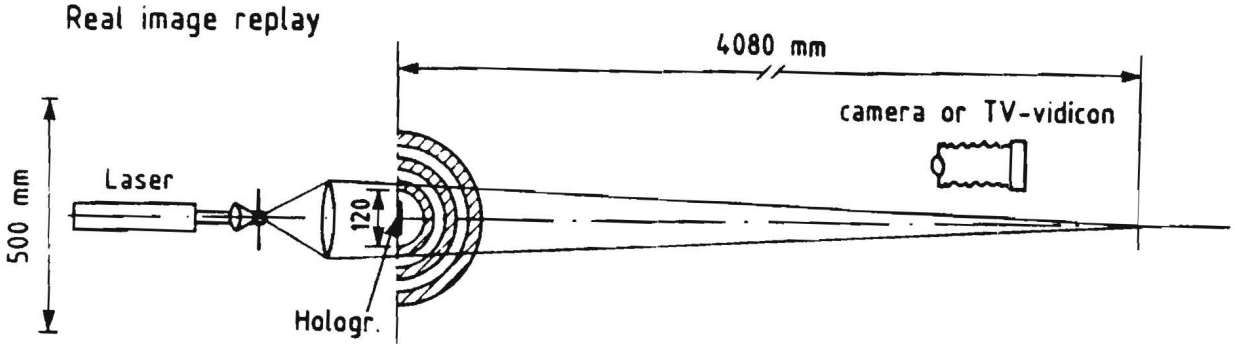

Fig. 6.9 Schematic for real image replay.

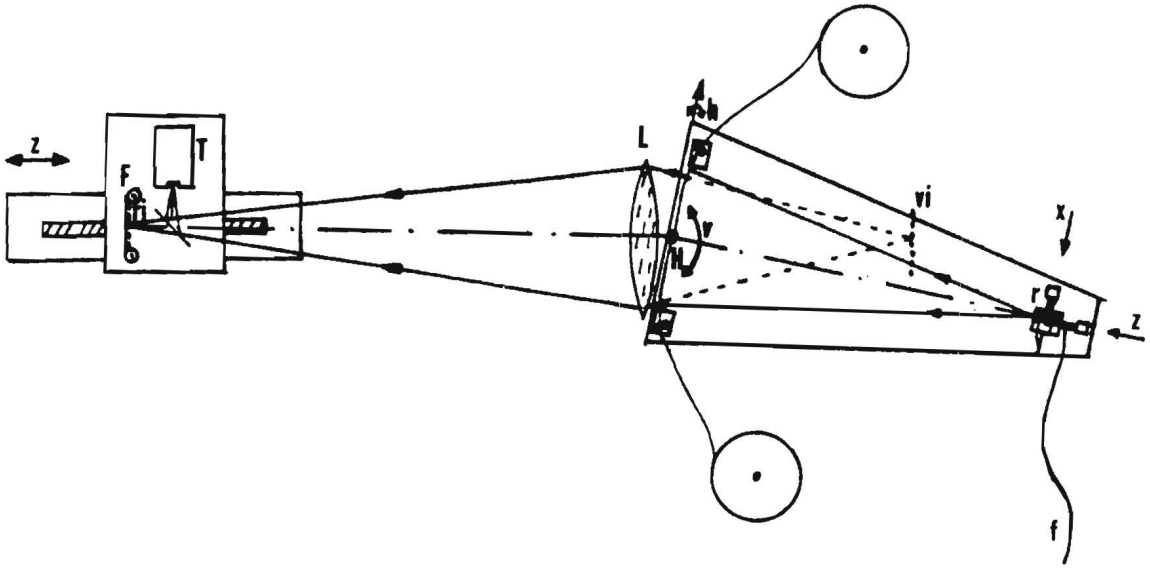

Fig. 6.10 Schematic for virtual image replay; f: single mode optical fiber, r: illuminating point source (output end of fiber), H: holographic film, L: imaging lens for creating a real image at F, F: photographic film to record the real image, and T: TV-camera.

6.3 Experimental Data from Test Holograms

Various tests in the laboratory, the empty bubble chamber, and the chamber filled with liquid were performed. This section collects the more important results obtained from these tests. Brief descriptions of the relevant laboratory setups and conditions are given. The results obtained from the holograms taken during the 1985 E-632 physics run are described in section 6.4.

Targets Used for the Laboratory and Warm Chamber Tests

The targets used for the laboratory and warm chamber tests were composed of standard resolution targets (the "1951 USAir Force resolution chart", Figure 2.7) placed 10 mm in front of a diffuse ground glass, and small diameter wires (20 μm diameter) on which 100-μm glass beads (n_g = 1.5) were glued individually or in clumps, (Figure 6.11). It can be seen from Figure 2.9 that the scattering functions are similar for bubbles in liquid Neon and glass beads in air at scattering angles of 20°, (Withrington, 1970). Thus 100-μm glass beads glued on thin wires are good approximation to the air bubbles in liquid Neon-Hydrogen when they are placed such that to scatter light at angles of 20°.

6.3.1 Resolution

It has already been noted, (Section 2.1.4), that the theoretical diffraction-limited resolution of the dark-field method is 39 μm at a distance 2 m from the hologram and with a film of size 60 mm. This resolution corresponds to 20 μm using the bubble chamber definition of the resolution, (cf. Section 2.1.4). It has been mentioned that the resolution of a system is also dependent upon other factors including the aberrations introduced by

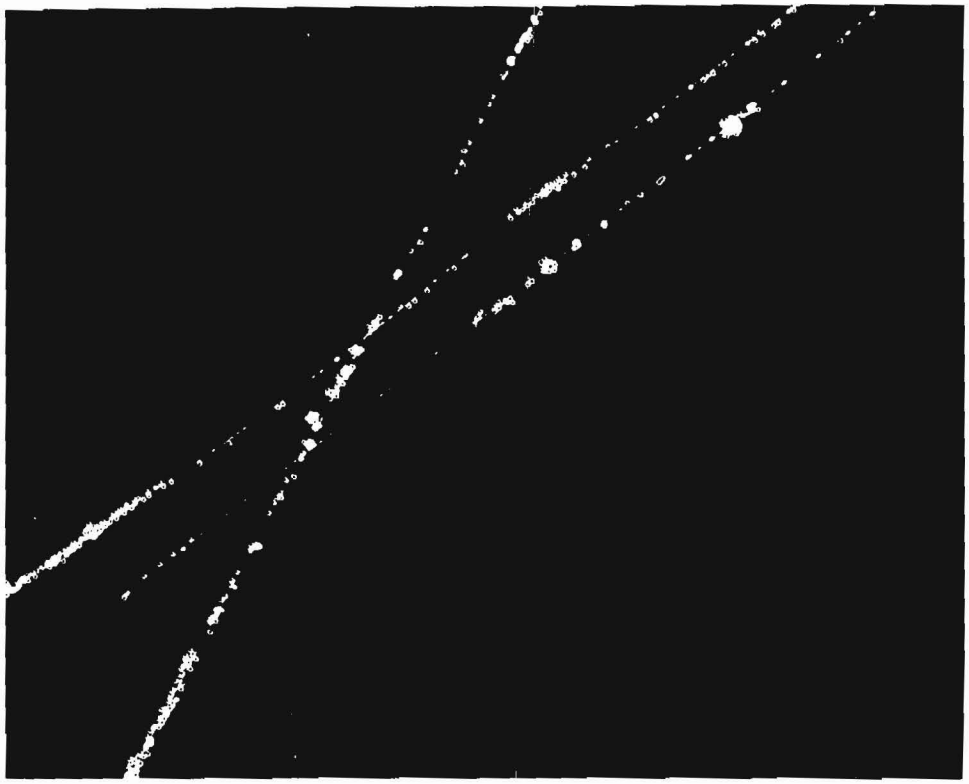

Fig. 6.11 Contact print of the 100-μm glass beads glued on 20-μm wires.

the optics and the processing procedure. A laboratory test was performed by Bjelkhagen (1984c) to investigate the effects of both factors on the resolution of the dark-field scheme. Here a summary of the results is given.

Three holographic setups were arranged, (Figure 6.12). In the first setup an output beam of a Helium-Neon laser (Spectra Physics 125, λ = 633 nm, 50 mW) diverged by a spatial filter (10 X objective lens and 25 μm diameter pinhole) comprised both the reference and object beams. The spatial filter was placed at 3.7 m from the hologram. The reference beam was taken from one edge of the illuminating Gaussian beam where the intensity was low compared to the central region of the beam, (loc. cit.).

The object (a typical target as explained above) was placed at 2 m from the hologram and the object beam made an angle of 6° with the reference beam. A K-value (cf. Equation [2.1.6]) of about 10 - 20 was measured in most of the experiments. In the second setup the spatial filter was replaced by the one-element dispersing lens; in the third setup a set of fisheye windows was placed in front of the hologram. Two different holographic materials were used: 10E75 plates and films, and 8E75HD plates. Two processing procedures were used: a) Kodak D-19 developer and Kodak Rapid Fixer without hardener, b) Kodak D-19 developer and Phenosaphranin ($C_{18}H_{15}ClN_4$) desensitizer replacing the fixing step, (loc. cit.).

A replay system in principle similar to the Fermilab replay facilities was used to reconstruct the holograms in virtual image. Figure 6.13 gives the resolution obtained in different holograms made with different experimental setups, different holographic materials, and different processing procedures, (loc. cit.). The best resolution (70 μm) was achieved with the

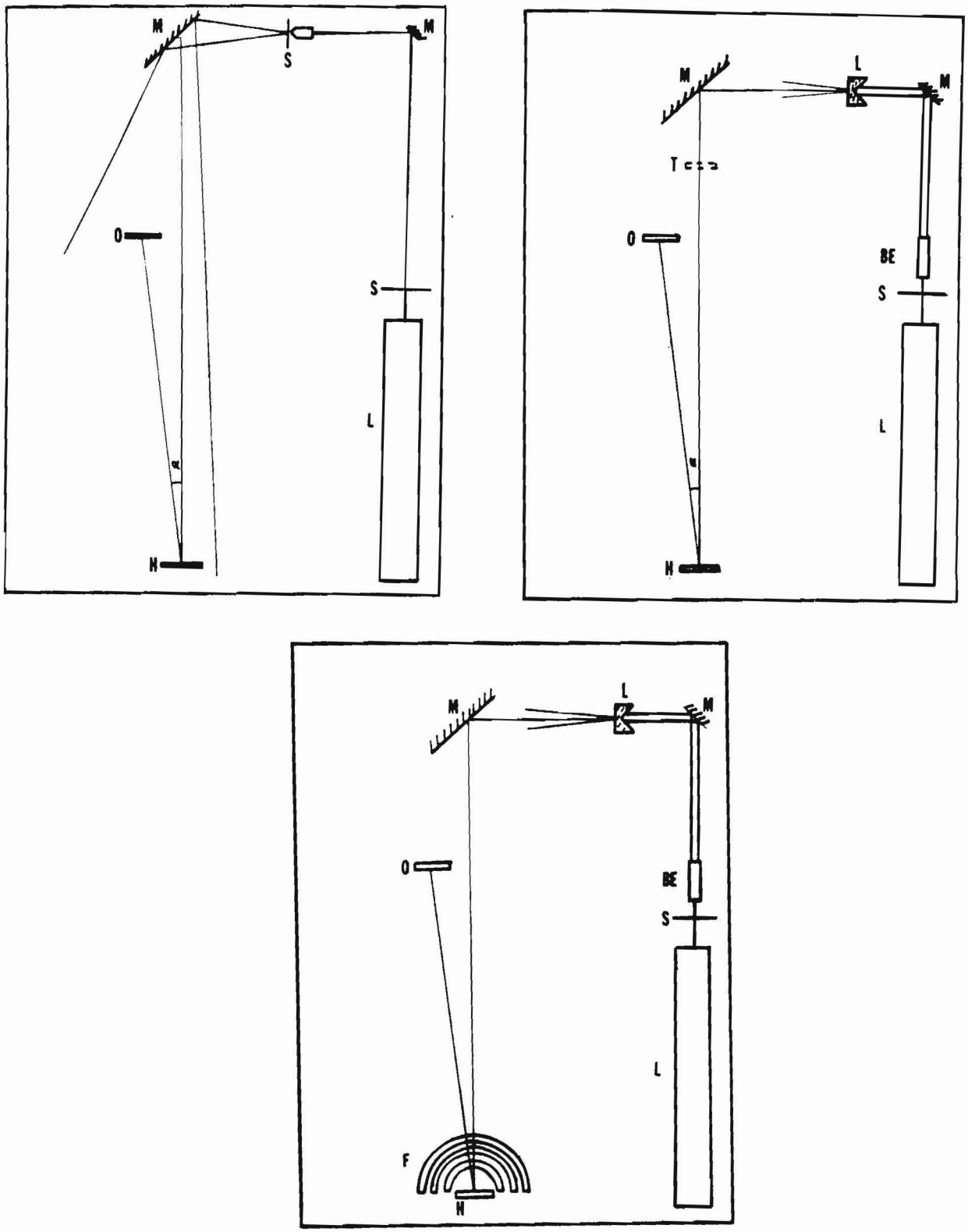

Fig. 6.12 Holographic arrangements used for the laboratory tests: (a) with spatial filter, (b) with one-element lens, (c) with one-element lens and fisheye. L: laser, S: shutter, BE: beam expander, M: mirror, SP: spatial filter L: one-element lens, T: position for glass plates, simulating turbulence, O: test object, H: holographic plate, distance (H - L): 3.65 m, distance (H - O): 2 m, illumination angle: 6.9°, (Bjelkhagen, 1984c).

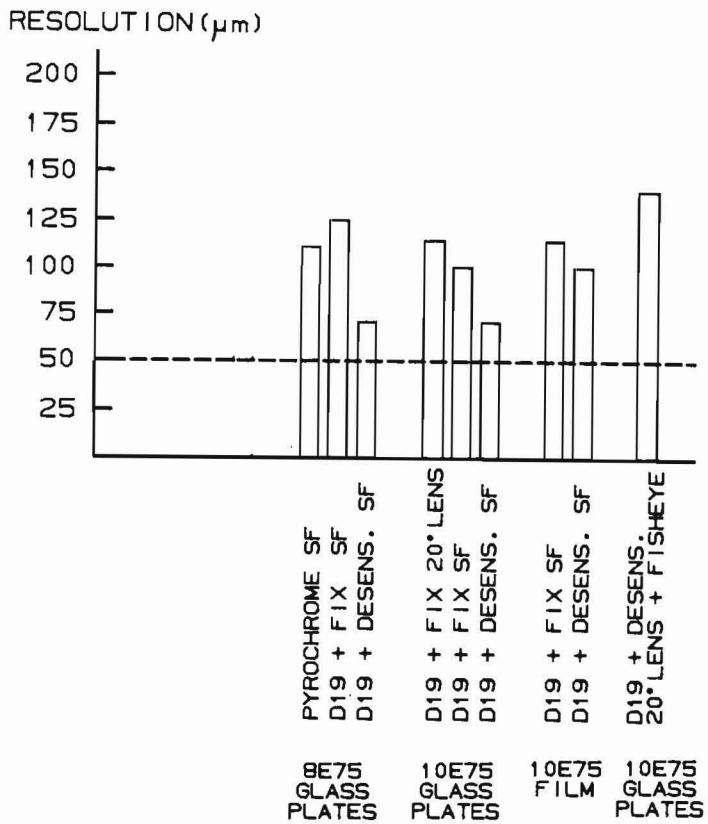

Fig. 6.13 Resolution obtained for various imaging procedures. The resolution target was viewed by a telescope in white and helium-neon laser light. The influence on resolution of the holographic image of test target due to different holographic materials, different processing techniques and different recording arrangements is shown, SF: spatial filter. (Bjelkhagen, 1984c).

first setup when using D-19 and desensitizing the holographic plate for both 10E75 and 8E75HD materials. The holograms developed with D-19 and fixed had a resolution of 100 μm. Using the dispersing lens instead of the spatial filter resulted in a small degradation of the resolution. However, placing the fisheye windows in front of the hologram resulted in worst resolution (140 μm) even when the hologram was desensitized. This may be attributed to the failure to use fisheye optics in reconstructing the hologram and the results will not be discussed further. Using 10E75 film rather than the plate degraded the resolution only by a small amount of 10 μm, (loc. cit.).

The above results show that the resolution obtained in the hologram is mostly sensitive both to the processing procedure and to the optical arrangements.

A more realistic study of the optimum resolution obtainable in the bubble chamber was a test in the warm, empty chamber. All the components of the experimental arrangement were the same as for the physics run except that the chamber was not filled with liquid. The target was placed near the holographic axis at 2 m from the holographic film. The best resolution obtained from these tests was 110 μm on a film processed with D-19 + phenidone and fixed.

6.3.2 Scotchlite Reflections

The object light emerging from the dispersing lens illuminated a large portion of the Scotchlite lining the bubble chamber. The Scotchlite retrodirected the light which was reflected again. This multiple-reflection of the illuminating light produced a source of diffuse background light coherent

and/or non-coherent with the reference beam. This light fogged the holographic film, reduced the signal to noise ratio, and the contrast of the image. As a consequence it became difficult to extract weak signals. There was also stray high-intensity light from the shining upper layer of Scotchlite, a mylar layer, which exposed the film and reduced the resolution of the image. Such effects were observed in the warm bubble chamber test where the resolution of a test target was measured as a function of the input beam diameter which resulted in variation of the illuminated Scotchlite area in the bubble chamber. The holograms were replayed (by J. Corrigan and the author) in a real image reconstruction using HOLRED. The results are given in Table 6.4. A resolution of ~ 120 μm was obtained for an input beam diameter d_p = 2.5 cm, and maximum angle of illumination θ_{imax} = 20 ° as compared to a resolution of ~ 210 μm for d_p = 4.4 cm and θ_{imax} = 26.5 °.

d_p (cm)	θ_{imax} °	$R_{vertical}$ (μm)	$R_{horizontal}$ (μm)
2.5	20.3	125	112
3.2	22.4	125	125
3.8	24.6	140	140
4.4	26.5	223	198

- Table 6.4 -

The reason that the vertical resolutions are not as good as the horizontal resolutions was due to optical alignment of the replay system.

6.3.3 Microboiling

An early test in the 1985 E-632 physics run showed that even though prolonging the laser pulse solved the boiling problem in the conventional pictures, it still gave rise to a small amount of "microboiling" near the laser window which partially destroyed the reference beam, giving "fuzzy" holograms. This microboiling in the reference beam path acts as would a ground glass and results in a diffuse reference beam. This effect was similar to that caused by the accumulation of dust or solidification of air on the cold laser window.

The microboiling was a dynamic process and did not always affect the holographic quality to the same degree and it was possible to obtain some good holograms even with sub-microsecond pulses. But the percentage of good holograms was low. A qualitative analysis of a sample of holograms taken on two different days with light pulses of variable duration but fixed total energy of about 600 mJ gave the following results; the holographic quality of the images was good for pulses of duration less than 200 ns, bad for submicroseconds pulses, average for pulses of duration 10 - 30 μs, good for 35 - 50-μs pulses, and bad for pulses of duration greater than 50 μs.

A reasonable explanation of the above observations is that for very short pulses, ($L_p < 0.9$ μs), the exposure was too fast to be affected by the microboiling. The exposure was most sensitive to microboiling effects for submicroseconds pulses where the peak power was sufficient to initiate the laser-induced boiling and the duration was long enough to spoil the reference beam during part of the exposure. For longer pulses, (10 - 50 μs), the microboiling was almost suppressed by the low power, and thus good quality images were obtained. However, for these long pulses the bubble growth

and/or movement also serves to degrade the visibility of the bubbles. Furthermore, for long exposures the reference beam wavefront was probably distorted by temperature (refractive index) variations and by the local turbulence of the liquid throughout the whole volume of the chamber. It can be seen that these effects would become increasingly pronounced for pulses with duration greater than 50 μs.

6.3.4 Turbulence

The effect of turbulence in the liquid is a rather difficult problem to formulate. There is evidence that small amounts of turbulence in both reference and object beam paths degrade the quality of the image. The effects of turbulence on holograms have been observed in small bubble chamber holography (Hervé et al., 1982). It has been concluded that the turbulence created along the object beam path was mainly responsible, (Benichou et al., 1985).

It was shown by Bjelkhagen (1984c) that a simulated turbulence using an uneven glass plate after the formation of the reference beam point source gives a distorted reference field which results in loss of the resolution when the hologram is reconstructed with an <u>undistorted</u> illuminating beam.

In the 15-foot Bubble Chamber no systematic test could be performed to study the effects of turbulence. In the non-expanding chamber, an investigation was made of a sample of sixty holograms. This showed that nine percent of the holograms had a speckle pattern with a structure which was of the sort expected from turbulence. Figure 6.14 shows the speckle pattern of one such hologram. These holograms had poor images of the diverging lens at the bottom of the bubble chamber. The recirculating pump operating during this test was a likely cause of this turbulence.

Another qualitative measure of the quality of reference beam can be obtained from observing the diffraction pattern of two parallel wires with sizes of 300 and 500 μm strung across the bubble chamber. The two wires were in the path of the reference beam in the bubble chamber. Figure 6.15 shows this diffraction pattern for a hologram made in the empty chamber and for a hologram made in the typical conditions of the expanding bubble chamber. It can be seen that in the first hologram 12 orders of diffraction fringes are visible while in the second one only 4 orders can be seen. This deterioration in the diffraction pattern of the hologram is most likely the result of the non-homogeneity in the path of reference beam created by the liquid.

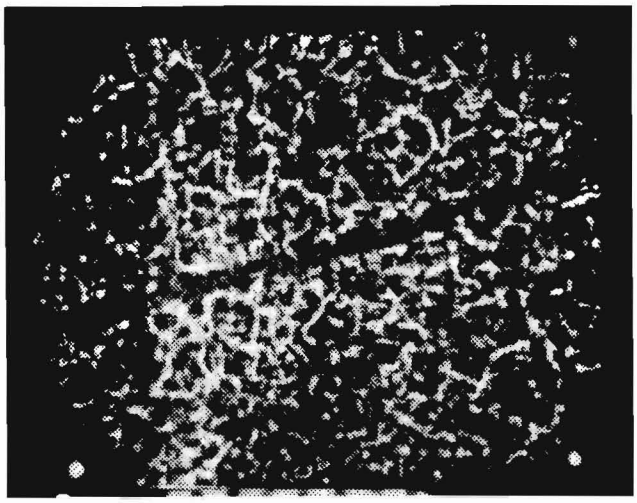

Fig. 6.14 A typical speckle pattern resulted from turbulence in the bubble chamber filled with neon-hydrogen liquid.

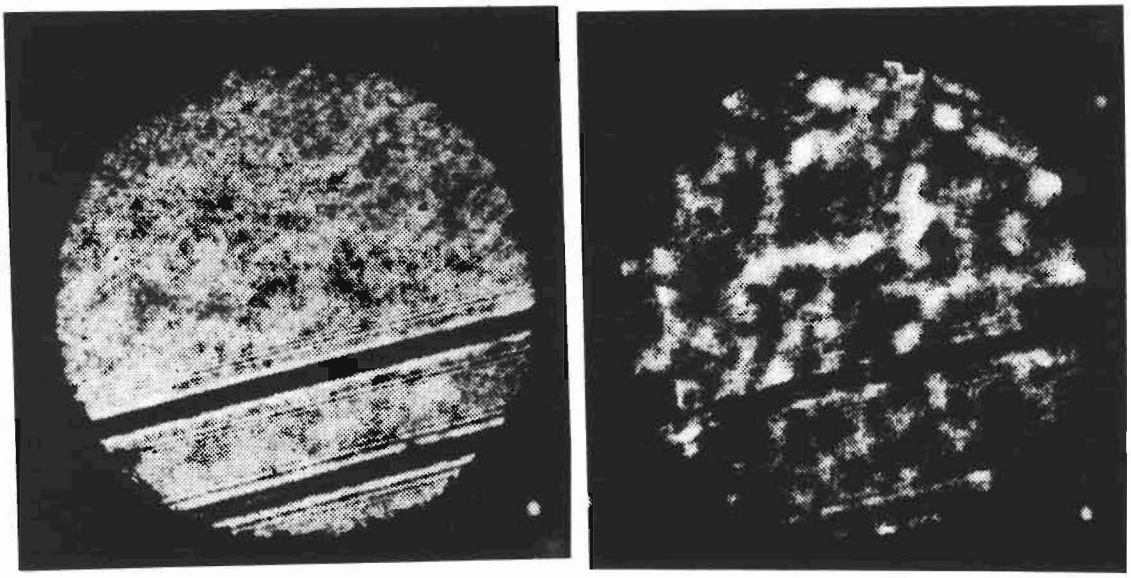

(a) (b)

Fig. 6.15 Typical speckle and diffraction patterns of wire passing the reference beam: (a) in the empty chamber, (b) in the bubble chamber filled with Neon-Hydrogen liquid.

6.4 Experimental Data from Holograms

6.4.1 The Experimental Data

Experimental Sample

The experimental data may be divided into three samples: neutrino events, cosmic ray tracks, and beam tracks (mainly through-going muons). Table 6.5 gives the holographic conditions for all the rolls in which these tracks were studied. This table specifies the same parameters as Table 6.3, and gives the sample and number of tracks studied for each roll. All the holograms studied were of amplitude type except for frames 1238 - 1268 in roll 2241, and frame 623 in roll 2243, which were phase holograms. Cosmic ray and beam tracks had to be used to obtain sufficient statistics for a detailed analysis of the holographable volume of the chamber. Section 6.4.5 discusses the efficiency and quality of the holographic events found. The holograms of cosmic ray and beam tracks used in the analysis were reconstructed using the Hawaii replay facility, and the holographic neutrino events were reconstructed using the Fermilab, Hawaii, and HOLRED replay facilities.[37]

Cosmic ray tracks were found by scanning the real image of the hologram. Beam tracks were first detected by scanning the conventional photographs, and their entrance and leaving points at the bubble chamber wall were digitized by the usual bubble chamber methods. Using these two points the point of closest approach to the holographic optical axis was calculated and this was used in locating the beam track in the holograms in a real image reconstruction. Once a track was located in the hologram, it

---

37. R. Burnstein, and R. Neon are acknowledged for providing the statistics from Fermilab replay facilities; J. Corrigan, R. Sekulin, and S. Sewell for providing the statistics from HOLRED.

was followed until its apparent end points (where it faded out) were found. The coordinates of these apparent end points were recorded and were characterized as to whether the track faded gradually or stopped abruptly. The quantitative validity of this somewhat subjective determination was tested by studying the shift in the coordinates of the end points when either the illuminating light of the replay system was increased or when it happened that the hologram was bleached. Both methods would be expected to increase the detectability of a weak image signal. However, no significant changes in the coordinates of the end points were observed using either method.

Roll	Frame	# of Tracks	L_P (μs)	E_P (mJ)	d_p (cm)	R_{hol} (cm)	θ_{imax} °	alignment	Δt (ms)	Sample
2241	1160-1200	14	40	600	2.5	410	20.3	centered	2	cosmic
2241	1209-1216	8	0.1	600	2.5	410	20.3	centered	2	cosmic
2241	1238-1268	61	10	600	2.5	410	20.3	centered	2	cosmic
2243	623	6	0.1	600	2.5	410	20.3	centered	2	cosmic
2273	1- 230	40	40	600	2.5	410	20.3	centered	2	beam
2309	2073	5	0.1	600	1.9	410	17.3	centered	2	cosmic
2323	2509-2516	10	18	150	1.3	420	15.9	offcenter	2	cosmic
2323	2536-2548	12	0.1	150	1.3	420	15.9	offcenter	2	cosmic
2323	1- 191	17	18	150	1.3	420	15.9	offcenter	2	cosmic

- Table 6.5 -

Bubble Diameter Measurements

Two methods were used to measure the apparent diameter of the replayed images of the bubbles. One was to project the bubble images on a

vidicon and to measure the apparent diameter of the bubble with a caliper. The other was to scan the bubble profile using an array of photodiodes or a TV camera in combination with an oscilloscope. In both methods it was difficult to determine the absolute diameter of the bubbles because they are surrounded during the growth process (expansion) with a cold layer of liquid and during the recondensation (recompression) with a warm layer of liquid of changing thickness and varying refractive index. Furthermore, the image size depends on the exposure, development of the film, and the intensity of the replay light. The last of these effects can be normalized when using an electronic instrument to project the bubble profile. In this case the replay light intensity can be adjusted for each bubble so that the peaks of the signal from the bubble image are normalized to the same level. Measuring this projection of the bubble image profile was also less sensitive to the diffraction effects of the liquid layers surrounding the bubble. In this method a sharp signal representing the bubble profile could be obtained and its diameter measured in terms of its full width at half maximum (fwhm) above the background noise.

A more serious problem with the bubble size measurements was the effective light scattered by the bubble. The whole area of a "back-lighted" bubble was not illuminated uniformly and the bubble images were not uniform circles. They were collections of small speckles with different brightness. When a bubble size was greater than several tens of micrometer its image was composed of a bright spot surrounded by a bright ring. The bright spots in the bubble images were not always centered. For a holographic system, the speckles of the bubble images were further dispersed (thus resulting in a larger effective bubble diameter) due to imperfections in

the reconstruction of the hologram. The existence of optical aberrations such as coma and astigmatism made it even more difficult to determine the "real" bubble size.

At Hawaii the effective bubble diameter was measured using a 2445 Tektronix oscilloscope which can be operated in the same horizontal scanning mode as standard TV cameras. The oscilloscope can be triggered by any of the horizontal lines of each field of the vidicon. The scanning line was positioned at about line # 150 of the vidicon's "field one" which corresponded to a reference point on the TV screen where the bubble was positioned. An intensity distribution across the bubble was displayed at the oscilloscope screen, (Figure 6.16). Based on the image of the bubble on the vidicon, it was decided whether the intensity distribution was depicting a single bubble with speckles or two adjacent bubbles. The structure in Figure 6.16 indicates that the bubble is composed of several speckles. If the intensity distribution of the bubble was saturated the argon replay laser intensity was adjusted until a Gaussian curve was obtained. The horizontal line was then scanned about lines adjacent to # 150 in order to find the maximum peak which depicted the center of the bubble. The full width at half maximum of the curve at this point gave the diameter of the holographic image, as replayed and recorded by the vidicon, was defined as the "effective bubble diameter." The conversion factor for the horizontal scale was 221 μm/μs with a resolution of $\pm$ 22 μm.

To determine the bubble diameter in a track 3 - 5 bubbles were measured on each track and the average value was used. The variations in the bubble size along one track were due to the range of the scattering angles for the bubbles and to the aberrations which depend on the bubbles

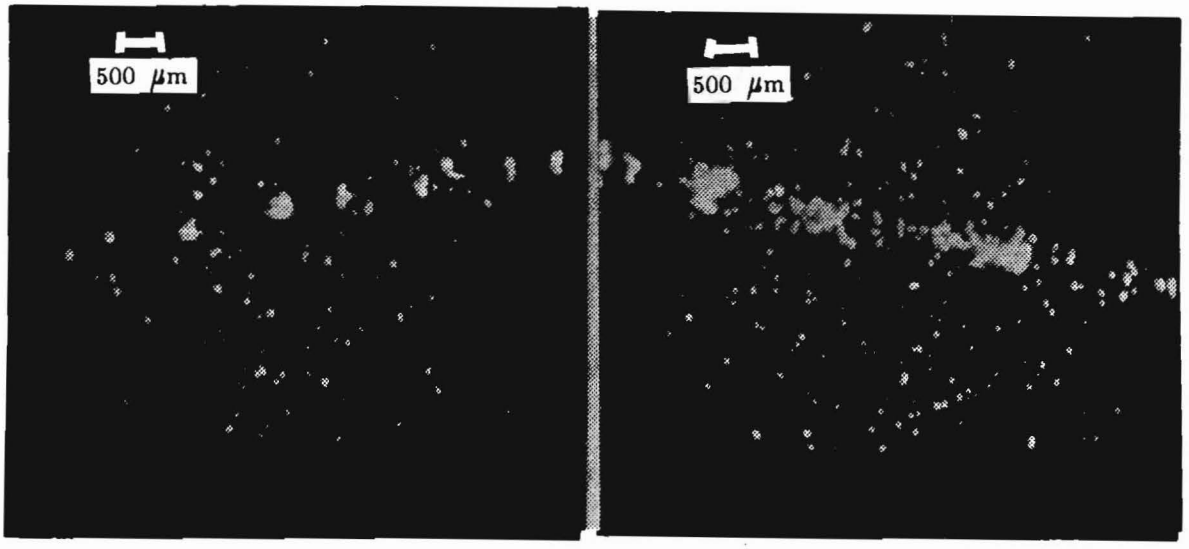

(a)

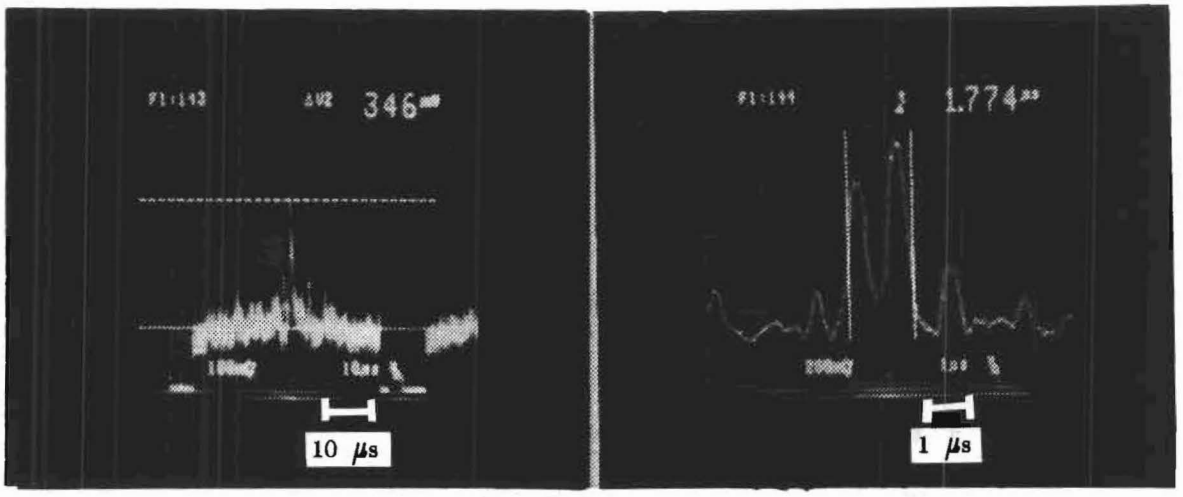

(b)

Fig. 6.16 (a) Examples of holographic bubble images recorded in 15-foot bubble chamber, (b) profile of a typical bubble image.

spatial coordinates. The fluctuations in bubble size measurements were determined by summing the fluctuations in quadrature for all the measurements. This uncertainty was calculated to be ± 170 μm which is rather large compared to the average 500 μm bubble diameter.

The average effective bubble diameter for the different data samples is calculated and listed below. The smallest bubble diameter was found to be 150 μm.

<u>Average effective bubble diameter (μm) from hologram images</u>

	$\bar{D} \pm \sigma_D \pm \delta_D$
Beam Tracks	: 500 ± 170 ± 170[38]
Cosmic Ray Tracks	: 540 ± 250 ± 170
All Data	: 520 ± 210 ± 170

<u>Average bubble diameter (μm) from high resolution photographs</u>

	$\bar{D} \pm \sigma_D$
Beam Tracks	: 380 ± 70

The cosmic ray tracks passing through the bubble chamber at random times can initiate boiling at the time the liquid is sensitized and thus will result in a wide range of bubble diameters at the time of hologram exposure. On the other hand, the beam tracks which are injected at a specific time over 2 ms range result in a narrow range of bubble diameters. The large values obtained for the bubble diameter of beam tracks is because the roll 2273, available for study, was taken at the time the bubble chamber was operated to give bubbles of the order of 500 μm after 1 ms. The laser beam was injected 2 ms after the beginning of the beam spill for this roll.

---

38. The first variations are the standard deviations of bubble diameters, and the second variations are the measuring errors.

An average bubble diameter of 380 ± 70 μm has been measured for a sample of 15 beam tracks using the high resolution photographs (roll 2273), and using the first method (using a caliper) for bubble size determination. This measurement agrees with the value 370 ± 70 μm obtained for roll 2230 (cf. Section 5.4). In both rolls the high resolution film was exposed about 1 ms after the beginning of the beam spill. Thus values of 500 μm for bubble sizes in holograms are not surprising since the holograms were exposed 1 ms after the high resolution photographs.

Why Cosmic Ray Tracks

The main concern of this analysis was to investigate i) the smallest detectable signal, ii) the resolution achieved, and iii) the experimentally visible holographic volume. A measurement of the end points and the bubble sizes of the tracks provide sufficient information for this analysis. The incentive to use beam tracks rather than cosmic ray tracks would be to study tracks with small bubble diameters and known time of occurrence, as provided by the EMI. Figure 6.17 shows that the effective average bubble diameter for beam tracks (500 ± 340 μm) was negligibly smaller than that of cosmic ray tracks (541 ± 420 μm). Figure 6.18 shows the distribution of bubble diameter (measured in holograms for the beam tracks) versus the time of occurrence of the tracks. No clear correlation can be established between the two parameters. However, with the large uncertainties in bubble sizes, the distribution is consistent with the expected curve as shown in the figure. The expected curve is obtained using an average bubble diameter of 500 μm for the time slot of 1600 μs. This allows a growth time of 1400 μs for these bubbles before the hologram is exposed. Using

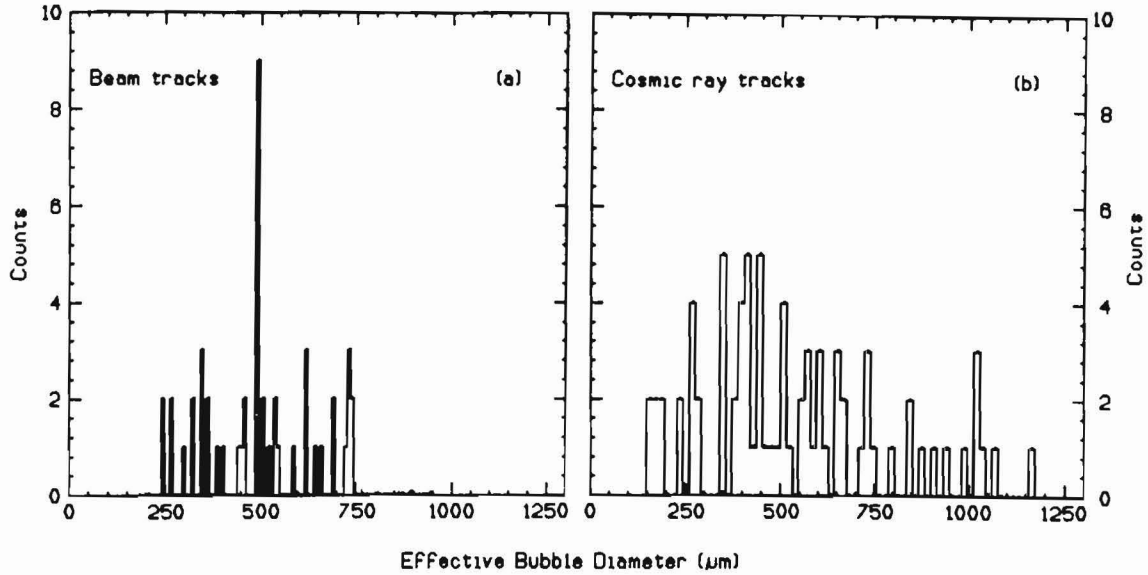

Fig. 6.17 Histograms of effective bubble diameters of (a) beam tracks, and (b) cosmic ray tracks measured in the holograms.

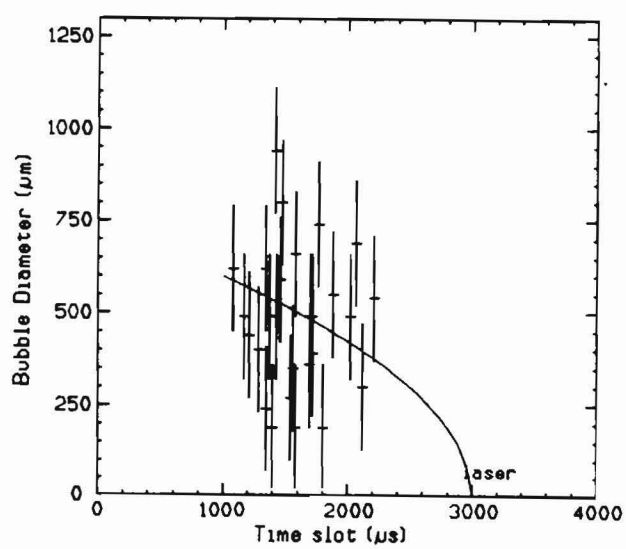

Fig. 6.18 Dependence of effective bubble diameter on "EMI-time slot" for beam tracks observed in the holograms. The laser was injected at time slot of 3000 μs.

Equation [2.2.11], a value for ´A´ can be obtained from which the remaining points on the curve can be calculated.

The cosmic-ray track data provide a sample of holograms exposed under different conditions. These holograms were analyzed to investigate the laser pulse-length dependencies of the hologram quality and the visible volume. They also gave a better understanding of the holographic fiducial volume since they are distributed more uniformly in the bubble chamber space than are the beam tracks. Most of the following analysis treats a track end-point as a single event independent from the other end point of the track. These points delimit the holographable volume defined by the region in which tracks of average timing are visible.

The Holographic Parameters

A complete definition of the holographic parameters was given in Section 2.2.2. Here a summary is given. Every point in bubble chamber space, (x, y, z), can be characterized by a set of holographic parameters,

θ_i : the illumination angle,

α : the scattering angle,

θ_{hol} : the holographic angle,

R_{hol} : the distance along the holographic axis from the camera,

R_{nor} : the normal distance from the point to the holographic optical axis,

d_l : the distance from the dispersing lens to the event,

d_f : the distance from the event to the holographic film,

BBR : the ratio of the object to reference beam intensities.

In order to determine the holographic characteristics of a single event (as stated, an end point of a track is called an "event") it is necessary to

establish its θ_i and R_{hol}. This information is sufficient to specify as independent variables the position of the event relative to the dispersing lens, the holographic camera, and the holographic axis. For example, a large θ_i and small R_{hol} mean that the event is not in a favorable position. This is because i) it is illuminated by large angle rays at a large distance from the dispersing lens, and thus the light intensity has fallen off by the square of the distance; ii) the event has a large angle of scattering, α, and thus the scattering function, $G(\alpha)$, is small; iii) the event is at a large distance from the holographic optical axis, and thus the adverse influence of bubble growth and movement are of larger importance.

6.4.2 Signal Detectability

The Beam Balance Ratio (BBR) of a bubble is a measure of the fringe modulation of the hologram and the detectability of that bubble, (i.e. the signal). The BBR which is calculated does not include any additional noise background from other sources, e.g. Scotchlite, to the signal. Furthermore, it does not include the effects of variations in the phase of the object beam due to growth or movement of the bubble which can reduce the fringe modulation of the hologram. Nevertheless, the BBR is a useful parameter to describe the light intensity distribution required to illuminate the bubbles sufficiently and thus to estimate the holographic fiducial volume. It is important to determine the limiting BBR, that corresponds to the smallest detectable signal. A bubble whose BBR is smaller than the limiting BBR cannot be detected.

For the end point of a track which has faded gradually a limiting BBR can be calculated. BBR is calculated by measuring the coordinates of the end points and the average effective bubble size of each track holographically. The techniques were described in Section 6.4.1. For every event the holographic parameters, θ_i, θ_{hol}, α, d_l, d_f, were then computed using the bubble chamber coordinates of each end point. The illuminating and scattering angles, θ_i and α, determined $F(\theta_i)$ and $G(\alpha)$, respectively. The light intensity distribution after the dispersing lens, $F(\theta_i)$, depends on the input laser beam profile (cf. Section 6.1.2). In this analysis a flat beam profile was assumed except in one case that is specified. Although the precise beam profile was not known, the flat beam profile is a useful first assumption for establishing the holographable regions.

The limiting BBR is calculated for three values of the reference beam intensity, since this intensity was not well known. The most probable value from the experimental observations (cf. Section 6.1.4) is about 1.0 $\mu J/cm^2$. The results are subdivided into four samples and are summarized in Table 6.6.

Data Sample (roll)	Average Limiting BBR $\pm \sigma_{BBR}$ ($\times 10^{-6}$)		
I_{ref} ($\mu J/cm^2$)	0.5	1.0	1.5
beam tracks 2273	0.50 ± 0.31	0.25 ± 0.31	0.17 ± 0.31
2241 - 2309	0.62 ± 0.41	0.31 ± 0.41	0.21 ± 0.41
2323	1.00 ± 0.36	0.50 ± 0.36	0.33 ± 0.36
All Data	0.74 ± 0.42	0.37 ± 0.42	0.25 ± 0.42

- Table 6.6 -

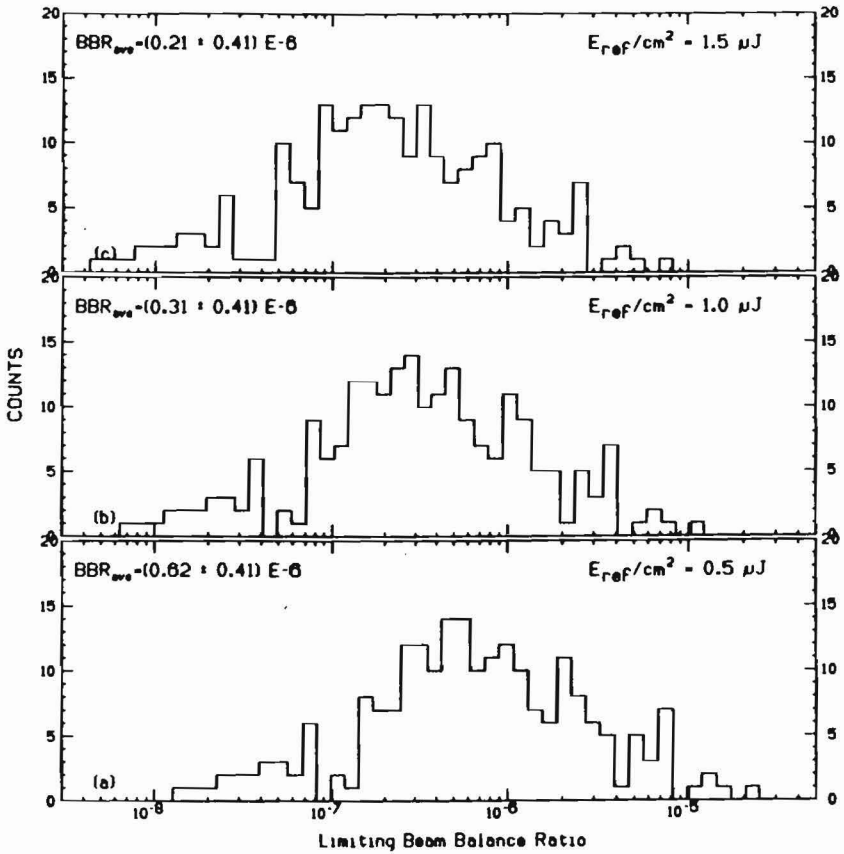

Fig. 6.19 Histograms of the limiting beam balance ratio using all data from period I for three values of reference beam energy.

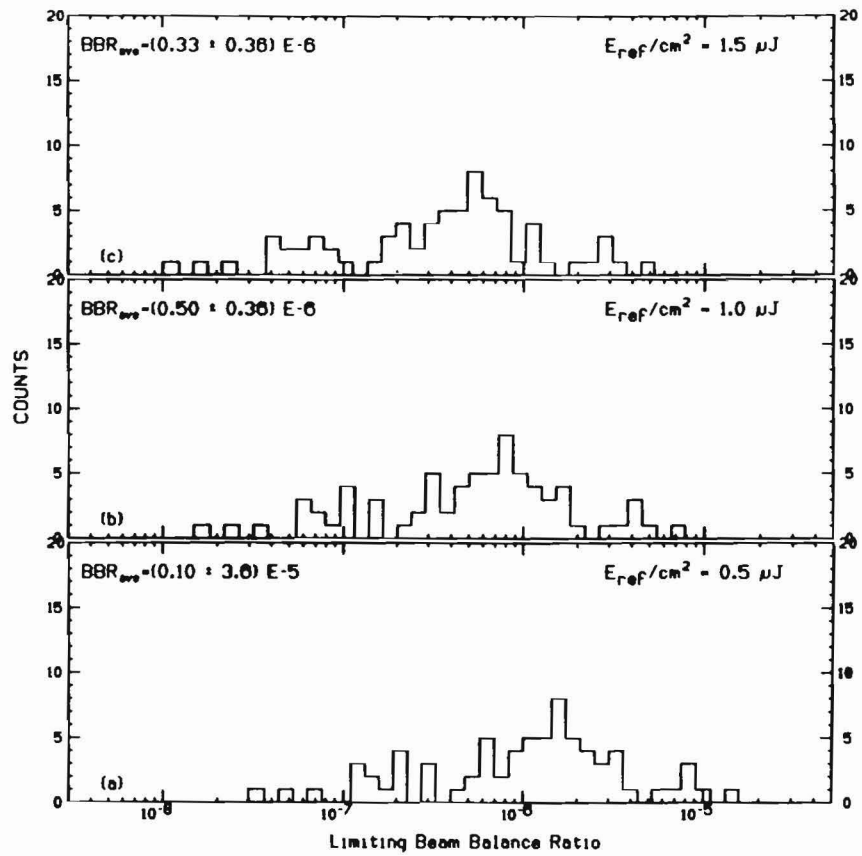

Fig. 6.20 Histograms of the limiting beam balance ratio using all data from period II for three values of reference beam energy.

Figures 6.19 - 6.20 show the histograms of the limiting BBR for all data from the two running periods. For a given set of data the histograms for different values of reference beam intensity are strictly similar except for a shift proportional to $1/I_{ref}$ along the axes. An increase in the reference beam intensity by a factor of two decreases the BBR by a factor of two. The slightly different structures of the histograms are a consequence of binning. For all the data a BBR value of $(0.37 \pm 0.42) \times 10^{-6}$ is obtained for $I_{ref} = 1.0\ \mu J/cm^2$. This value sets a lower limit on the detectable BBR value.

Theoretical determination of the locus of points with the smallest detectable BBR for a given effective bubble size specifies the theoretical volume in which bubbles of certain diameter can be detected, i.e. it gives the holographic fiducial volume for that bubble size. Figure 6.21 gives the theoretical holographic fiducial volume as a function of the limiting BBR value for bubbles of effective size of 100, 200, 300, and 500 μm. The volume is calculated throughout the fiducial volume of the conventional photography for cubes of size of 250 cm^3, and by specifying a range of limiting BBR for each of the bubble sizes. Two observations may be made: 1. the volume decreases drastically for the larger limiting BBR values; 2. the volume decreases rapidly for the smaller bubble sizes at larger limiting BBR values. For the average limiting BBR value obtained from the experimental data, $(0.37 \pm 0.42) \times 10^{-6}$, fiducial volumes of 0.21, 1.5, 3.4, and 4.5 m^3 are obtained for the above listed bubble sizes, respectively. It can be concluded from these results that a large fiducial volume is obtained for the holographic conditions that give small limiting BBR values.

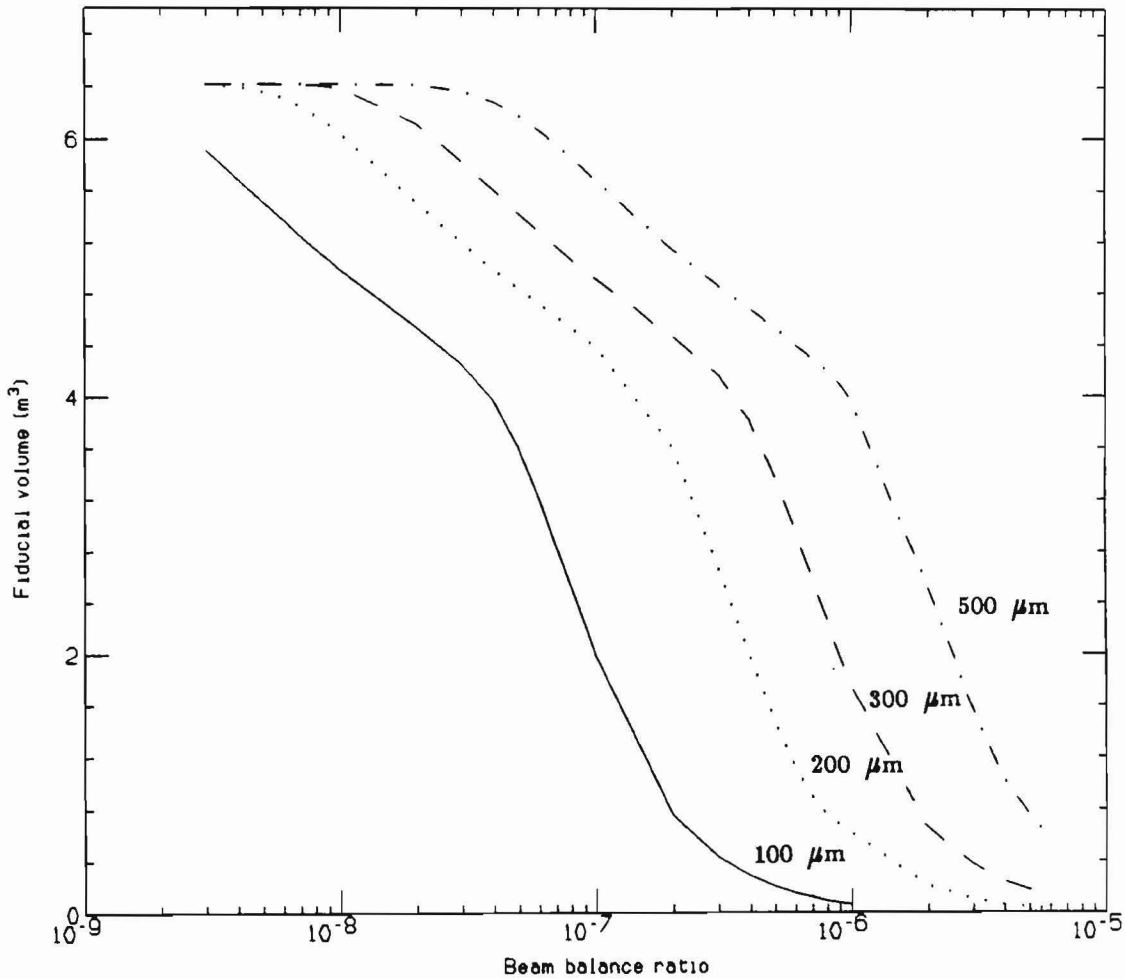

Fig. 6.21 The holographic volume as a function of beam balance ratio for 100, 200, 300, and 500-μm bubble diameters.

The definition of the limiting BBR implies the existence of a single, unique value below which no signal is detected. But the experimental data are spread over a large range of values. This contradiction raises questions about the BBR calculations. In addition to small uncertainties in determination of the track end point coordinates, there are three poorly known parameters in the BBR calculations: a) the laser beam profile, (i.e. $F(\theta_i)$), b) the scattering function, $G(\alpha)$, for coherent illumination of the 75/25 % Ne/H_2 mix, and c) the actual bubble diameter. The following discussion is intended to investigate the relation between these three parameters and BBR, and to deduce the possible causes of the dispersion in the limiting BBR values.

Various scatter plots of the limiting BBR versus the holographic parameters, and the bubble diameter will be used for this discussion. These distributions have been plotted for several data samples: beam tracks, beam and cosmic ray tracks together before the lens was moved, (period I), cosmic ray tracks after the lens was moved, (period II), various pulse lengths, and all data combined. As the same distribution is obtained for all cases, the sample of ´all data´ is used for the remainder of the discussion.

For comparison with theory, the BBR values are also calculated and plotted assuming a bubble of constant diameter 525 μm located uniformly throughout the volume of the bubble chamber in steps of 250 cm^3 cubes, (5 cm steps in x and y, and 10 cm steps in z). The boundaries for the bubble chamber fiducial volume in these calculations were chosen to be: $-195 < x < +195$ cm, $-195 < y < +195$ cm, $-100 < z < +100$ cm, and $\theta_i < 27°$ which is the maximum illumination angle.

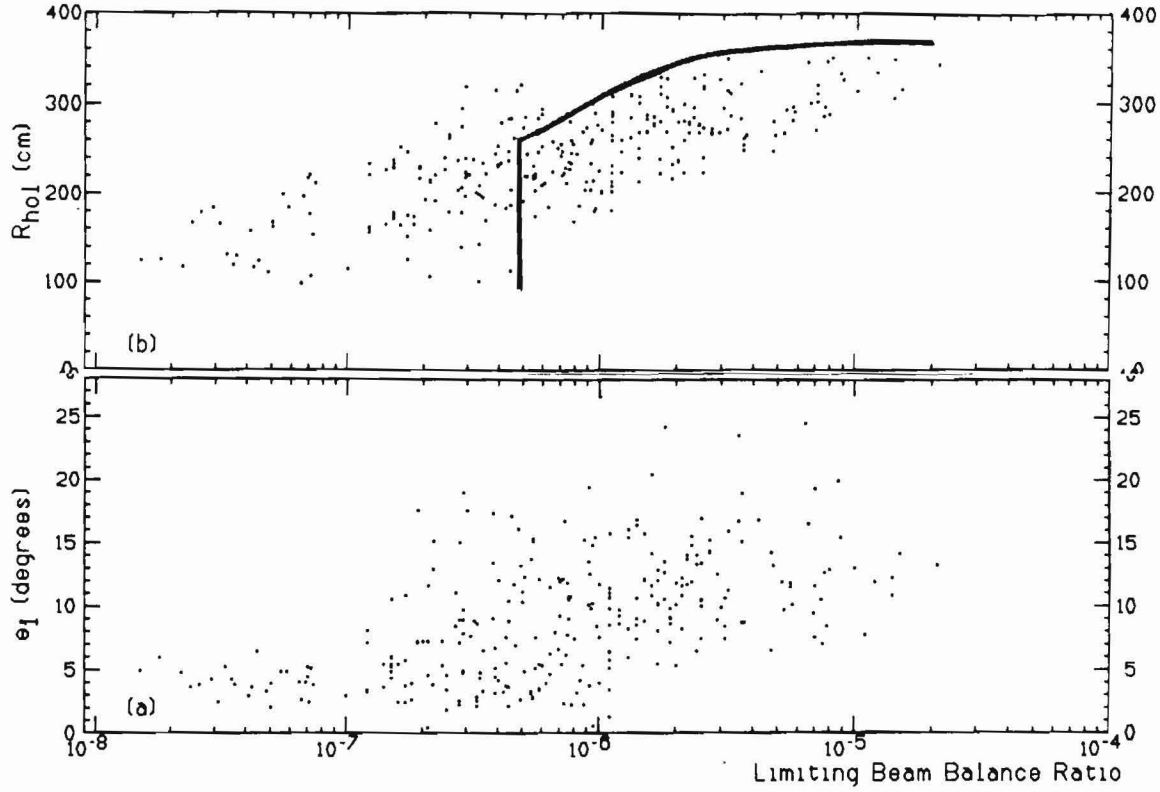

Fig. 6.22 Dependence of experimental limiting beam balance ratio on θ_i and R_{hol} for an input laser beam with flat spatial profile.

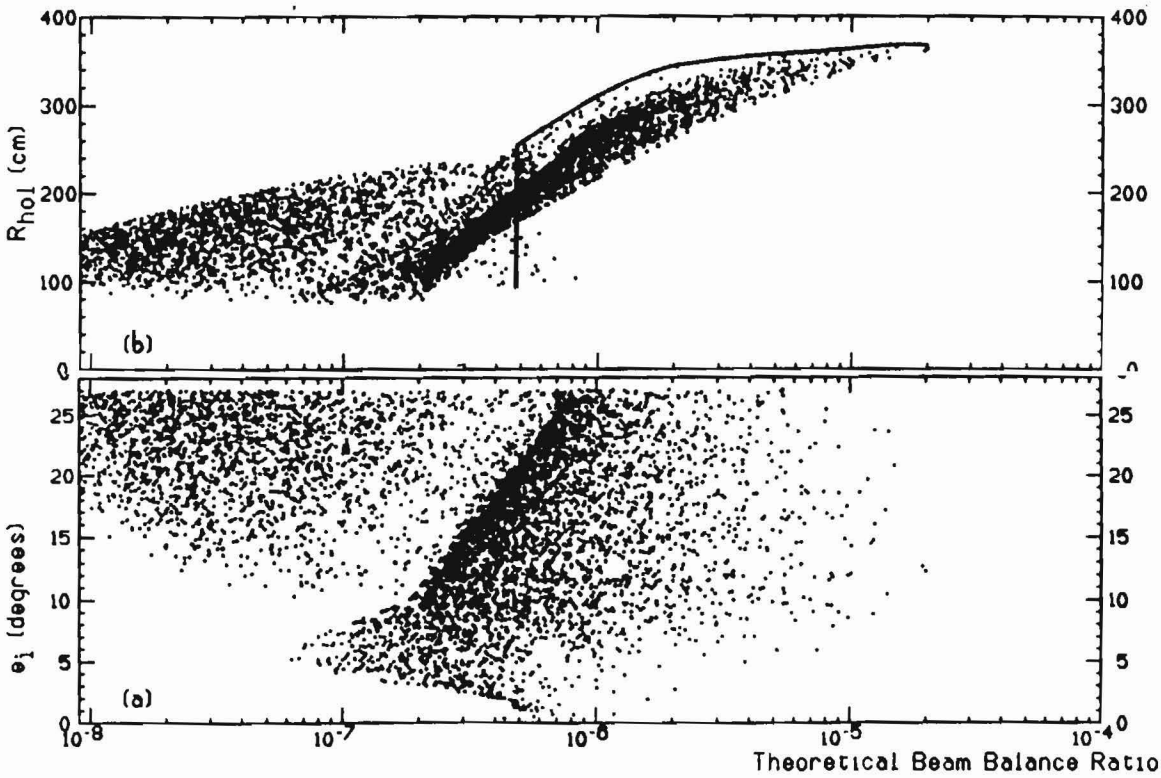

Fig. 6.23 Dependence of theoretical beam balance ratio on θ_i and R_{hol} for an input laser beam with flat spatial profile.

a) BBR as a Function of $F(\theta_i)$

Since there is no exact knowledge of the profile of the input beam onto the dispersing lens, the intensity distribution of light after the lens is not known either. To first approximation, it was assumed that the input beam has a flat profile.

To understand how $F(\theta_i)$ affects the BBR values, the latter are plotted versus θ_i and R_{hol} for both the experimental data and theoretical values, Figures 6.22 and 6.23, respectively. For experimental data, it is the limiting BBR which is plotted; for theoretical calculations all values of BBR are plotted. The distributions of the experimental BBR-θ_i and BBR-R_{hol} resemble that of the theoretical distributions, and have a definitive form which is of interest. Ideally, it is expected that the same limiting BBR value is obtained for the whole range of the illumination angles. The existence of a range of the limiting BBR values for every θ_i in Figure 6.22a can be explained by the uncertainty in the bubble diameter measurements (see below). However, the fact that smaller limiting BBR values are obtained for smaller illumination angles remains unexplained. For BBR-R_{hol} distribution, the situation is more complicated; a range of larger BBR values is obtained for larger R_{hol} (Figure 6.23a). For example, in the case that an average limiting BBR of 0.37×10^{-6} is obtained, it is expected that only larger values of limiting BBR are observed for $R_{hol} > 260$ cm. This limiting case is drawn by hand on Figure 6.23b, and is then superimposed on Figure 6.22b. The deviation of BBR-R_{hol} distribution from the expected curve in Figure 6.22b is also explained by the bubble diameter measurements (see below).

The reason that there are no data for $R_{hol} < 90$ cm in BBR - R_{hol} scatter plot is because the applied cut excludes points with $z > +110$. It should be noted that the theoretical scatter plots are shifted to right or left if the constant bubble diameter is set to larger or smaller values than 525 μm. For example, for a bubble diameter of size 225 μm the plot is shifted towards smaller BBR values by a factor of 4.5. This would account for the existence of experimental data in the range of 0.1E-7 < BBR < 0.8E-7.

To test whether the variation of BBR with θ_i and/or R_{hol} depends on the input beam profile, the data points are recalculated using a Gaussian input beam profile. The scatter plots are shown in Figure 6.24. The BBR values are shifted towards right (larger values), as expected (cf. Figure 6.5). But the plots have similar shapes as those with the flat beam profile. An attempt was made to obtain a light intensity distribution using the average limiting BBR value and recalculating the intensity. This attempt gave no conclusive results. This is most probably due to the fact that the data are collected from holograms exposed by different laser pulses of variable spatial profile. In Section 6.4.7, it is stated that small variations in temporal coherence and total energy of the laser has been observed from pulse to pulse. No statements can be made about local variations in spatial profile, and as a consequence about the energy distribution of the laser output from pulse to pulse. Small variations in the spatial profile of the beam can result in variations of the light distribution in the bubble chamber and thus directly affect the experimental limiting BBR calculations. Unfortunately, this problem can not be solved with our present knowledge.

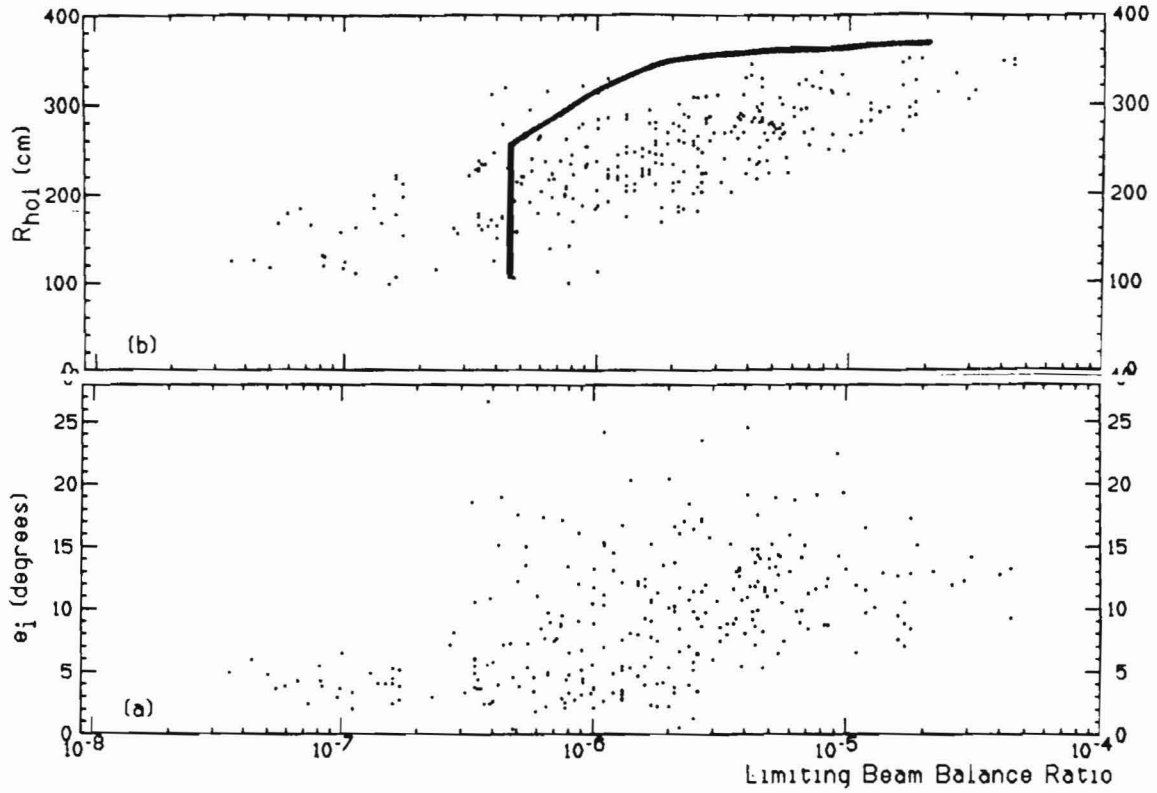

Fig. 6.24 Dependence of experimental limiting beam balance ratio on θ_i and R_{hol} for an input laser beam with gaussian spatial profile.

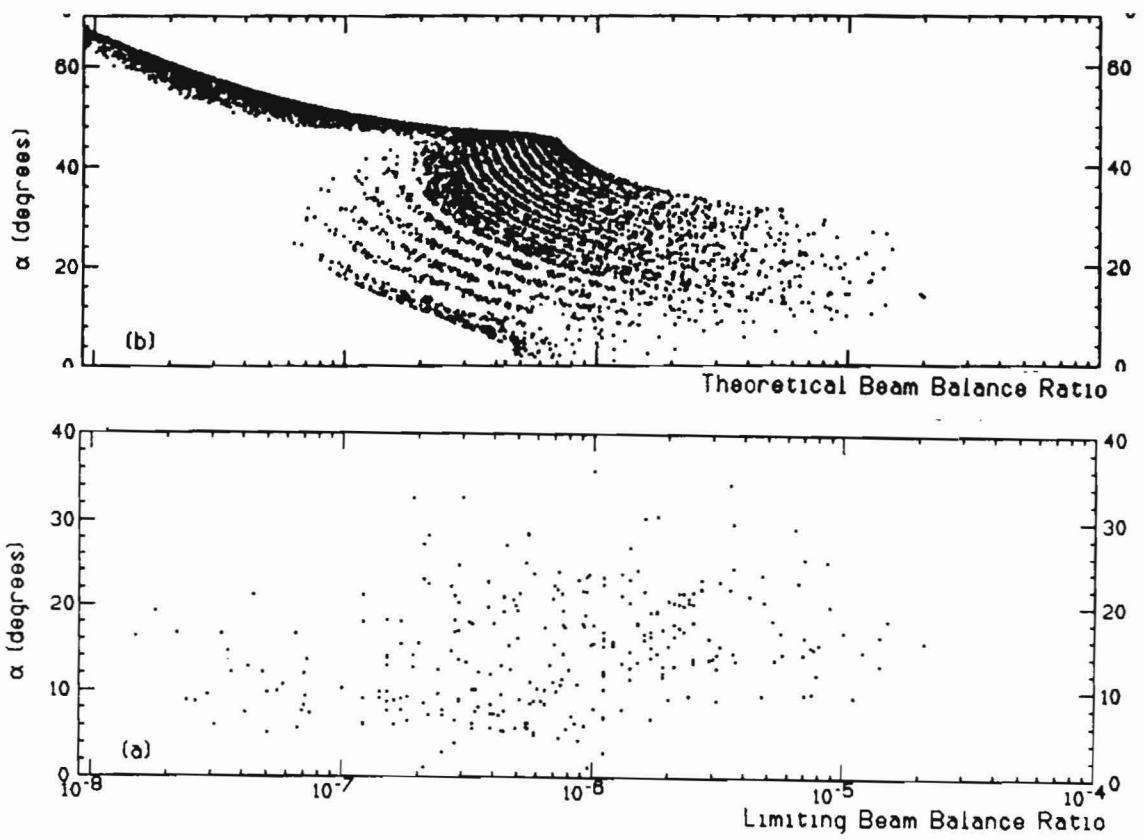

Fig. 6.25 Dependence of (a) experimental and (b) theoretical beam balance ratio on α for an input laser beam with flat spatial profile. The strips in the theoretical scatter plot are an artifact of the computer program used.

b) BBR as a Function of $G(\alpha)$

Figure 6.25 shows the distribution of BBR values versus α for both experimental data and theoretical calculations. The strips in the theoretical scatter plot are an artifact of the computer program used. These distributions are not informative and the same general comments as in case of the other two distributions can be made. The scatter plot of experimental limiting BBR versus α does not imply any distinct influence of scattering function on the calculated BBR.

c) BBR as a Function of Bubble Diameter

To ensure that the errors in bubble diameter measurements are not biasing the sample, a constant bubble diameter, 525 μm, was used to recalculate the limiting BBR values of the experimental data. Figure 6.26 shows the scatter plots of the experimental limiting BBR versus θ_i and R_{hol} for this bubble diameter. If the dispersion in these plots was a result of the bubble diameter measurements, using a constant bubble diameter a constant BBR should have been obtained for a given θ_i. It can be seen that most of the dispersion of the sample has been eliminated using the constant bubble diameter. This effect is in particular pronounced in Figure 6.26b. This result gives a strong evidence that the uncertainties in the bubble diameter measurements are rather large.

Another hypothesis in considering the effect of the bubble diameter on the limiting BBR values is that the smaller BBR values are obtained for smaller bubble diameters, giving an asymmetric distribution of BBR versus bubble diameter. This can be accounted for by the fact that the smaller bubbles grow faster (Equation [2.2.11]) which results in larger fringe motion and thus less visibility of the bubble, (Equation [2.2.15]). This situation is

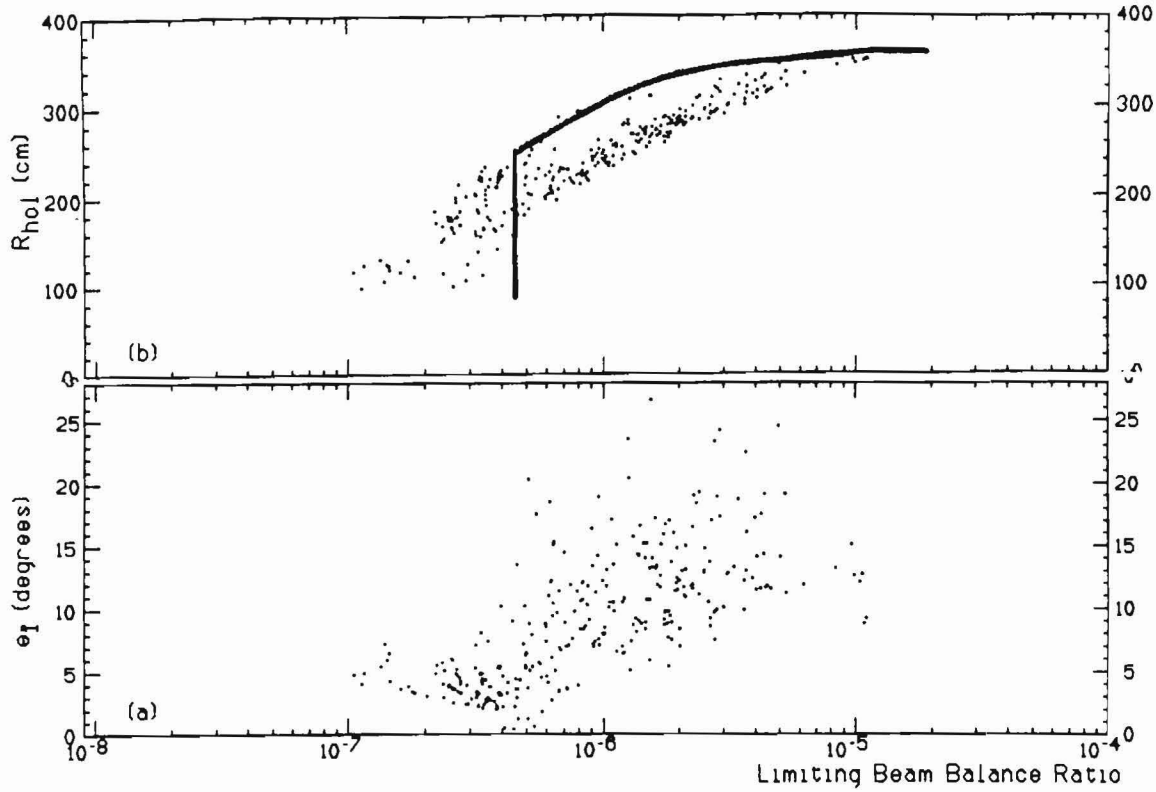

Fig. 6.26 Dependence of experimental limiting beam balance ratio on θ_i and R_{hol} for an input laser beam with flat spatial profile, and a constant bubble diameter (525 μm).

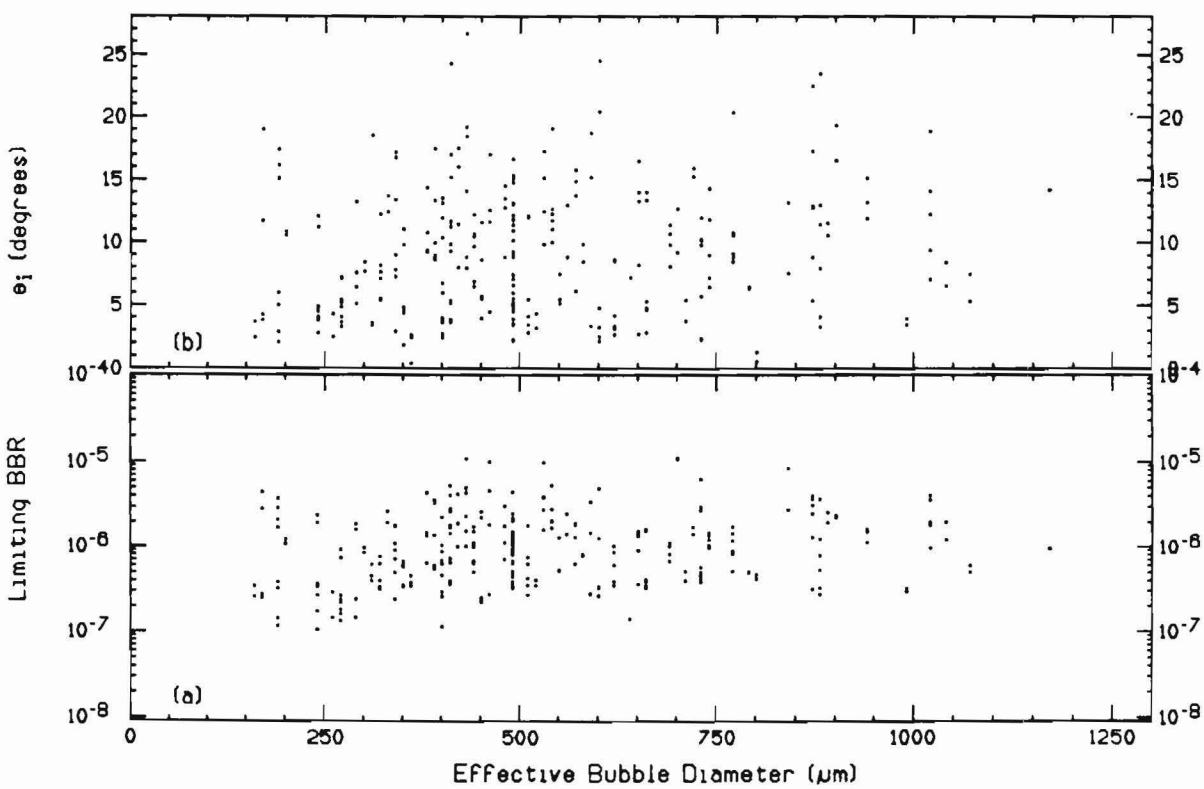

Fig. 6.27 Dependence of effective bubble diameter on experimental limiting beam balance ratio and θ_i.

more complicated when taking into account the position of the bubble. For smaller bubbles at larger illumination angles the bubble growth and movement enhances the fringe motion of the interference pattern (Equation [2.2.12]).

In a study of the validity of the above hypothesis two plots have been made for the experimental data: the effective bubble diameter is plotted versus the limiting BBR and θ_i, (Figure 6.27). As can be seen from these two distributions, no dependence of limiting BBR on the bubble diameter is observed. Moreover, bubbles of all sizes are distributed uniformly for different values of θ_i. If the hypothesis was correct, a smaller limiting BBR should have been observed for smaller bubble diameters.

6.4.3 Resolution

The subject of resolution has been discussed a number of times throughout this dissertation, (cf. Sections 2.4 and 6.3.1). The effective smallest bubble diameter obtained from the physics run holograms was 150 μm (see Section 6.4.1 for a detailed description of measuring method and the errors associated with it). However, this value does not set a lower limit for the best resolution which can be achieved with this system because there were no studies performed to investigate whether the tracks with bubble diameters of 100 μm and known time of occurrence were resolved in holograms. The results from various tests can be summarized as following:

diffraction-limited resolution (theoretical, Section 2.1.4)	20 μm
laboratory test (Section 6.3.1)	100 μm
empty-chamber test (Section 6.3.2)	110 μm
cold-chamber test	150 μm

6.4.4 Holographic Fiducial Volume

The shape and size of the holographic fiducial volume was determined for two samples: all data from running period I, and all data from running period II. The results are illustrated using two methods.

a) Figures 6.28(a-u) - 6.29(a-k) show x - y slices of the observed holographic fiducial volume at a series of z´s for the two samples, respectively. The slices in z are in steps of 10 cm in Figure 6.28 and 20 cm in Figure 6.29. The larger stepping in z for the latter is more useful because better statistics are available. A single end point is labelled by symbol ´1´ regardless whether the track stops or fades. The holographic optical axis is labelled by the symbol ´*´ for each cross section. Hand-drawn contours indicate the BBR range (see below).

For the first sample (all data before the lens was moved), the cross sections between $-65 < z < +45$ cm have the largest population of data points. For the second sample (all data after the lens was moved), most of the points lie in the cross sections between $-90 < z < -11$ cm.

In order to illustrate the position of the data points with respect to the theoretical holographic boundaries, a set of theoretical curves are made which divides the holographic fiducial volume with $\theta_i < 27°$ into several regions, each with an average BBR. This average BBR is calculated using the measured average bubble diameter, 525 μm for the first sample and 488 μm for the second sample. The contours of the different regions of the theoretical curves are mapped onto the experimental curves in Figures 6.28 - 6.29. The coding for the BBR values increases alphabetically in steps of 0.5E01 with A in the range of 0.1E-10 - 0.5E-10. This coding is tabulated in Appendix IIb.

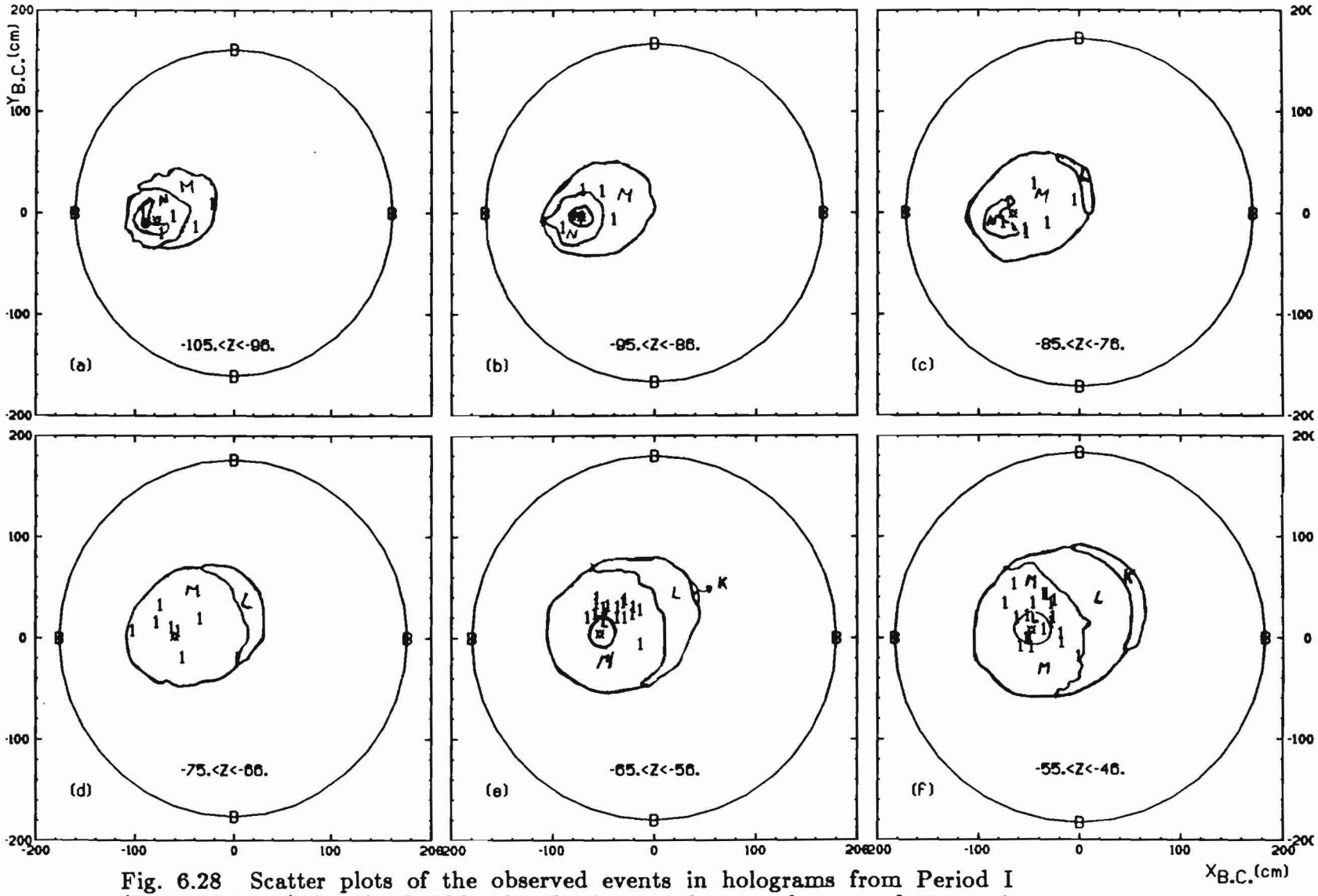

Fig. 6.28 Scatter plots of the observed events in holograms from Period I (depicted by 1) for the bubble chamber's x-y plane, and steps of 10 cm in z. Shown are hand drawn contours of different beam balance ratio which are labelled with letter-codes (see Appendix IIb), and the intersection of the holographic axis with the x-y plane.

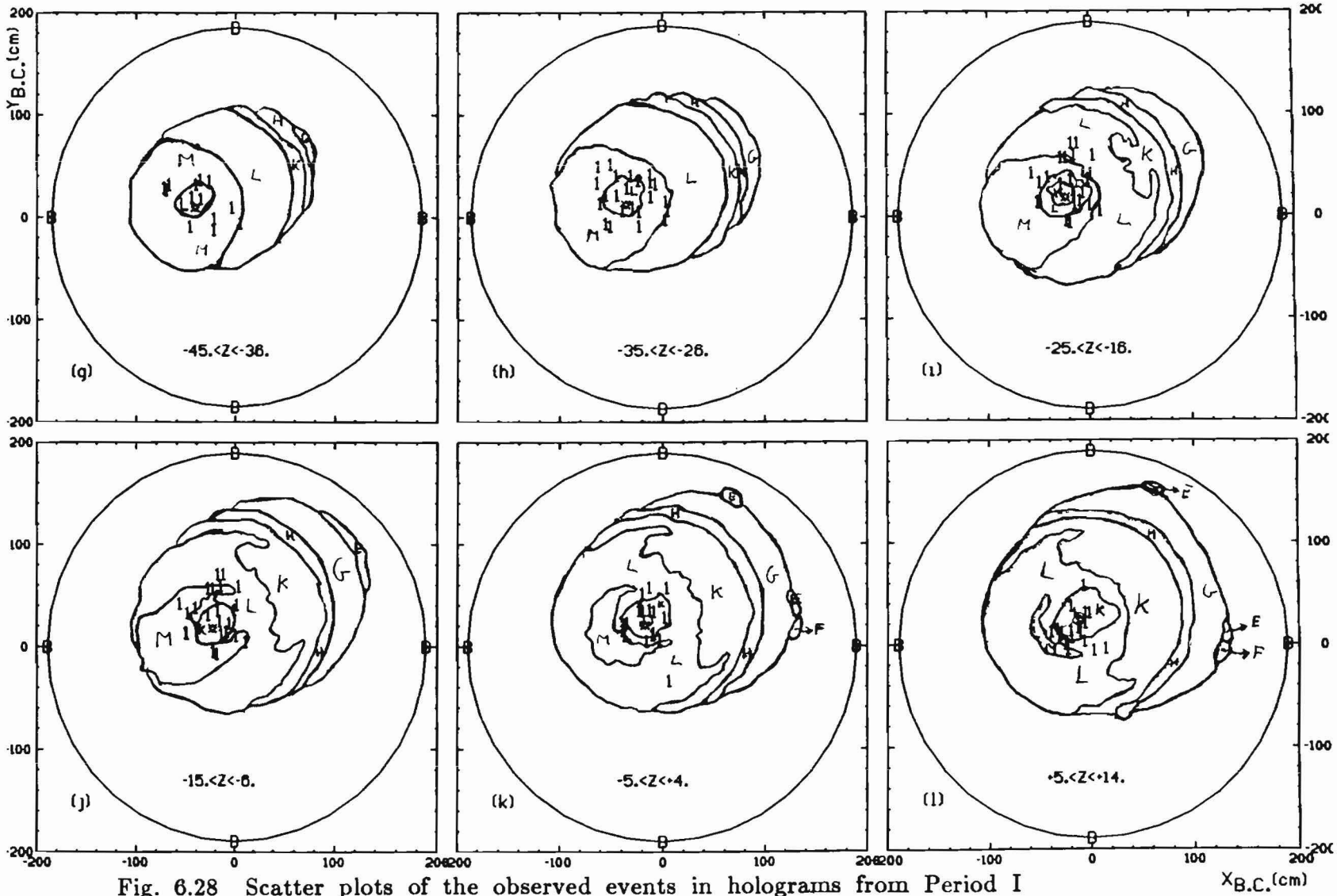

Fig. 6.28 Scatter plots of the observed events in holograms from Period I (depicted by 1) for the bubble chamber's x-y plane, and steps of 10 cm in z. Shown are hand drawn contours of different beam balance ratio which are labelled with letter-codes (see Appendix IIb), and the intersection of the holographic axis with the x-y plane.

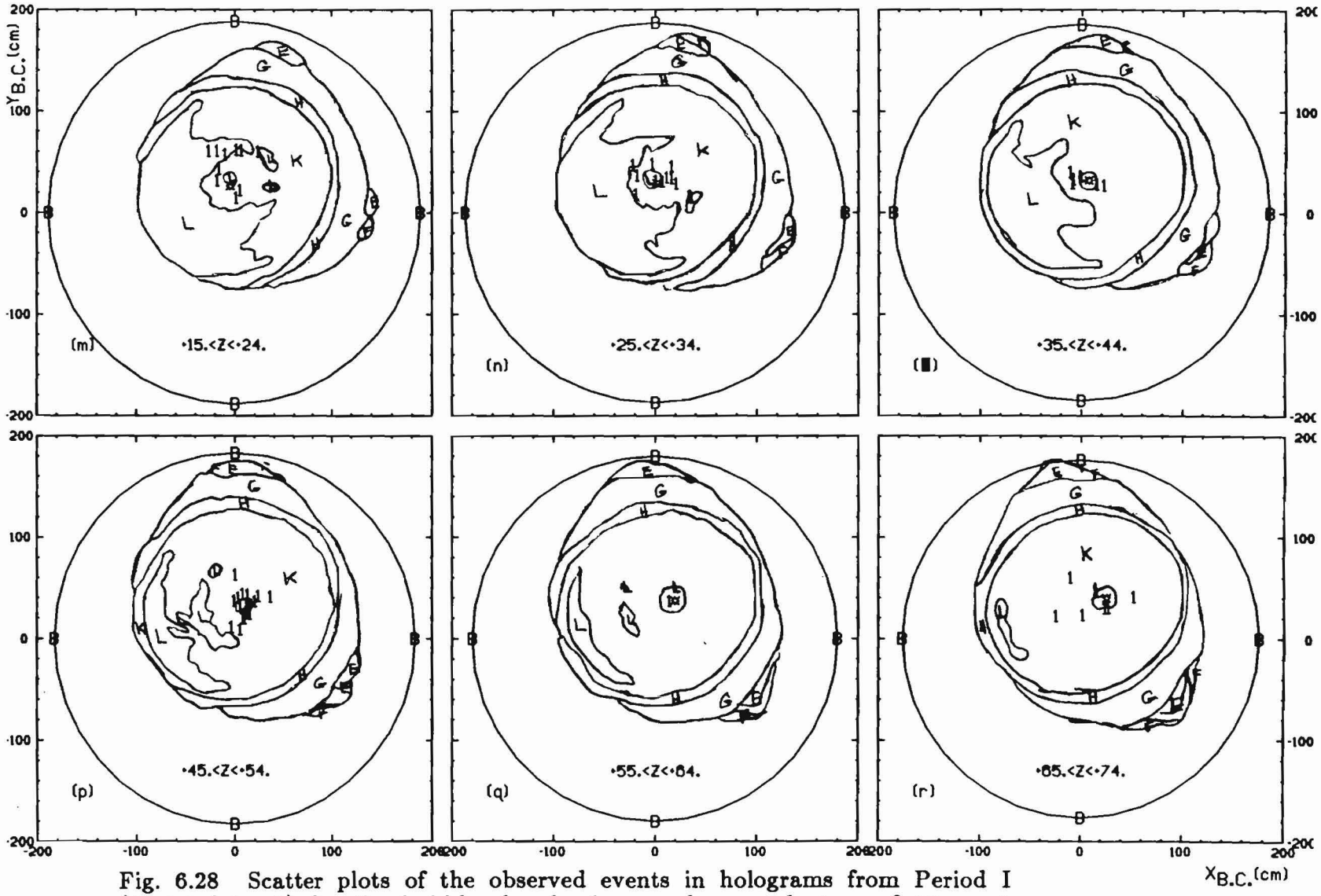

Fig. 6.28 Scatter plots of the observed events in holograms from Period I (depicted by 1) for the bubble chamber's x-y plane, and steps of 10 cm in z. Shown are hand drawn contours of different beam balance ratio which are labelled with letter-codes (see Appendix IIb), and the intersection of the holographic axis with the x-y plane.

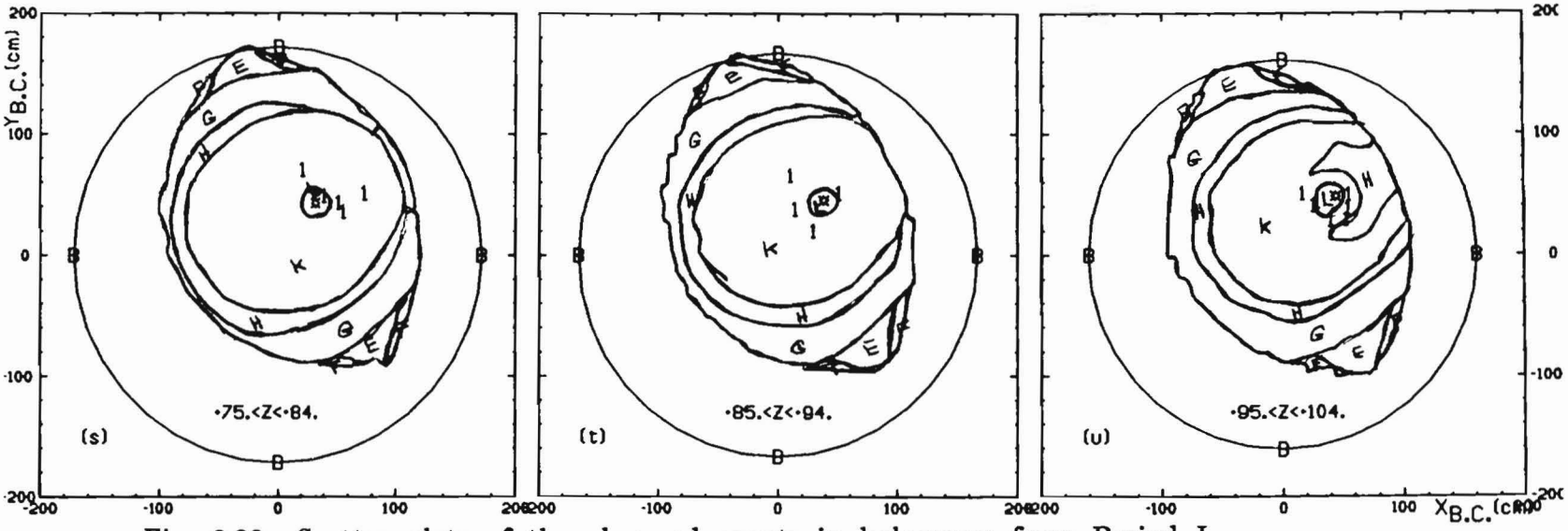

Fig. 6.28 Scatter plots of the observed events in holograms from Period I (depicted by 1) for the bubble chamber´s x-y plane, and steps of 10 cm in z. Shown are hand drawn contours of different beam balance ratio which are labelled with letter-codes (see Appendix IIb), and the intersection of the holographic axis with the x-y plane.

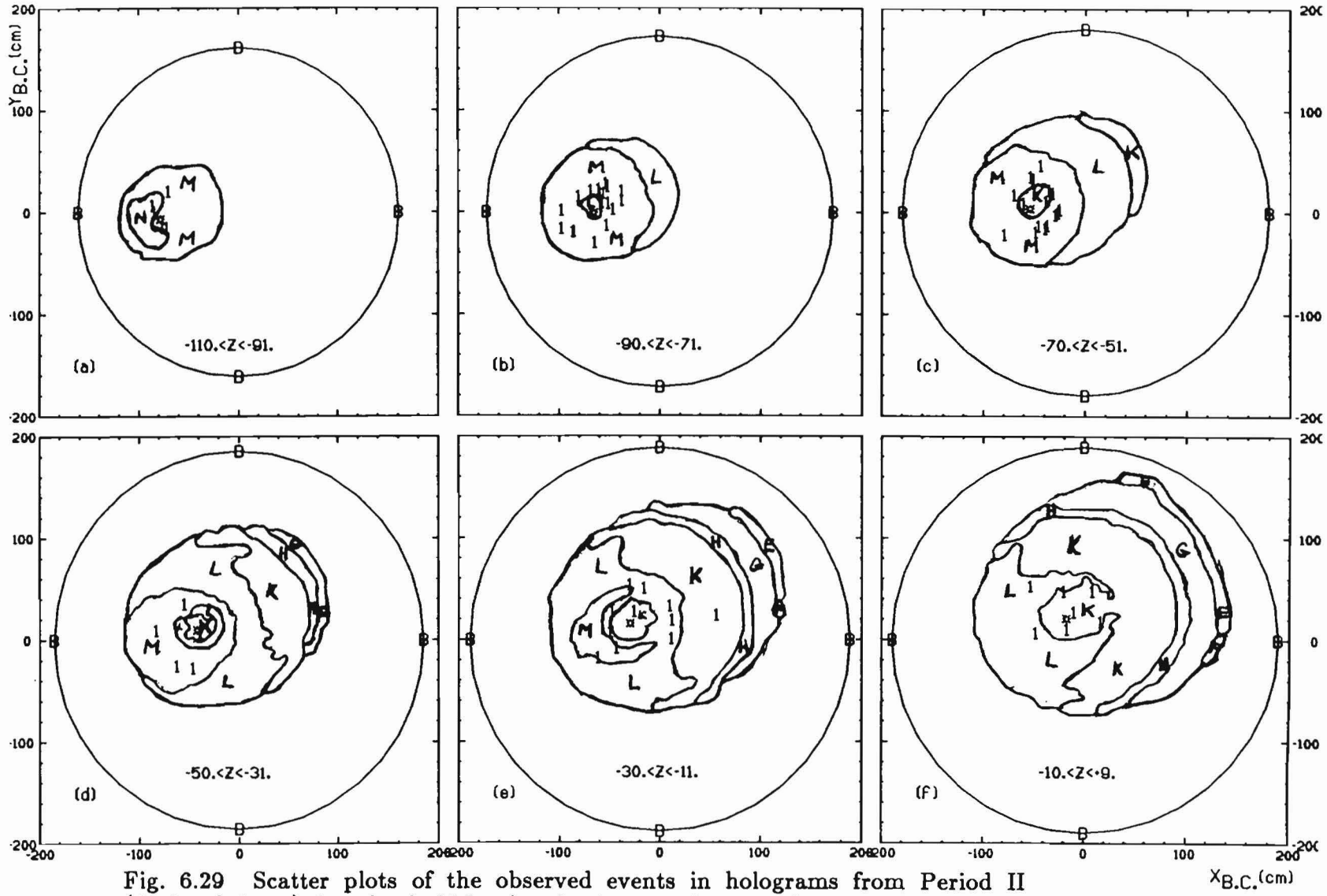

Fig. 6.29 Scatter plots of the observed events in holograms from Period II (depicted by 1) for the bubble chamber's x-y plane, and steps of 20 cm in z. Shown are hand drawn contours of different beam balance ratio which are labelled with letter-codes (see Appendix IIb), and the intersection of the holographic axis with the x-y plane.

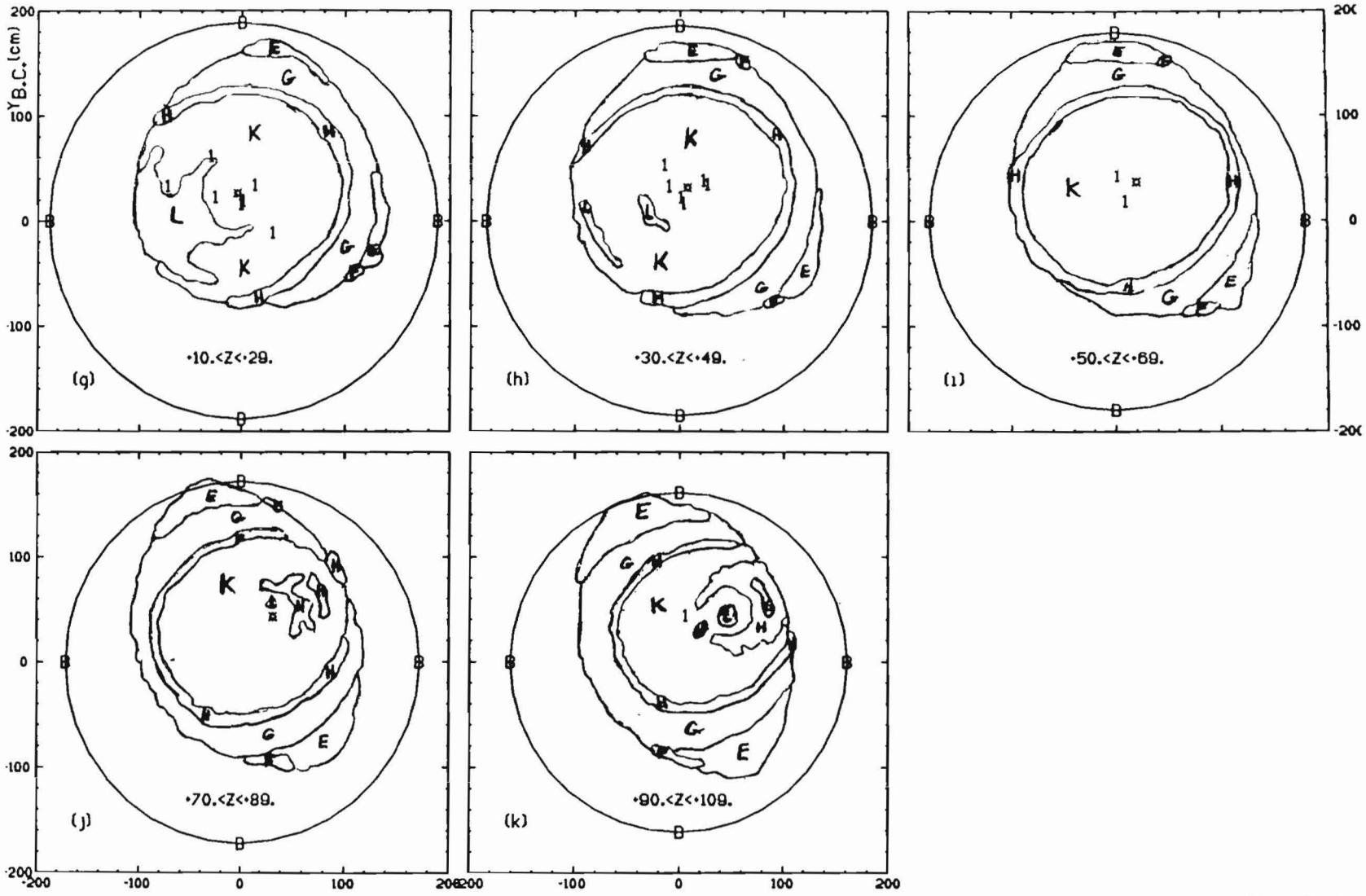

Fig. 6.29 Scatter plots of the observed events in holograms from Period II (depicted by 1) for the bubble chamber's x-y plane, and steps of 20 cm in z. Shown are hand drawn contours of different beam balance ratio which are labelled with letter-codes (see Appendix IIb), and the intersection of the holographic axis with the x-y plane.

Using these contours and assuming that the visibility of the tracks is limited by a limiting BBR, the distribution of the points about the holographic axis can be examined. The data points are distributed within M - K regions, 0.1E-06 < BBR < 0.5E-05, throughout the entire depth of z. This variation is within the root mean square of the effective average bubble diameter. Errors of ± 226 μm of the bubble diameter shifts the BBR values by one order of magnitude up or down. If there were no uncertainty in the bubble diameter measurements, the data points would fall on the BBR contours.

b) Figures 6.30 - 6.31 show a three dimensional illustration of the holographic volume in the bubble chamber space for both sets of the data.[39] In preparing these plots the viewing angle and the rotation about z axis could be varied. The best viewing angle was found to be at 10° counterclockwise from the x-y plane and no drastic change in shape of the volume was observed when the x-y plane was rotated about z. The results are presented for 0° rotation about z and a viewing angle of 10° counterclockwise from the x-y plane. The data are grouped together in z cross sections of 10 cm and 20 cm for the two sets, respectively. In these figures all data points are joined together for a given z to give an impression of an ellipse about the optical axis.

Comparing the two volumes depicted by Figures 6.30 - 6.31 it can be seen that moving the lens 10 cm back along the holographic optical axis has shifted the maximum populated cross section down by 30 cm in the z direction. This can also be seen in the two dimensional pictures. Also, there seems to be a larger volume covered for the second set of data points

---

39. G. Saitta is acknowledged for providing these plots.

at about R_{hol} = 200 cm. It should be noted that the data for the first set of samples is taken with a range of pulse lengths between 0.1 - 40 μs, (184 data points for pulses of duration 0.1 - 20 μs and 80 for 40-μs pulses), and the data for the second set is taken with the pulse lengths of 0.1 and 18 μs, (24 for 0.1-μs pulses and 54 for 18-μs pulses). Thus, the above variations do not seem to be a function of pulse length.

Another interesting observation is that there exists an asymmetry about the holographic axis: there is a larger volume which can be obtained to the right of the axis. This is explained by the fact that the incident laser beam profile appeared to be slightly more intense at its right semi-circle on entering the dispersing lens.

To determine the size of the experimental visible volume the minimum convex area including the data is calculated for each slice of z between -110 cm to +110 cm[40] and this area is multiplied by the steps in z, 10 cm. The expected volumes, excluding the z values smaller than -110 cm and larger than +110 cm, are calculated for two sets of data to include i) the BBR values greater or equal to the average, and ii) the lower-limit BBR values corresponding to each case. Table 6.7 gives the volumes observed experimentally, those expected theoretically with above listed requirements, and also their ratios to the total bubble chamber fiducial volume (14 m^3) for both periods. It can be seen that the volume observed is smaller by a factor of 3 - 18 than the value expected assuming an average limiting BBR. Possible reasons for this low efficiency are the subject of next section.

---

40. The Hawaii replay machine allowed measurements in the range of -110 < z < +110 cm.

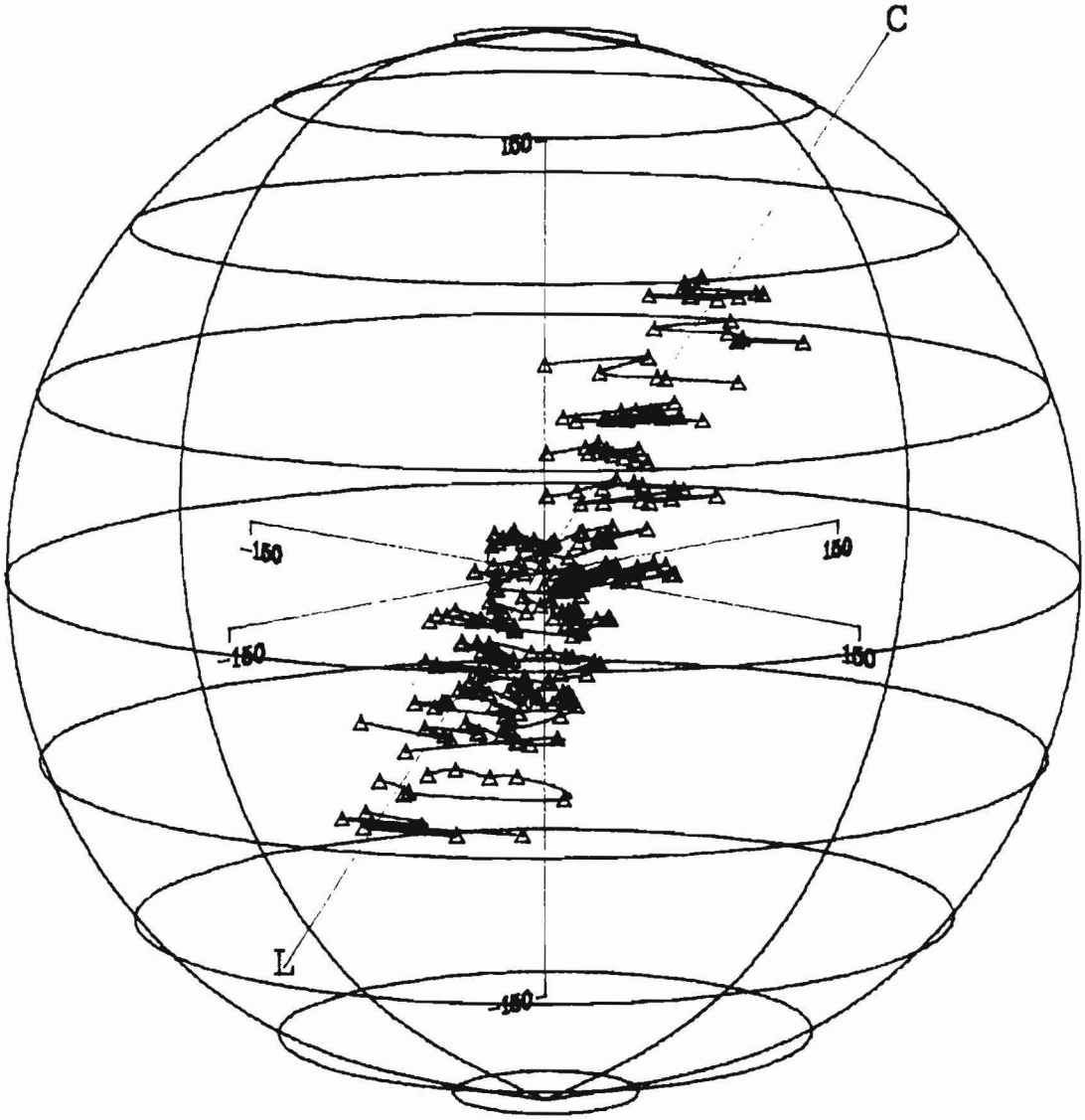

Fig. 6.30 Observed holographic fiducial volume for the experimental data from Period I. The viewing angle is 10° counterclockwise from the x-y plane. L: the dispersing lens, C: the holographic camera

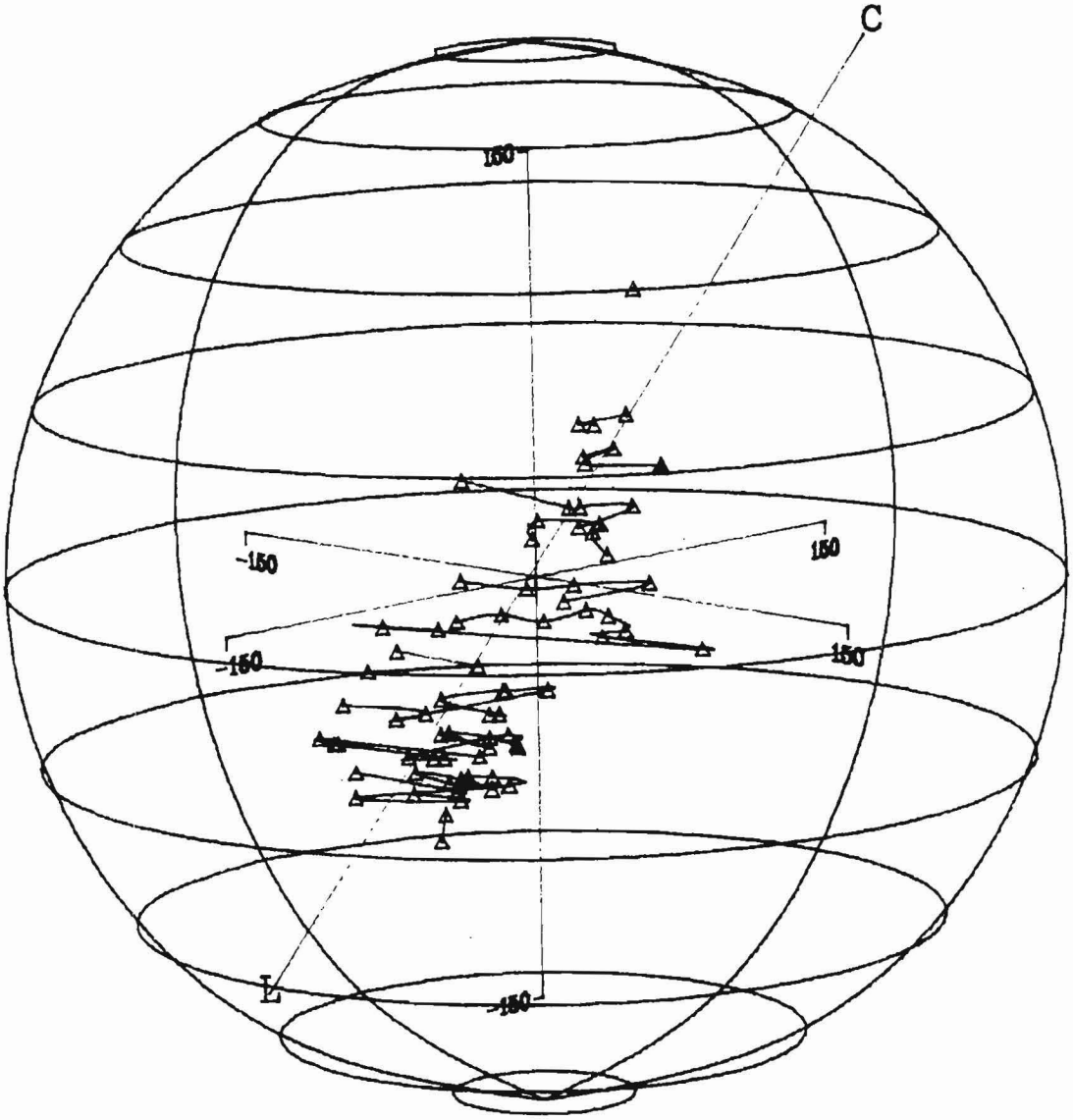

Fig. 6.31 Observed holographic fiducial volume for the experimental data from Period II. The viewing angle is 10° counterclockwise from the x-y plane. L: the dispersing lens, C: the holographic camera

Period I						
BBR	Volume (m^3)			Percentage (%)		
≥	Expected	Observed	Total	Exp/Tot	Obs/Tot	Obs/Exp
0.62 E-06	1.76	0.48	14	13	3	27
0.50 E-07	5.07	0.48	14	36	3	10
Period II						
0.10 E-05	0.64	0.23	14	5	2	36
0.19 E-06	4.15	0.23	14	30	2	6

- Table 6.7 -

6.4.5 Holographic Efficiency

In the last section, it was shown not only that small Expected/Total efficiencies are obtained as a result of the limiting BBR values, but also that the efficiencies, (Observed/Expected), are small. In this section is given a discussion of the appropriate cuts on the holographic parameters to be used when scanning the holograms in order to increase the scanning efficiency. The possible causes for the small efficiencies of Observed/Expected are also discussed.

Beam Tracks

The procedure for locating beam tracks in the holograms has been described in Section 6.4.1. Once the closest approach to the holographic optical axis is calculated for a track, a holographic fiducial volume cut is applied. The cuts are applied to θ_i and R_{hol} of the event instead of its BBR value. This is done to avoid the uncertainties arising from $F(\theta_i)$ and $G(\alpha)$ in calculating the expected BBR. As mentioned before, the parameters

θ_i and R_{hol} would give sufficient information about the spatial characteristics of the event.

In order to find the appropriate limits, a number of different cuts were applied to a sample of tracks which have been located in the conventional photographs. In Table 6.8 code A denotes the ideal situation in which all tracks in the volume illuminated by a 2.5 cm diameter input beam (i.e. the volume with $\theta_i < 20°$ and whole range of R_{hol}) are expected to be observed. The small Observed/Expected efficiency of 12 % indicates that BBR values at large angles are too small to be detected. Codes B - F denote various cuts in which only tracks with their point of closest approach having θ_i and R_{hol} smaller than the given values are expected to be observed. Each cut is usually defined by two sets of values since for $R_{hol} < 180$ cm, a smaller θ_i cut must be used due to the light fall off with distance. A pictorial presentation of cuts B and F is given in Figure 6.32. Table 6.8 gives the limits and the Observed/Expected efficiencies for each cut. The terminology used in this table and the subsequent discussion is given below.

Observed Tracks : the number of beam tracks within the holographic cut scanned in the conventional photographs and also found in the holograms.

Unobserved Tracks: the number of beam tracks within the holographic cut scanned in the conventional photographs but not found in the holograms.

Expected Tracks : Observed + Unobserved beam tracks.

Efficiency : Observed / total beam tracks for a given cut.

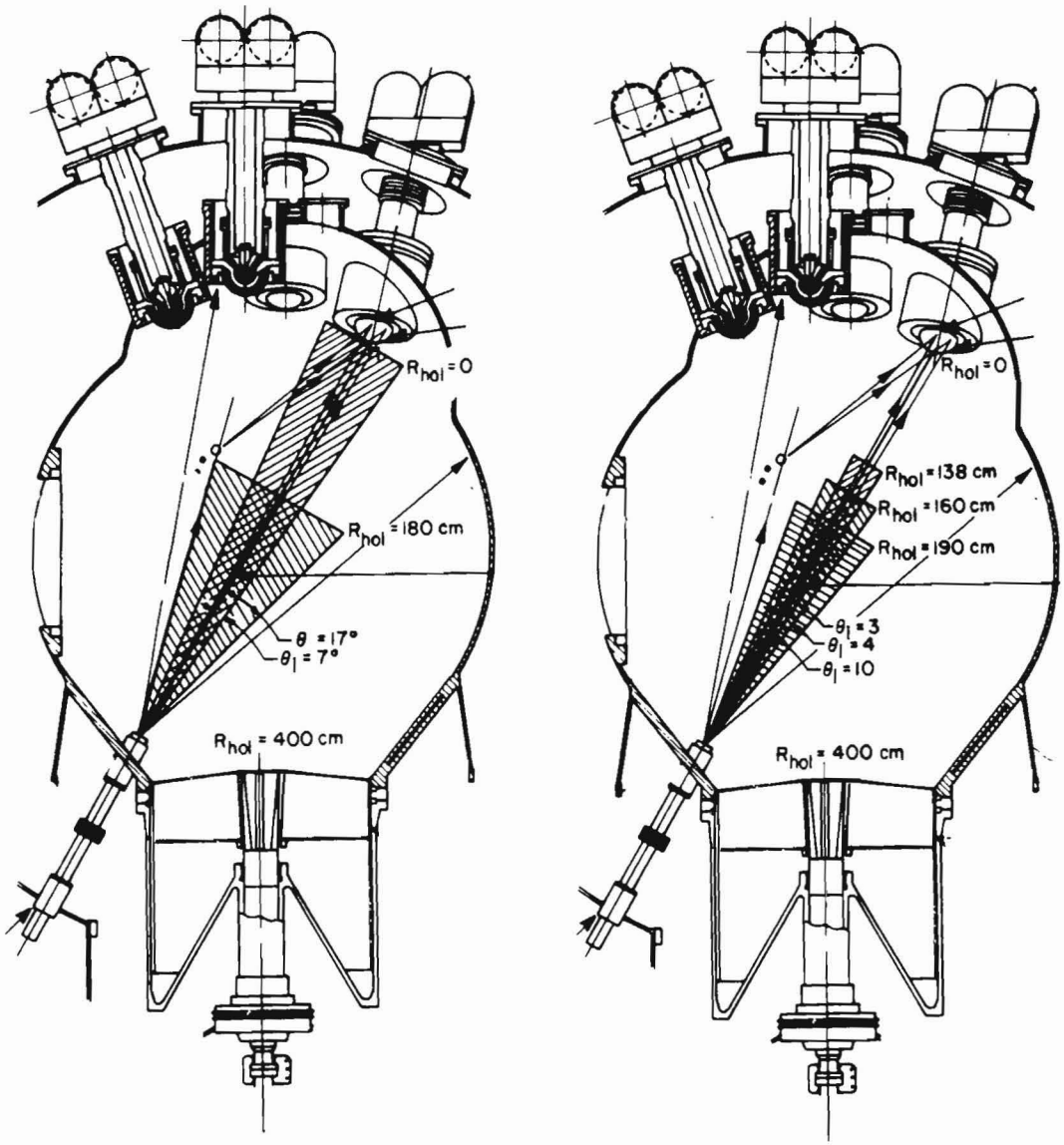

Fig. 6.32 An illustration of the holographic parameter cuts used: (a) Cut B, (b) Cut F.

	Applied Cut			Number of		
Code	$\theta_i <$ (Degree)	$R_{hol} \geq$ (cm)	$R_{hol} <$ (cm)	Observed Tracks	Total Tracks	Efficiency (%)
A	20			36		12
B	17 7	180	 180	36	208	17
C	12 5	180	 180	33	132	25
D	10 4	180	 180	29	110	26
E	9 3	180	 180	25	92	27
F	10 4 3 0	190 160 138	 190 160 138	28	94	30

- Table 6.8 -

Table 6.8 indicates that as the θ_i for each cut gets smaller, the efficiency rises, including almost all data points. Going from cut-B to cut-C only three event points are excluded and from C to D four are excluded. However, the gain in efficiency is small going from cuts-C to D to E, (about 1 % increase), and reduces the statistics. Therefore, we consider cut C as the most reasonable one. It should be noted that the cuts (B - E) are step functions. A more realistic cut, (although it is still step-wise), is cut F. For cut F the highest efficiency, 30 %, is obtained.

In order to explain this inefficiency in finding the beam tracks which lie in the fiducial volume defined by cut-C, a number of possible dependencies were explored.

a) Ping Number (cf. p. 39)

Figure 6.33(a-b) shows histograms for Observed and Unobserved beam tracks as a function of accelerator beam "ping number." The ratio of (Unobserved / Observed) beam tracks for the three ping numbers is 2.8 ± 0.4, 5.3 ± 1.2, 4.4 ± 0.8, respectively. This ratio is somewhat high for ping number 2 (where the statistics are low), but no definitive conclusion can be drawn. It is interesting to note that the total number of beam tracks within cut-C are much higher for ping number 1, (53), as compared to the other two ping numbers, (19 and 27), respectively.

b) Hologram Quality

The hologram quality was determined by a single scanner examining visually the holograms in a virtual-image mode using a Helium-Neon laser. The holograms were rated between 1 and 6 qualitatively, with 6 representing a hologram as a "very good" one. Figure 6.33(c-d) shows that finding the beam tracks in the holograms was apparently independent of the quality judgement.

c) Hologram Density

The hologram density was measured using a densitometer as an average over five data points at five fixed regions of the hologram. The densitometer aperture was a slit with 2 × 4 mm dimensions. Ideally it would be preferred to use a densitometer with an integrated read-out. However, the density measurement using a slit aperture is useful for giving a qualitative comparison of different holograms. Figure 6.33(e-f) shows that the average hologram density for those with Observed beam tracks is slightly lower, (0.72 ± 0.10), as compared to those with Unobserved beam tracks, (0.79 ± 0.03). This might be accounted for if some of the exposure on the

film were the result of variable sources of "noise," especially in the reference beam. An increase in density would label an increase in noise level and therefore a decrease in the efficiency for finding the beam tracks.

d) Holographic Parameters

Figure 6.34 shows the scatter plots for the Observed (pluses) and Unobserved (squares) beam tracks as functions of θ_i, α, and a third holographic parameter, respectively, plotted against R_{hol}. The third parameter is the calculated ratio of the expected light scattered by a bubble to the square of the effective bubble radius (BBR x I_{ref} / $(r)^2$), (cf. Equation [2.2.2]). It is a geometric expression which depends only on the position of the bubble and excludes the bubble diameter uncertainty. This scatter plot shows that no track is observed when this combined holographic parameter is smaller than 0.1E-9 J/cm^2. However, most of the Unobserved tracks lie in the same range as the Observed ones.

e) Time Slot

Figure 6.35 shows a histogram of the "time slot" for beam tracks which were Observed in holograms (pluses), and Unobserved (squares). The injection of the neutrino beam into the bubble chamber was completed at about the 3000 μs "time slot" when the laser beam was injected into the bubble chamber. The time windows which included the Observed and Unobserved samples are 1100 - 2300 μs, w_1, and 900 - 2500 μs, w_2, respectively. Since most of the Unobserved beam tracks lie within the same "time slots" as Observed ones, it is not possible to explain the missing tracks as caused either by destructive phase modulation (from a long bubble growth time) or by small bubble sizes (short growth time).

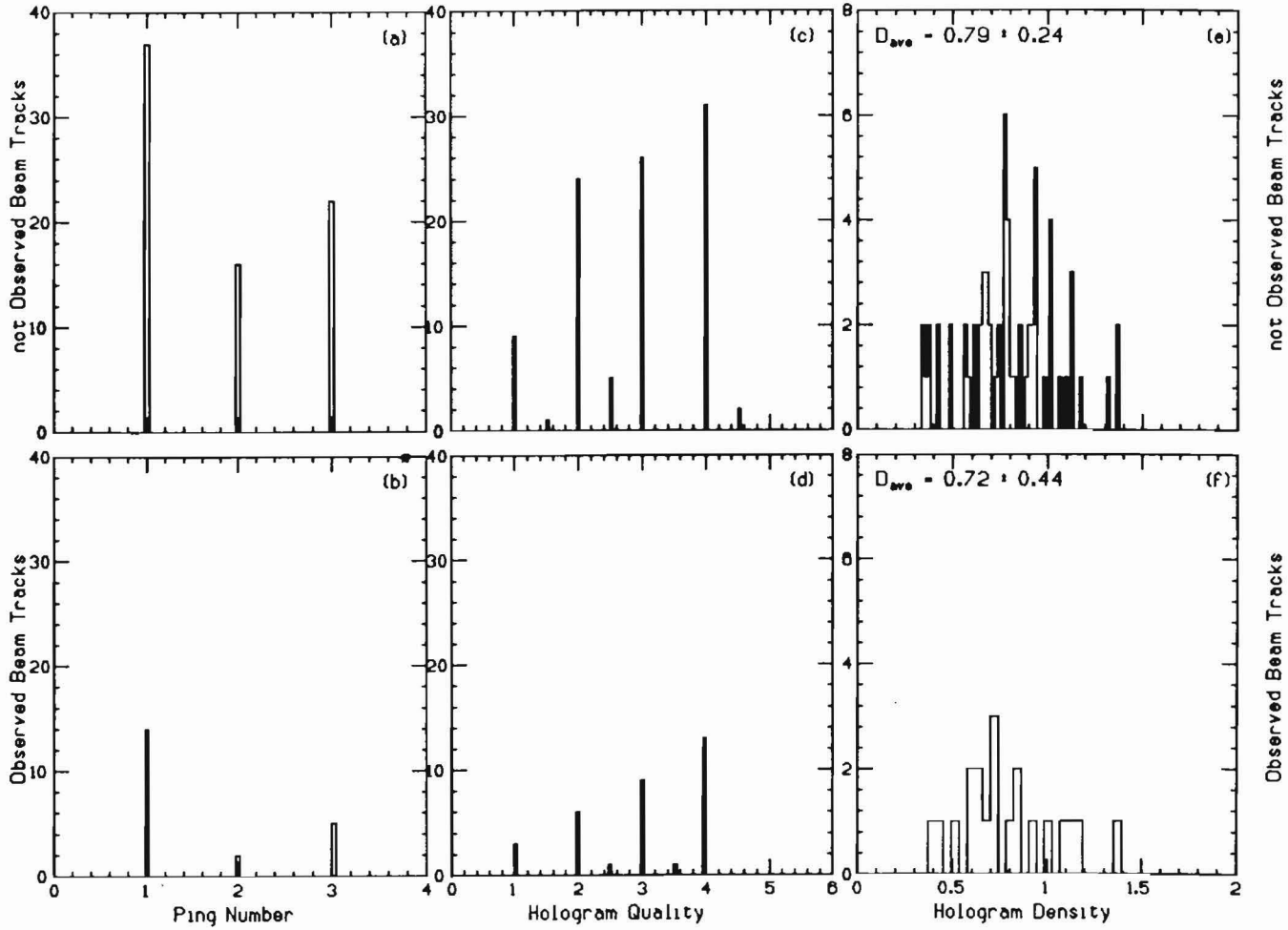

Fig. 6.33 Dependence of the Observed/Unobserved beam tracks on (a-b) ping number, (c-d) hologram quality, (e-f) hologram density.

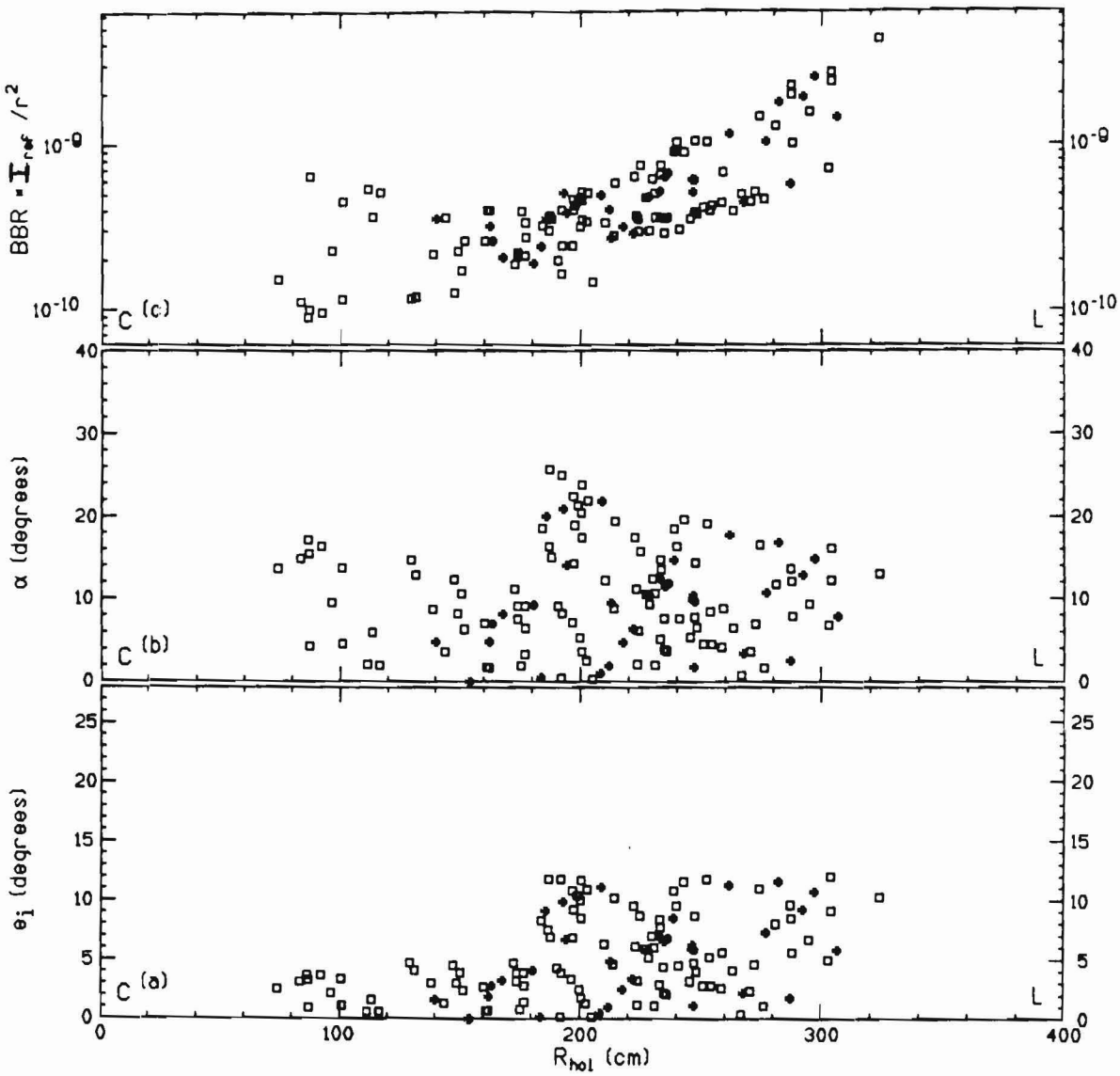

Fig. 6.34 Dependence of the Observed/Unobserved beam tracks on θ_i, α, and $[(BBR \times E_{ref}) / r^2]$; Pluses: Observed, squares:Unobserved.

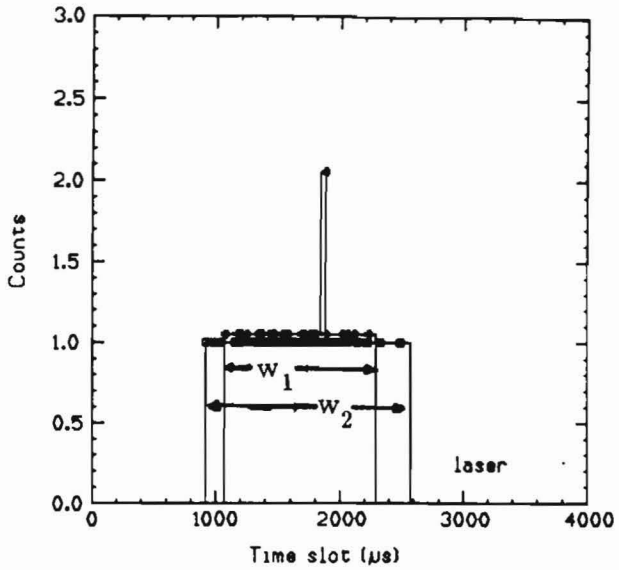

Fig. 6.35 Dependence of the Observed/Unobserved beam tracks on EMI time slot; Pluses: Observed, squares:Unobserved.

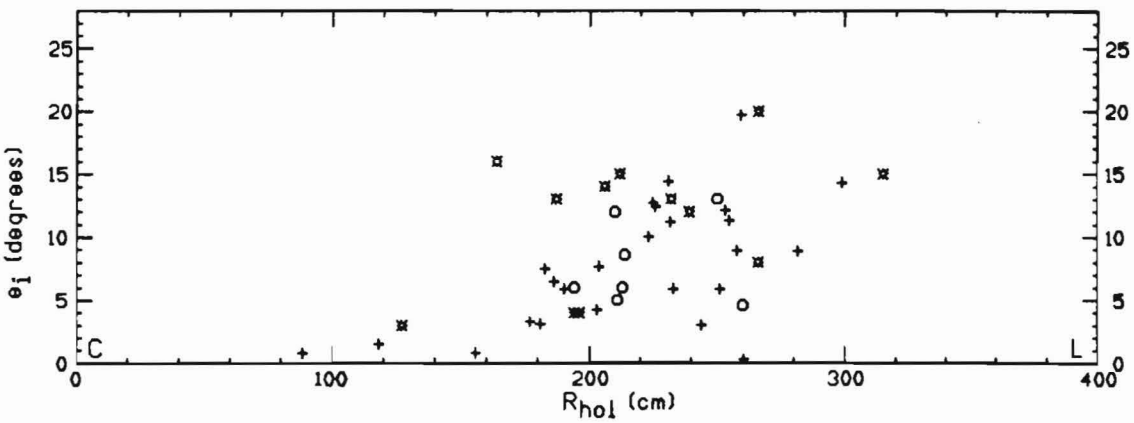

Fig. 6.36 Distribution of the holographic events reconstructed at circles: Fermilab, pluses: Hawaii, stars: Holred replay facilities.

Although some of the missing tracks can be accounted for by the above analysis, there is no obvious reason for missing most of the Unobserved tracks which are characterized by exactly the same parameters as the Observed ones. Three other possible explanations for the missing tracks are: an inefficiency of the holographic scanning and illumination during replay, the presence of scattered light as a source of noise in the reconstruction at the smaller angles, and additional nonuniformity in the illuminating beam during recording. No exploration of the last possibility was made during the 1985 bubble chamber run.

Neutrino Events

The efficiency for finding neutrino events in the holograms varied from one roll to another for several reasons among which were: a) over-exposing or under-exposing the holograms due to failures of the electronic feedback circuitry, b) improper development of the holograms, c) variations in the operating conditions of the bubble chamber, and d) variations in the operating conditions of the laser. It was not worthwhile to obtain an efficiency rate as a function of all these variables since the actual corrections were not studied in detail. A study was performed to obtain the efficiency rates for the two rolls, 2273 and 2327. The conditions under which the bubble chamber and the holographic system were operated for these two rolls are given in Tables 1.1 and 6.4, respectively. The most important difference is that for roll 2327 the dispersing lens was moved back and a smaller chamber volume was illuminated. Thus, as in the case of roll 2323, smaller efficiencies are expected for roll 2327. Table 6.9 gives the total number of conventional pictures and holograms per roll, the total number of events observed in the conventional pictures, those expected to be seen in

the holograms with no cuts applied, and those observed in the holograms. This table also gives the following efficiency rates: (Expected holographic events/Total observed conventional events), (Observed holographic events/Total observed conventional events), and (Observed holographic events/Expected holographic events).

roll	# con. pix.	# hol.	# observed con. event	# expected hol. event	# observed hol. event	Efficiency (%) Exp/Tot	Obs/Tot	Obs/Exp
2273	917	900	175	12	7	6.8	4.0	58
2327	2098	1040	466	10	4	2.1	0.9	40

- Table 6.9 -

The Exp/Tot efficiency is very low for roll 2327 for the holograms since half of the roll was under-exposed. It is interesting to note that the efficiency to find an event in roll 2273 was 58 %. This efficiency, (Obs/Exp), was only 25 % for beam track in the same roll. The reason for this difference can be seen from Figure 6.36 which shows the distribution of angle of illumination of the events found as a function of R_{hol}. Events with large θ_i were observed; this was most likely due to the fact that a pattern recognition procedure was used in the search for events. However, the events at large angles usually have very poor quality and only give impression of bubbles on the vidicon. The distribution in Figure 6.36 shows that most of the events are located within a cylinder of radius of one meter centered at R_{hol} = 200 cm, as expected.

(b)

(a)

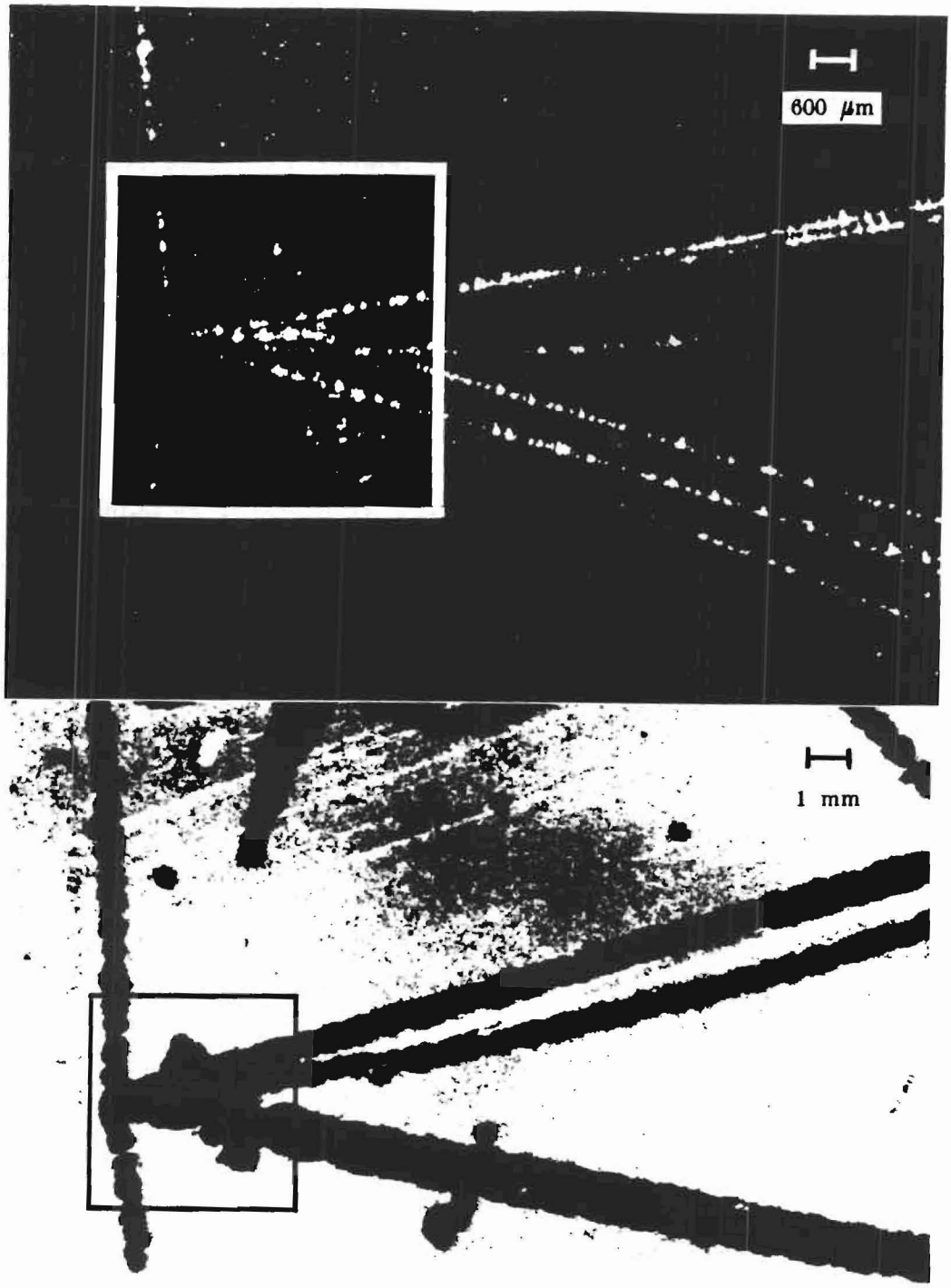

Fig. 6.37 Comparison of the vertex region of a neutrino event imaged in (a) a conventional photograph, (b) a hologram.

An example of what holography can achieve is given in Figure 6.37. Figure 6.37a is a conventional photograph of a neutrino event taken 12 ms after the beam injection in bubble chamber with magnification of 6 from real space. The bubbles are of the order of $\lesssim$ 1 mm diameter. Figure 6.37b is a picture of the same event photographed from its reconstructed holographic image at Fermilab with the magnification of 10 from real space. Here the bubbles are much smaller (190 μm diameter), since the hologram was taken only 2 ms after the beam injection. Where large bubbles in conventional photographs obstruct the details of a close-in-interaction at a distance of about 2 cm from the primary vertex, holograms with bubbles of smaller diameter can allow a detailed study of this secondary interaction.

6.4.6 Pulse Length Dependence

Theoretical calculations describing the effects of the bubble growth and/or movement as a function of exposure time shows that for pulse durations $\gtrsim$ 10 μs, the object beam's optical path may change by several $\lambda/10$, (cf. Section 2.2.5). This would result in the degradation of the bubble image and could demolish the image completely. Here, using experimental data from beam tracks and cosmic rays, a comparison is given of distribution of the holographic parameters for different pulse lengths. Figure 6.38 shows the scatter plots for θ_i, α, and R_{nor} versus R_{hol} for data taken in the first running period, and with pulse durations of 0.1, 10, 20, and 40 μs. As in case of the holographic efficiency rate determination, these three holographic parameters are chosen instead of BBR values in order to avoid the uncertainties in $F(\theta_i)$, $G(\alpha)$, and the bubble size measurements.

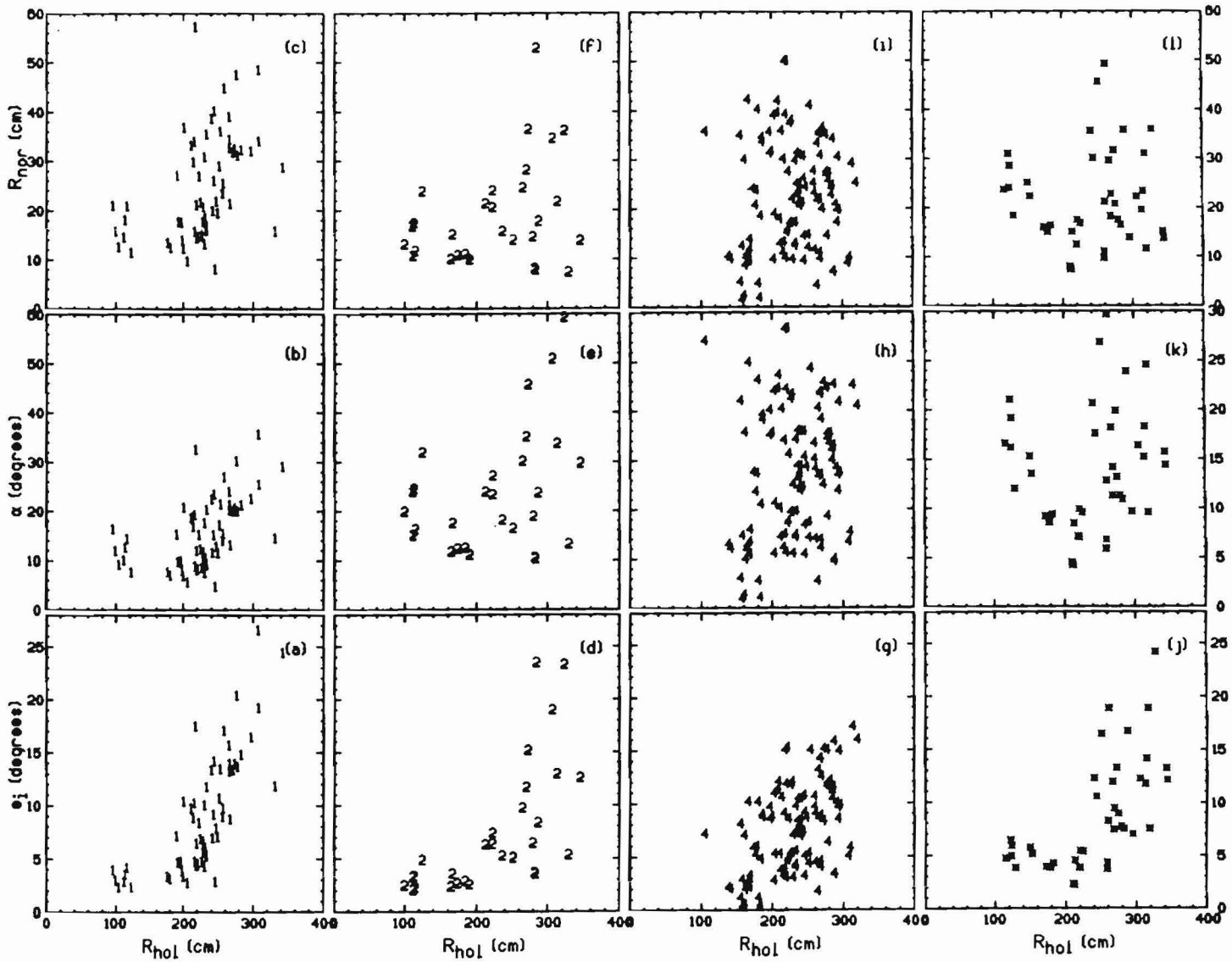

Fig. 6.38 Distributions of the holographic parameters of the observed track end-points for four light-pulse durations; 1: 10 μs, 2: 20 μs, 4: 40 μs, stars: 120 ns.

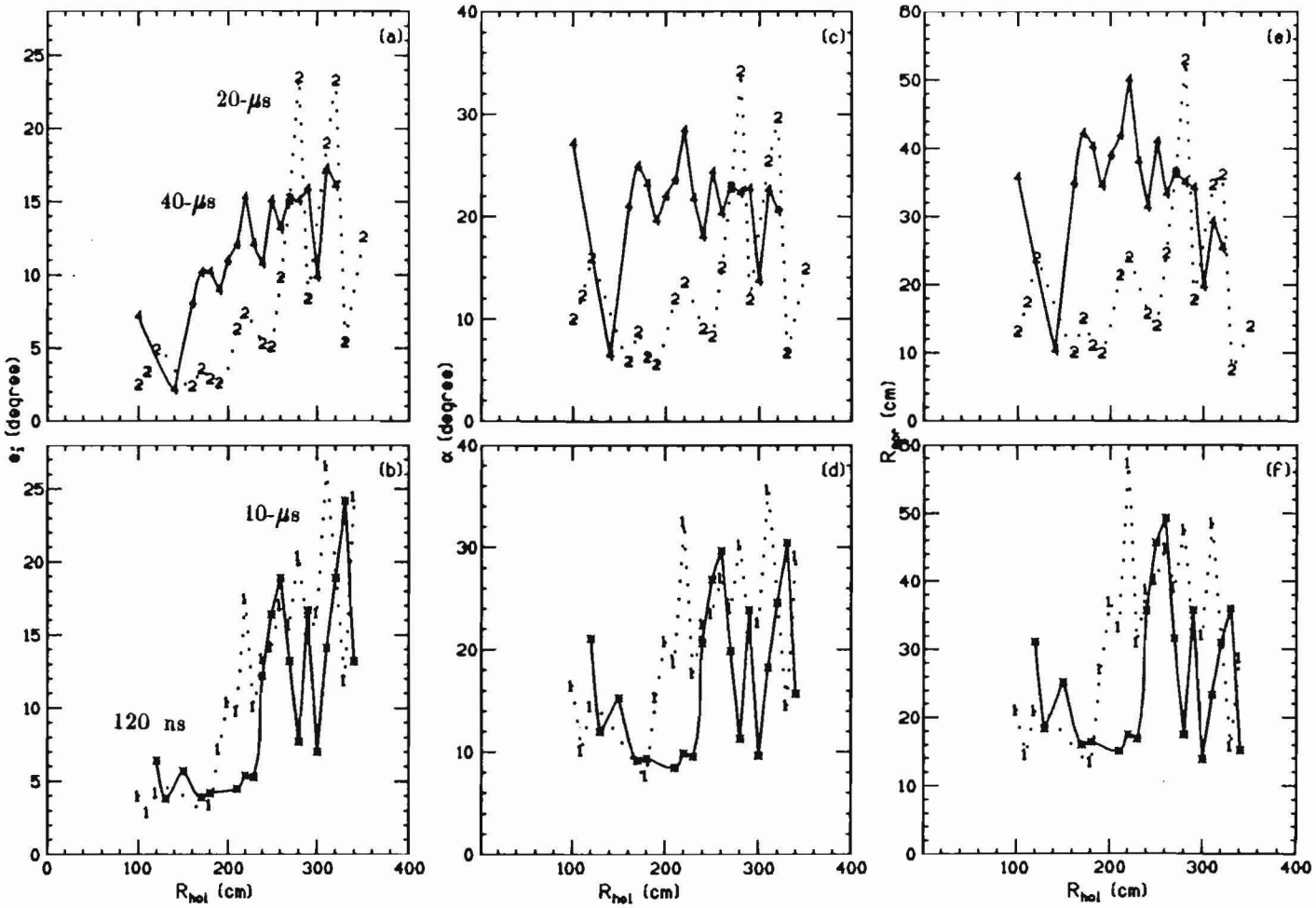

Fig. 6.39 Distributions of the maximum values of the holographic parameters of the observed track end-points for four light-pulse durations; 1: 10 μs, 2: 20 μs, 4: 40 μs, stars: 120 ns.

The scatter plots include all data for each pulse length regardless of whether the end point was of a track that stopped abruptly or that faded gradually. For a given value of R_{hol} a number of values exists for each of the holographic parameters, as expected. This is both because the illuminating beam was not a symmetric cone about the reference beam and because the tracks have different bubble sizes and thus different detectability. However, our concern here is with the distribution of the maximum values of the holographic parameters. Figure 6.39 gives maxima of the parameters for each bin of R_{hol} for the pulse lengths.

It can be seen that similar curves are obtained for pulse lengths of 0.1, 10, 20, and 40 μs. Since the phase shift of a bubble becomes more drastic the further the bubble is from the optical axis, it might be expected that the maxima for R_{nor} would decrease with increasing pulse lengths. This trend was not observed; the largest R_{nor} (50 cm) was observed for 40-μs pulses.

An approximate evaluation of the holographic fiducial volume for each set of data gives 0.30, 0.42, 0.37, and 0.31 m^3 for pulses of duration of 0.1, 10, 20, and 40 μs, respectively. The largest volume was obtained for 10-μs pulses and this volume decreased with increasing pulse lengths for 20- and 40-μs pulses, as expected. The small volume obtained for Q-switched pulses may be explained by the poor quality of these pulses and the small statistics. The Q-switched pulses used were produced by Version-4 circuitry, (cf. section 4.2.4). They were often accompanied with post-lasing which could result in a degradation of hologram quality.

Another number to note is the rate of "observed tracks" per hologram for each pulse length. From Table 6.5 these rates were 1.8, 2.0, 0.40, and

0.17 for the pulses with increasing lengths, respectively. This result confirms those of the laboratory tests (cf. Section 4.2.4) which showed that the diffraction efficiency of the holograms gets worse for the longer pulse durations.

6.4.7 Hologram Quality Variation with Ping (cf. p. 39)

When the holograms were not spoiled due either to improper performance of the laser or the feedback circuit, or to incompatibility of the laser light output power with the operating condition of the bubble chamber (microboiling), a systematic variation was observed for holograms taken in the expanding chamber as a function of ping number. The ping dependence of holograms had three signatures.

1. The density of holograms increased with ping numbers,[41] (Figure 6.40).
2. Laser-induced boiling increased with ping numbers, (Figure 6.41).
3. A less uniform, bigger size speckle pattern appeared on the holograms with larger ping numbers, (Figure 6.40).

Further observations were made for holograms taken in non-expanding and empty chamber. For a non-expanding chamber filled with liquid a sample of sixty holograms were examined in search of signature (3). Nine percent of holograms had a speckle pattern with a structure which was caused by turbulence since the recirculating pump was operating. These holograms had poor images of the dispersing lens. Otherwise no systematic variations in the speckle patterns of the holograms was detected. For a

---

41. The averaged density for a sample of 60 holograms were measured to be: $D_{ping1} = 0.38 \pm 0.03$, $D_{ping2} = 0.42 \pm 0.04$, $D_{ping3} = 0.47 \pm 0.05$.

warm empty chamber the holograms taken varied as a function of ping number, carrying signature (1) only (that is their density increased with ping numbers (Figure 6.42)).

What Caused these Variations

Although an immediate guess for the cause of these variations might be instability of the laser, it was shown that once the laser was in a stable operational mode it would produce holograms of consistent quality. The following observations confirm this statement.

1. The laser output energy varied by ± 5 % for 40 μs pulses and by ~ ± 9 % for shorter pulse durations, (Figure 4.8).
2. No variation in the laser output energy for 40 μs pulses was observed as a function of ping number: $E_{ping1} = 2.1 \pm 0.2$ J, $E_{ping2} = 2.1 \pm 0.1$ J, $E_{ping3} = 2.2 \pm 0.2$ J.
3. A test of the coherence length for various pulse durations, showed no variation in coherence length of the pulses as a function of ping number, (cf. Section 4.2.4).
4. No apparent variation in the beam profile was observed in examination of the burn patterns. However, this method is rather insensitive to small variations of the beam profile.

One explanation for the increase in density of the holograms might lie in a change of the dispersing lens curvature due to heating, so that more light is spilt into the reference beam. This extra light in the reference beam would only have to be of the order of tenths of microjoules to increase the hologram density by the order of 0.1. The increase in density is merely due to a more intense reference beam since the existence of this signature for the empty chamber holograms eliminates the possibility of

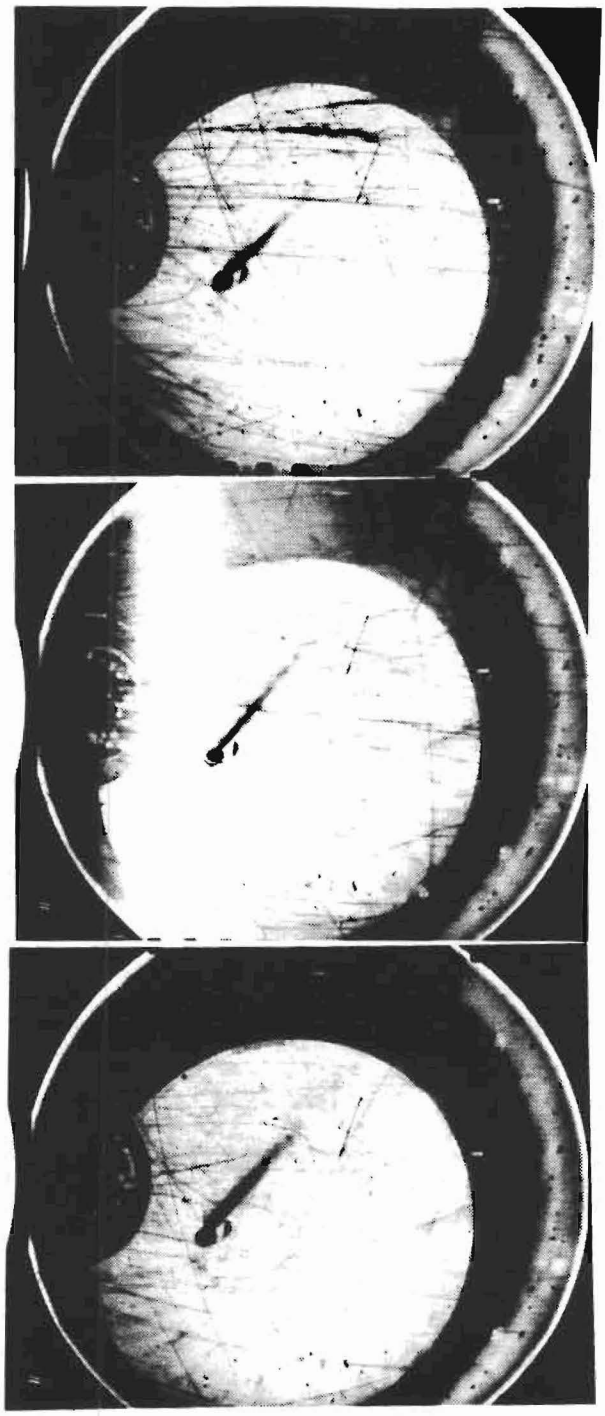

Fig. 6.41 Variation of the laser-induced boiling with ping number.

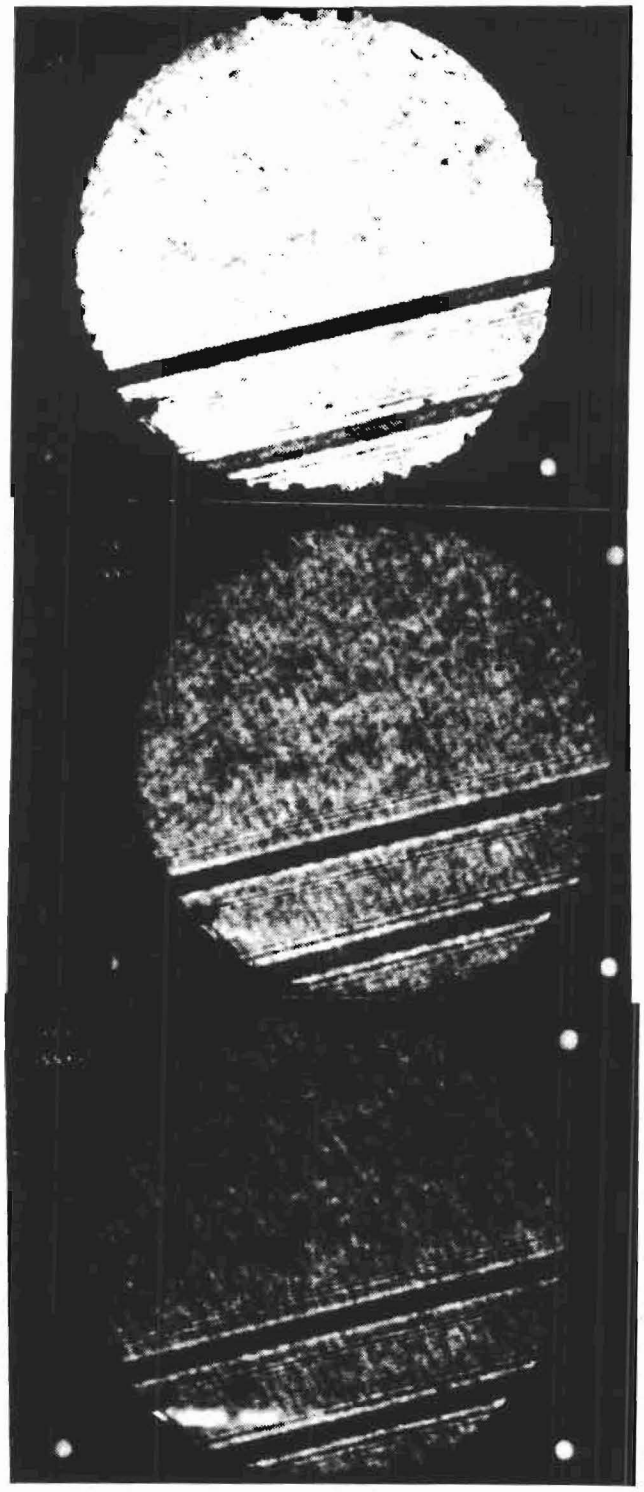

Fig. 6.42 Variation of the hologram density with the ping number. The holograms were exposed in the empty, warm chamber.

6.5 Summary

In this chapter, a presentation of dark-field holography for the 15-foot Bubble Chamber is given. A useful volume of 0.48 m^3, 3 % of the 14 m^3 total fiducial volume of the bubble chamber, has been successfully recorded holographically. The reasons for the small holographic volume have been discussed in great detail. Among the most important ones are the following:

a) The diffuse light scattered by the retrodirective Scotchlite was an important source of background noise. Coherent background light lowers the contrast and thus results in a lower resolution. Non-coherent background light fogs the film and lowers the brightness. These effects resulted in a large limiting BBR and consequently a small fiducial volume.

b) Light-pulses of 40-μs duration resulted in holograms which had a poor diffraction efficiency, and were subject to the bubble growth and/or movement effects. These long pulses also resulted in a distorted reference beam which could not be reproduced at reconstruction stage.

Other less important reasons were the poor laser-beam profile close to the aspheric lens, lack of a monitoring system to record the light-pulse characteristics, and lack of a quality film-processing procedure.

However, despite the problems mentioned above which are now well-understood, the experience with holography in the 1985 E-632 run has proven that the dark-field holographic technique is a feasible procedure. This technique has been upgraded in the second E-632 physics run in the forthcoming summer 1987 run. The major modifications are the following:

a) A new aspheric lens has been designed and built, to give an illuminated volume of 5 m^3, 30 % of total fiducial volume of the bubble chamber.

b) The upper section of the bubble chamber, approximately within a radial distance of 1 m from the holographic camera, is covered with baffles. More than ninety-five percent of laser light illuminating these regions is absorbed, reducing the background noise to a negligible amount.

c) Light-pulses of duration in the range of 2 - 10 μs will be used for exposing the holograms. A new pulse-stretching circuit, using FET switches and positive voltages to switch on the Pockels cell, has both improved the pulse-shape and the reproducibility of the pulse-length and pulse-energy.

d) The initial output beam transverse intensity distribution will be preserved by imaging it with an optical relay system. This system, composed of a set of focusing and collimating lenses, is designed, built, and installed in the laser beam path from the laser room to the bubble chamber.

e) An elaborate monitoring system using CCD cameras, powermeter, and various apertures and mirrors will be used to record the light-pulses characteristics.

f) Film processing procedure will be improved by better control of the humidity and temperature of the environment under which the exposed film is stored prior to processing.

It is hoped that this improved system will be successful in recording holographically high-energy neutrino interactions.

CONCLUSION

A high resolution imaging system with resolving power $\lesssim$ 100 μm must be used in large-volume bubble chambers in order to efficiently study the massive short-lived particles with lifetimes $\lesssim 10^{-12}$ s. Among the most interesting possibilities is the direct observation of the still undetected ν_τ in a proposed neutrino beam-dump experiment using the 15-foot Bubble Chamber. The main advantage of the holographic method over conventional photography in the 15-foot Bubble Chamber is its ability to reconstruct sharp images of bubble tracks of diameter ~ 100 μm over the entire depth of the chamber.

In this thesis, various aspects of 15-foot Bubble Chamber holography, in particular the dark-field (one-beam) method, have been investigated. In the development of this holographic method, several complementary optical systems were designed, built, and used for the first time.

The problem of holographing bubbles at large angles, where the light scattered by the bubble has fallen off in proportion to the light scattering coefficient, is analogous to that of particle analysis --determination of size, shape, position, orientation, and velocity of microscopic particles-- using a holographic system. Here, as in the 15-foot Bubble Chamber, a special diverging lens can be designed and built to give a light intensity distribution which increases with the scattering angle.

Stretching the light-pulses from 20 ns to sub-microseconds and up to 100 μs is appealing for all applications where the laser pulse strikes a medium which has a dynamic or damage threshold. Among the most

interesting applications is the transport of high intensity laser light through optical fibers. Furthermore, the increased coherence length of these prolonged pulses makes them attractive for holography of large volumes where the path difference between the reference and object beams can be very large.

The automated replay facilities built for the 15-foot Bubble Chamber holography, although specific to these holograms, have proven to be useful for the systematic reconstruction of a large number of holograms. The use of fiber optics to carry the laser light from the light source to the imaging optics has reduced the problem of transferring and positioning the beam through mirrors.

Since many problems were encountered with the current system, alternative holographic methods have been proposed and tested for the 15-foot Bubble Chamber. The most promising method is a bright-field, two-beam system which uses Scotchlite for illuminating the bubble tracks and fiber optics for transporting the laser light to the bubble chamber. However, there are still some technical difficulties associated with such a system which remain to be solved.

The holographic systems developed for the 15-foot Bubble chamber are complex and use the most advanced techniques. The design and development of a holographic system for this cryogenic chamber is a difficult problem because of the limited availability of space, restricted access to the chamber, the non-conventional optics, and the large volume of the chamber. For a successful high energy physics experiment, where high statistics data are needed, the holographic system used must operate with high reproducibility and reliability factors.

REFERENCES

--- Akbari, H., and Bjelkhagen, H., "Holography in 15-foot Bubble Chamber at Fermilab," Proc. of SPIE (Practical Holography), Vol. 615, pp. 7-12, Jan. 1986.

--- Allison, W., et al., "A Prototype Experiment to Study Charmed Particle Production and Decay using a Holographic High Resolution Hydrogen Chamber (HOLBC) and the European Hybrid Spectrometer," CERN/SPSC 80-116, SPSC/P 154, 1980.

--- Argan, P. E., and Gigli, A., "A New Detector of Ionizing Radiation. The Gas Bubble Chamber," Nuovo Cimento, Vol. 3, p. 1171, 1956.

--- Arsen´ev, V. A., Matveev, I. N., and Ustinov, N. D., "Nanosecond and Microsecond Generation in Solid-State Lasers (review)," Sov. J. Quantum Electron, Vol. 7, No. 11, pp. 1321-1332, Nov. 1977.

--- Askar´yan, G. A., et al., "The Effects of a Laser Beam in a Liquid," Soviet Phys. JETP., Vol. 17., No. 6., pp. 1463-1465, Dec. 1963.

--- Baland, J. F., et al., "Proposal to Study the Production of Charm and Bottom Particles using a Holographic Bubble Chamber (HOBC)", CERN/SPSC/80-120, SPSC/P 155, 1980.

--- Baltay, C., Bregman, M., Hibbs, M., Schaffer, A., Harigel, G., Eisler, F., Cence, R., Brucker, E. B., and Hart, T. R., "Talk at BEBC Users Meeting," CERN, Nov. 1982.

--- Benichou, J. L., Hervé, A., Johansson, K. E., Lecoq, P., Olivier, P., Roosen, R., Tavernier, S. P. K., Van Beek, G., Williams, O.R., "A

Study of Bubble Chamber Operating Conditions for Holographic Image Recording," Nucl. Inst. and Meth., Vol. 214, pp. 245-251, 1983.

--- Bjelkhagen, H., "Holographic Recording Materials and the Possibility to Increase their Sensitivity," CERN/EF 84-7, 1984a.

--- Bjelkhagen, H., Harigel, G., Pouyat, F., Seidl, W., Baltay, C., Bregman, M., Hibbs, M., Schaffer, Eisler, F., Cence, R., Brucker, E. B., and Hart, T. R., "Holographic Recording of Cosmic Ray Tracks in BEBC," Nucl. Inst. and Meth., Vol. 227, pp. 437-451, 1984b.

--- Bjelkhagen, H., "Investigation on the Resolution that can be obtained with the Baltay Holographic Arrangement for the 15-foot Bubble Chamber," Proc. Workshop on Holographic Techniques and Applications, Strasbourg, pp. 7-49, 1984c.

--- Bjelkhagen, H., Pouyat, F., Kasper, P., Miranda, E. E., Sekulin, R. L., Venus, W., and Walton, L., "Test of High Resolution Two-Beam Holography in a model of the Big European Bubble Chamber, BEBC," Nucl. Inst. and Meth., Vol 220, pp. 300 - 308, 1984d.

--- Bjelkhagen, H., Sekulin, R. L., and Walton, L., "Recent Developments in Two-Beam Holography in Large Bubble Chambers including the Use of Optical Fibers," Proc. Workshop on Holographic Techniques and Applications, Strasbourg, pp. 51 - 68, 1984e.

--- Blinov, G. A., Krestnikov, Iv., S., and Lomenov, M. F., "Measurement of the Ionizing Power of Particles in a Bubble Chamber," Soviet Phys. JETP, Vol. 4, p. 661, 1956.

--- Born, M., and Wolf., E., "Principles of Optics," The Macmillan Company, New York, 1964.

--- Brown, J. L., Glaser, D. A., and Perl, M. L., "Liquid Xenon Bubble Chamber," Phys. Rev., Vol. 102, p. 586, 1956.

--- Callen, W. R., Pantell, R. H., and Warszawski, J., "Phase Stretching of Q-Switched Lasers," Opto-Electron., Vol. 1, pp. 123-127, Aug. 1969.

--- Cence, R.,J. "E-632 Holography Development," University of Hawaii, Internal Report IR-85-82, 1982.

--- Collier, R. J., Burckhardt, C. B., and Lin, L. H., "Optical Holography," Academic Press, New York, 1971.

--- Costa, G., Fischer, W. E., Fogli, G. L., Froyland, J., Gerber, H., and Nyborg, P., "Kinematics and Symmetries," ed. Nikolic, M., Vol. 1, 1979.

--- Dainty, J. C., "Speckle Statistics and the Detection of Images in Hologram Reconstructions of Bubble Chamber Tracks and other Objects," PH.D. Thesis, Imperial College of Science and Technology, 1972.

--- Davies, G. E., "Scattering of Light by an Air Bubble in Water," Journal of The Opt. Sco. of America, Vol. 45, No. 7, pp. 572 - 581, 1955.

--- Denisyuk, Yu. N., "Photographic Reconstruction of the Optical Properties of an Object in Its Own Scattered Radiation Field," Sov. Phys. Dokl., Vol. 7, p. 543, 1962.

--- Derrick, M., "Comparisons of Charm and Beauty Production in e^+e^- Annihilations and Neutrino, Muon and Hadronic Collisions," Int. Conf. on Phys. in Coll., Blacksburg, ed. Trower, P., and Bellini, G., pp. 459 - 495, 1981.

--- Dykes, M., Lecoq, P., Gusewell, D., Hervé, A., Wenninger, H., Royer, H., Hahn, B., Hugentobler, E., Ramseyer, E., and Baretav, M., "Holographic Photography of Bubble Chamber Tracks: A Feasibility Test," Nucl. Inst. and Meth., Vol. 179, pp. 487-493, 1981.

--- Eckardt, V., Lecoq, P., Wenig, S., Wiatrowski, E., "A Holographic High Pressure Streamer Chamber," Nucl. Inst. and Meth., Vol. 225, pp. 651-655, 1984.

--- Eisler, F., "High Spatial Resolution Particle Physics Detectors," Nucl. Instr. & Meth., Vol. 163, p. 105, 1979.

--- Fisk, H. E., "Production of Charm and New Particles in Neutrino-Nucleon Interactions," 10th Int. Symp. on Lepton and Photon Interactions at High Energy, Bonn, ed. Pfeil, W., pp. 703 - 729, 1981.

--- Gabor, D., "A New Microscope," Nature, Vol. 149, p. 470, 1942.

--- Glaser, D. A., "Progress Report on the Development of Bubble Chambers," Nuovo Cimento, Vol. 11, Suppl. No. 2, p. 361, 1954.

--- Gordon, A. L., and Webster, J. M., "Optical Beam Relaying," Central Electricity Generating Board Report, Marchwood Engineering Laboratories, England.

--- Jackson, J. D., "Classical Electrodynamics," John Wiley & Sons, Inc., 1975.

--- Jones, M, private communication, University of Hawaii, 1986.

--- Haridas, P., Hafen, E., Pless, I., Harton, J., Dixit, S., Goloskie, D., and Benton, S., "Detection of short-lived Particles Using Holography," Opt. Eng., Vol. 24, No. 5, pp. 741-745, Sept. 1985.

--- Harigel, G., Riche, J., Horlitz, G., Wolff, S., "Numerical Calculations of the Recompression Time of Bubbles in Liquid Hydrogen Bubble Chambers," Unpublished 1968.

--- Harigel, G., Hilke, H. J., Linser, G., Schenk, F., "On the Formation of Narrow Bubble Tracks by a Laser Beam in Argon, Nitrogen and Hydrogen Bubble Chambers," Nucl. Inst. and Meth., Vol. 188, pp. 517-520, 1981a.

--- Harigel, G., Hilke, H. J., Linser, G., "On Bubble Tracks Formation by a Laser in BEBC Filled with Hydrogen," CERN/EF 81-8, June 1981b.

--- Harigel, G., Bjelkhagen, H., Pouyat, F., Seidl, W., Baltay, C., Bregman, M., Hibbs, M., Schaffer, Eisler, F., Cence, R., Brucker, E. B., and Hart, T. R., "Holographic Recording of Cosmic Ray Tracks in BEBC," Photonics Applied to Nuclear Physics: 2, Nucleophot, Strasbourg, pp. 69-71, 1984.

--- Harigel, G., Baltay, C., Bregman, M., Hibbs, M., Schaffer, A., Bjelkhagen, H., Hawkins, J., Williams, W., Nailor, P., Michaels, R., and Akbari, H., "Pulse Stretching in a Q-Switched Ruby Laser for Bubble Chamber Holography," App. Opt., Vol. 25, No. 22, pp. 4102-4110, 1986.

--- Hariharan, P., "Optical Holography," Cambridge University Press, 1984.

--- Hervé, A., Johansson, K. E., Lecoq, P., Olivier, P., Pothier, J., Veillet, L., Waurick, G., and Tavernier, "Performance of the Holographic Bubble Chamber HOBC," Nucl. Inst. and Meth., Vol. 202, pp. 417-426, 1982.

--- Hilke, H. J., "On the Formation and Application of Laser Induced Ionization Tracks in Gases," Nucl. Inst. and Meth., Vol. 174, pp. 145-149, 1980.

--- Hordvik, A., "Pulse Stretching Utilizing Two-Photon-Induced Light Absorption," IEEE J. Quantum Electron, Vol. QE-6, PP. 199-203, Apr. 1970.

--- Horlitz, G., Wolff, S., and Harigel, G., "Bubble Growth and Bubble Densities in Bubble Chambers Filled with Neon/Hydrogen Mixtures," Nucl. Inst. and Meth., Vol. 117, pp. 115-124, 1974.

--- Hugentobler, E., Hahn, B., and Steinrisser, F., "Relativistischer Zuwachs der Blasendichte von Supuren schneller Teilchen in einer Freon-Blasenkammer," Helv. Phys. Acta, Vol. 36, pp. 601-621, 1963.

--- Kenney, V. P., Shephard, W. D., Madden, W. B., and Harrington, E. A., "Design Consideration for the Use of Neon-Hydrogen Mixtures in the 12-Foot Hydrogen Bubble Chamber," ANL-BBC 92, 1967.

--- Koechner, W., "Solid-State Laser Engineering," Springer-Verlag New York Inc., 1976.

--- Lecoq, P., Wenig, S., Wiatrowski, E., Eckardt, V., "Holography and Dark Field Illumination as Light Resolution Recording Technique for High Pressure Streamer Chambers," Photonics Applied to Nuclear Physics:2 Nucleophot, pp. 120-135, Dec. 1984.

--- Leith, E. N., and Upatneiks, J., "Reconstructed Wavefronts and Communication Theory," J. Opt. Soc. Amer., Vol. 55, p. 1566A, 1965.

--- Lovberg, R. V., Wooding, E. R., and Yeoman, M. L., "Pulse Stretching and Shape Control by Compound Feedback in a Q-Switched Ruby Laser," IEEE J. Quantum Electron, Vol. QE-11, No. 1, pp. 17-20. Jan. 1975.

--- Majka, R., "Progress toward a Diffusion Suppressed Holographic Streamer Chamber," Photonics Applied to Nuclear Physics:2 Nucleophot, pp. 136-156, Dec. 1984.

--- Marshall, F. R., and Roberts, D. L., "Use of Electro-optical Shutters to Stabilize Ruby Laser Operation," Proc. IRE, Vol. 50, p. 2108, Oct. 1962.

--- Matthews, B. J., "Measurement of Fine particulate in Pollution Control," TRW System Group.

--- Merritt, F., et al., "Production of Same-Sign Dimuons by 0-800 Gev Neutrinos and Antineutrinos," Proceedings of 13th Annual Mtg. of Div. of Particles and Fields of the APS, Salt Lake City, Utah, 1987.

--- Mishin, V. I., "Ruby Laser for Generating Microsecond Light Pulses having a Narrow Spectrum" Pri. Tekh. Eskp., No. 4, pp. 181-182, Aug. 1971.

--- Morrison, D. R. O., "Holography for Large Volume Bubble Chamber and Neutrino Physics," Proc. of a meeting on the application of holographic techniques to bubble chamber physics, Edited by R. L. Sekulin, Rutherford and Appelton Lab., pp. 221-239, 1981.

--- Nailor, P. R., "HOLRED," Proc. Workshop on Holographic Techniques and Applications, Strasbourg, pp. 83-94, 1984

--- Neumann, D. B., "Holography of Moving Scenes," Journal of Opt. Soc. of America, Vol. 58, No. 4, pp. 447-454, 1968.

--- Pantell, R. H., and Warszawski, J., "Laser Power Stabilisation by means of Nonlinear Absorption," Appl. Phys. Lett., Vol. 11, pp. 213-215, Oct. 1967.

--- Perkins, D. H., "Introduction to High Energy Physics," Addison-Wesley Publishing Company, second edition, 1982.

--- Perl, M. L., et al., "Evidence for Anomalous Lepton production in e^+ - e^- Annihilation, Phys. Rev. Letters, Vol. 355, p. 1489, 1975.

--- Peters, M. W., and Cence, R. J., "Design, Construction and Testing of a Holographic Measuring Machine," Proc. Workshop on Holographic Techniques and Applications, Strasbourg, pp. 95-98, 1984

--- Peyrou, C., "Bubble Chamber Principles," Bubble and Spark Chambers, ed. Shutt, R. P., Vol. 1, pp. 19-59, 1967.

--- Plesset, M. S., and Zwick, S. A., "The growth of Vapor Bubbles in Superheated Liquids," J. Appl. Phys., Vol. 25, p. 493, 1954.

--- Poesposoetiopto, F. H., and Hugentobler, E., "A Study on Bubble Formation in the Bubble Chamber," Helvetica Physica. Acta., Vol., 43, pp. 203-222, 1970.

--- Pouyat, F., "Preliminary Tests on Holography in BEBC," Proc. Workshop on Holographic Techniques and Applications, Strasbourg, pp. 227-237, 1981.

--- Ramseyer, E., Hahn, B., Hugentobler, E., "BIBC, A High Resolution Heavy Liquid Miniature Bubble Chamber," Nucl. Inst. and Meth., Vol. 201, pp. 335-340, 1982.

--- Reay, N. W., "Tagging Charm with Decay Lengths," Int. Conf. on Phys. in Coll., Blacksburg, ed. Trower, P., and Bellini, G., pp. 424 - 438, 1981.

--- Royer, H., "Choice of the Recording Arrangement for Bubble Chamber Holography," Proc. Workshop on Holographic Techniques and Applications, Strasbourg, pp. 117-122, 1981.

--- Safety Report, 15-foot Bubble Chamber, Fermi National Accelerator Laboratory, Batavia, IL, 1972.

--- Sekulin, R. L., "Holography with HOLEBC," Photonics Applied to Nuclear Physics: 1, Nucleophot, Strasbourg, pp. 75-86, 1981.

--- Seitz, F., "On the Theory of the Bubble Chamber," Phys. Fluids, Vol. 1, p. 2, 1958.

--- Smart, W. M., private communication, Fermi National Accelerator Laboratory, 1985.

--- Smith, H. M., "Principles of Holography," John Wiley & Sons, New York, 1975.

--- Stamberg, R. C., and Gillespie, D. E., "Laser-Stimulated Nucleation in Bubble Chamber," J. Appl. Phys., Vol. 37, pp. 459-461, 1966.

--- Tavernier, S. P. K., "Holographic Image Recording in Visual Particle Detectors," Nucl. Inst. and Meth., Vol. 225, pp. 642-649, 1984.

--- Thomas, C. H., and Price, E. V., "Feedback Control of a Q-Switched Ruby Laser," IEEE J. Quantum Electron., Vol. QE-2, pp. 617-623, Sept. 1966.

--- Trilling, G. H., "The Properties of Charmed Particles," Phys. Rep., Vol. 75, No. 2, pp. 57 - 124, 1981.

--- Ushida, N., et al., "Limits to $\nu_\mu,\nu_e \rightarrow \nu_\tau$ Oscillations and $\nu_\mu,\nu_e \rightarrow \tau^-$ Direct Coupling," Phys. Rev. Letters, Vol. 57, No. 23, Dec. 1986.

--- Welford, W. T., "Obtaining Increased Focal Depth in Bubble Chamber Photography by an Application of the Hologram Principle," Appl. Opt., Vol. 5, No. 5, pp. 872-873, May 1966.

--- Welford, W. T., "Bubble Chamber Principles," Bubble and Spark Chambers, ed. Shutt, R. P., Vol. 1, pp. 233-312, 1967.

--- Welford, W. T., "Bubble Chamber Holography," Proc Int. Conf. on Bubble Chamber Technology, edited by M. Derrick, pp. 1024-1038, 1970.

--- Wooding, E. R., and Yeoman, M. L., "A Laser Scattering Homodune Technique for Studying Plasma Drift Waves," Proc. 10th Int. Conf. Phenomena in Ionized Gases, P. 417, 1971.

--- Withrington, R. J., "Light Scattering by Bubbles in a Bubble Chamber," App. Optics, Vol 7, No. 1, pp. 175 - 181, 1968.

--- Withrington, R. J., "Bubble Chamber Holography," Proc. The Eng. Uses of Holography, edited by E. R. Robertson, and J. M. Harvey, Cambridge, pp. 267-278, 1970.

--- Young, J. F., Murray, J. E., Meles, R. B., and Harris, S. E.,"Q-Switched Laser with Controllable Pulse Length," Appl. Phys. Lett., Vol. 18, pp. 129-130, Feb. 1971.

APPENDIX I

Ia 5-μs Pulse Circuitry (Version 2)

Figure I.1 shows a layout of the circuit. The inductance was removed, and a 1-MΩ resistor provided a path for the 330-pF capacitor to discharge thus allowing the krytron to retrigger for the next pulse. Since longer pulses required a current flow from the phototube over a longer period of time, the addition of a 0.02-μF capacitor and 1-KΩ resistor in parallel with the phototube allowed storage of charge in addition to that provided by the capacitance of coaxial wires between the power supply (C = 0.004 μF) and phototube. Reliable 5-μs pulses with repetition rates of 0.75 pulses/minute were obtained, (Figure I.2). For time intervals shorter than 1.5 min. 25 % of pulses were shorter in length and spikier.

Ib. Tens of Microseconds Pulse Circuitry (Version 3)

To prolong the pulses beyond 5 μs the Q-switching speed of the Pockels cell had to be reduced. The pulse length dependence on the Q-switching speed has been discussed by Arsen´ev (1977). A slow switching speed does not initiate depletion of the population inversion as rapidly and leaves much more photon density to be modulated by the feedback loop. Slow Q-switching could also result in the shrinkage of the beginning spike. Figure I.3 shows a layout of the circuit. A 0.04-μF capacitor across the 2-MΩ resistor decreased the krytron resistance and increased the exponential rise time of the potential on the krytron side of the Pockels cell to 20 μs. The lower trace in Figure I.4 shows the behavior of this potential. The

upper trace is the potential on the phototube side of the Pockels cell. When the light hits the phototube, this voltage rises to 500 V and, after a time delay of 30 μs determined by 0.03-μF capacitance and 1-KΩ resistance, goes to zero with a decay time of 450 μs, determined by the 0.03 μF and the 15 MΩ.

Long pulses, up to 100 μs, were produced by this circuit. However most of the pulses exhibited post-lasing, a large spike at the beginning, and an amplitude jitter with large magnitude, (Figure I.5). The post-lasing was due to the population inversion which, as a result of the slow switching speed, was not depleted during the main pulse. The large spike, almost ten times higher in magnitude than the average amplitude, was a result of the high-gain JK laser cavity, while the amplitude jitter of the rest of pulse was due to slow response time of the feedback loop compared with the photon density variations.

A remedy for the first two problems is to operate the oscillator at very low flashlamp voltages and a large Pockels cell delay (~ 1.35 ms). Pulses of 25 - 85-μs duration could then be produced by varying the flashlamp voltage in range of 1.65 - 1.85 kV. These pulses still had large jitter in the amplitude and their intensity decreased with time as the population inversion depletes. The pulses from the oscillator had a low energy since the cavity had low gain at small pump voltages and the Pockels cell delay was long. The amplification of the pulses through the rest of the laser system was also small (only a few hundreds of millijoules) as the amplifiers had their maximum gain at fixed time delays of ~ 1.2 ms.

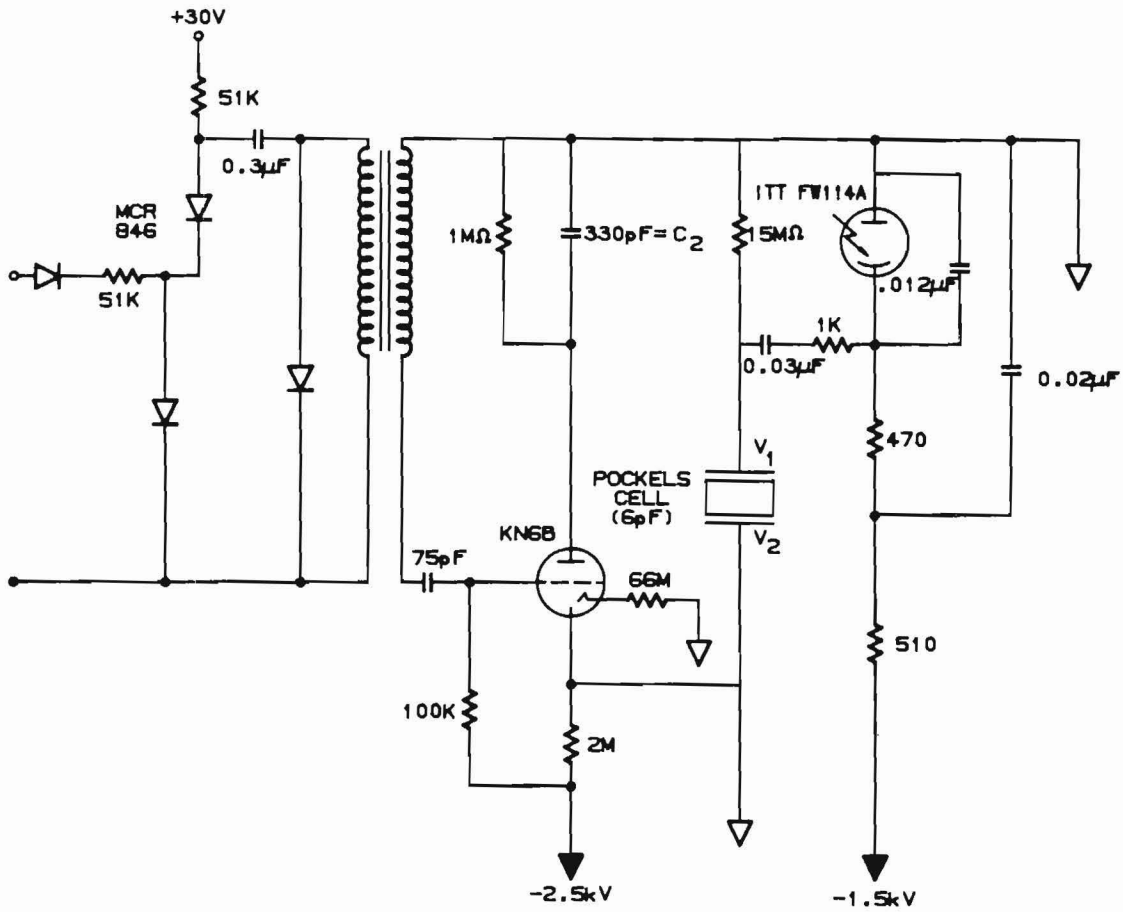

Fig. I.1 5-us stretched pulse circuit, Version 2.
FW114A-phototube, KN6B-kryton.

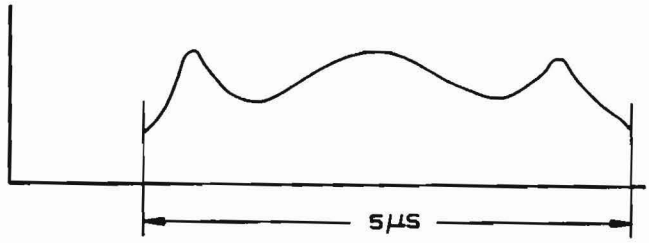

Fig. I.2 Typical output from Version-2 circuit.

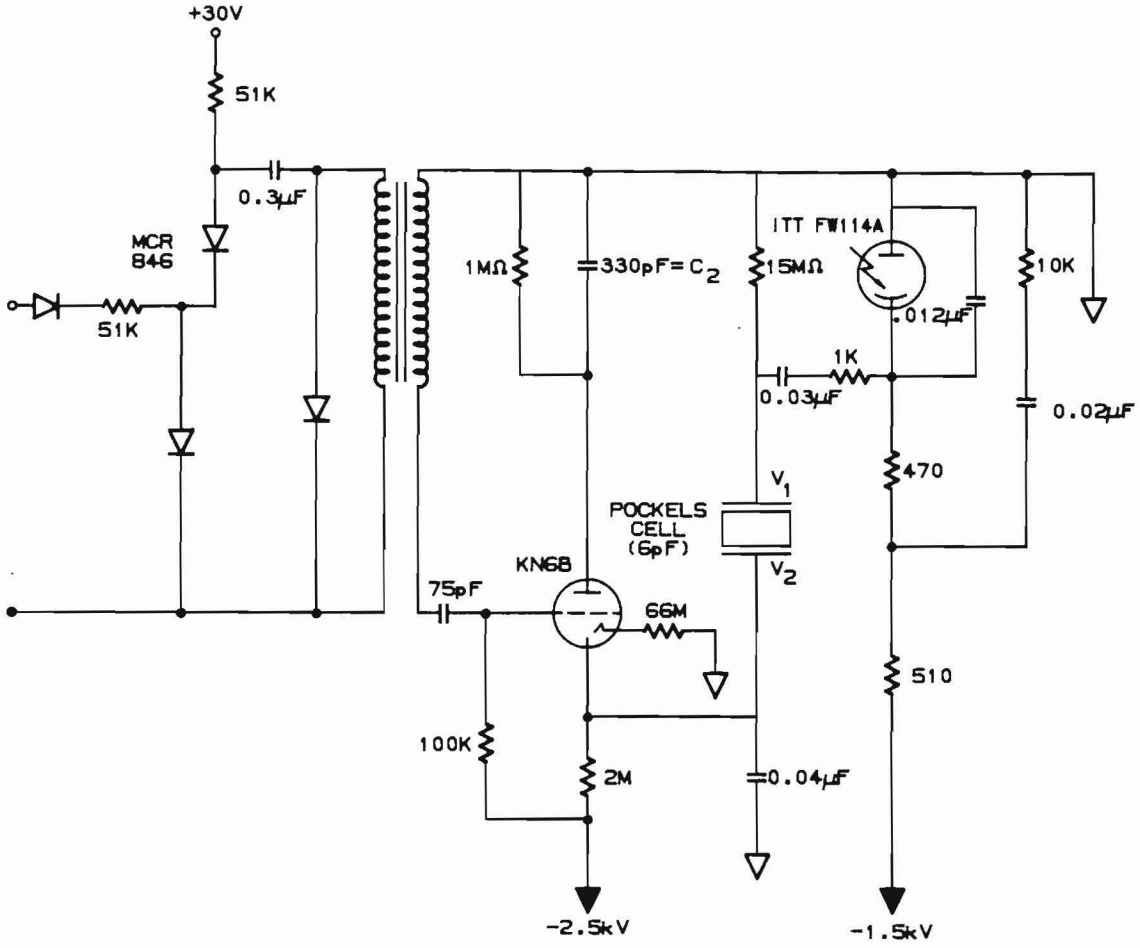

Fig. I.3 Stretched pulse circuit for the JK laser, Version 3. FW114A-phototube, KN6B-kryton.

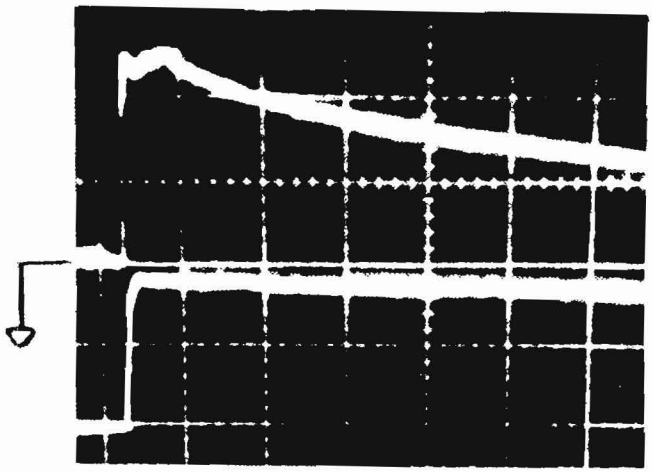

Fig. I.4 Voltage waveform on the two sides of the Pockels cell (500 μs/div): The upper trace is the feedback voltage V_1 (200 V/div). The lower trace is the voltage on non-feedback side V_2 (500 V/div). The initial value of V_2 is -1000 V.

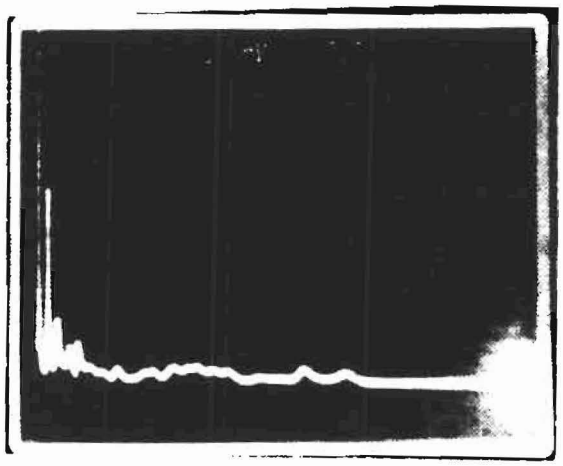

Fig. I.5 Typical light output of the Version-3 circuit.

APPENDIX II

IIa Holographic Alignment

There were two procedures used to align the laser beam from the laser room through the vacuum pipe onto the dispersing lens, and into the bubble chamber. This alignment was critical both for having the reference beam land on the hologram, and for obtaining a symmetric illumination cone about the reference beam. One way to align the beam was to center the beam on each mirror in the pipe by adjusting the previous mirror, and then onto the the dispersing lens. A Helium-Neon laser was used with its optic axis carefully aligned with that of the ruby laser. The Tee junction before the laser entrance window of the chamber was used as a reference point for the alignment and also the center of the diverging lens. This method was accurate, but tedious, and it was not possible to use it when the chamber was cooled down.

The second way was to search for the reference point source by exposing holograms for different positions of the sliding aperture placed before the tee junction. First, a slit of width of 0.64 cm was scanned along one direction of a region approximately 2.54 cm in diameter, (Figure II.1a), which contained the reference beam. The slit test determined one coordinate of the point from which the reference beam diverged to yield holograms with visible diffraction pattern of the wires strung across the chamber. The size of this overlap region of the two positions of the slit was 0.32 cm. The second coordinate was then determined by scanning a 0.64 cm diameter aperture along this slit position, (Figure II.1b). In this fashion the

coordinates of the reference beam were determined within a square of 0.32 cm side, (Figure II.1b). Now if the beam were not tilted in the pipe, it would be symmetric on the dispersing lens with the reference beam at the center of the lens. And if the reference beam was created only from a point source the density on the hologram and the image of the lens would be invariant for holograms made with apertures of various sizes, 0.64, 1.3, 1.9, and 2.5 cm diameter. In fact this proved to be the case in the first test of this method. The density,[42] speckle pattern, and the lens image from the holograms were independent of aperture size. Yet after the dispersing lens was moved back 10 cm from its original position, the alignment of the beam by this method became difficult, and a perfect alignment was never really accomplished. In this case, although the coordinates of the reference beam were determined with the described procedure, due to a slight tilt of the beam traveling in the pipe there was some light scattered from the inner wall of the tube, (with the lens on one end of it and the window on the other end), so that the density[43] of the holograms varied with the aperture size. Multiple images of the lens and a variation in the speckle pattern of the holograms[44] were seen which further implied the existence of extraneous point sources acting as secondary reference beams.

---

42. The density of the holograms were 1.1 for all four apertures.

43. The density of holograms for apertures of 0.6, 1.3, 1.6 cm were 0.48 ± 0.01, 0.72 ± 0.08, 0.91 ± 0.12, respectively.

44. a) A small structure at the left corner of hologram which grew bigger with bigger aperture sizes.
    b) Cross hatched structure which appeared for 1.6 cm aperture and overwhelmed the hologram for 1.9 cm aperture.

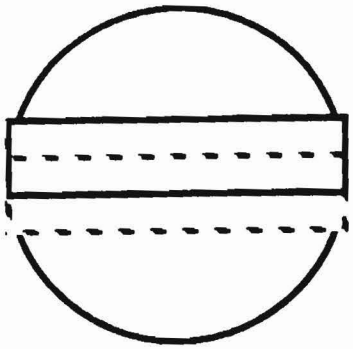

(a)

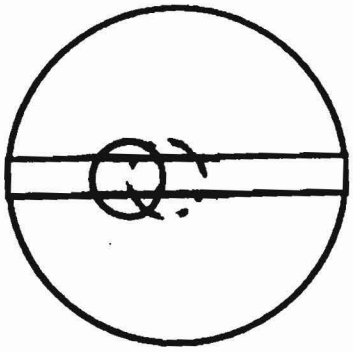

(b)

Fig. II.1 Determination of the coordinates of reference beam point source using a) a slit, and b) a circular aperture.

IIb Holographic Parameter Codings

Symbols for a range of Beam Balance Ratio (BBR) values.

Symbol	<BBR≤
A	.1E-10 - .5E-10
B	.5E-10 - .1E-09
C	.1E-09 - .5E-09
D	.5E-09 - .1E-08
E	.1E-08 - .5E-08
F	.5E-08 - .1E-07
G	.1E-07 - .5E-07
H	.5E-07 - .1E-06
K	.1E-06 - .5E-06
L	.5E-06 - .1E-05
M	.1E-05 - .5E-05
N	.5E-05 - .1E-04
O	.1E-04 - .5E-04
P	.5E-04 - .1E-03
Q	.1E-03

The coordinates for the holographic film and the dispersing lens in its original and moved position in the bubble chamber coordinate system.

	X(cm)	Y(cm)	Z(cm)
Holographic Film :	+ 96.2	+ 71.8	+185.4
Dispersing Lens : (original)	-111.0	- 21.6	-153.5
Dispersing Lens : (moved)	-116.4	- 24.0	-162.4

APPENDIX III

H. H. Bingham, J. Lys, G. P. Yost
University of California, Berkeley

G. T. Jones, R. Jones, S. O'Neale, K. Varvell
University of Birmingham

M. Barth, E. de Wolf, P. Marage, J. Moreels,
L. Verluyten, S. Willocq, J. Sacton
Univ. Libre de Bruxelles

H. Drevermann, K. Geissler,
D. R. O. Morrison, P. Schmid, H. Wachsmuth
CERN

N. K. Rao, V. K. Gupta, S. K. Badyal,
G. L. Kaul, Devanand, P. V. K. S. Bhabha
Jammu University

I. S. Mittra, J. M Kohli,
J. B. Singh, P. M. Sood, T. K. Mukerjee
Punjab University

H. Bjelkhagen, W. Smart, L. Voyvodic
Fermi National Accelerator Laboratory

R. Cence, F. Harris, V. Jain,
M. Jones, M. Peters, V. Peterson
University of Hawaii

R. Burnstein, J. Hanlon, R. Naon, H. Rubin
Illinois Institute of Technology

R. Campbell, D. Miller, P. Nailor
Imperial College

M. Aderholz, L. Deck, N. Schmitz, W. Wittek
Max-Planck Institut fuer Physik & Astrophysik

P. Allport, G. Corrigan, G. Myatt
Oxford University

D. Deprospo, M. Kalelkar, R. Plano
Rutgers University

J. Guy, R. Sekulin, S. Sewell, W. Venus
Rutherford Appleton Laboratory

J. P. Baton, Ch. Coutures, P. Kasper, M. Neveu
Centre d´Etudes Nucléaires, Saclay

H. Akbari, F. Kafka, R. H. Milburn, G. Saitta, J. Schneps
Tufts University